Characterization of Halogen Bonds with Multinuclear Magnetic Resonance in the Solid-State, X-ray Crystallography, and Quantum Chemical Calculations

Jasmine Viger-Gravel

A Thesis Submitted to the Faculty of Graduate and Postdoctoral Studies at the University of Ottawa in Partial Fulfillment of the Requirements for the Degree of

Doctor of Philosophy in Chemistry

Ottawa-Carleton Chemistry Institute
Department of Chemistry
Faculty of Science
University of Ottawa

uOttawa

ABSTRACT

Solid-state nuclear magnetic resonance (SSNMR) has proven to be a useful tool in the characterization of non-covalent interactions such as hydrogen bonding and cation-π interactions. In recent years, the scientific community has manifested a renewed interest towards an important class of non-covalent interaction, halogen bonding (XB), as it has applications in various fields such as crystal engineering and biological processes. This dissertation demonstrates that NMR parameters measured in the solid state are sensitive to changes in electronic structure, which are caused by halogen bonds.

A series of halogen bonded compounds exhibiting interactions between different diiodoperfluorobenzenes (*p*- $C_6F_4I_2$, *o*- $C_6F_4I_2$, *sym*- $C_6F_3I_3$, *p*- $C_6H_4I_2$) and various halogen bond acceptors have been synthesized as part of this work. These new halogen bonded compounds were characterized with a combined theoretical and experimental SSNMR, X-ray diffraction (XRD) methods. The complete multinuclear magnetic resonance spectroscopy of the nuclei involved directly in the halogen bond (^{13}C, $^{14/15}N$, ^{31}P, ^{77}Se, $^{35/37}Cl$ and $^{79/81}Br$) were recorded at multiple magnetic fields (4.7, 9.4, 11.75 and 21.1 T). The specialized SSNMR experiments provided high-resolution spectra of quadrupolar nuclei, which were WURST-QCPMG or solid-echo type experiments combined with the variable offset cumulative spectral (VOCS) method, as for spin 1/2 nuclei cross polarization magic angle spinning (CPMAS) experiments were usually appropriate.

This dissertation will discuss successful applications of SSNMR spectroscopy to characterize halogen bonds, it will demonstrate the significant changes in NMR observables in the presence of XB interaction and thus establish that NMR parameters are very sensitive

to halogen bonding interaction. Furthermore, this work explains why the NMR parameters are correlated with the halogen bonding interaction. The different trends observed between the NMR observables and the halogen bonding were further understood with a ZORA-DFT natural localized molecular orbital (NLMO) study.

ACKNOWLEDGEMENTS

Firstly, I would like to thank my doctoral supervisor, Dr. David Bryce. I am thankful to have met Dave and have been part of the Bryce lab. I first became an honours student in Dave's group in 2010, there, I developed a love of NMR. This passion ensured the undertaking of a Masters, where my project seemed to come to an end too quickly. Hence, with the encouragement of Dave, I discovered I had it in me to pursue my graduate studies and accomplish a doctoral thesis. Thank you for your guidance and for sharing your knowledge of SSNMR. Thank you for sending me to multiple international conferences over the past years where I have had the opportunity to present my research, I have benefited so much from those experiences. Thank you for always being available to discuss our projects and science. Over the years, I have appreciated tremendously how you reply to your emails so quickly, and, to give an example of this devotion, I will always remember that time you came in on a Saturday to help me when I was having trouble with the MAS probe. Thank you for your generosity, and the times the Bryce lab goes out for beers (on you!), it builds team spirit.

Secondly, I would like to thank the professors' part of the examination committee of the current dissertation: Dr. Natalie Goto (University of Ottawa), Dr. Jaclyn Brusso (University of Ottawa), Dr. Maria DeRosa (Carleton University), and my external examiner for reading my dissertation. Professor Brusso and Professor Goto are also acknowledged for their part in my Ph. D. committee over the past years.

Thirdly, I would like to thank a few member of the department of chemistry that had a special role in my formation. I was always very appreciative of their counsel and their mentorship. I view Glenn as my role model; you are an amazing NMR manager. I

will always remember the first time I asked you a question when I was an undergraduate student: Jasmine, what do you want NMR to tell you? That is when I learned that NMR is a powerful technique, if you know what you are looking for, there is the right experiment for it. I aspire to be a great NMR manager where I can troubleshoot problems as successfully as yourself. Eric, you are the first NMR spectroscopist to have taught me how to correctly setup any echo experiment at the 900 facility. Thank you, it is skills and knowledge I will use all my career! Dr. Victor Terskikh, thank you for making every visit to the 900 MHz memorable ones, and especially successful ones since we yielded amazing results there. I also thank Ilia Korobkov for his contribution to the collection of single-crystal data reported in this thesis and his knowledge that he shared openly with me. Dr. Tara Kell, thank you for your training and advice in the acquisition of powder diffraction experiments. Thank you Dr. Alain St-Amant for taking me as a TA, it was a pleasure to work with you those last four years. I will always be grateful to have been chosen for the JCEMolChem program, as it was an unforgettable experience. I also thank you, Marta Cepek, for your time, your kind words of encouragements, and your help in the teaching of English grammar.

I would like to thank other staff members of our chemistry department. Josée and Annette, thank you for your assistance, guidance, as well as answering my multiple questions in regards to our department over the years. I would like to thank Lorraine Houle for making all the administrative tasks so easy (you are efficient!), as well as making them enjoyable! Thank you for your support and concern for my well-being during my graduate studies. Thank you Daniel Lafleur for always helping me out when I needed specialized laboratory equipment. Thank you for making the glass stoppers, without them I would not have been able to collect publishable results.

My time in the Bryce Lab would not have been the same without Dr. Kevin Burgess and Dr. Frédéric Perras. I met these guys in second year of our undergraduate studies in a physics class, and I never thought I would spend the next eight years with them, but what a wonderful eight years it has been. Fred, your passion for NMR is intoxicating, thank you for updating us every day with the new papers out there, you've helped me keep up! Also, your ability to make everything look easy has helped me push my limits. Kevin, as you know, I have always valued your insight and opinion, either if its regarding SSNMR, synthesis or personal questions, thank you. Also, Kevbeau, I am grateful for facetime as I miss our daily talks all the time, at least now we can have long talks every once in a while. We have been through so much, undergrad, Paris, and Ph.D.! Your support in all those events has been much appreciated. I also want to thank you guys for keeping it light in the office; we've had a lot of great laughs! Merci aussi à *Mr. Mousteille qui pense que le papier de ma thèse est poreux.*

I know want to mention previous and present members of the Bryce Lab, who have contributed to my experience in the last four and half years. Firstly, thank you Dr. Igor Moudrakovski for your encouragement during the summer 2015 when I was down because of my *mononucleosis*, it was not an easy time. I also want to thank Dr. Cory Widdifield, Dr. Becky Chapman, Dr. Andy Lo, Joseph Weiss, for sharing their expertise at the beginning of my studies. Cory helped setup my first ^{14}N WURST-QCPMG experiment on the 9.4 T magnet, an experiment I now use often and he was a great mentor to all of us in the laboratory. Thank you Cory for showing us the importance of attention to detail and for giving me constructive comments on my papers. Becky, thank you for your explanation on multiple of the NMR principles, as well as being a female role model. I am glad to have worked with my good friends Rob Attrell, and Elisabeth Messner-Henning, both of whom

I met in undergrad. Rob thank you for teaching me Gaussian and CASTEP calculations, that skill came handy during my Ph.D. Liz, I am so happy we have had the opportunity to have met each other, I cherish our friendship. Thank you for bringing my attention to the JCEMolChem program, it changed my life and shaped my career in Chemistry. Dr. Se-Woung Oh, you showed us how to work hard and there is no such thing as NMR time booking issues: book overnight! I look forward to my eventual trip to Seoul.

I would like to thank the current members of the Bryce lab who I have had the chance to work with over the last year or so, Patrick Szell, Scott Southern, and Yijue Xu (Collette). Pat, I am happy to see you are as involved and passionate of halogen bonding as I am. Your passion pushed you to pursue a summer internship in one of the best crystal engineering labs in Italy; I am thrilled for you! Can't wait to see which paper you will publish. Scott, I am envious of your cool, calm and collected figure in front of an audience when answering questions after a talk. I have to practice that allure. Good job on finishing your first tetral bond paper, I wish you more success like that one! Collette, I am thankful to have worked with you this past year. Your positive attitude and great laugh have made the last stressful year much more enjoyable. On top of that, you are a great learner, and independent student, which are great skills for a graduate student. Good luck in your Masters!

I have also had the opportunity to work with multiple undergraduate students who have helped with my various research projects: Mustafa Zeybek, Sophie Leclerc, Julia Meyer, and Nuiok Dicaire. Sophie, we worked on the hardest project together, and it payed off! I could not have pulled it off without your organisation skills and optimism. Also, I value the friendship we built during that time. Julia, your ability to multitask and your drive are impressive! Also, I thank you for keeping the project alive during the summer I was

sick with *mononucleosis*. I was lucky to have a student that was autonomous like yourself. Best of luck with your graduate studies! Nuiok, you were also a student with drive. I am still impressed, you volunteered in our lab at the age of 16 years old and you got involved in multiple projects! I also want to acknowledge multiple honours and summer students as well as international students or professors whom have made the Bryce lab an enjoyable place to work on a everyday basis, : Mélanie Ouellette, Matthew Leclerc, Devon Fyson, Cedric Farthouat, Dr. Zheng Ping Wu, Jessica-Lee Maiorino, Yang Xu, Aurore Lebrun, Prisca Hendarsa, Arnaud Pinchaud, Samuel El Mestiri and the current summer students: Michael West, Sumaya Mohamed, Russell Gill, Jeremy Chi Hung Chin, Ludovic Brunet, Amanda Alain, Syed Abdul-Wasay, and Tanya Yeuchyk.

Finally, I want to thank my friends and family for their continuous support. Your encouragements were the motivation I needed, I acknowledge you: Tanya, Kim, Vero, Isa, Janick, Anne4, Carolyn. Your friendship brought a balance that was much needed during the course of my graduate studies. Merci Mom et Dad, your love and devotion to my upbringing have brought me here today. I am forever grateful to have parents who are dedicated to the success of their girls like yourself. Thank you to my sister Jade for being my best friend, we always have the best time together. We share the same sense of humour; you get me and only you can figure out what I am singing. I also want to thank my extended family for their support during the last years: Pierre, Micheline, Marc-André and Vanessa. Mon amoureux, Bruno, je t'aime. Merci pour ta patience, ta générosité et ta nouvelle capacité de me faire rire (). I look forward to the adventures awaiting us, I would not want to live anyone of them without you.

TABLE OF CONTENTS

LIST OF FIGURES

LIST OF TABLES

LIST OF ABBREVIATIONS

1D, 2D, 3D	one, two or three dimensional
au.	atomic units
AO	atomic orbital
acq	acquire
ADF	Amsterdam Density Functional
B3LYP	Becke three parameter Lee-Yang-Parr
BOA	Born-Oppenheimer Approximation
Bu	butyl
CASTEP	Cambridge Serial Total Energy Package
CCDC	Cambridge Crystallographic Data Centre
CP	cross polarization
CPMAS	cross polarization magic angle spinning
CS	chemical shift
CSA	chemical shift anisotropy
CT	central transition
CW	continuous wave
DE	dead time
DFT	density functional theory
DNA	deoxyribonucleic acid
DSO	diamagnetic spin-orbital coupling
EFG	electric field gradient
Et	ethyl
FC	Fermi-contact coupling
FC × SD	Fermi-contact spin-dipolar cross coupling
FID	free induction decay
FT	Fourier transformation
GGA	generalized gradient approximation
GIPAW	gauge-including projector-augmented-wave
HB	hydrogen bonds
Hz	hertz
ICDD	International Centre for Diffraction Data
IR	infrared
IUPAC	International Union of Pure and Applied Chemistry
kHz	kilohertz
LCAO	linear combination of atomic orbitals
MAS	magic angle spinning
mb	millibarn (1 mb= $1\cdot 10^{-31}$ m^2)
Me	methyl
MHz	megahertz
MO	molecular orbital
MS	magnetic shielding

n.a.	natural abundance
NBO	natural bonding orbital
NLMO	natural localized molecular orbital
NMR	nuclear magnetic resonance
o-$C_6F_4I_2$ or 1, 2- DITFB	*ortho*- diiodotetrafluorobenzene
PAS	principal axis system
PBE	Perdew Burke Ernzerhof
p-$C_6F_4I_2$ or 1, 4- DITFB	*para*- diiodotetrafluorobenzene
p-$C_6H_4I_2$ or 1, 4- DIB	*para*- diiodobenzene
PDB	Protein Data Bank
Ph	phenyl
ppm	parts per million
Pr	propyl
PSO	paramagnetic spin-orbital coupling
PXRD	powder X-ray diffraction
QCPMG	quadrupolar Carr-Purcell-Meiboom-Gill
QI	quadrupolar interaction
QIS	quadrupole induced shift
ref.	reference
revPBE	revised Perdew Burke Ernzerhof
RF	radio frequency
RMSD	root-mean-square deviation
S/N	signal to noise
SD	spin-dipolar coupling
SSNMR	solid-state nuclear magnetic resonance
ST	satellite transition
TPPM	two pulse phase modulation
TPSS	Tao Perdew Staroverov Scuseria
TZP	triple-zeta with polarization functions
VOCS	variable offset cumulative spectrum
WURST	wideband uniform-rate and smooth truncation
XB	halogen bonds
XC	exchange-correlation
XRD	X-ray diffraction
ZORA	zeroth-order regular approximation

LIST OF SYMBOLS

Å	Angstrom ($1.0 \cdot 10^{-10}$ m)
a_c, b_c, c_c	unit cell parameters
B_1	transverse magnetic field strength
B_{eff}	effective magnetic field strength
B_o	magnetic field
C	unit cell with two lattice points on two opposite faces
C_n	proper *n*-fold rotation about an axis
C_Q	quadrupolar coupling constant
$\ddot{\boldsymbol{D}}$	dipolar coupling vector
d	separation between two reflecting lattice planes
$d_{\sum vdW}$	sum of the van der Waals radii
$d_{X\cdots Y}$	distance between the halogen and the nucleophile
E_D	dispersion energy
E_{mag}	magnetic moment energy
E_{m_l}	energy of eigenstate
E_{Z,m_l}	Zeeman energy
$E_{Q,m_l}^{(I)}$	first order QI energy
$E_{Q,m_l}^{(II)}$	second order QI energy
$E_{xc}[\rho(r)]$	exchange and correlation (XC) functional
e_o	fundamental charge ($1.60 \cdot 10^{-34}$ J s)
F	face centered unit cell
F_{hkl}	structure factor
$\lvert F_{hkl}\rvert^2$	intensity of a reflection (*hkl*)
$\lvert F(\boldsymbol{H})\rvert$	amplitude of structure factor
h	Planck's constant ($6.62607 \cdot 10^{-34}$ J s)
$\hbar$	Planck constant/2π ($1.0546 \cdot 10^{-34}$ J s)
h_c	dimension of unit cell
(*hkl*)	Miller indices
$\boldsymbol{H}$	scattering vector in reciprocal space ($\boldsymbol{H}$= h$\boldsymbol{a}_c$+ k$\boldsymbol{b}_c$ +l$\mathbf{c}_c$)
$\hat{H}$	Hamiltonian operator
$\hat{H}_D$	direct dipolar coupling Hamiltonian
$\hat{H}_J$	indirect spin-spin coupling Hamiltonian
$\hat{H}_Q$	quadrupolar interaction Hamiltonian
$\hat{H}_Z$	Zeeman Hamiltonian
$\hat{H}_\sigma$	magnetic shielding Hamiltonian
$\hat{H}_Q^{(I)}$	first order QI Hamiltonian
$\hat{H}_Q^{(II)}$	second order QI Hamiltonian

I	spin quantum number
$\hat{I}$	nuclear spin operator ($\hat{I} = [\hat{I}_X, \hat{I}_Y, \hat{I}_Z]$)
I_C	body-centered unit cell
i	inversion
$\ddot{\mathbf{J}}$	*J*-coupling second rank tensor
J_{ani}	aniotropic *J*-coupling
J_{iso}	isotropic *J*-coupling
K	Kelvin
K	reduced spin-spin coupling tensor
k_B	Boltzmann constant ($1.381 \cdot 10^{-23}$ J K^{-1})
K_α	high intensity X-ray radiation
$\boldsymbol{M}$	bulk magnetization vector
m_l	spin magnetic quantum number, eigenstate
$\boldsymbol{M}_x$	net magnetization in the *x* plane
$\boldsymbol{M}_y$	net magnetization in the *y* plane
$N_{\alpha \text{ or } \beta}$	Boltzmann population state α or state β
N^α, N^β	number of spin up and spin down electrons orbitals
P	simple unit cell
P_{exc}, P_{ref}	WURST pulse
$Q_{a \text{ or } b}$	point charge
Q	quadrupole moment
r	internuclear distance
$\boldsymbol{r}$	spatial coordinates (x, y, z)
R_{DD}	dipolar coupling constant
R_{eff}	effective dipolar coupling constant
R_{XB}	normalized distance parameter
S	spin angular momentum
s	second
S_n	improper *n*-fold rotation about an axis
T	tesla
T	temperature
T[ρ(r)]	kinetic energy functional
T_1	spin lattice or longitudinal relaxation time
T_2	spin-spin or transverse relaxation time constant
T3, T4	thyroid hormone receptors
t_p	pulse direction
$U_{(r)}$	Coulombic force
U[ρ(r)]	Coulomb functional
$\ddot{\boldsymbol{V}}$	EFG tensor
V_{ii}	EFG tensor principal component (ii= 11, 22, 33)
V_{PAS}	EFG tensor in its principal axis system

$V_{(r)}$	electrical potential
W_{jj}	NBOs are expressed in atomic orbital
Z	nucleus charge
α, β, γ	Euler angles
$\alpha_c, \beta_c, \gamma_c$	unit cell angles
α_p	polarizability
$\alpha(\boldsymbol{H})$	phase of structure factor
γ	gyromagnetic ratio
$\varepsilon_{(r)}$	electric field
ΔE	difference between energy states m_l
ΔJ	*J*-coupling anisotropy
$\Delta\nu_{1/2}$	line-width at half height
$\Delta\nu_{m,m-1}$	breadth of the powder pattern of a quadrupolar nuclei
η_Q	EFG tensor asymmetry parameter
θ	general angle
θ_c	glancing angle (XRD)
θ_p	angle of maximum intensity pulse
θ_R	angle between B_o and the spinning axis for magic angle spinning
δ_{ii}	CS tensor principal component (*ii*= 11, 22, 33)
δ_{iso}	isotropic chemical shift
κ	chemical shift tensor skew
λ	wavelength
$\boldsymbol{\mu}$	magnetic moment
μ_o	permeability of free space ($4\pi \cdot 10^{-7}$ T^2 J^{-1} m^3)
μs	microsecond
$\boldsymbol{\mu}_{ind}$	induced dipolar moment
ν	frequency expressed in Hz
ν_L	Larmor frequency expressed in Hz
ν_{MAS}	spinning speed
ν_Q	quadrupolar frequency
$\pi/2$	90 degrees in radians
$\rho(r)$	electron density
$\ddot{\boldsymbol{\sigma}}$	magnetic shielding second rank tensor
σ_{mp}	mirror plane
σ-hole	positive region of electrostatic potential
σ_{ii}	MS tensor principal component (*ii*= 11, 22, 33)
$\ddot{\boldsymbol{\sigma}}_{PAS}$	magnetic shielding tensor in its PAS
$\tau_1, \tau_2, \tau_3, \tau_4$	delays
ϕ_j^{NLMO}	NLMO orbital
φ	Kohn-Sham orbitals

Ψ	wavefunction
Ω	chemical shift tensor span
Ω_n	set of strongly localized NBOs resembling Lewis dot formula
Ω_{off}	offset
ω_1	transverse frequency
ω_{eff}	effective field in frequency
ω_L	Larmor frequency expressed in rad s^{-1}
$\omega_{rot.\ fram}$	angular frequency in the rotating frame
$\wedge$	symbol indicates a quantum mechanical operator
$^\circ$	degree

STATEMENT OF AUTHENTICITY

I certify that the results presented in this dissertation are my own work and research, in addition I had the most significant role in the preparation of all manuscripts. All ideas and references to other work are fully acknowledged in accordance with the standard referencing of the scientific community. I acknowledge my supervisor Dr. David L. Bryce for his guidance in the research projects as well as being invaluable in the writing and editing of the individuals manuscripts. Dr. Ilia Korobkov is acknowledged for solving the single-crystal X-ray diffraction structures. I acknowledge Ms. Sophie Leclerc and Ms. Julia E. Meyer in their assistance with the synthesis of some halogen bonded compounds as well as the acquisition of routine NMR spectra (i.e. ^{13}C or ^{31}P). The following Chapters of this dissertation are based on published work in peer-reviewed journals:

Chapter 3: J. Viger-Gravel, S. Leclerc, I. Korobkov, D. L. Bryce, (2013) Correlation Between ^{13}C Chemical Shifts and the Halogen Bonding Environment in a Series of Solid *para*-Diiodotetrafluorobenzene Complexes. *CrystEngComm*, 15: 3168-3177.

Chapter 4: J. Viger-Gravel, S. Leclerc, I. Korobkov, D. L. Bryce, (2014) Direct Investigation of Halogen Bonds by Solid-State Multinuclear Magnetic Resonance Spectroscopy and Molecular Orbital Analysis. *J. Am. Chem. Soc.*, 136: 6929-6942.

Chapter 5: J. Viger-Gravel, J. E. Meyer, I. Korobkov, D. L. Bryce, (2014) Probing Halogen Bonds with Solid-State NMR Spectroscopy. Observation and Interpretation of $J(^{77}Se, ^{31}P)$ Couplings in Halogen-Bonded P=Se···I Motifs. *CrystEngComm*, 16: 7285-7297.

Chapter 6: J. Viger-Gravel, I. Korobkov, D. L. Bryce, (2011) Multinuclear Solid-State Magnetic Resonance and X-ray Diffraction Study of Some Thiocyanate and Selenocyanate Complexes Exhibiting Halogen Bonding. *Cryst. Growth Des.*, 11: 4984-4995.

THESIS SCOPE AND OBJECTIVES

Halogen bonds are a class of non-covalent interactions which have sparked interest in the scientific community in the last two decades due to their applications in diverse areas of research. Therefore, Chapter 1 is dedicated to the definitions of a chemical bond and non-covalent interactions followed by a brief perspective on the emergence of halogen bonds in the literature and the recently established definition of the halogen bond by the International Union of Pure and Applied Chemistry (IUPAC). The nature of the halogen bond will be described in terms of the forces that influence the interaction. Finally, Section 1.3 discusses why halogen bonds are highly interesting to the scientific community.

This thesis focuses on characterizing newly synthesized halogen bonded (XB) compounds with modern solid-state Nuclear Magnetic Resonance (SSNMR) techniques. NMR is a powerful tool permitting the complete molecular and electronic structure determination of materials at the atomic level in a non-destructive manner. NMR also has the advantage of observing dynamic processes within a material and distinguishes between different polymorphs structures for a given material. SSNMR is an advantageous method to study solids, as it characterizes bulk material of powdered or amorphous states at the atomic level even when long-range crystalline order is absent, unlike diffraction techniques. The reasoning behind using SSNMR to characterize XB is described later in Section 2.4.

Furthermore, the work focuses on the reasons why the NMR parameters will vary depending on the local halogen bonded environment. The three key objectives are: (1) to acquire benchmark NMR parameters of new halogen bonded compounds and describe them in the context of the related NMR data, (2) gather theoretical results generated from

quantum calculations to compliment the experimental observed data, and (3) define clear trends between the observed NMR parameters and the halogen bonding interaction.

Chapter 2 covers the theory of SSNMR, and the experimental methods used to analyze the novel halogen bonded compound. Chapter 2 will also cover basic computational concepts such as density functional theory (DFT). The various software packages that implement this level of theory will also be presented along with an overview of their different advantages. Finally, a brief section on the fundamentals of X-ray crystallography (XRD) and powder X-ray diffraction (PXRD) will be included. X-ray crystallography will be the method used to characterize the local halogen bonded geometry of the various synthesized compounds. This work is a symbiosis of experimental and theoretical approaches correlating NMR observables and halogen bonded structures in the solid state.

In Chapter 3, halogen bonding compounds exhibiting the C—I···X^- (where X = Br or Cl) halogen bonded motifs will be investigated using ^{13}C SSNMR. It will demonstrate how the ^{13}C isotropic chemical shift of the carbon covalently bonded to iodine (C—I···X^-) is correlated to the XB interaction.

In Chapter 4, it will be shown that the quadrupolar NMR parameters are sensitive probes of halogen bonds in a series of compounds containing C—I···X^-···I—C (where X = Br or Cl) halogen bonded motifs. This Chapter will validate how the $^{79/81}Br$ and $^{35/37}Cl$ quadrupolar coupling constants and asymmetry parameters vary as a function of the I···X^-···I angle. This experimentally observed correlation will be explained in terms of simple molecular orbitals, where a natural localized molecular orbital (NLMO) analysis conducted on a cluster model validates the established experimental trends.

In Chapter 5, measurements of $J(^{31}P,^{77}Se)$ couplings in both ^{31}P and ^{77}Se CPMAS SSNMR spectra will be presented for the first time in compounds featuring -P=Se···I-C- halogen bonded motifs. Also, it will prove how the $J(^{31}P,^{77}Se)$ values are dependent on their halogen bonding environment. An NLMO analysis will reveal the major contributing orbitals to *J*-coupling, as well as the relationship between the changes in the *J*-coupling constants and the halogen bonding interaction. Thus, Chapter 5 will show how a different NMR observable has a dependence on the halogen bonding interaction through correlations between their local halogen bonded geometry and electronic structure.

In Chapter 6 is presented a study of the bidentate halogen bond acceptors thiocyanate (SCN^-) and selenocyanate ($SeCN^-$) moieties in the new halogen bonded compounds of the form $(R_4NSCN)_x(p\text{-}C_6F_4I_2)_y$ and $(R_4NSeCN)_x(o \text{ or } p\text{-}C_6F_4I_2)_y$. XRD will be used to elucidate their crystal structures after which, correlations between the local halogen bonding environment of the compounds and the NMR chemical shift tensors of the probed nuclei (e.g. ^{13}C, ^{77}Se, and $^{14/15}N$) involved directly and indirectly in the halogen bond could be established. The results are compared with simple thiocyanate and selenocyanate salts where distinct changes in the NMR parameters in the presence of halogen bonds are observed. Those results are correlated in terms of the XB interaction and interpreted in the context of Ramsey's theory. Additionally, in order to corroborate experimental findings, DFT will be used to compute the shielding tensors of the synthesized compounds.

1 INTRODUCTION TO HALOGEN BONDS

1.1 CHEMICAL BONDS

The formation of a molecule results from various interactions between atoms under specific conditions. Chemists have multiple models to describe bonding in molecules, one of them being *orbitals*, which is an approximation to a wavefunction of the electrons and nuclei describing a system.[1] From the Born-Oppenheimer approximation (BOA), it is possible to separate the wavefunction into a product of electronic wavefunction and nuclear wavefunction. The BOA allows the sole consideration of the electronic wavefunction, and orbitals also describe an area of probability for finding electrons. The *linear combination of atomic orbitals* (LCAO) is a second useful approximation that describes the orbitals mentioned above as a combination to define a molecule. Hence, orbitals are a visual model for the chemist generated by quantum mechanical calculations and are not physically observable. Lewis, as early as 1916, [2] described chemical bonds by using the orbital model. For example, a chemical bond is often defined as the distribution and delocalization of electron density over an entire molecule and may be experimentally observed with diffraction methods (*vide infra*). The orbital model will predict the presence of a chemical bond when the interacting atomic orbitals overlap, thus indicating shared electron density. Figure 1.1 shows an example of an orbital energy level diagram for dihydrogen. The diagram shows the lower energy bonding orbital of H_2 (σ_{1s}), which is the addition of the constructive atomic *s* orbitals of two hydrogen atoms is possible because the σ_{1s} bond is more stable upon formation. The antibonding orbital (σ_{1s}^{*}) is the sum of opposite phases of the atomic hydrogen orbitals, resulting in destructive interference, a less stable bond upon formation.

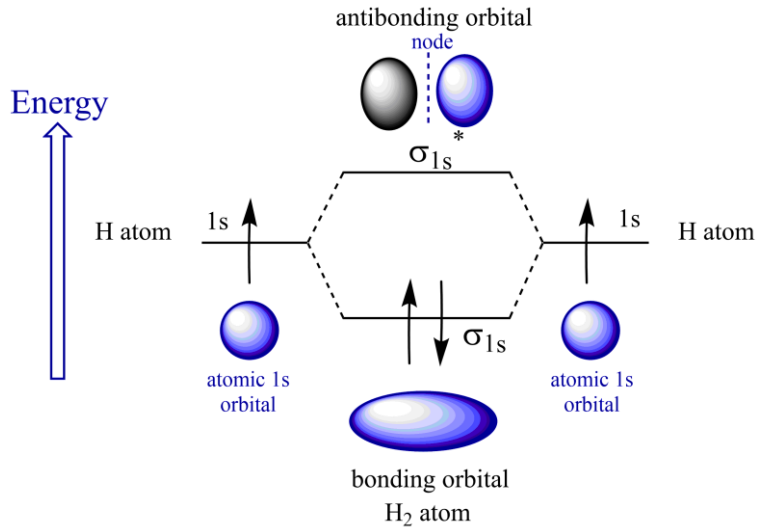

Figure 1.1 Orbital energy diagram for H_2 molecule.

The various types of chemical interactions are classified depending on the atoms involved in bonding: (1) covalent bond, (2) ionic bond, (3) metallic bond, (4) non-covalent interactions.[3] A covalent bond results from sharing valence electrons between two interacting atoms, and yields new chemical species with properties differing from the original atoms or molecules. Ionic bonds result from the attraction between oppositely charged ions such as in sodium chloride. Metallic bonds occur in metals, which lose electrons easily due to their low ionization energy. Let's consider the "electron sea" model,[3] the valence electrons come together from all the atoms in the lattice and then are delocalized over the entire metal. The metal is held together by the positively charged metal atoms attracting the sea of electrons. Covalent, ionic and metallic bonds are usually considered short-range interactions with distances between the bonding atoms shorter than 2 Å, and

are classified as strong bonds and have a range of bond energies 60- 870 kJ·mol^{-1} (F_2 and HCN, respectively), 756 kJ·mol^{-1} (NaCl), 60-180 kJ·mol^{-1} (Li_2 and Li-Metal, respectively), respectively for example. [6] Electrostatic – or non-covalent – interactions are driven by different types of intermolecular forces. Intermolecular forces were first observed by van der Waals, in 1873, and often lead to molecular clusters, which affects the physical properties of the observed system. [4] Non-covalent interactions are considered weak as they are one or two orders of magnitude smaller than covalent bonds.[5] The stabilizing energy of a non-covalent interaction varies between 4 - 84 kJ·mol^{-1}, and the interaction usually occurs at distances of several Angstroms. Presented here is a review of the intermolecular forces.

Coulombic Forces

Coulombic forces ($U_{(r)}$) arise from ions separated by a distance (r) and point charge (Q) which is defined in Equation 1.1:

$$U_{(r)} = -\frac{{e_o}^2}{4\pi\mu_o}\frac{Q_a Q_b}{r^2} \quad [1.1]$$

where e_o is the elementary charge (1.602 ·10^{-19} C), and μ_o is the permeability constant (8.854·10^{-12} C^{2}J^{-1}m^{-1}).[6] Coulombic forces are strong long-range interactions, they can arise from dipole-dipole interactions or dipole-ion interactions (*vide infra*).

Dipolar Forces and Ion-Dipole Force

Dipolar forces exist between all polar molecules. By definition, polar molecules have permanent dipoles: the barycenter of the positive and negative regions of the molecule do not coincide. The dipolar force is a result of the attraction between the dipoles of the neighboring molecules or atoms. Their energy is equal to the sum of their Coulombic contributions.[3]

An ion-dipole force occurs between mixtures of ionic compounds and polar compounds. In the case of sodium chloride in water, for example, the cation interacts with the negative dipole of water. These interactions depend on the orientation of the dipole with respect to the ion, and they play a vital role in solvation.

Polarization Forces

Polarization forces exist between induced charges among molecules or atoms. They induce a dipole moment (μ_{ind}) that is proportional to the polarization field (E_p) and the coefficient of proportionality of polarizability (α_p) as described in Equation 1.2.[6]

$$\mu_{ind} = \alpha_p E_p \quad [1.2]$$

Polarization forces are also known as Debye forces in the case of dipoles in thermal rotation neighboring a non-polar molecule.

Dispersion Forces

A dispersion interaction occurs from instantaneous and observable changes in the electron distribution within a molecule or atom.[3] That phenomenon is also known as an instantaneous electric dipole that fluctuates rapidly; it will temporarily induce a dipole to its neighbor, thus creating an instantaneous attraction of the dipole. The dispersion energy (E_D) takes the following form:

$$E_D = -\frac{3{\alpha_o}^2 h\nu}{4(4\mu_o)^2 r^6} \quad [1.3]$$

where *hv* is the energy, and dispersion is a short electrostatic interaction $(r^6)^{-1}$. Dispersion is not a weak interaction, it is the most important contribution to attractive forces and is the third term in the van der Waals interaction, also known as the London dispersion force.

Charge Transfer

A charge transfer type bond requires a good electron acceptor (i.e. high electron affinity) and an electron-donating system (i.e. low ionization energy).[6] An example of a charge transfer complex is $I_2 \cdots C_6H_6$. In that complex, there is a flow of electrons from the donor (π- system) to the acceptor (iodine). The molecular interaction occurs when the pair permits a low energy barrier overlap between the lowest unoccupied orbital of the acceptor and the highest occupied molecular orbital of the donor permitting the flow of electrons.[7] Usually, the interaction is accompanied by a change in intramolecular and intermolecular distances, as well as a change in their relative orientation.

1.2 HALOGEN BONDING INTERACTION

This dissertation is interested in a particular type of non-covalent interaction: the halogen bond. A brief overview of the background of this non-covalent interaction will be presented followed by a rigorous definition where the various intermolecular forces will prove useful to explain the nature of the halogen bond. Finally, the importance of halogen bonds for the scientific community will be discussed.

1.2.1 *History of Halogen Bonds*

The recognition of a halogen bonding interaction is not new but remained until recently mostly undefined. Guthrie, in 1863, reported the first dihalogen molecule forming a complex with a Lewis base, I_2-NH_3.[8] Benesi and Hildebrand, in 1948, published the first donor-acceptor molecule between I_2 and benzene.[9, 10] Mulliken, in 1950, observed similar

complexes among ethers and carbonyl derivatives, and explained the interaction in terms of charge transfer type bonds.[11, 12] Bent, in 1968, published a review of the similarities of hydrogen and halogen bonding.[13] Hassel (Nobel Prize in Chemistry 1969) demonstrated, in 1970, the importance of halogen atoms in molecular self-assembly phenomena.[14] He also described the interactions as charge transfer bonds. Dumas *et al.* was the first to name the charge transfer type bond as *halogen bond* for complexes containing pyridine, THF, or anisole and silamethane or tetrahalomethane.[15]

Although halogen bonds have had a direct impact on all research fields where molecular recognition and self-assembly processes are important,[16] up until the 1990s, very few studies had been conducted on the specific nature and underlying mechanism surrounding the halogen bond. Since then, the scientific community has rallied around the question: how to define this forgotten non-covalent interaction?

1.2.2 *Halogen Bonding Definition*

A workshop funded by the International Union of Pure and Applied Chemistry (IUPAC) in 2012 on halogen bonds (XB)[17] released a general definition of the halogen bond.

> "A halogen bond occurs when there is evidence of a net attractive interaction between an electrophilic region associated with a halogen atom in a molecular entity and a nucleophilic region in another, or the same, molecular entity.[18] A typical halogen bond is denoted by the three dots in R—X···Y—Z. R—X is the *halogen bond donor*, X is any halogen atom with an electrophilic (electron-poor)

region, and R is a group (see p. 1118 in ref. 17) covalently bound to X. In some cases, X may be covalently bound to more than one group (see p. 1118 in ref. 17). It may also form more than one halogen bond. Y is the *halogen bond acceptor* and is typically a molecular entity (see p. 1142 in ref. 17) possessing at least one nucleophilic (electron rich) region." [19]

1.2.2.1 *Sigma-hole*

Halogens are electronegative atoms and are usually viewed as negative in character when participating in a covalent bond. Brink, Murray, and Politzer used molecular electrostatic potential surfaces to explain such an interaction between the halogen and a nucleophilic site.[20] The electrostatic potential is a real physical property that may be obtained by diffraction methods (cf. Section 2.3) or theoretically with quantum calculations. It describes the complete charge distribution in a system and is described in Equation 1.6.[21]

Firstly, let's recall Coulomb's force (Equation 1.1), which is an interaction between two-point charges separated by a distance (r). The integration of that force ($U_{(r)}$) will provide its energy as shown in Equation 1.4:

$$\Delta E_{(r)} = \int_{r=\infty}^{r} U_{(r)} dr = \int_{r=\infty}^{r} k \frac{Q_a Q_b}{r^2} cos\theta dr \quad [1.4]$$

where k is a constant and θ is the angle between r and $U_{(r)}$. An electric field ($\varepsilon_{(r)}$) and an electrostatic potential ($V_{(r)}$) are created by a point charge in its surrounding space, and those phenomena are mathematically described in Equation 1.5:

$$\varepsilon_{(r)} = k \frac{Q_a}{r^2} \text{ and } V_{(r)} = k \frac{Q_a}{r} \quad [1.5]$$

Secondly, it is convenient to take into consideration that for molecules or complexes, the nuclei and electrons can be viewed as point charges. A force ($U_{(r)}$) is felt at a point charge (Q) when placed at a distance (r) from a second-point charge (Q_a). That force is equal to the product of the $\varepsilon_{(r)}$ and the charge ($U_{(r)}= Q\varepsilon_{(r)}$), and its associated energy is proportional to the electric potential ($\Delta E_{(r)}= QV_{(r)}$).

Finally, the $V_{(r)}$ created at any point **r** can be obtained by the sum over all nuclei and the integration of electron density (ρ(r)). The electrostatic potential is described in Equation 1.6 for a nucleus A with charge Z located at r_a:

$$V_{(r)} = \sum_A \frac{Z_A}{|r_a - \boldsymbol{r}|} - \int \frac{\rho(\boldsymbol{r'})d\boldsymbol{r'}}{|\boldsymbol{r'} - \boldsymbol{r}|} \quad [1.6]$$

where r′ designates the infinite number of points in space.

Calculated electrostatic potential is usually computed for the molecular surface of the molecule with a contour equal to an electronic density of 0.001 au.[22] The $V_{(r)}$ surface of a covalently bonded halogen reveals anisotropy: a positive electrostatic potential region at the far end of the R—X bond, which is surrounded by negative electrostatic potential.[23, 24] The positive region is known as the *σ-hole*[25, 26, 27, 28, 29, 30] and its magnitude depends on the nature of the halogen nucleus and the electron-withdrawing power of the R fragment. In general, the strength of the halogen bonding interaction increases with increasing polarization ability of the atom: F << Cl < Br <I. In particular cases, fluorine has been observed to form a halogen bond: CN—F, F_2, FOF, $(NO_2)_3C$—F.[30, 31, 32, 33,34] This is possible because the σ-hole is less negative than the surrounding negative electrostatic potential surface, and the nucleophile has an electric field strong enough to induce a positive

region on fluorine. Depicted in Figure 1.2 are the electrostatic potentials of the trifluoromethane halogens,[35] where the σ-hole is present in red.

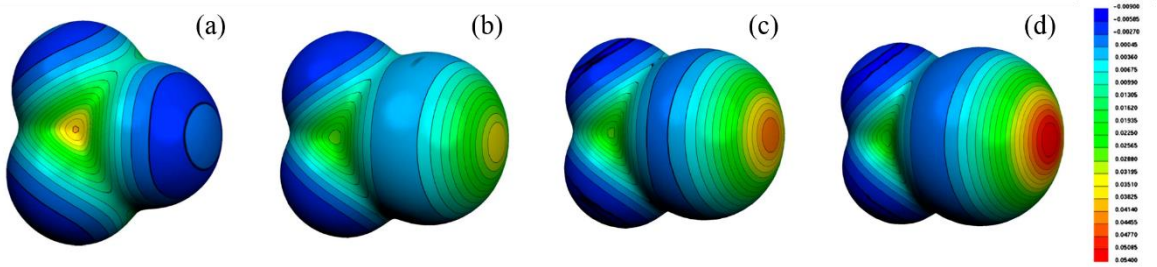

Figure 1.2 The molecular electrostatic potential, in Hartrees at 0.001 au. isodensity surface of (a) CF_4, (b) CF_3Cl, (c) CF_3Br, and (d) CF_3I evidence the increasing presence of a σ-hole, where the negative electron density is designated by the blue region and the positive region is shown in red. (Figure adapted from Clark *et al.*[24])

Halogen bonding interactions are highly directional due to the positive nature of the σ-hole. The position of the σ-hole along the R—X bond explains the near linearity (close to 180°) of the interaction.[23, 21] Another characteristic feature of a halogen bond is their ability to form short contacts with the nucleophilic site. The conditions for a short contact is the distance between the halogen, and the nucleophile ($d_{X\cdots Y}$) must be less than the sum of the van der Waals radii[36,37] of the respective atoms ($d_{\sum vdW}$).[19] The normalized distance parameter ($R_{XB} = d_{X\cdots Y} / d_{\sum vdW}$) is the ratio of those distances and is one measure of the extent of the halogen bonding interaction (i.e. if $R_{XB} < 1$, then XB interaction is present).

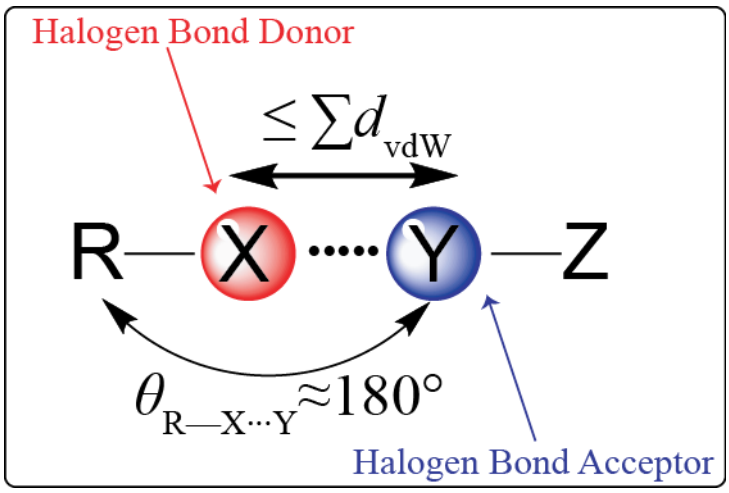

Figure 1.3 Scheme describing the key features of a halogen bonding interaction.

1.2.2.2 *Nature of Halogen Bonding Interaction*

The exact nature of the halogen bond is still disputed, the bonding contributions of this non-covalent interaction often depend upon the individual interacting species and the various intermolecular forces are: (1) electrostatic effects, (2) charge transfer, (3) polarization and (4) dispersion.

Bent, Hassel, and Mulliken first described halogen bonding as a charge transfer type bond.[11, 13, 14] It is still sometimes described as having a significant donor/acceptor component. In some cases, charge transfer occurs from the negative site Y to a σ*-antibonding orbital of the halogen bond donor, R—X.[38] The charge transfer phenomenon is shown in Figure 1.4 for the symmetric trihalide Cl_3^-, which is an extreme case of halogen bonding.[38]

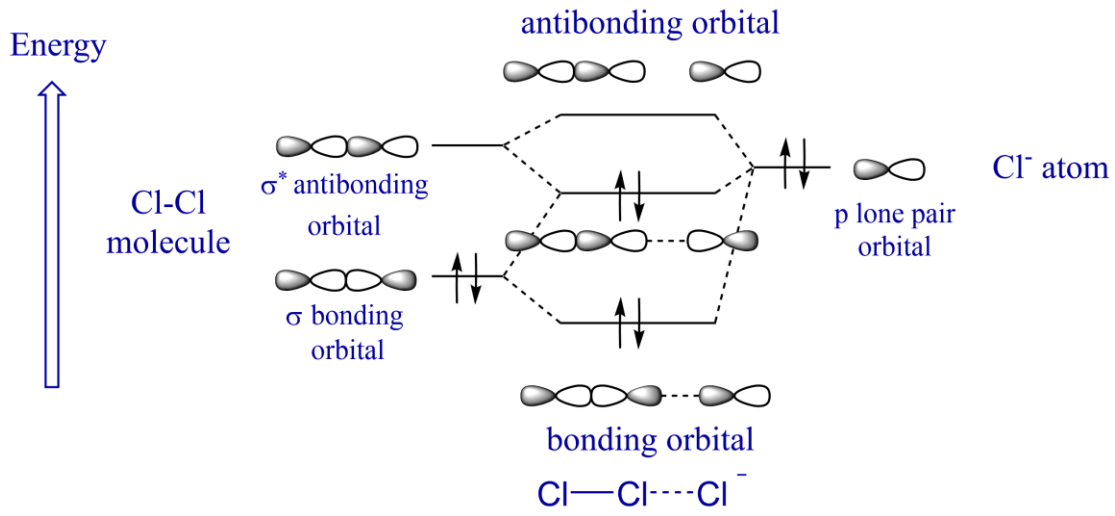

Figure 1.4 Orbital energy level diagram of Cl—Cl···Cl⁻, representing the electron donation from the p lone pair orbital of Cl^- to the σ* antibonding orbital of Cl-Cl.

The nature of a halogen bond is also described as electrostatically-driven.[39] However, there are other effects that may govern the interaction such as polarization and dispersion. Polarization describes the electronic density of the σ-hole for halogen bonded complexes. The electric fields of the nucleophilic site and the positive σ-hole induce electronic density redistribution around the halogen and the nucleophilic site (redistribution in the direction following Y to X : $\overleftarrow{R\text{—}X} \cdots \overleftarrow{Y}\text{—}Z$).[40, 41] Dispersion effects involving nuclear-electronic interactions can also play a role in this non-covalent interaction when the σ-hole is weakly positive.[42, 43, 44]

Computational studies can be misleading because the level of theory and basis sets used (Section 2.2) may render the polarization and charge transfer effects indistinguishable. Wang *et al.* stress that the two effects, aforementioned, are experimentally distinguishable. Hence, they are distinctive physical phenomena.[45] Charge transfers are due to excitation of

the electrons between the halogen bond donor and acceptor, while polarization effects are due to the delocalization of the electrons inside the halogen bonded components.

1.2.2.3 *Similarities to Hydrogen Bonding*

Halogen bonds are in many ways analogous to hydrogen bonds (HB).[46] Halogen and hydrogen bonding can be treated as an attractive interactions between an electrophile (the hydrogen or halogen) and a nucleophilic site.[47] Both interactions donate electron density from the nucleophilic to electrophilic part of the molecule. Hydrogen bonding is the most well-known electron acceptor and non-covalent interaction.[48] Notably, the directionalities of the two types of bonding interactions tend to differ.[49] Politzer and his group also determined the presence of a σ-hole along the hydrogen bond.[50,51] The positive region of the electrostatic potential surface of a hydrogen bond tends to be more spherical, hence present in the entirety of the surface, like a Lewis acid.[52] Consequently, the spherical distribution of the $V(r)$ creates less directional interactions than the analogous XB.[51]

Hydrogen bonds cover a wide range of bond energy. The range includes weak interactions with energies as low as 2 $kJ \cdot mol^{-1}$ (e.g. $CH_4 \cdots OH_2$)[53] to stronger interactions with interaction energies as high as 167 $kJ \cdot mol^{-1}$ (e.g. $F—H \cdots F^-$).[54] Hence, the energy associated with halogen bonds (8-40 kJ mol^{-1})[29, 33] is intermediate between weak and strong hydrogen bonds.[55] For example, hydrogen bonds will be stronger than halogen bonds when fluorine or chlorine donors are involved, and they will have the same order of magnitude for the bromine or iodine. In the latter case, when the halogen bond donor is iodine ($I_2 \cdots I^-$, 200 kJ mol^{-1}) or astatine (At), the interaction will be stronger than HB.[56]

Furthermore, these interactions (halogen and hydrogen bonds) will compete when placed in the same media.[41] Di Paolo and Sandfordy observed the phenomenon experimentally: different IR bands appeared for compounds crystallized in the presence of reagents capable of halogen bonding.[57] Their study stated that compounds that co-crystallize with either hydrogen or halogen bonds will preferentially do so via the halogen moiety.[58] However, Aakeröy and Spartz, emphasized the similarities between the strength of the hydrogen and halogen bond donors. In their study, the competing interactions lead to complicated structural analysis in order to determine the dominant one.[59] For example, in the case of the co-crystal 4,4´-bipyridyl-*N*,*N*´-dioxide *para*-diiodotetrafluorobenzene (*p*-DITFB), both HB and XB interactions compete for one acceptor molecule, and the *N*-oxide (i.e. acceptor site) simultaneously engages in both non-covalent interactions through a bifurcated bond.[60] Structures of starting material of cocrystal are shown in Figure 1.5. A study by Jones *et al.* of the XB complex, methyldiphenylphosphine oxide *p*-DITFB (see Figure 1.5), demonstrated that changes in the reaction conditions will affect the dominant non-covalent interaction, XB or HB, as is the case when the stoichiometric amounts of initial components are varied.[61]

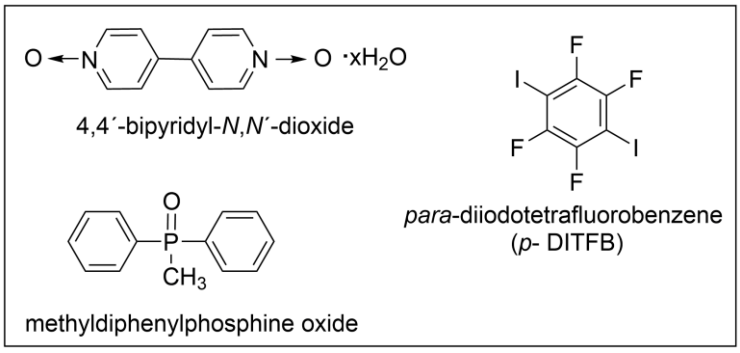

Figure 1.5 Scheme of starting materials in the co-crystal 4,4´-bipyridyl-*N*,*N*´-dioxide *para*-diiodotetrafluorobenzene and methyldiphenylphosphine oxide *p*-DITFB.

1.2.2.4 *Other Non-Covalent Interactions*

Other well-known non-covalent interactions such as cation···π,[62] anion···π,[63] π-π stacking, [64] CH···π[65] are commonly studied in supramolecular chemistry (Section 1.3.3) and have energies varying between 2-120 kJ mol^{-1}. Moreover, Politzer and his group demonstrated that the σ-hole is a phenomenon not only limited in explaining the hydrogen or halogen bond but also to bonding in general for other atoms in Groups from the periodic table.[41] The electrostatic potential of other Groups also indicated a positive region of $V_{(r)}$ surrounded by a negative region of $V_{(r)}$. They coined this phenomenon *σ-hole bonding*, which refers to the positive region of electrostatic potential participating in the non-covalent interaction. However, the Politzer group emphasizes that the observation of such a bond is not new: they have been observed, fifty years ago, between covalently bonded atoms from periodic Groups 14-16 and Lewis bases.[66, 67] Later, Metrangolo *et al.* published an article to establish a convention for naming the various non-covalent interactions. The proposed terminology takes into account σ-hole bonding and identifies it according to the periodic Group containing the atom representing the electrophilic site of the complex.[68]

The chalcogen bonds designate an interaction between elements of Group 16 as an electrophile.[69] An example of this type of bond is observed between sulfur and chloride in a derivative of thiamine, which is a vitamin of the B complex.[70]

Analogous to chalcogen bonds, Group 14 and 15 elements demonstrate the capability to interact with a nucleophilic site. The interactions were named tetral bonds (Group 14)[71] [72] and pnicogen bonds (Group 15).[73,74,75] Politzer *et al.* revealed that the less polarizable and the most electronegative atoms of Group 14-16 (C, N, O and F) will not have a positive electrostatic region.[41] Still, as mentioned, fluorine can form a halogen bond when the

conditions are favorable (recall Section 1.2.2.1, this is applicable for a σ-hole in tetral bond). Some calculations have demonstrated the possible presence of tetral bonds in compounds where carbon is the electrophile.[76,77,78] Also, the molecular electrostatic potential surface shows evidence of strong tetral bonds between the silicon atoms for a cluster of three $F_3Si—O—SiF_3$ (108 and 155 kJ mol^{-1}).[79]

1.3 Applications of Halogen Bonding Interactions

1.3.3 *Crystal Engineering Applications*

The goal of supramolecular chemistry is to establish strategies that permit the design of a specific system. These strategies are based on informed choices, where, as an example, the properties of the starting material components are known. Crystal engineering is a branch of supramolecular chemistry that uses intermolecular forces to assemble molecular components.[80] Useful concepts used in crystal engineering are *self-assembly* and *synthon*. *Self-assembly* is a spontaneous process, under thermodynamic control, of small chemical entities to form a large system.[81] A supramolecular *synthon* is a structural unit that is part of the supermolecule, which can be assembled with intermolecular interactions by a conceivable synthetic pathway.[82]

Only in the last decade or so have halogen bonds taken a more prominent role in crystal engineering, partly because they are more directional than the analogous hydrogen bonds and have the property of being *tunable*. *Tunability* is a term often used to describe the variation in the strength of the interaction depending on the halogen bond acceptor or donor involved in a system. The adjustment of the strength of the interaction also affects the properties of the halogen bonded complex. Furthermore, halogen bonds have the

capacity to align their components with specific orientations, which are appealing in the architecture of supramolecular, [83] or functional materials, such as anion-organic frameworks[84,85] and crystalline assemblies[86,87] with applications in liquid crystals,[88] and conducting materials or magnetic molecular materials.[89, 90]

Imakubo and Kato, in 1995, introduced the first conducting material engineered with halogen bonds. It consisted of an organization of a radical cation between a halogen bond donor, the cationic iodotetrathifulvalence (EDT-TFF-1), and halogen bond acceptor composed of bromide- or iodide- $Ag(CN)_2^-$ salts. [91] Yamamoto *et al.* reported a supramolecular conducting nanowire composed of an insulating sheet self-assembled by halogen bonds between tetraiodoethene and counter anions (Br^-, I^-) around the conducting material (EDT-TFF).[92]

Metrangolo *et al.* developed basic approaches to synthese one and two dimensional (1D, or 2D, respectively) architectures using halogen bonding interactions. A 1D network involves ditopic halogen-bond donors and acceptors.[93] Usually, the ditopic halogen bond donor is DITFB. The halogen-bond acceptor will either have two electron lone pairs or will have two different acceptor sites. The literature abounds with examples of such assemblies where infinite 1D zigzag chains are formed with such building blocks. Examples exist where the non-covalent interaction propagates through the XB motif in the following crystal structures: the I···N—aryl motif is found in 2,3,5,6-tetramethyl-1,4-benzodicarbonitrile *p*-DITFB,[94] the I···N≡C motif is formed in 1,4-bis(3-quinolyl)-1,3-butadiyne *p*-DITFB,[95, 96] the I···N-aryl motif is present in 4,4´-bipyridine 1,3- or *o*- DITFB[97] and in the analogous 4,4´-bipyridine 1,3- or 1,2- dibromotetrafluorobenzene (see structures of molecules in

Figure 1.6).[98] In this dissertation, most XB networks form 1D architectures using this approach.

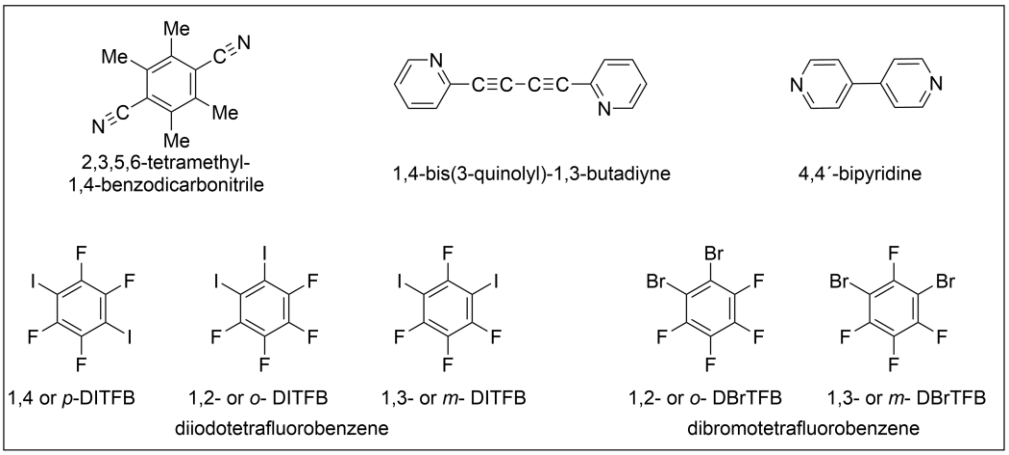

Figure 1.6 Scheme of starting material compounds in co-crystals forming 1D XB networks: 2,3,5,6-tetramethyl-1,4-benzodicarbonitrile *p*-DITFB, 1,4-bis(3-quinolyl)-1,3-butadiyne *p*-DITFB, 4,4´-bipyridine 1,3- or *o*- DITFB, and 4,4´-bipyridine 1,3- or 1,2-dibromotetrafluorobenzene.

Similarly, a halogen bond acceptor acting as tridentate components generate two-dimensional networks. A tridentate component will orient the non-covalent interaction in a roughly orthogonal direction. Self-assembly of onium halides with dihalocarbons forms *honeycomb-type* structures with I···I—C type XB motifs. An example is depicted in Figure 1.7.

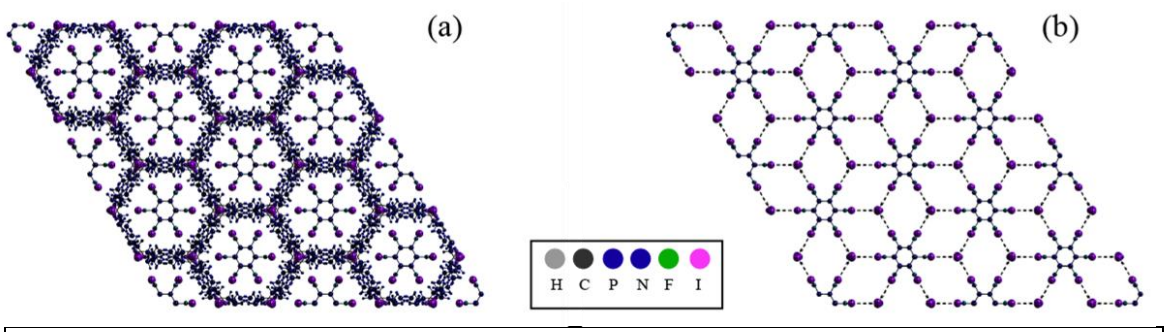

Figure 1.7 Two-dimensional halogen bonded honeycomb network for co-crystals of tetraethyl(phosphonium$_{0.5}$:ammonium$_{0.5}$) iodide and *sym*- $C_6F_3I_3$. [99] Figure generated with Diamond 4.0 software and the crystal structure code in CCDC is 665601.

Akin, three-dimensional (3D) architectures can be formed by using tetradentate modules. Such networks are present in the halogen bond complex tetraphenylphosphonium iodide diiodoacetylene or tetrakis(4-pyridyl)pentaerythritol 1,6-diiodoperfluorohexane (See Figure 1.8).[100, 101] Aakeröy and coworkers successfully employed the linear property of XB interactions combined with the knowledge of 2D crystal engineering to predict the formation of a dimeric halogen-bonded discrete capsule where I···N motifs are present between calixarenes.[102] Tothadi and Desariju synthesized 3D halogen bonded complexes by incorporating both hydrogen and halogen bonds. Their crystal engineering strategy is based on the size and shape of the starting molecules, as well as established synthons such as acid···amide and I···ON_2 interactions.[103]

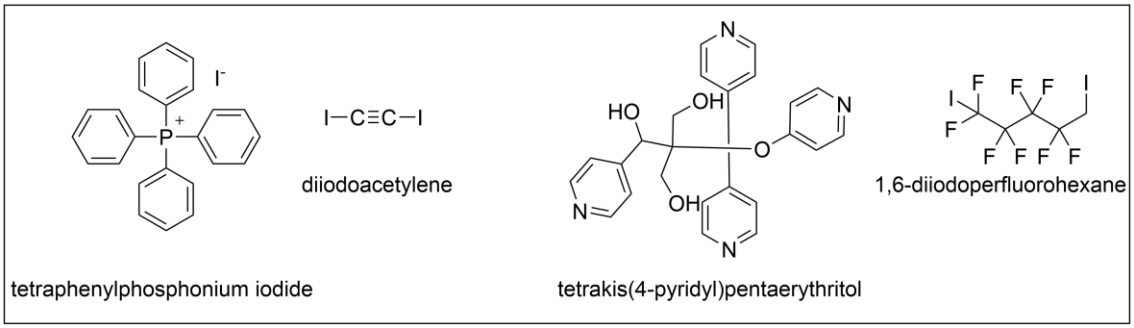

Figure 1.8 Scheme of starting material compounds in co-crystals forming 3D XB networks: tetraphenylphosphonium iodide diiodoacetylene or tetrakis(4-pyridyl)pentaerythritol 1,6-diiodoperfluorohexane.

1.3.4 *Biological Applications*

The importance of halogen bonds has been shown in the formation of complexes with halogen-substituted ligands and their biological substrates.[104] Most biological systems are not naturally halogenated. Halogens are being incorporated into proteins, nucleic acids, binding ligands or recognition systems to solve their crystal structures using XRD (Section 2.3).[105, 106] The proper understanding of halogen bonding will help establish their significance in biological systems, where they have been observed in molecular recognition and folding processes, as well as in ligand binding.[107, 108, 109]

A survey realized in 2004 in the search engine of the Protein Data Bank (PDB) first identified the halogen bonds in biomolecular systems.[109] The halogen bond was found to be widespread throughout the database and prompted the usual interaction between a halogen bond acceptor (O, N, S) and donor (halogen) forming short contacts ($R_{XB} < d_{VdW}$) with a near linear angle between the acceptor and donor.[110] More recent surveys of the PDB now list 600 biomolecular halogen bonds,[111,112, 113] demonstrating how they are essential to structures of biomacromolecules such as and proteins or nucleic acids. It should

be noted that the geometry of halogen bonds is the property used to identify the intermolecular interaction in biological systems. To avoid misinterpreting a short contact arising from close packing from a true halogen bond, the distance criteria is key. Hence, the presence of a halogen bond in a biomolecule is accepted when $R_{XB} \leq 0.96$, 0.97, 0.98 for Cl, Br and I, respectively.

The thyroid hormones are examples of naturally iodinated molecules. Molecular recognition enables the halogen bond donor thyroxine to interact with the thyroid hormone receptors (T3 or T4) to regulate the metabolism. Also, thyroxine recognizes its extracellular transport protein transthyretin.[114,115,116] This is shown in Figure 1.9.

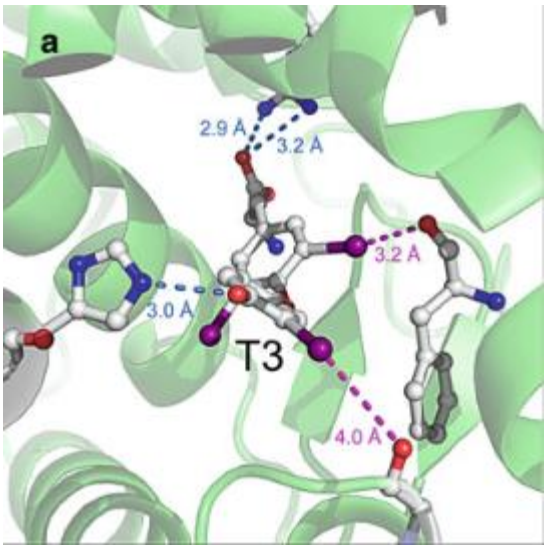

Figure 1.9 Interaction of thyroid hormone receptor TRβ: (a) with 3,5,3´-triiodo-L-thyronine (T3) (PDB code 1XZX). (Figure inspired from P.S. Ho[110]).

The crystal structure of the enzyme aldose reductase with a halogenated inhibitor revealed short Br···O halogen bonding interactions forcing the deoxyribonucleic acid (DNA) into four-stranded Holliday junction. These interactions account for the fold

selectivity against binding of the inhibitor and is also an example of the effect of halogen bonds on molecular conformation.[109]

Also, because they have potential in pharmacology, an interesting class of halogen bond donors are inhibitors of proteins. The protein kinases are an example where halogen bonds have been observed to act as inhibitors.[119] Protein kinase is a primary target for treatment of chronic inflammatory diseases, neurodegenerative disorders, cancers[117] and others.

Furthermore, 20 % of pharmacological compounds presently used or found in clinical trials are halogenated molecules.[110] Hence, XB have been heralded for their potential in drug design to generate inhibitors against critical targets.[118, 119, 120] In a tutorial review by Parisini *et al.*, small halogenated molecules were analyzed for their affinity to their biological counterpart. They studied essential drugs such as inhibitors of HIV-1 reverse transcriptase and systematically determined patterns of substituents which could potentially direct halogen bonds and increase binding affinity.[121] Further, applications for halogen bonds to transport anions across lipid bilayer membranes has proven successful as they are more lipophilic than the analogous hydrogen bonds already used in the field.[122] The interest of anion transport is also driven by the possible medicinal use in treating cystic fibrosis.[123]

1.4 Benchmark Data for Halogen Bonds

Over the past decade, halogen bonds have been extensively characterized by X-ray diffraction (XRD) in the solid state[90, 124] or with computational predictions.[125] Multiple groups have investigated how to perform quantum calculations to best reproduce this

particular type of electrostatic interaction, halogen bonds. The Hobza group has been involved in reproducing accurate energy and geometry calculations and in the determination of the nature of halogen bonds by developing semi-empirical quantum mechanical methods to describe XB.[126,127,128] Another invested theoretical group involved in the theoretical characterization of halogen bonds are Karpfe.[129]

Simultaneously, Legon and coworkers have made significant contributions to understanding halogen bonds in the gas phase.[130,131] They have examined experimentally how the structures of halogen-bonded complexes depend on the nature of the halogen and the Lewis base with the use of rotational spectroscopy. Among the parameters that can be extracted from such experiments are the halogen nuclear quadrupolar coupling constants, C_Q, which give quantitative information about the electric field redistribution associated with the halogen bonding process.[132,133]

Also, XB has sparked interest in the development of anion binding[134, 135, 136, 137, 138] and catalysis.[139] The Taylor group has made progress to report thermodynamic data for these non-covalent interactions in the design of multidentate receptor design in the solution phase.[140,141,142,143] The Erdelyi group has also committed to the characterization of halogen bonds in the solution phase with NMR.[144,145,146,147] In addition, infrared and Raman spectroscopy have proven to be successful methods for characterizing XB in cryogenic solutions as the halogen stretching frequency is Raman active for the starting material and halogen bonded system.[148, 149]

Using the search engine Web of Science, there are now 1071 publications in the literature for the keywords *halogen bond* as a topic search (from 2001 to May 6th, 2015). This represents an increase of 267 % compared to the years 1900 to 2000 (yielded 401

results), thus demonstrating the growing interest of the scientific community towards this particular non-covalent bond. Here, the main focus was describing the nature of the interaction and its main applications. There are many more interesting reviews on the subject of halogen bonds that may be consulted for more in-depth information on the subject.[150,151]

The work in this dissertation focuses on the characterization of halogen bonds with NMR in the solid state. As will be discussed in more detail in the following Chapters, the analogous hydrogen bond has been successfully characterized with SSNMR methods.[152] Hence, it will be shown that the same method can be employed for halogen bonds, such is the objective of the present thesis.

1.5 REFERENCES FOR CHAPTER 1

1 J. Autschbach, (2012), *J. Chem. Edu.* 89, 1032.

2 G. N. Lewis, (1923), *Valence nd the Structure of Atoms and Molecules*, Chemical Catalog Co., New York, NY.

3 N. J. Tro, (2013), *Principles of Chemistry : A Molecular Approach second edition,* Glenview, IL, Pearson Education, Inc.

4 J. D. van der Waals, (1988), *On the Continuity of the Gaseous and Liquid States*, J. S. Rowlinson (Ed.), Mineola, NY, Dover Phoenix Editions.

5 K. Müller-Dethlefs, P. Hobza, (2000), *Chem. Rev.*, 100, 143.

6 A. Gerschel, (1995), *Liaisons intermoléculaires : Les forces en jeu dans la matière condensée*, Paris, France, CNRS Éditions.

7 C. J. Bender, (1986), *Chem. Soc. Rev.*, 15, 475.

8 F. Guthrie, (1863), *J. Chem Soc.*, 16, 239.

9 H. A. Benesi, J.H. Hildebrand, (1948), *J. Am. Chem. Soc.*, 70, 2832.

10 H. A. Benesi, J.H. Hildebrand, (1949), *J. Am. Chem. Soc.*, 71, 2703.

11 R. S. Mulliken, (1950), *J. Am. Chem. Soc.*, 72, 600.

12 R. S. Mulliken, (1952), *J. Phys. Chem.*, 56, 801.

13 H. A. Bent, (1968), *Chem. Rev.*, 68, 587.

14 O. Hassel, (1970), *Science*, 497.

15 J. – M. Dumas, M. Kern, J. L. Janier-Dubry, (1976), *Bull. Soc. Chim. France*, 1785.

16 P. Metrangolo, F. Meyer, T. Pilati, G. Resnati and G. Terraneo, (2008), *Angew. Chem. Int. Ed.*, 47, 6114.

17 D. L. Bryce, (2012), *Chem. Int.*, 34, 27.

18 P. Muller. (1994), *Pure Appl. Chem.*, 66, 1077.

19 G. R. Desiraju, P. S. Ho, L. Kloo, A. C. Legon, R. Marquardt, P. Metrangolo, P. A. Politzer, G. Resnati, K. Rissanen, (2013), *Pure Appl. Chem.*, 85, 1711.

20 T. Brinck, J. S. Murray, P. Politzer, (1993), *Int. Quantum Chem.*, 43, 73.

21 P. Politzer, J. S. Murray, T. Clark, (2015), *Top. Curr. Chem.*, 358, 19.

22 R. F. W. Bader, M. T. Carroll, J. R. Cheeseman, C. Chang, (1987), *J. Am. Chem. Soc.*, 109, 7968.

23 P. Politzer, J. S. Murray, (2013), *ChemPhysChem.*, 14, 278.

24 T. Clark, M. Hennemann, J. S. Murray, P. Politzer, (2007), *J. Mol. Model.*, 13, 291.

25 J. S. Murray, K. Paulsen, P. Politzer, (1994), *Proc Indian Acad. Sci. Chem. Sci.*, 106, 267.

26 F. F. Awwadi, R. D. Willett, K. A. Peterson, B. Twamley, (2006), *Chem. Eur. J.*, 12, 8652.

27 P. Politzer, P. Lane, M. C. Concha, Y. Ma, J. S. Murray, (2007), *J. Mol. Model.*, 13, 305.

28 T. Clark, M. Hennemann, J. S. Murray, P. Politzer, (2007), *J. Mol. Model.*, 13, 291.

29 P. Politzer, J. S. Murray, T. Clark, (2010), *Phys. Chem. Chem. Phys.*, 12, 7748.

30 P. Politzer, J. S. Murray, M. C. Concha, (2007), *J. Mol. Model.*, 13, 643.

31 M. Göbel, B. H. Tchichananov, J. S. Murray, P. Politzer, T. M. Klapötke, (2009), *Nat. Chem.*, 1, 229.

32 D. Chopra, T. N. Guru Row, (2011), *CrystEngComm*, 13, 2175.

33 P. Metrangolo, J. S. Murray, T. Pilatti, P. Politzer, G. Resnati, G. Terraneo, (2011), *CrystEngComm*, 13, 6593.

34 P. Metrangolo, J. S. Muray, T. Pilati, P. Politzer, G. Resnati, G. Terraneo, (2011), *Cryst. Growth Des.*, 11, 4238.

35 R. W. Troff, T. Mäkelä, F. Topić, A. Valkonen, K. Raatikainen, K. Rissanen, (2013), *Eur. J. Org. Chem.*, 1617.

36 A. Bondi, (1964), *J. Phys. Chem.*, 68, 441.

37 R. D. Shannon, (1976), Acta Crystallogr., Sect. A: Found. Crystallogr., 32, 751.

38 B. Pinter, N. Nagels, W. A. Herrebout, F. De Proft, (2013), *Chem. Eur. J.*, 15, 519.

39 A. S. Jones, (2013), *J. Am. Chem. Soc.*, 135, 7005.

40 M. Solimannejad, M. Malokani, I. Alkorta, (2010), *J. Phys. Chem. A*, 114, 12106.

41 P. Politzer, K. E. Riley, F. A. Bulat, J. S. Murray, (2012), *Comput Theo. Chem.*, 998, 2.

42 K. E. Riley, J. S. Murray, P. Politzer, M. C. Concha, P. Hobza, (2009), *J. Chem. Theory Comput.*, 5, 155.

43 K. E. Riley, P. Hobza, (2008), *J. Chem. Theory Comput.*, 4, 232.

44 K. E. Riley, P. Hobza, (2013), *Phys. Chem. Chem. Phys.*, 15, 17742.

45 C. Wang, D. Danovich, Y. Mo, S. Shaik, (2014), *J. Chem. Theory Comput.*, 10, 3726.

46 E. Parisini, P. Metrangolo, T. Pilati, G. Resnati, G. Terraneo, (2011), *Chem. Soc. Rev.*, 40, 2267.

47 E. Arunan, G. R. Desiraju, R. A. Klein, J. Sadlej, S. Scheiner, I. Alkorta, D. C. Clary, R. H. Crabtree, J. J. Dannenberg, P. Hobza, H. G. Kjaergaard, A. C. Legon, B. Mennucci, D. J. Nesbitt, (2011), *Pure Appl. Chem.*, 83, 1637.

48 P. Metrangolo, H. Neurich, T. Pilati and G. Resnati, (2005), *Acc. Chem. Res.*, 38, 386.

49 Z. P. Shields, J. S. Murray, P. Politzer, (2010), *Int. J. Quant. Chem.*, 110, 2823.

50 J. S. Murray, M. C. Concha, P. Lane, Hobza, P. Politzer, (2008), *J. Mol. Model.*, 14, 699.

51 Z. P. Shields, J. S. Murray, P. Politzer, (2010), *Int. J. Quantum Chem.*, 110, 2823.

52 S. J. Grabowski, (2013), *Phys. Chem. Chem. Phys.*, 15, 7249.

53 J. J. Novoa, B. Tarron, M. H. Whangbo, J. M. Williams, (1991), *J. Chem. Phys.*, 95, 5179.

54 S. Gronert, (1993), *J. Am. Chem. Soc.*, 115, 10258.

55 A. Mukherjee, S. Tothadi, G. R. Desiraju, (2014), *Acc. Chem. Res.*, 47, 2514.

56 C. B. Aakeröy, M. Fasulo, N. Schultheiss, J. Desper, C. Moore, (2007), *J. Am. Chem. Soc.*, 129, 13772.

57 T. Di Paolo, C. Sandorfy, (1974), *Chem. Phys. Lett.*, 26, 466.

58 E. Corradi, S. V. Meille, M. T. Meissina, P. Metrangolo, G. Resnati, (2000), *Angew. Chem., Int. Ed.*, 39, 1782.

59 C. B. Aakeröy, C. L. Spartz, (2015), *Top. Curr. Chem.*, 358, 155.

60 M. T. Messina, P. Metrangolo, W. Panzeri, T. Pilati, G. Resnati, (2001), *Tetrahedron*, 57, 8543.

61 S. Y. Oh, C. W. Nickels, F. Gracia, W. Jones, T. Fríščić, (2012), *CrystEngComm*, 14, 6110.

62 H. J. Schneider, (2009), *Angew. Chem., Int. Ed.*, 48, 3924.

63 P. Gamez, T. J. Mooibroek, S. J. Teat, J. Reedijk, (2007), *Acc. Chem. Res.*, 40, 435.

64 C. Janiak, (2000), *J. Chem. Soc., Dalton Trans*., 3885.

65 M. Nishio, (2004), *CrystEngComm*, 6, 130.

66 D. B. Miller, H. H. Sisler, (1955), *J. A. Chem. Soc.*, 77, 4998.

67 J. A. Kapecki, J. E. Baldwin, (1969), *J. Am. Chem. Soc.*, 91, 1120.

68 G. Cavallo, P. Metrangolo, T. Pilati, G. Resnati, G. Terraneo, (2014), *Cryst. Growth and Des.*, 14, 2697.

69 G. E. Garrett, G. L. Gibson, R. N. Straus, D. S. Seferos, M. S.; Taylor, (2015), J. Am., Chem. Soc., (dois: 10.1021/ja512183e).

70 N. H. Hu, W. Liu, K. Aoki, (2000), *Bull. Chem. Soc. Jpn.*, 73, 1043.

71 S. P. Thomas, M. S. Pavan, T. N. Guru Row, (2014), *Chem. Commun.*, 50, 49.

72 S. J. Grabowski, (2014), *Phys. Chem. Chem. Phys.*, 16, 1824.

73 J. E. Del Bene, I. Alkorta, G. Sanchez-Sanz, J. Elguero, (2012), *J. Phys. Chem. A*, 116, 3056.

74 S. Scheiner, (2013), *Acc. Chem. Res.*, 46, 280.

75 S. Zahn, R. Frank, E. Hey-Hawkins, B. Kirchner, (2011), *Chem. Eur. J.*, 17, 6034.

76 Q. Li, X. Guo, X. Yang, W. Li, J. Cheng, H.-B. Li, (2014), *Phys. Chem. Chem. Phys.*, 16, 11617.

77 P. R. Varadwaj, A. Varadwaj, B.-Y. Jin, (2014), *Phys. Chem. Chem. Phys.*, 16, 17238.

78 D. Mani, E. Arunan, (2014), *J. Phys. Chem. A*, 118, 10081.

79 A. Bauz, T. J. Mooibroek, A. Frontera, (2013), *Angew. Chem. Int. Ed.*, 52, 12317.

80 J. M. Lehn, (1988), *Angew. Chem. Int. Ed.*, 27, 89.

81 L. F. Lindoy, I. M. Atkinson, (2000), *Self-Assembly in Supermolecular Systems*, Cambrige, UK, The Royal Society of Chemistry Cambridge.

82 G. R. Desiraju, (1995), *Angew. Chem. Int. Ed.*, 34, 2311.

83 L. Meazza, J. A. Foster, K. Fucke, P. Metrangolo, G. Resnati, J. W. Steed, (2013), *Nat. Chem.* 5, 42.

84 H. M. Yamamoto, J.- I. Yamaura, R. J. Kato, (1998), *J. Am. Chem. Soc.*, 120, 5905.

85 J. Lieffrig, O. Jeannin, M. Fourmigué, (2013), *J. Am. Chem. Soc.*, 135, 6200.

86 P. Metrangolo, Y. Carcenac, M. Lahtinen, T. Pilati, K. Rissanen, A. Vij, G. Resnati, (2009), *Science*, 323, 1461.

87 H. S. El-Sheshtawy, B. S. Bassil, K. I. Assaf, U. Kortz, W. M. Nau, (2012), *J. Am. Chem. Soc.*, 134, 19935.

88 D. W. Bruce, (2008), Halogen-bonded Liquid Crystals, P. Metrangolo, G. Resnati (Eds.), *Halogen Bonding: Fundamentals and Applications: Structure and Bonding*, (pp.161-180), Berlin, UK, Springer.

89 M. Fourmigué, (2008), *Halogen Bonding in Conducting or Magnetic Molecular Materials*, P. Metrangolo, G. Resnati (Eds.), *Halogen Bonding: Fundamentals and Applications: Structure and Bonding*, (pp.181-207), Berlin, UK, Springer.

90 M. Fourmigué, (2009), *Curr. Opin. Solid State Mater. Sci.*, 13, 36.

91 T. Imakubo, H. Sawa, R. Kato, (1995), *Synth. Met.*, 73, 117 2.

92 H. M. Yamamoto, Y. Kosaka, R. Maeda, J. Yamaura, A. Nakao, T. Nakamura, R. Kato, (2008), *ACS Nano*, 2, 143.

93 P. Metrangolo, G. Resnati, T. Pilati, S. Biella, (2008), *Halogen Bonding in Crystal Engineering*, P. Metrangolo, G. Resnati (Eds.), *Halogen Bonding: Fundamentals and Applications: Structure and Bonding*, (pp.105-136), Berlin, UK, Springer.

94 A. Crihfield, J. Hartwell, D. Phelps, R. B. Walsh, J. L. Harris, J. F. Payne, W. T. Pennington, T. W. Hanks, (2003), *Cryst. Growth Des.*, 3, 313.

95 D. Britton, W. B. Gleason, (2002), *Acta Crystallogr. Sect. E Struct. Rep. Online*, 58, o1375.

96 R. Liantonio, P. Metrangolo, T. Pilati, G. Resnati, (2002), *Acta Crystallogr. Sect. E Struct. Rep. Online*, 58, o575.

97 P. Metrangolo, F. Meyer, T. Pilati, R. Resnati, G. Terraneo, (2007), *Acta Crystallogr. Sect. E Struct. Rep. Online*, 63, 04243.

98 R. B. Walsh, C. W. Padgett, P. Metrangolo, Resnati, T. W. Hanks, W. T. Pennington, (2001), *Cryst. Growth Des.*, 1, 65.

99 J. Grebe, G. Geiseler, K. Harms, K. Dehnicke, (1999), *Z. Naturforsch B: Chem. Sci.*, 54, 77.

100 M. Ghassemzadeh, K. Harms, K. Dehnicke, (1996), *Chem. Ber.*, 126, 259.

101 P. Metrangolo, F. Meyer, T. Pilati, D. M. Prosperpio, G. Resnati, (2007), *Chem. Eur. J.*, 13, 5765.

102 C. B. Aakeröy, A. Rajbanshi, J. Desper, (2011), *Chem. Commun.*, 47, 11411.

103 S. Tohadi, G. R. Desiraju, (2013), *Chem. Commun.*, 49, 7791.

104 E. Parisini, P. Metrangolo, T. Pilati, G. Resnati, G. Terraneo, (2011), *Chem. Soc. Rev.*, 40, 2267.

105 J. Xie, L. Wang, N. Wu, A. Brock, G. Spraggon, P. G. Schultz, (2004), *Nat. Biotechnol.*, 22, 1297.

106 T. Beck, T. Gruene, G. M. Sheldrick, (2010), *Acta Crystallogr., Sect. D: Biol. Crystallogr.*, 66, 374.

107 M. G. Sarwar, D. Ajami, G. Theodorakopoulos, I. D. Petsalakis, J. J. Rebek Jr., (2013), *J. Am. Chem. Soc.*, 135, 13672.

108 D. Manna, G. Mugesh, (2012), *J. Am. Chem. Soc.*, 134, 4269.

109 P. Auffinger, F. A. Hays, E. Westhof, P. S. Ho, (2004), *Proc. Natl. Acad. Sci. U. S. A.*, 101, 16789.

110 P. S. Ho, (2015), *Biomolecular Halogen Bonds*, *Halogen Bonding I, Impact on Materials Chemistry and Life Sciences* (pp. 241-276), P. Metrangolo, G. Resnati (eds.),Switzerland, Springer.

111 M. R. Scholfield, C. M. Vander Zander, M. Carter, P. S. Ho, (2013), *Protein Sci.*, 22, 139.

112 P. Zou, F. Tian, J. Zou, Z. Shang, (2010), *Mini Rev. Med. Chem.*, 10, 309.

113 S. K. Panigrahi, G. R. Desiraju, (2007), *Proteins*, 67, 128.

114 A. Wojtczak, V. Cody, J. R. Luft, W. Pangborn, (2001), *Acta Crystallogr., Sect. D: Biol. Crystallogr.*, 57, 1061.

115 D. Manna, G. Mugesh, (2012), *J. Am. Chem. Soc.*, 134, 4269.

116 N. F. Valadares, L. B. Salum, I. Polikarpov, A. D.Andricopulo, R. C. Garratt, (2009), *J. Chem. Inf. Model.*, 49, 2606.

117 N. Yamaguchi, Y. Yamamura, K. Koyama, E. Ohtsuji, J. Imanishi, T. Ahishara, (1990), *Cancer Res.*, 50, 7008.

118 Y. Lu. T. Shi, Y. Wang, H. Yang, X. Yan, X. Luo, H. Jiang, W. Zhu, (2009), *J. Med. Chem.*, 52, 2854.

119 A. R. Voth, P. S. Ho, (2007), *Curr. Top. Med. Chem.*, 7, 1336.

120 R. Wilcken, X. Liu, M. O. Zimmermann, T. J. Rutherford, A. R. Fersht, A. C. Joerger, F. M. Boeckler, (2012), *J. Am. Chem. Soc.*, 134, 6810.

121 E. Parisini, P. Metrangolo, T. Pilati, G. Resnati, G. Terraneo, (2011), *Chem. Soc. Rev.*, 40, 2267.

122 A. Varga Jentszsh, S. Matile, (2015), *Top. Curr. Chem.*, 358, 205.

123 P. A. Gale, R. Pérez-Tomás, R. Quesada, (2013), *Acc. Chem. Res.*, 46, 2801.

124 T. J. Mooibroek, P. Gamez, (2013), *CrystEngComm*, 15, 4565.

125 Q. Z. Li, B. Jing, R. Li, Z. B. Liu, W. Z. Li, F. Luan, J. B. Cheng, B. A. Gong, J. Z. Sun, (2011), *Phys. Chem. Chem. Phys.*, 13, 2266.

126 M. Dubecky, R. Derian, P. Jurecka, L. Mitas, P. Hobza, M. Otyepka, (2014), *Phys. Chem. Chem. Phys.*, 16, 20915.

127 M. H. Kolar, P. Carloni, P. Hobza, (2014), *Phys. Chem. Chem. Phys.*, 16, 19111.

128 M. Dubecký, P. Jurečka, R. Derian, P. Hobza, M. Otyepka, L. Mitas, (2013), *J. Chem. Theory, Comput.*, 9, 4287.

129 A. Karpfen, (2008), *Theoretical Characterization of the Trends in Halogen Bonding*, P. Metrangolo, G. Resnati (Eds.), *Halogen Bonding: Fundamentals and Applications: Structure and Bonding*, (pp.1-15), Berlin, UK, Springer.

130 A. C. Legon, (2010), *Phys. Chem. Chem. Phys.*, 12, 7736.

131 J. Grant Hill, A. C. Legon, D. P. Tew. N. R. Walker, (2015), *Top. Curr. Chem.*, 358, 43.

132 A. C. Legon, (2008), *The Interaction of Dihalogens and Hydrogen Halides with Lewis Bases in the Gas Phase: An experimental Comparison of the Halogen Bond and Hydrogen Bond*, P. Metrangolo, G. Resnati (Eds.), *Halogen Bonding: Fundamentals and Applications: Structure and Bonding*, (pp.17-64), Berlin, UK, Springer.

133 A. C. Legon, (1999), *Angew. Chem. Int. Ed.*, 38, 2686.

134 N. L. Kilah, M. D. Wise, C. J. Serpell, A. L. Thompson, N. G. White, K. E. Christensen, P. D. Beer, (2010), *J. Am. Chem. Soc.*, 132, 11893.

135M. G. Chudzinski, C. A. McClary, M. S. Taylor, (2011), *J. Am. Chem. Soc.*, 133, 10559.

136 F. Zapata, A. Caballero, N. G. White, T. D. W. Claridge, P. J. Costa, V. Félix, P. D. Beer, (2012), *J. Am. Chem. Soc.*, 134, 11533.

137 L. C. Gilday, T. Lang, A. Caballero, P. J. Costa, V. Félix, P. D. Beer, (2013), *Angew. Chem. Int. Ed.*, 52, 4356.

138A. C. Jentzsch, D. Emery, J. Mareda, S. Nayak, P. Metrangolo, G. Resnati, N. Sakai, S. Matile, (2012), *Nat. Commun*., 3, 1.

139 S. Walter, F. Kniep, E. Herdtweck, S. M. Huber, (2011), *Angew. Chem. Int. Ed.*, 50, 7187.

140 M. G. Chudzinski, C. A. McClary, M. S. Taylor, (2011), *J. Am. Chem. Soc.*, 133, 10559.

141 M .G. Chudzinski, M. S. Taylor, (2012), *J. Org. Chem.*, 77, 3483.

142 T. M. Beale, M. G. Chudzinski, M. G. Sarwar, M. S. Taylor, (2013), *Chem. Soc. Rev.*, 42, 1667.

143 M. G. Sarwar, B. Dragisic, E. Dimitrijevic, M. S. Taylor, (2013), *Chem. Eur. J.*, 19, 2050.

144 M. Bedin, A. Karim, M. Reitti, A.-C.C. Carlsson, F. Topic, M. Cetina, F. Pan, V. Havel, F. Al-Ameri, V. Sindelar, K. Rissanen, J. Gräfenstein, M. Erdelyi, (2015), *Chem. Sci.*, (doi: 10.1039/C5SC01053E).

145 A.-C.C. Carlsson, A.X. Veiga, M. Erdelyi, (2015), *Top. Curr. Chem.*, (doi: 10.1007/128_2014_607).

146 S. B. Hakkert; M. Erdelyi, (2015), *J. Phys. Org. Chem.*, 28, 226.

147 M. Erdelyi, (2014), *Nature Chemistry*, 6, 762.

148 D. Hauchecorne, A. Moiana, B. J. van der Veken, W. A. Herrebout, (2011), *Phys. Chem. Chem. Phys.*, 13, 10204.

149 D. Hauchecorne, R. Szotak, W. A. Herrebout, B. J. van der Veken, (2009), *ChemPhysChem*, 10, 2105.

150 P. Metrangolo, G. Resnati, (2008), *Halogen Bonding, Structure and Bonding*, D. M. Mingos (ed.), Heidelberg, Germany, Spinger.

151 P. Metrangolo, G. Resnati (eds.), (2015), *Halogen Bonding I, Impact on Materials Chemistry and Life Sciences*, Switzerland, Springer.

152 A. E. Aliev, K. D. M. Harris, (2004), *Probing Hydrogen Bonding in Solids Using Solid State NMR Spectroscopy*, D. M. P. Mingos (Ed.*), Supramolecular Assembly via Hydrogen Bonds I, Structure and Bonding* (pp. 1-54), Berlin, Germany, Spinger.

2 SOLID-STATE NUCLEAR MAGNETIC RESONANCE, QUANTUM CALCULATIONS AND X-RAY CRYSTALLOGRAPHY: THEORY AND METHODS

2.1 INTRODUCTION TO PRINCIPLES OF SSNMR

Particles are composed of atoms, which are, themselves, composed of electrons and nuclei. The scientific field of nuclear magnetic resonance (NMR) spectroscopy focuses on the physical properties of atomic nuclei, in particular, nuclear magnetism.

When a magnetic nucleus is in the presence of a magnetic field ($\boldsymbol{B_o}$) it is associated with a magnetic moment ($\boldsymbol{\mu}$) and its energy (E_{mag}) will be given by the dot product of the vectors:

$$E_{mag} = -\boldsymbol{\mu} \cdot \boldsymbol{B_o} \quad [2.1]$$

In 1922 Otto Stern (Nobel Prize in Physics, 1943) and Walter Gerlach conducted an experiment that demonstrated that all nuclei possess an intrinsic physical property known as *spin*.[1] In 1928, Wolfgang Pauli (Nobel Prize in Physics, 1945) experimentally observed and explained the presence of (electron) *spin* in a magnetic field.[2] It was Paul Dirac (Nobel Prize in Physics, 1933) who fully formulated the relativistic quantum theory where *spin* and *positron* emerged naturally.[3,4]

The next theoretical sections will demonstrate how nuclear spins contribute significantly to the mathematical manipulations used to derive the NMR principles.

2.1.1 *The Zeeman Interaction*

Spin possesses an intrinsic angular momentum. Quantum mechanics is necessary for the correct description of spin angular momentum. Spin angular momentum is

quantized and is represented by the spin quantum number I (I = 0, 1/2, 1, 3/2, …) and the spin magnetic quantum number m_I (m_I = I, I-1, …, -I). Nuclei that possess I greater than zero are said to be *NMR active*. Spin angular momentum is different from classical angular momentum, which is visualized as a rotating object along an axis with a directional vector. Since it is difficult to visualize a phenomenon such as spin, it is sometimes represented similarly to the way a top revolves about an axis (hereafter known as *precession* and depicted in Figure 2.1). The magnitude of the spin angular momentum (S) is given by:

$$S = \hbar\sqrt{I(I+1)} \quad [2.2]$$

where $\hbar$ is Planck's constant/2π ($1.0546 \cdot 10^{-34}$ J s). Any nuclei with a spin quantum number generates a magnetic moment proportional to the spin angular momentum as shown in Equation 2.3:

$$\hat{\boldsymbol{\mu}} = \gamma\hat{\boldsymbol{S}} \quad [2.3]$$

where γ is the gyromagnetic ratio (an isotope property), and the ^ symbol indicates a quantum mechanical operator.[5]

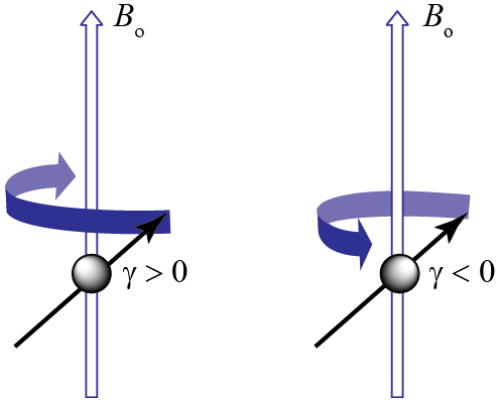

Figure 2.1 Nuclear precession for a nucleus with a positive and negative gyromagnetic ratio. (Figure inspired from Levitt[5]).

When a nucleus is placed in an external magnetic field (B_o) the energy levels are no longer degenerate; they are divided into eigenstates ($2I$+1). This interaction is known as the Zeeman effect.[6,7] The energy of each state is given by Equation 2.4 and the difference between energy states (ΔE) is shown in Equation 2.5.

$$E_{m_l} = -m_l \hbar \gamma B_o \quad [2.4]$$

$$\Delta E = \hbar \gamma B_o \quad [2.5]$$

Figure 2.2 shows the energy level diagrams for a spin 1/2 nucleus and a spin 3/2 nucleus with a positive γ.

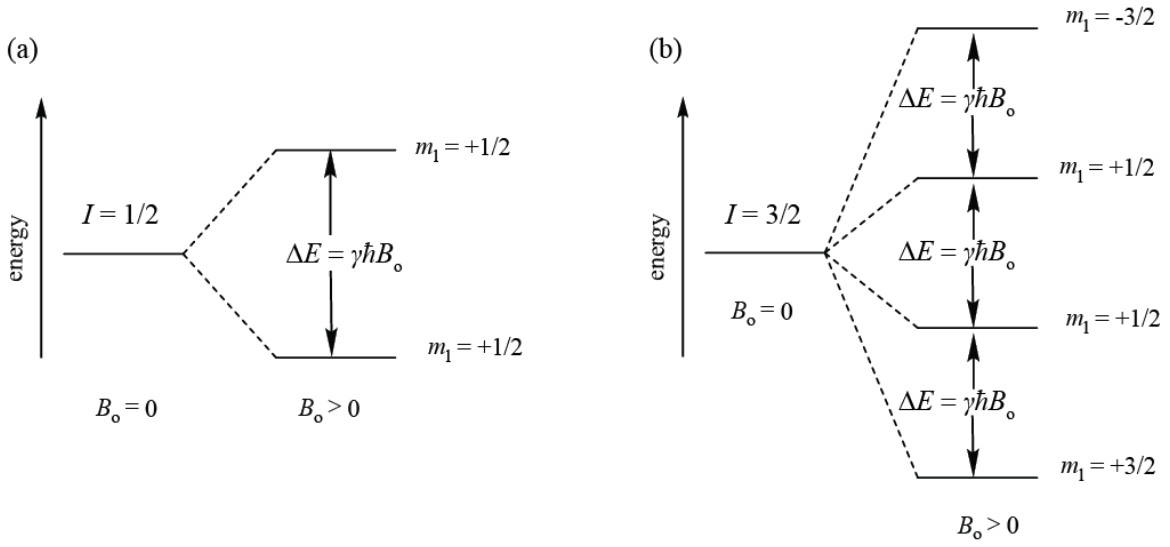

Figure 2.2 Zeeman energy states for a nuclei with (a) I = 1/2 and (b) 3/2 with a $\gamma > 0$.

One can determine the energy for a macroscopic sample consisting of a population of nuclear spins, but not for a single nucleus. The eigenstates in a magnetic field are associated with different energies and will follow the Boltzmann distribution. The Boltzmann distribution predicts that the nuclear spin population (N) of a state (α or β) lower

in energy is more populated and decreases exponentially for higher energy levels, at constant temperature (T). Equation 2.6 describes the difference in nuclear spin population expected with the Boltzmann distribution.

$$\frac{N_\alpha}{N_\beta} = e^{-\frac{\Delta E}{k_B T}} = e^{-\frac{\hbar \gamma B_0}{k_B T}} \quad [2.6]$$

where k_B is the Boltzmann constant ($1.381 \cdot 10^{-23}$ J K^{-1}).[8]

To increase the difference in spin population (N_α/N_β), one can increase the magnetic field, which will increase the energy gap between the eigenstates, or one can lower the temperature and use nuclei with larger γ ratio values.

2.1.2 *NMR Signal Detection*

To manipulate the spin populations from one energy state to the other when they are placed in a magnetic field, electromagnetic radiation equal to the energy gap (the radiofrequency (RF) radiation in the electromagnetic spectrum) is used. In this section, the response of nuclear spins to an applied RF field is explained before reviewing the fundamental NMR interactions.

Once the sample of interest is placed in a magnetic field, the sum of the $\boldsymbol{\mu}$ of each particle will yield a net bulk magnetization vector known as the nuclear spin magnetic moment $\boldsymbol{M}$. $\boldsymbol{M}$ will align along the z-axis as shown in Figure 2.3(a). When an RF field is applied via the coil situated in the x-y plane, the magnetization vector will be "tipped" away from the z-axis and will rotate like a sweeping a cone with a constant angle along β, see Figure 2.3(b). This motion of the nuclear spin angular momentum is referred to as *spin*

precession.[9,5] The frequency of such a precession is known as the Larmor frequency and is equal to:

$$v_L = -\frac{\gamma B_o}{2\pi} \text{ or } \omega_L = -\gamma B_o \quad [2.7]$$

The Larmor frequency is dependent on B_o and γ of the nucleus observed and can be expressed in Hz (v_L) or rad·s^{-1} (ω_L). This permits the detection of a signal for the *x*- and *y*-component of the magnetization vector of $\boldsymbol{M}$, which exhibits precession along the *z*-axis oscillating at a frequency ω_{xt} as described by the Equations in 2.8 (Figure 2.3(c)).[9]

$$\boldsymbol{M}_x = \boldsymbol{M}sin\beta cos\omega_{xt} \text{ and } \boldsymbol{M}_y = \boldsymbol{M}sin\beta sin\omega_{xt} \quad [2.8]$$

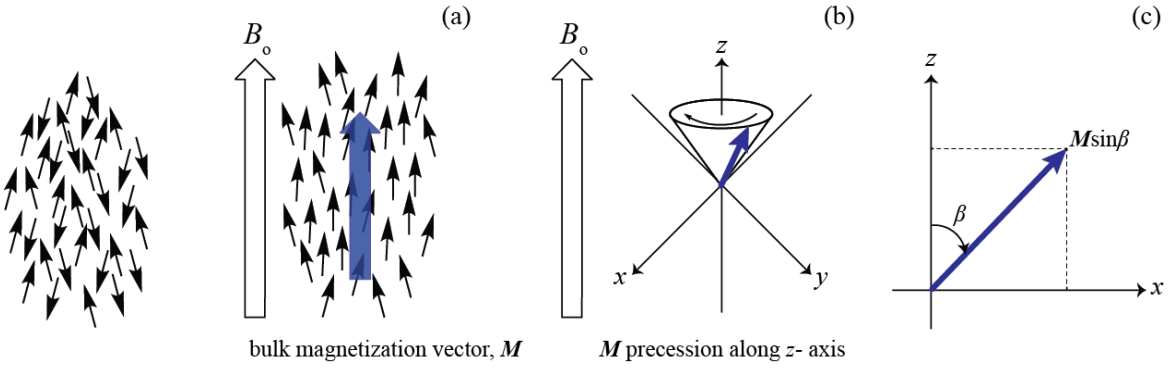

Figure 2.3 (a) Scheme of the bulk magnetization of individual magnetic moments, (b) the vector model of Larmor precession, and (c) the *x*-component of magnitude $\boldsymbol{M}$ through the tilting of the angle β as detected by NMR. (Figure inspired from Keeler.[9])

When an RF pulse is applied to the coil along the *x*-axis, it generates a magnetic field (B_1) about that axis, which oscillates into two counter-rotating components ($B_1^{\pm}$). Figure 2.4 shows the B_1^- component rotating in the clockwise (negative sense) oscillating frequency of $-\omega_{1t}$. In a rotating frame where the oscillating frequency is equal to $-\omega_{1t}$, the field will appear static. Moving the rotating frame removes its time dependency to the field.[9]

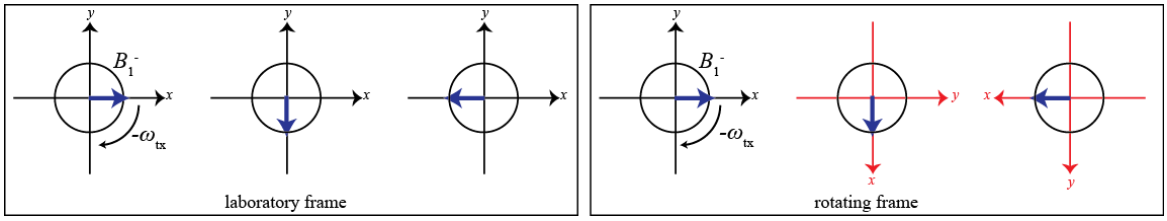

Figure 2.4 The B_1^- field is in a fixed axis system in the laboratory frame, whereas the axis system is mobile in the rotating frame.

In the rotating frame at an angular frequency of $\omega_{\text{rot. fram.}}$, the magnetization appears to precess at the difference between ω_L and the rotating frame frequency and is called the offset, Ω_{off} ($\Omega_{off} = \omega_L - \omega_{\text{rot. frame}}$ and $\Delta B = -\Omega_{off}/\gamma$). The applied magnetic field in the rotating frame of reference is affected by the magnetic field of the applied RF pulse (B_1) and the reduced field caused by the offset. The resulting effective field is shown in Figure 2.5 and described in Equation 2.9. Hence, in the rotating frame of reference, the reduced field along the *z*-axis can be much smaller than the applied magnetic field and can influence B_1.

$$B_{eff} = \sqrt{{B_1}^2 + \left(\frac{\omega_o - \omega_{rot.fram.}}{\gamma}\right)^2} \quad [2.9]$$

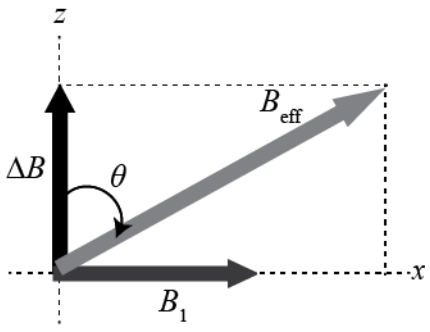

Figure 2.5 Effective field in the rotating frame of reference. (Figure inspired from Keeler.[9])

A more detailed description of the specific NMR experiments for solids relevant to this work will be explained in detail in the later section 2.1.4 Solid-State NMR Methods.

2.1.3 *Fundamental Nuclear Magnetic Interactions*

Explanation of the concepts and conventions used when discussing SSNMR spectroscopy of ^{13}C, $^{14/15}$N, ^{77}Se, $^{35/37}$Cl, and $^{79/81}$Br nuclei (directly involved in the halogen bonding interaction) follows. The Hamiltonian operator ($\widehat{H}$) for a given nucleus in an external magnetic field is:

$$\widehat{H} = \widehat{H}_{\mathrm{Z}} + \widehat{H}_{\mathrm{Q}} + \widehat{H}_{\sigma} + \widehat{H}_{\mathrm{D}} + \widehat{H}_{\mathrm{J}} \quad [2.10]$$

where $\widehat{H}_{\mathrm{Z}}$ represents the Zeeman Hamiltonian, $\widehat{H}_{\mathrm{Q}}$ is the Hamiltonian for the quadrupolar interaction, $\widehat{H}_{\sigma}$ is the magnetic shielding Hamiltonian, $\widehat{H}_{\mathrm{D}}$ is the direct dipolar coupling Hamiltonian, and $\widehat{H}_{\mathrm{J}}$ is the indirect nuclear spin-spin coupling Hamiltonian. The four interactions (quadrupolar, magnetic shielding, direct dipolar coupling, and indirect nuclear spin-spin coupling) are treated as perturbations to the Zeeman interaction. As the Zeeman interaction has already been addressed (*vide supra*), the Hamiltonian operator ($\widehat{H}_Z$) describing this interaction can be written as:

$$\widehat{H}_Z = -\gamma B_o \hat{I}_Z \quad [2.11]$$

where $\hat{I} = [\hat{I}_X, \hat{I}_Y, \hat{I}_Z]$ is a nuclear spin operator, hence $\hat{I}_Z$ is the nuclear spin operator along the *z*- axis .

In the following sections, the nuclear magnetic interactions relevant to this work will be addressed in detail.

2.1.3.1 *Magnetic Shielding and Chemical Shift Anisotropy*

Before discussing chemical shift (possibly one of the most significant NMR parameters), the concept of magnetic shielding (MS) interaction must be considered. A new magnetic field is created by the interaction of the applied external magnetic field with the electrons in a molecule so that the total field at the nucleus is given by Equation 2.12 and the interaction is known as magnetic shielding.[10]

$$B_{nucleus} = (1 - \sigma)B_o \quad [2.12]$$

The Hamiltonian in Equation 2.13 describes the effect of MS interaction in an NMR spectrum. MS is generally represented as a second rank tensor ($\ddot{\boldsymbol{\sigma}}$). Diagonalization of $\ddot{\boldsymbol{\sigma}}$ yields the orientation of its principal axis system (PAS) relative to the external axis system. In the PAS, the three principal components of the symmetric $\ddot{\boldsymbol{\sigma}}$ tensor are by convention ordered as $\sigma_{11} \leq \sigma_{22} \leq \sigma_{33}$.[11]

$$\hat{H}_\sigma = -\gamma B_o \ddot{\boldsymbol{\sigma}} \hat{I} \quad [2.13]$$

$$\begin{pmatrix} \sigma_{XX} & \sigma_{XY} & \sigma_{XZ} \\ \sigma_{YX} & \sigma_{YY} & \sigma_{YZ} \\ \sigma_{ZX} & \sigma_{ZY} & \sigma_{ZZ} \end{pmatrix} \overset{PAS}{\Longrightarrow} \begin{pmatrix} \sigma_{11} & 0 & 0 \\ 0 & \sigma_{22} & 0 \\ 0 & 0 & \sigma_{33} \end{pmatrix} \quad [2.14]$$

A simple formula relates a given shielding tensor component to the chemical shift (CS) tensor component when a suitable shielding reference exists. The CS is reported in units of parts per million (ppm) of B_o:

$$\delta_{ij} = \frac{\sigma_{ref} - \sigma_{ij}}{1 - \sigma_{ref}} \cdot 10^6, \ \delta_{11} \geq \delta_{22} \geq \delta_{33} \quad [2.15]$$

The isotropic shielding (σ_{iso}) or chemical shift (δ_{iso}) is the average of the three principal components of the $\ddot{\boldsymbol{\sigma}}$ and CS tensors, respectively, and is shown in Equation 2.16. The

Maryland convention [12] is used in this work to report the CS and MS tensor parameters.[13,14,15] The span (Ω) designates the breadth of the powder pattern and is shown in Equation 2.17. The skew (κ) represents its asymmetry and ranges between ±1, as expressed in Equation 2.18.

$$\delta_{iso} = \frac{\delta_{11}+\delta_{22}+\delta_{33}}{3} \quad [2.16]$$

$$\Omega = \sigma_{33} - \sigma_{11} \approx \delta_{11} - \delta_{33} \quad [2.17]$$

$$\kappa = \frac{3(\sigma_{iso}-\sigma_{22})}{\Omega} \approx \frac{3(\delta_{22}-\delta_{iso})}{\Omega} \quad [2.18]$$

In a crystalline powdered solid sample, the resulting NMR spectrum is a statistical distribution of all the crystallites in different orientations with respect to the magnetic field, yielding a broad resonance. These broad resonances are known as *powder patterns* and are characterized by orientation-dependent inhomogeneous broadening (anisotropy). Shown in Figure 2.6 are spectra simulated using chemical shift anisotropy (CSA).

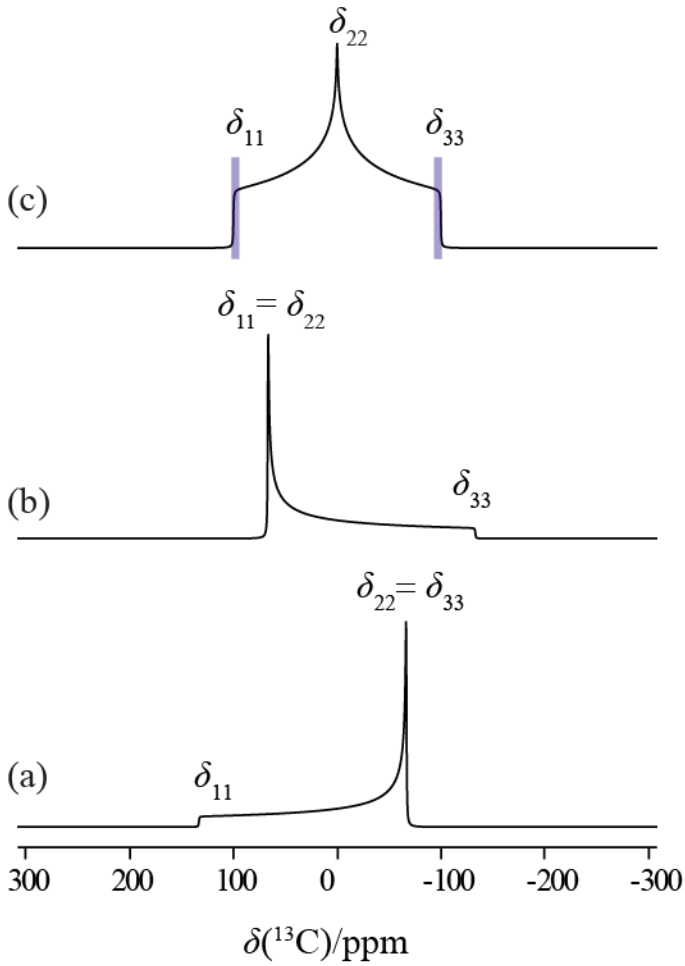

Figure 2.6 Simulated (WSolids program) static spectra for spin I = 1/2 nuclei, ^{31}P at a magnetic field of 9.4 T as an example (ν_L = 162.16 MHz) and the δ_{iso} value is set to 0 ppm. Shown on the spectra are the CS tensors using the Maryland convention, where the span (Ω) is equal to 200 ppm. The skew (κ) is equal to 0 in (a), and the spectrum is said to be axially symmetric when the skew is equal to (b) κ = +1.0, or (c) κ = -1.0. When the powder pattern is axially symmetric, two of the principal components have the same value: $\delta_{11} = \delta_{22}$ for κ = +1.0 and $\delta_{22} = \delta_{33}$ for κ = -1.0.

2.1.3.2 *Quadrupolar Interaction*

When the spin quantum number I, of a nucleus, is greater than 1/2, it will be associated with a nuclear electric quadrupolar moment (Q). This means that the nuclear charge distribution around the nucleus is no longer uniform. As illustrated in Figure 2.7,

when the value of *Q* is positive the nuclear charge distribution will be a prolate spheroid and when *Q* is negative the distribution will be an oblate spheroid.

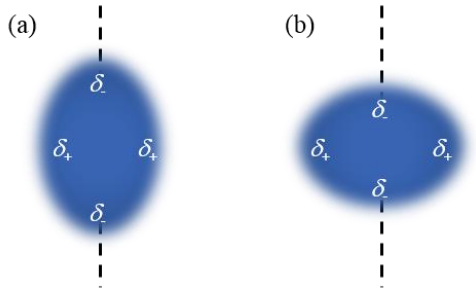

Figure 2.7 Qualitative representation of the nuclear charge distribution for $I > 1/2$ with a positive *Q* value and prolate spheroid distribution (a) and negative *Q* value and oblate spheroid distribution (b), where the partial electric charge, $\pm\delta$ is shown in the scheme.

The *Q* will interact with the electric field gradient (EFG) at the nucleus creating the quadrupolar interaction (QI). The QI is observed in our NMR spectra and results in a broadened resonance with a characteristic line shape. The QI Hamiltonian shown in Equation 2.19 is necessary when considering the study of integer spin nuclides like ^{14}N (I = 1) or half-integer nuclei such as $^{35/37}$Cl (I = 3/2) and $^{79/81}$Br (I = 3/2), which will be encountered in this work. The diagonalized QI Hamiltonian expanded into its PAS is shown in Equation 2.20

$$\hat{H}_Q = \frac{eQ}{4I(2I-1)\hbar}\hat{I}\ddot{\boldsymbol{V}}\hat{I} \quad [2.19]$$

$$\hat{H}_Q^{\,PAS} = \frac{eQ}{6I(2I-1)}\left[V_{11}\left(3I_X{}^2 - I^2\right) + V_{22}\left(3I_Y{}^2 - I^2\right) + V_{33}\left(3I_Z{}^2 - I^2\right)\right] \quad [2.20]$$

where *e* is the fundamental charge (1.602 176 · 10^{-19} C).

The EFG tensor ($\ddot{\boldsymbol{V}}$) is expressed as a traceless symmetric 3 X 3 matrix shown in Equation 2.21. When the $\ddot{\boldsymbol{V}}$ tensor is diagonalized, it provides three traceless principal

components defined as $|V_{33}| \geq |V_{22}| \geq |V_{11}|$, allowing the determination of the relative orientation of the EFG tensor PAS with respect to the molecular frame.

$$\begin{pmatrix} V_{XX} & V_{XY} & V_{XZ} \\ V_{YX} & V_{YY} & V_{YZ} \\ V_{ZX} & V_{ZY} & V_{ZZ} \end{pmatrix} \overset{PAS}{\Longrightarrow} \begin{pmatrix} V_{11} & 0 & 0 \\ 0 & V_{22} & 0 \\ 0 & 0 & V_{33} \end{pmatrix} \quad [2.21]$$

The EFG components may be fully described using the quadrupolar coupling constant (C_Q) and asymmetry (η_Q) parameters :

$$C_Q = \frac{eV_{33}Q}{h} \quad [2.22]$$

$$\eta_Q = \frac{V_{11} - V_{22}}{V_{33}} \quad [2.23]$$

$$V_{33} + V_{22} + V_{11} = 0 \quad [2.24]$$

where h is Planck's constant ($6.62607 \cdot 10^{-34}$ J s), and the measurement of C_Q is directly related to the largest principal component of the EFG tensor.

Even if the QI is usually an overwhelming interaction in the SSNMR spectrum, it is important to note that the presence of CSA can be observed. This is the case in most of the quadrupolar SSNMR spectra presented in this work. As both CS and EFG tensor interactions are diagonalized, their relative tensor orientation in the PAS can be connected with respect to the external magnetic field. Figure 2.8 depicts an additional set of three parameters known as the Euler angles[16] that have been introduced to relate the orientation of the CS and EFG tensors.

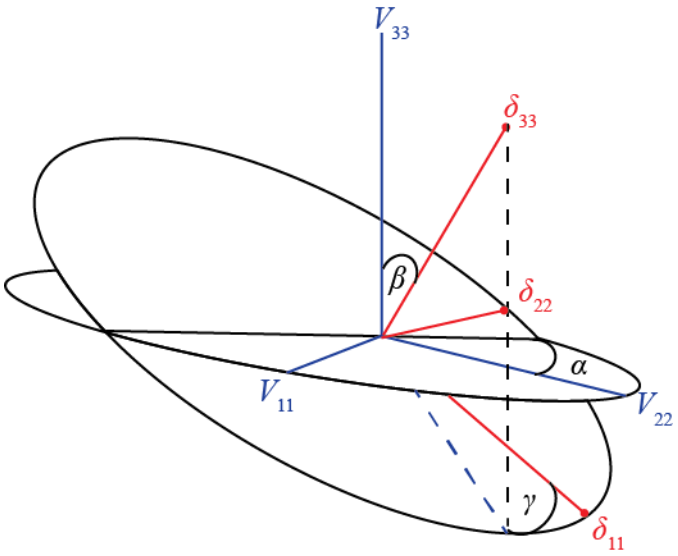

Figure 2.8 Depiction of the Euler angles α, β, and γ used for relating the PAS of the EFG tensor and the CS tensor PAS in the frame of reference.

2.1.3.2.1 Effect of the Quadrupolar Interaction on the SSNMR Line Shape

The quadrupolar interaction is treated as a perturbation to the Zeeman interaction. Using perturbation theory, the QI Hamiltonian can be written as:

$$\hat{H}_Q = \hat{H}_Q{}^{(I)} + \hat{H}_Q{}^{(II)} + \hat{H}_Q{}^{(III)} + \cdots$$

where $\hat{H}_Q{}^{(I)}$ indicates the Hamiltonian for the first order QI effect, $\hat{H}_Q{}^{(II)}$ for the second order QI, and so on. The QI will mainly affect the Zeeman eigenstates, m_l shown in Equation 2.25:

$$E_{m_l} = E_{Z,m_l} + E_{Q,m_l}{}^{(I)} + E_{Q,m_l}{}^{(II)} + \cdots \quad [2.25]$$

where E_{m_l} is the total energy of eigenstate m_l, E_{Z,m_l} is the energy of the Zeeman spin states, and the first and second order QI are indicated by $E_{Q,m_l}{}^{(I)}$ and $E_{Q,m_l}{}^{(II)}$, respectively. If the

system is placed in a strong magnetic field then it is assumed that the Zeeman interaction is much stronger than the QI, and only the first-order QI needs to be considered. Equation 2.26 shows this using θ and ϕ polar coordinates orienting the EFG tensor into its PAS with respect to the external magnetic field. However, when the Zeeman interaction is not much stronger than the QI, the higher terms in the perturbation Hamiltonian series need to be addressed.[17] Equation 2.27 describes $E_{m_l}^{Q\,(II)}$. Corrections up to second order QI are sufficient for splittings caused to the Zeeman interaction that are less than ~1/10.[18]

$$E_{m_l}^{Q\,(I)} = -\gamma\hbar B_o m_l + \frac{e^2qQ}{4I(2I-1)}\left(\frac{3cos^2\theta-1}{2}\right)(3{m_l}^2 - I(I+1)) \quad [2.26]$$

$$E_{m_l}^{Q\,(II)} = -\left(\frac{e^2qQ}{4I(2I-1)}\right)^2\left(\frac{m_l}{\omega_L}\right)\left\{-\frac{1}{S}(I(I+1)-3{m_l}^2\right\}\left(3+{\eta_Q}^2\right)+$$

$$\frac{1}{28}(8I(I+1)-12{m_l}^2-3)\left[\left({\eta_Q}^2-3\right)(3cos^2\theta-1)+6\eta_Q sin^2\theta cos2\phi\right]+$$

$$\tfrac{1}{8}(18I(I+1)-34{m_l}^2-5)\left[\begin{array}{c}\left(\frac{1}{140}(18+{\eta_Q}^2)\right)(35cos^4\theta-30cos^2\theta+3)\\+\frac{3}{7}\eta_Q sin^2\theta(7cos^2-1)cos2\phi+\frac{1}{4}{\eta_Q}^2 sin^4\theta cos4\phi\end{array}\right] \quad [2.27]$$

Figure 2.9 is the energy level diagram emphasizing the energy corrections of the Zeeman interaction by first and second order QI for a nucleus with a spin of $I = 3/2$.

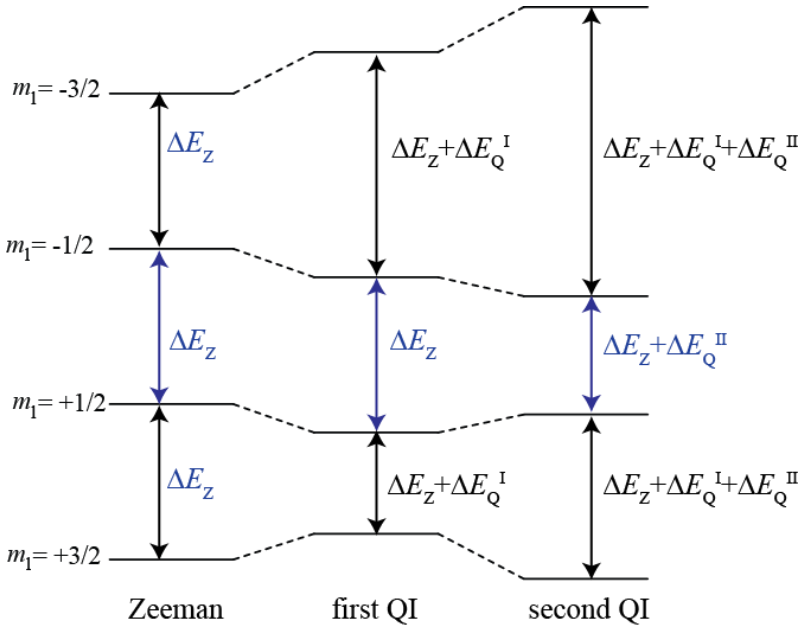

Figure 2.9 The energy level diagram first and second QI interaction on I = 3/2 nuclei with energy correction.

According to the energy equation of the eigenstate of the QI, the energy of the central transition (CT, $m_l = +1/2 \leftrightarrow m_l = -1/2$) is unaffected by the first order QI interaction. The value of the quadrupolar frequency (ν_Q)[23] is determined by the difference between the eigenstate ($\Delta m_l = 1$) values. For a nucleus with spin I = 5/2, each separation between m_l $\pm 1/2 \leftrightarrow \pm 3/2$, and $\pm 3/2 \leftrightarrow \pm 5/2$ designates the satellite transitions. The value of ν_Q is proportional to C_Q as described in Equation 2.28.

$$\nu_Q = \frac{3C_Q}{2I(2I-1)} \quad [2.28]$$

However, the CT is affected by the second-order QI interaction and the second-order quadrupolar shift is given by Equation 2.29. The breadth of the CT of the powder pattern under static conditions is described by Equation 2.30.

$$\Delta\nu_{m,m-1} = \frac{-3}{40}\left(\frac{{C_Q}^2}{\nu_L}\right)\left(\frac{I(I+1)-9m(m-1)-3}{I^2(2I-1)^2}\right)\left(1+\frac{{\eta_Q}^2}{3}\right) \quad [2.29]$$

$$\Delta\nu_{+\frac{1}{2}\leftrightarrow-\frac{1}{2}} = \left(\frac{25+22\eta_Q+{\eta_Q}^2}{4144}\right)\left(\frac{3{C_Q}^2}{(2I)(2I-1)^2}\right)\left(\frac{I(I+1)-\frac{3}{4}}{\nu_L}\right) \quad [2.30]$$

Examples of CT selective static SSNMR spectra of a quadrupolar spin 3/2 nucleus, where only the QI is observed (no CSA), are shown in Figure 2.10. These simulations are performed using the WSolids1 software,[19] which treats the QI as described here, a perturbation to the Zeeman interaction up to second order QI. It has been observed in the literature that this approximation fails when the Zeeman interaction is comparable to the QI or when the Zeeman interaction is small, or the nuclei has a low γ, or large *Q*, and or large EFG tensors.[20,21] When such a situation arises, perturbation theory to second order QI is not a suitable expression to describe the NMR line shape. The QUEST software developed by Perras *et al.* has been made available to the scientific community to simulate such broad spectra by using «exact» methods when the second-order perturbation theory is invalid.[22]

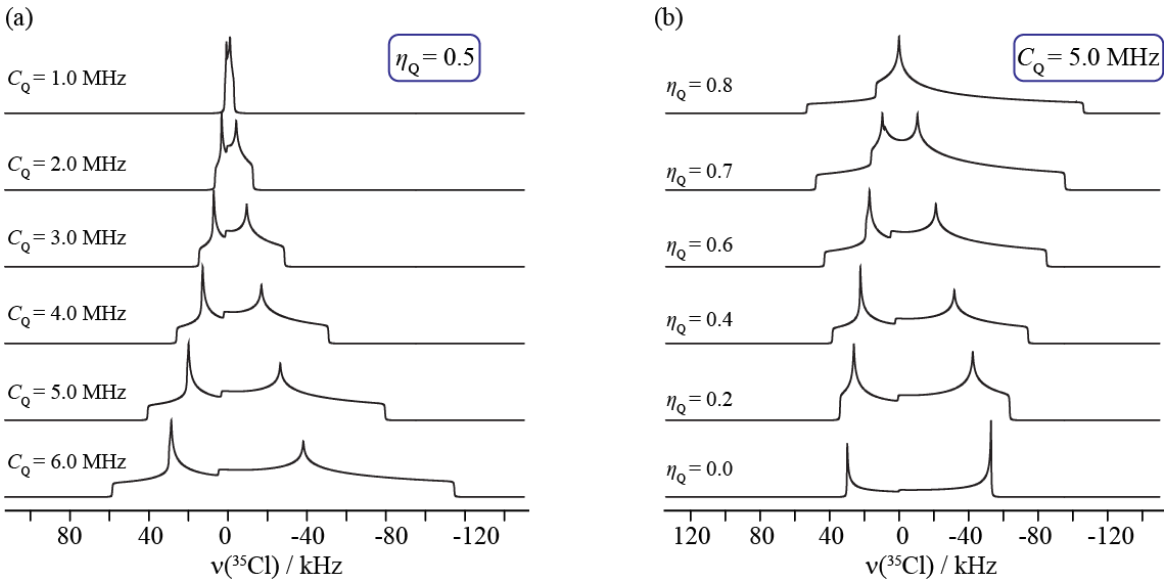

Figure 2.10 Quadrupolar static SSNMR spectrum of the CT under first order perturbation theory. In this example the quadrupolar nuclei ^{35}Cl (I = 3/2) at a field of 9.4 T ($\nu_L(^{35}Cl)$ = 39.26 MHz) is used where the isotropic shift is equal to 0 Hz. In (a) the asymmetry parameter is fixed to 0.5 and the C_Q value is varied. In (b) the C_Q value is fixed at 5 MHz and the η_Q is varied.

2.1.3.3 *Direct Dipolar Coupling*

Direct dipole-dipole coupling results from the interaction between the magnetic fields generated by each nuclear spin moment.[23] The total dipolar coupling Hamiltonian is given by Equation 2.31.[24]

$$\widehat{H}_D = hR_{DD}\hat{I}_1\ddot{\boldsymbol{D}}\hat{I}_2 \quad [2.31]$$

The dipolar coupling Hamiltonian between two different nuclei with spin quantum numbers I_1, I_2 and gyromagnetic ratios γ_1, γ_2 can be written as follows:

$$\widehat{H}_D = (\gamma_I\gamma_2\hbar^2)\left(\frac{\mu_o}{4\pi}\right)\left\{\frac{\hat{I}_1\cdot\hat{I}_2}{r^3} - 3\left(\frac{(\hat{I}_1\cdot\hat{r})(\hat{I}_1\cdot\hat{r})}{r^5}\right)\right\} \quad [2.32]$$

where $\hat{r}$ is the internuclear vector. The dipolar coupling vector $\ddot{\boldsymbol{D}}$ may be diagonalized in its PAS with respect to the external magnetic field, resulting in a perfectly axially-symmetric first rank tensor.

$$\widehat{H}_{\mathrm{D}}^{\ PAS} = hR_{\mathrm{DD}}[\hat{I}_{1X} \quad \hat{I}_{1Y} \quad \hat{I}_{1Z}]\begin{pmatrix}1 & 0 & 0\\ 0 & 1 & 0\\ 0 & 0 & -2\end{pmatrix}\begin{bmatrix}\hat{I}_{2X}\\ \hat{I}_{2Y}\\ \hat{I}_{2Y}\end{bmatrix} \quad [2.33]$$

This through-space interaction is represented by the dipolar coupling constant (R_{DD}) and is related to the inverse cube of the internuclear distance (r) as shown in Equation 2.34.[25]

$$R_{\mathrm{DD}} = \frac{\mu_0}{4\pi}\frac{\hbar\gamma_1\gamma_2}{2\pi}\langle {r_{I_1I_2}}^{-3}\rangle \quad [2.34]$$

Dipolar coupling is observed between heteronuclear spin pairs in this work: either between the quadrupolar nuclide ^{14}N (I = 1) and ^{13}C (I = 1/2) or, between the nucleus ^{31}P (I = 1/2) and ^{77}Se (I = 1/2). The dipolar coupling interaction causes huge line broadening, which is usually a hindrance for an NMR spectroscopist because it causes a loss in resolution. This effect will be observed in most spin 1/2 nuclei SSNMR spectra presented in this work. The reason for this is that the compounds studied contain iodine, which has a quadrupolar nucleus with a large quadrupole moment. However, when the dipolar coupling interaction is resolved it is one of the most significant experimental measurements of the internuclear distance, geometry, and conformation of the observed compound.[26] This interaction is also referred to as *through-space coupling*. Figure 2.11 illustrates the theoretical ^{13}C static and magic angle spinning (Section 2.1.4.1.1) NMR spectra for a ^{14}N, ^{13}C spin pair with R_{DD} = 1400 Hz and C_{Q}(^{14}N) = -2.0 MHz at 9.4 T.

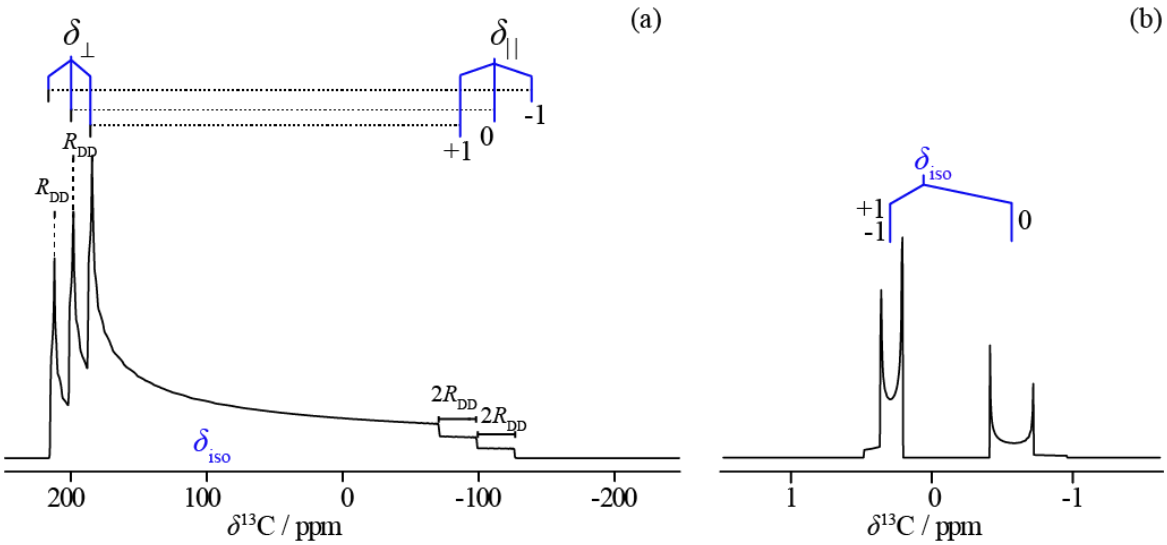

Figure 2.11 Simulated NMR line shapes for a ^{14}N, ^{13}C spin pair with R_{DD}= 1400 Hz, $C_Q(^{14}N)$ = -2.0 MHz at 9.4 T, and CSA: δ_{iso} = 100 ppm, Ω = 300 ppm, κ = +1. The EFG tensor is assumed to be axially symmetric with the largest principal component parallel to the ^{14}N, ^{13}C dipolar vector. The splitting arises from ^{14}N nuclide Zeeman eigenstates ± 1, 0.

2.1.3.4 *Indirect Nuclear Spin-Spin Coupling*

The indirect nuclear spin-spin coupling (*J*-coupling) is an interaction between nuclear spins mediated by intervening electrons.[23] This through-bond coupling is a very informative tool as it is a direct probe of molecular connectivity. The Hamiltonian may be written in the following way:

$$\hat{H}_J = h\hat{I}_1 \ddot{\mathbf{J}} \hat{I}_2 \quad [2.35]$$

The *J*-coupling interaction is represented as a second rank tensor ($\ddot{\mathbf{J}}$). Diagonalization of $\ddot{\mathbf{J}}$ yields the orientation of its PAS relative to the external axis system. In the PAS, three principal components result for the symmetric $\ddot{\mathbf{J}}$ tensor.

$$\begin{pmatrix} J_{XX} & J_{XY} & J_{XZ} \\ J_{YX} & J_{YY} & J_{YZ} \\ J_{ZX} & J_{ZY} & J_{ZZ} \end{pmatrix} \overset{PAS}{\Longrightarrow} \begin{pmatrix} J_{11} & 0 & 0 \\ 0 & J_{22} & 0 \\ 0 & 0 & J_{33} \end{pmatrix} \quad [2.36]$$

The isotropic *J*-coupling (J_{iso}) is the average of the three principal components of the $\ddot{\mathbf{J}}$ tensors, and the anisotropic part (ΔJ) of *J* is usually very small. Even though ΔJ is small, it is still observed in SSNMR spectra. Experimentally, the R_{DD} and ΔJ interactions are determined as a single value, the effective dipolar coupling constant R_{eff}. These interactions have been observed in some of the work presented in this thesis.

$$R_{\text{eff}} = R_{\text{DD}} - \frac{\Delta J}{3} \quad [2.37]$$

According to Ramsey's theory,[11] five mechanisms contribute to *J*-coupling: (1) diamagnetic spin-orbital (DSO) coupling, (2) paramagnetic spin-orbital (PSO) coupling, (3) Fermi-contact (FC) coupling, (4) spin-dipolar (SD) coupling, and (5) Fermi-contact spin-dipolar (FC · SD) cross-coupling.[11] The dominant term, FC, is the interaction between the nuclear and electron spins when the electrons are at the nucleus. The magnitude of the FC *J*-coupling is usually indicative of *s* orbital overlap between the nuclei. The DSO and PSO terms are responsible for the electron interactions between the nuclear spin angular momentum and orbital angular momentum. Similarly, the FC term accounts for the interaction between the nuclear spin angular momentum and orbital angular momentum of the nucleus.

The reduced spin-spin coupling tensor (*K*) is often reported instead of the *J*-coupling as it is independent of the gyromagnetic ratios.

$$K_{I_1 I_2} = \frac{4\pi^2 J_{I_1 I_2}}{\gamma_1 \gamma_2 h} \quad [2.38]$$

J-couplings are on the order of several to a hundred Hertz. Hence, it is an interaction that is usually observed in solution and spin 1/2 nuclei. However, *J*-couplings have recently been observed experimentally between quadrupolar nuclei for various inorganic systems in the solid state.[27] Experimentally observing *J*-coupling was a challenging task as SSNMR spectrum of quadrupolar nuclei will span over multiple kHz and the *J*-coupling interactions are small in comparison (few Hz).

2.1.4 *Solid-State NMR Methods*

Spins will undergo a relaxation phenomenon. There are two different mechanisms. The first is spin-lattice or longitudinal relaxation, T_1: the time constant for the build up of magnetization, $\boldsymbol{M}$, is reached along the direction of the external magnetic field. The second is spin-spin or transverse relaxation, T_2: a loss of phase coherence (decay of magnetization) among the nuclei after a RF pulse, and is less than or equal to T_1. The line-width of the NMR signal will depend on T_2 (line-width at half height, $\Delta\nu_{1/2}=1/\pi T_2$).[28]

The one-pulse experiment consists of applying an RF field of pulse length and power equal to $\pi/2$ in the *x* direction. A $\pi/2$ pulse is used to obtain the maximum intensity of the NMR signal and is directed as shown by Equation 2.39.

$$\theta_p = \omega_1 t_p \quad [2.39]$$

where t_p is the duration of the pulse and θ_p is the angle.[29] This is understood when one looks at Figure 2.5 above and now relates this to the effective field in frequency units, as shown in Equation 2.40.

$$\omega_{\text{eff}} = \sqrt{{\omega_1}^2 + {\Omega_{\text{off}}}^2} \quad [2.40]$$

The net magnetization that reached equilibrium along the *z*- axis after a certain delay ($5 \cdot T_1$) will be redirected along the *–y*- axis; this phenomenon is also known as *transverse magnetization*. The movement of the magnetization may be followed in Figure 2.12. The magnetization precesses in the transverse plane at the offset (Ω_{off}) and the variation of magnetization with time (t) may be determined as vectors precessing through the angle $\Omega_{\text{off}}t$.[9] The components are equal to:

$$\boldsymbol{M}_{\text{x}} = \boldsymbol{M} sin\Omega_{\text{off}}t \text{ and } \boldsymbol{M}_{\text{y}} = -\boldsymbol{M} cos\Omega_{\text{off}}t \quad [2.39]$$

The NMR signal is detected as a free induction decay (FID) in the time domain and a mathematical operation known as the Fourier transformation[30,31] transfers the information into the frequency domain yielding the NMR spectrum. The NMR spectrum contains all the information of the interactions previously discussed: MS, QI, D, and *J*-coupling.

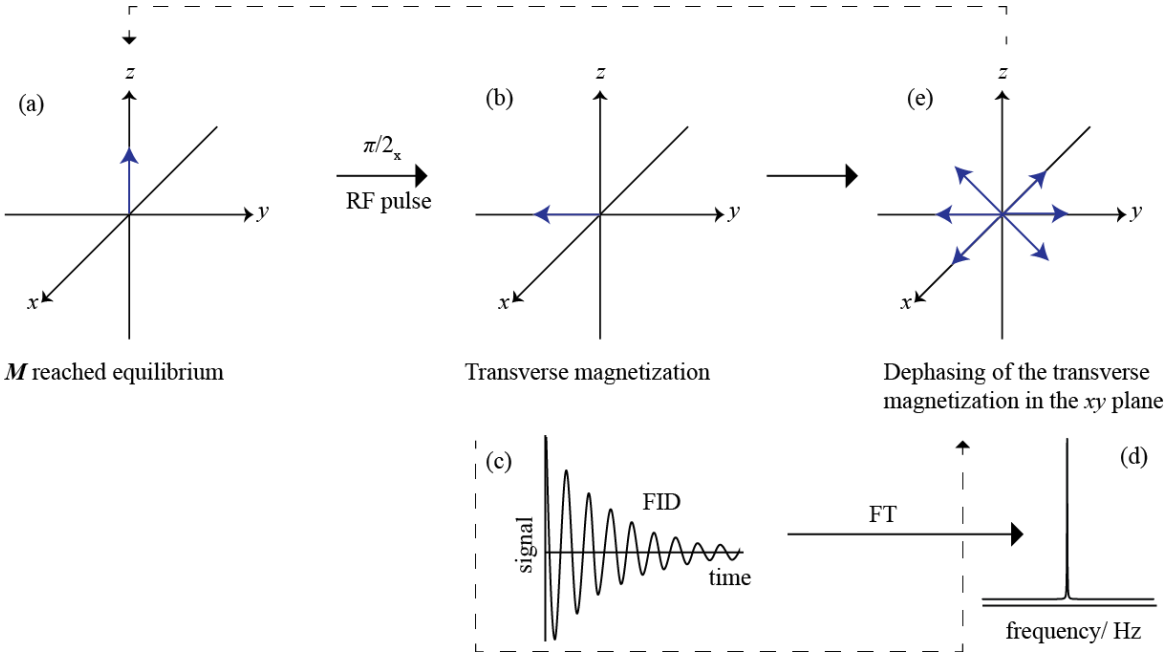

Figure 2.12 Vector model of the t_p NMR radiofrequency field pulse and delivery of the NMR signal. In (a) the Boltzmann equilibrium is reached, and the net magnetization vector is aligned with the external magnetic field, ***M***. After an RF pulse of $\theta_p = \pi/2_x$ in (b) the ***M*** vector is now in the *xy* plane, and is called the transverse magnetization. The NMR signal is detected as an FID in (c) and the FT of the signal yields the spectrum in the frequency domain in (d). To increase the signal of the spectrum, multiple experiments are acquired such as described here. Before repeating each step, a delay of about 5 times T_1 is necessary to reach the Boltzmann equilibrium and perform another RF pulse. During this interval, the spins will dephase in the transverse plane as shown in (e).

However, sometimes a single pulse experiment (also referred to as a Bloch decay) is insufficient to recover all of the information desired from the system under study.

2.1.4.1 *Signal and Resolution Enhancement Methods:*

A static SSNMR spectrum as stated previously is a statistical distribution of all orientations of the crystallites in the powder sample. The spectrum contains the

information of all of the NMR interactions with their full tensor form, which are orientation-dependent. Obtaining the full tensor information is an advantage in SSNMR, however, when multiple crystallographically non-equivalent nucleus sites are present in the sample, there is an overlap of the powder patterns and resolution is low. NMR spectroscopists have developed methods to enhance resolution and sensitivity for such experiments. Here are presented the most commonly used methods in the solid-state NMR field as well as the experiments used for this work.

2.1.4.1.1 Magic Angle Spinning

A resolution method routinely used by SSNMR spectroscopists is magic angle spinning (MAS). The experimental setup for the sample is shown in the inset of Figure 2.13. A sample is placed about an angle θ_R with respect to the external magnetic field (θ_R, B_o), which is equal to 54.74º. The angle relates the orientation of the interaction tensor fixed in the molecular frame. It varies with time as the molecule rotates with the sample.[32] Hence, spinning the sample about that axis will have the effect of averaging the anisotropy associated with the Zeeman interaction (no mixing of the Zeeman interaction, i.e. second order QI). Concretely, for spin 1/2 nuclei, it will suppress CSA, heteronuclear dipolar coupling (diminished homonuclear dipolar coupling), and for quadrupolar nuclei, MAS will remove first order QI and reduce second order QI as shown in Figure 2.13.

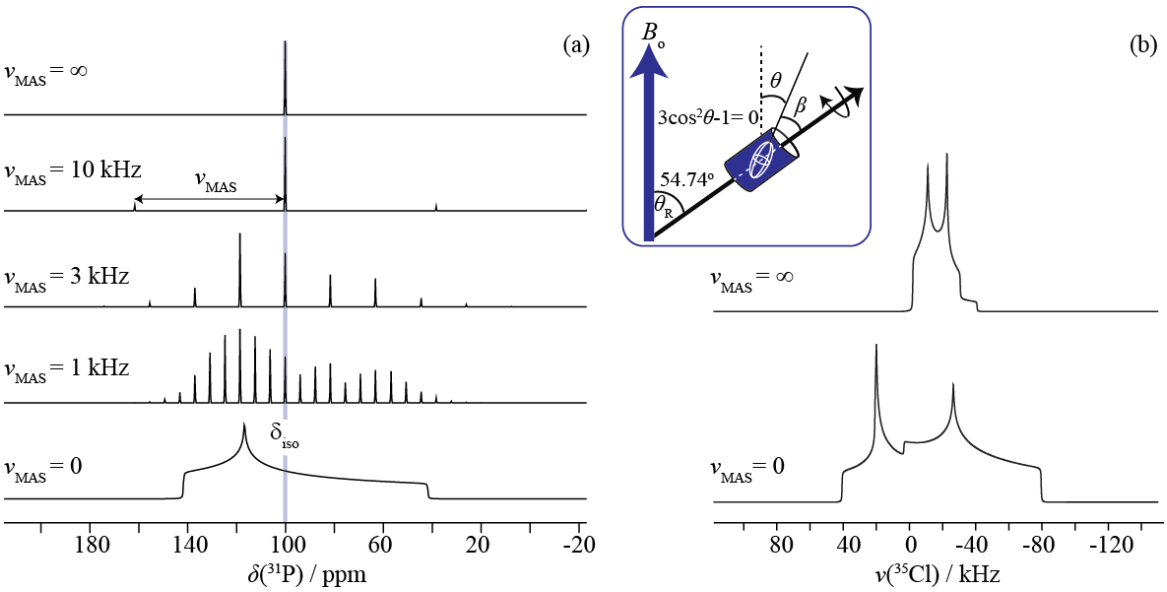

Figure 2.13 (a) Simulated MAS spectra for a spin 1/2 nucleus acquired at 9.4 T, where CSA dominates the powder pattern (Ω = 100 ppm, κ = 0.5, δ_{iso}= 100 ppm). The Figure illustrates how using slow MAS spinning speeds makes it possible to obtain the powder pattern with spinning sidebands. As the MAS frequency is increased the isotropic peak becomes evident. (b) Simulated MAS spectra for a quadrupolar nucleus, I = 3/2 (C_Q = 5 MHz, η_Q = 0.4 and δ_{iso}= 0 Hz). The MAS spectrum of a quadrupolar nucleus will not have the appearance of a solution spectra as it does not average out the second-order quadrupolar interaction. The inset shows the scheme of the MAS sample setup: the rotor is placed at 54.74 º and spun along that axis.

The mathematical explanation of the magic angle is the dependency of the interactions mentioned above on the average of the orientation ($3cos^2\theta_R - 1$) term. For the case of CSA, a sample is placed in a rotor at the angle θ_R (angle between B_o and the spinning axis) and two other angles stand out (Figure 2.13 inset): the angle β between the principal z-axis of the CS tensor and the spinning axis, and the angle θ between the principal z-axis and the B_o. The angle controlled experimentally is θ_R and when that value is equal to 54.74º, the $3cos^2\theta_R - 1$ term is zero and so the average will also be null.[18,33,34]

$$\langle 3cos^2\theta - 1\rangle = \frac{1}{2}(3cos^2\theta_R - 1)(3cos^2\beta - 1) \quad [2.40]$$

When the spinning speed is fast enough to suppress the anisotropy (3 to 4 times greater than the anisotropy), only the isotropic chemical shift is observed, similar to what is observed in a solution spectrum for a spin 1/2 nucleus (see Figure 2.13(a)). If the spinning speed does not average out the anisotropy, spinning sidebands are observed at resonances spaced at integer multiples of the spinning speed (ν_{MAS}) from the δ_{iso} resonance. Slowly spinning the sample will generate a spinning sideband manifold mimicking a static spectrum. Although the δ_{iso} peak is not necessarily the most intense resonance of the spinning sidebands, it is the only spinning sideband that does not change position with spinning speed, hence permitting its identification. Spinning sidebands can be very useful in the determination of CSA as will be shown through this work. It should also be noted that CSA is proportional to the external magnetic field; when the B_o increases so does the CSA. Higher magnetic fields are not always advantageous for spin 1/2 nuclei, because the intensity of the signal is dispersed throughout the line shape and it may be difficult to acquire a spectrum with a respectable S/N ratio.[35]

For quadrupolar nuclei, the MAS spectrum is 3 to 4 times narrower than the static spectrum[36] and the powder pattern depends only on the EFG tensors. This phenomenon makes it easier to simulate the powder pattern when the CSA and Euler angles may be removed (only depends on three parameters instead of nine).

2.1.4.1.2 Proton Decoupling

Proton decoupling is used in of all the experiments for this work because the heteronuclear dipolar coupling interaction between ^{1}H and the observed nuclei is

overpowering. The removal of the dipolar coupling interaction permits observation of the signal of the desired nucleus. The pulse sequence used in the decoupling scheme is varied to be as powerful as possible, but also to be as gentle on the laboratory equipment as possible. The simplest and most effective way to decouple protons is to apply an RF field at the frequency of the protons' resonance while acquiring the FID on the nucleus of interest. This is shown in the pulse sequences given in the later sections and is usually referred to as continuous-wave (CW).[37] However, this work uses other decoupling schemes, such as two pulse phase modulation (TPPM)[38] and a variation of this known as SPINAL64.[39] By optimizing the pulse length and phase in the pulse sequences, the TPPM and SPINAL64 schemes greatly reduce residual line widths from dipolar coupling, and enhance the resolution and sensitivity for the nucleus of interest; for example, ^{13}C or $^{35/37}Cl$. The decoupling schemes are continuous cycles composed of two pulses for TPPM with opposite phases (Equation 2.43), whereas SPINAL uses those phases to construct a super cycle where the phases and angles are slightly varied (Equations 2.43 and 2.45).

$$\text{TPPM}=P\bar{P}, \text{ where } P = 165(10)^\circ \text{and } \bar{P}=165(\text{-}10)^\circ \quad [2.41]$$

$$\text{SPINAL, Q} = [165(10)^\circ 165(\text{-}10)165(15)165(\text{-}15)]\cdot[165(20)^\circ 165(\text{-}20)165(15)165(\text{-}15)]$$
$$\bar{\text{Q}} = [165(\text{-}10)^\circ 165(10)165(\text{-}15)165(15)]\cdot[165(\text{-}20)^\circ 165(20)165(\text{-}15)165(15)] \quad [2.42]$$

$$\text{SPINAL64} = \text{Q}\bar{\text{Q}}\bar{\text{Q}}\text{Q}\ \bar{\text{Q}}\text{QQ}\bar{\text{Q}} \quad [2.43]$$

2.1.4.1.3 Cross Polarization Pulse Sequence

Cross polarization (CP) is a signal enhancement experiment used to increase the signal of a dilute spin (e.g. ^{13}C, ^{15}N, ^{77}Se) for dipolar coupled nuclei. Dilute spins tend to

be associated with long T_1 relaxation times because the homonuclear dipolar interaction that stimulates this relaxation mechanism is almost absent. The CP pulse sequence (Figure 2.14) operates by transferring spin magnetization from the abundant spin to the dilute spin when the frequencies are equal, increasing sensitivity and, therefore, the signal to noise (S/N) ratio by a factor of $\gamma_{\text{abundant}}/\gamma_{\text{dilute}}$.[40] Hence, this experiment helps with two main points: (1) an increase in S/N ratio for the dilute spin and (2) it decreases experimental time. To achieve this magnetization transfer, the Hartmann-Hahn match must be satisfied and is defined as:

$$\gamma_{\text{H}} B_1(^1\text{H}) = \gamma_{\text{X}} B_1(\text{X}) \quad [2.44]$$

where γ is the gyromagnetic ratio and B_1 is the magnetic field. In this example, the proton is the abundant nucleus, and X is the dilute nucleus.

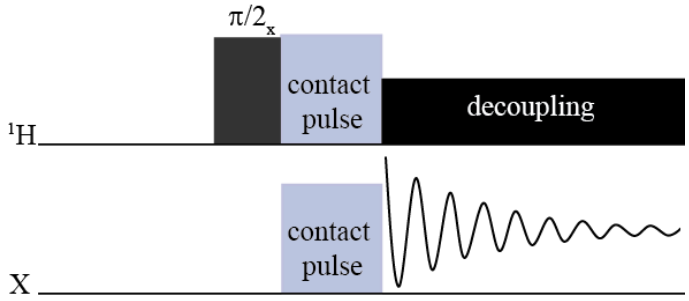

Figure 2.14 Cross polarization pulse sequence.

A decrease in experimental time is achieved, since the T_1 mechanism for the experiment will be directed by the abundant spin, where homonuclear dipolar coupling interactions are present and trigger the relaxation.[32] CP is routinely used under MAS spinning conditions (CPMAS) for spin 1/2 nuclei.[41,35] It has been demonstrated in the literature that CPMAS is inefficient for quadrupolar nuclei due to its time dependence

component in the energy state with the rotor period when spinning;[42,43] however it is possible to obtain a signal enhancement when the sample is static.[44,45]

2.1.4.1.4 Refocusing Experiment: Hahn Echo and Solid Echo Pulse Sequence

When acquiring the spectrum of a broad powder pattern some issues of distorted line shapes may arise. Refocusing experiments are usually the solution for remedying those distortions that are a result of rapid FID decay. Spin dephasing, which is constant with time, can be refocused using spin-echo experiments and are shown in Figure 2.15.

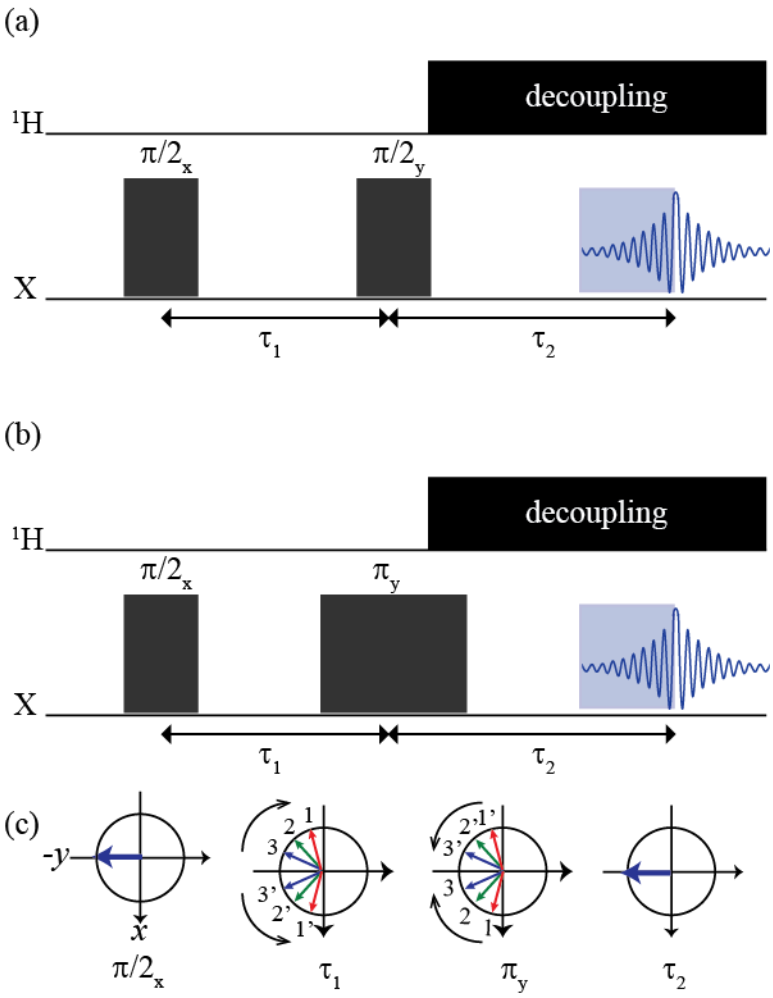

Figure 2.15 Solid echo (or quadrupolar echo or Solomon echo) pulse sequence in (a) is used to overcome line broadening from the quadrupolar coupling interaction or homonuclear dipole-dipole coupling. Hahn echo (spin echo) pulse sequence in (b) usually used to overcome FID distortions caused by CSA or heteronuclear dipole-dipole coupling. (c) Vector model of Hahn echo where the colored arrows depict experiment and dephasing.

Dephasing of the spin may be caused by magnetic field inhomogeneity, local magnetic field susceptibility, CSA, dipolar coupling, or quadrupolar interaction.[46] The spin echo pulse sequence[47] is shown in (b), and its corresponding vector model is shown in (c). The sequence begins with an initial $\pi/2_x$ pulse to create magnetization along the *y*-axis of

the rotating sample, known as the excitation pulse. The magnetization vector rotates in the *x*-*y* plane. This is usually followed by a dephasing period during a delay (τ_1). After a second π_x pulse is applied, the spins are flipped in the transverse plane, thus refocusing the initial pulse. Again the pulse rotates in the *xy* plane during a delay period (τ_2). At the end, the FID is collected in the *y*- axis forming a spin-echo where one can choose to process all the data points when the full echo is acquired or simply half the echo (remove the other data points). The solid echo experiment uses two $\pi/2$ pulse.[48,49] It is observed to produce uniform excitation, yielding cleaner line shape when compared to the Hahn echo experiment (pulse sequence in Figure 2.15(a)). This uniform excitation will, unfortunately, yield a lower signal when compared to a Hahn echo experiment, by a factor of about two.[50] However, this is acceptable when the QI is overwhelming. Cleaner line shapes, where discontinuities are obvious, might permit the observation of CSA in those circumstances.

2.1.4.1.5 WURST-QCPMG Experiment

The acquisition of a static quadrupolar nuclei powder pattern may span over hundreds of kHz to MHz. They are also known as ultra-wideline spectra. Short and high-power RF fields must be used to uniformly excite a large bandwidth; however the RF fields used are usually limited by hardware, which is ~200 kHz amplitudes, and depends on the Q factor of the NMR probe. Hence, an ultra-wideline spectrum cannot be observed in one spectral window. The broad spectra are acquired in multiple pieces that are co-added to yield the full powder pattern. This is achieved by varying the offset frequency in a stepwise fashion, known as the variable offset cumulative spectra (VOCS) acquisition method.[51]

Another possibility to acquire ultra-wideline spectra of quadrupolar nuclei is proposed by Bhattacharyya and Frydman,[52] where a chirped pulse, such as WURST[53], is used. A chirped pulse is a shaped pulse were the adiabatic condition is not met because sweeping rates are too fast or low RF powers are used, which has the effect of no longer enhancing the signal by satellite inversion or saturation of the CT.[54] Also, a WURST pulse has a round-off shape of amplitude profile, its phase is a quadratic function of time, and it has linear sweep rate of effective frequency. The use of a chirped WURST pulse was observed to excite broader bandwidth (frequency range) uniformly than a instead of a square pulse in a single spectral window, and simultaneously permits control of the RF field strength and durations, which are usually limited by the probe. In this work, the further modified pulse sequence by O'Dell and Schurko is used.[55] They integrated the sensitivity enhancement technique of quadrupolar Carr-Purcell-Meiboom-Gill (QCPMG) [56] henceforth known as WURST-QCPMG, where the pulse sequence is depicted in Figure 2.16.

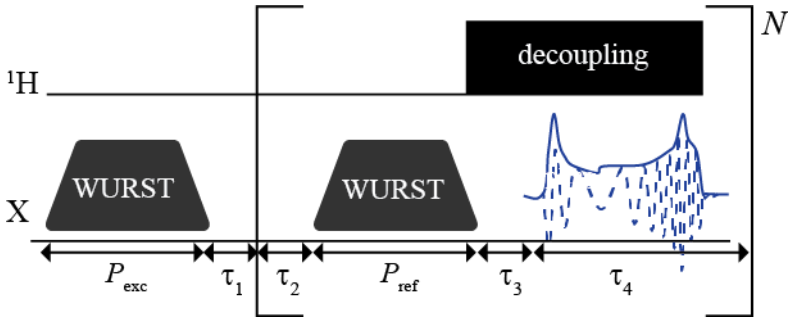

Figure 2.16 WURST-QCPMG pulse sequence.

After the first WURST pulse (P_{exc}) and delay (τ_1), there are two short delays (τ_2 and τ_3) necessary for the time switch between the transmission and acquisition modes.

Following this is the QCPMG enhancement part, which is a refocusing loop that will be repeated *N* times, and consists of a second WURST pulse ($P_{ref} = P_{exc}$) and acquisition time (full echo, τ_4). The FIDs acquired with WURST-QCPMG result in frequency dispersed echoes where the time domain amplitude reflects the frequency domain signal intensity. They are not FT; they are treated with absolute value/magnitude mode were a series of spikelets, separated by τ_4^{-1}, mimics the powder pattern. This method can also be combined with the VOCS technique, which is now commonly used for the acquisition of wideline quadrupolar nuclei in SSNMR spectroscopy.

2.2 QUANTUM CHEMICAL CALCULATIONS

Computational methods are used as a complementary technique to the SSNMR experiments performed, because it is possible to obtain NMR parameters such as *J*-couplings, MS tensors, and EFG tensors. Here, quantum calculations are also used as a helpful tool to understand the halogen bonding interaction in terms of our NMR parameters, which will be described in details in the later Chapters. In this section, the different density functional theory (DFT) methods used to calculate the NMR parameters for the non-covalent interactions presented in this work are discussed. The NMR parameters were extracted using a modified version of EFGShield program.[57]

2.2.1 *Density Functional Theory*

DFT calculations, contrarily to *ab initio* calculations, are not based on the Schrodinger equation ($H\Psi=E\Psi$). *Ab initio* calculations try to solve the exact wave function

(Ψ) to describe the behaviour of all the *N* electrons in a system. DFT will approximate the wave function to its electron density (ρ(r)), where the energy in the ground state is determined by its electronic density, such as in Equation 2.47.

$$E = E[\rho(r)] \quad [2.45]$$

The partitioning of the electron density is described by Kohn-Sham orbitals (φ) (*not* wavefunctions), described in Equation 2.48.

$$\rho(r) = \sum_{a=1}^{N^\alpha} |\varphi_a^\alpha|^2 + \sum_{a=1}^{N^\beta} \left|\varphi_a^\beta\right|^2 \quad [2.46]$$

where N^α is the number of spin-up electrons' orbitals, and N^β is the number of spin down electrons' orbitals. The Kohn-Sham approach breaks down the total energy into three functional terms: (1) the kinetic energy functional T[ρ(r)], (2) the Coulomb functional U[ρ(r)], and (3) the exchange and correlation (XC) functional E_{xc}[ρ(r)], and is shown in Equation 2.49.

$$E[\rho(r)] = \mathrm{T}[\rho(r)] + \mathrm{U}[\rho(r)] + \mathrm{E_{XC}}[\rho(r)] \quad [2.47]$$

The XC functional term accounts for the approximation errors from the true kinetic and coulombic functionals. However, they are not accounting for interactions such as repulsion and attraction between the electrons and nuclei. It is an unknown functional and will remain so.[58] Multiple approximations of the XC functional exist and have been tried in this work in various software packages and will be described in the sections below.

2.2.2 *Gaussian'09 Software*

The Gaussian'09 software package[59] is used to calculate *J*-coupling, MS, and EFG tensor parameters. The Gaussian'09 software permits the study of cluster models. This is useful when studying a particular part of the crystal structure, for example, halogen bonds. All cluster models of the experimental compounds are generated from the X-ray crystal structure, which include the molecules participating in the non-covalent interaction, and truncate the other atoms at ~4 - 5 Å away from the system of interest. This has the advantage of decreasing computational time and cost, and does not usually affect the calculated NMR parameters.

When calculating the theoretical NMR parameters, there was always the challenge of selecting an appropriate level of theory to reproduce the observed experimental electrostatic interactions. The selection of the level of theory to reproduce electrostatic interactions is limited by the available level of theory to calculate NMR parameters. This work uses mainly hybrid-DFT level of theory such as B3LYP[60] and TPSS[61] functional terms, in combination with the Gaussian'09 basis sets developed by Pople (i.e. 6-311G+) as they provided reproducible calculations of the observed NMR parameters.[59]

2.2.3 *ADF*

This work also uses the Amsterdam Density Functional (ADF) Theory software version 2009.01[62] to calculate NMR tensor parameters for cluster models. In addition to this, the ADF program has the ability to evaluate accurately all required atomic matrix elements and to permit the implementation of the zeroth-order regular approximation

(ZORA) formulism.[63,64,65] As well, it has the capacity of calculating and viewing the natural localized molecular orbital (NLMO)[66] in terms of NMR parameters.

ZORA

MS, *J*-coupling, and the QI are dependent on the electron motion close to the nucleus in question. A heavier nucleus with greater electronic mass requires a relativistic correction to account for its velocity, as the core electrons will travel closer to the speed of light. As a result, the radial functions of the s and p electrons are contracted naturally accompanying a decrease in the effective nuclear charge of the d and f electrons.

The ZORA formalism accounts for scalar and spin-orbit relativistic effects, which have an important effect on the core orbitals (s orbital matrix in the calculations) for a heavy element when calculating NMR parameters.[67] The ZORA formalism is derived from the Dirac equation of the wave function and the Pauli approximation. The Zora formalism will demonstrate how the relativistic effects predict relative anisotropy for the J̈ tensor.[63,64,65] The spin-orbit effect will factor splitting of the orbital energy levels when there is coupling between the electron spin and the orbital electrons' angular momentum.[68] When the chemical shift tensor for a nucleus bound to a heavy element is calculated, scalar and spin-orbit relativistic effects need to be accounted for in the calculations in order to reproduce experimental observations. A heavy atom will induce large, lower-frequency shifts through a polarization mechanism on the NMR nuclei bound to it. This phenomenon is known as the *heavy-atom effect*[69] and it is observed in the halogen bonded systems studied in this work. Scalar relativistic effects mainly cause a modification of the overall electronic structure in the system under study.[67]

NLMO

The orbital-based analysis of the calculated NMR parameters permits the establishment of different contributions in a visual support that chemists are familiar with: molecular orbitals (MO). The modern localized molecular orbital analysis is obtained from the set of canonical MO and applying a unitary transformation to obtain the maximum and minimum localization criterion. In the ADF code,[70] the natural bonding orbital (NBO) is used to determine the NLMO through the formalism as written below:

$$\phi_j^{NLMO} = \Omega_j W_{jj} + \sum_{n \neq j}^{NBO} \Omega_n W_{nj}\,, where\ \Omega_n = \sum_r^{AO} \varphi_r B_{rn} \quad [2.48]$$

where the Ω_n are a set of strongly-localized NBOs resembling the Lewis dot formula, and W_{jj} and NBOs are expressed in atomic orbital (AO) basis set, $\varphi_r B_{rn}$. The NLMO orbital, ϕ_j^{NLMO}, is the sum of the localized Ω_j term corresponding to its parent NBO, and the remaining terms represent delocalization of the electron density.[66] The resulting Lewis-type NLMOs can be visualized with the graphical user interface (GUI) program adfview and are represented by core functions, lone pairs, and bonding orbitals.

The exchange-correlation functional used with the ADF software is the generalized gradient approximation (GGA). The $E_{xc}[\rho(r)]$ term is expressed as an electronic gradient distribution to provide a more realistic account of the inhomogenous electronic distribution in a molecule. The hybrid DFT functional revised PBE was employed in this work.[71,72] The basis sets used for all atoms were Slater-type triple-zeta with polarization (TZP) functions incorporated in the ADF software's library, as well as the relativistic optimized (ZORA/TZP) version functions, when necessary.

2.2.4 *GIPAW-DFT*

DFT plane wave method calculations on periodic structures are possible using the gauge-including projector augmented-wave (GIPAW)[73] methods for NMR calculations in the Cambridge Serial Total Energy Package (CASTEP version 4.1, Materials Studio 3.2).[74,75] The crystal structure is described as an infinite crystal lattice, which is the ideal case for solids. This is modeled with three-dimensional plane waves for the valence electron density and yet modeled with pseudopotential schemes for the electron core density.[76] The calculation of all-electron properties from pseudopotential schemes is possible when GIPAW is used, which include translational invariance in the presence of a magnetic field. In these calculations, a plane-wave basis set is used to describe the electronic band and is defined by the *cut-off* energy and *k*-point grid. The energy *cut-off* will be a representation of the quality of the calculation (enables convergence), and the *k*-point grid is the number of sample points used in a primitive cell in reciprocal space.[76] In this work, GIPAW-DFT calculations are not often successful because the unit cell of the X-ray crystal structures reported for this work are very large (~ >1000 Å) and the calculations do not converge. The level of theory used for these calculations is the PBE functional[71,72] under the GGA approximation.

2.3 X-RAY CRYSTALLOGRAPHY

2.3.5 *Fundamentals of X-ray Diffraction*

X-rays are generated by bombarding a metal with high-energy electrons that will decelerate and generate a continuous range of wavelengths called *Bremsstrahlung*

combined with high-intensity peaks (K_α). This electromagnetic radiation is used in a method known as X-ray crystallography to reveal the position of every atom in a molecule and determine its conformation in 3D. However, a single crystal of the system of interest must be obtained because the high electron density it produces permits scattering of the X-ray. This is an important component of this technique as will be discussed below in relation to the diffraction phenomenon. X-ray crystallography is a complementary technique used in this work. Single crystal X-ray crystallography methods permit the determination of chemical bond distances and angles. This allows the halogen bonded environment to be determined from X-ray measurements and to be related to the variation in the NMR parameters.

Modern X-ray crystallography methods developed by Nobel Prize winners William Henry Bragg and William Lawrence Bragg[77], use a monochromatic beam of X-rays while rotating the single crystal until a reflection is detected. Single-crystal diffraction patterns are measured by using a four-circle diffractometer as depicted in Figure 2.17 below.

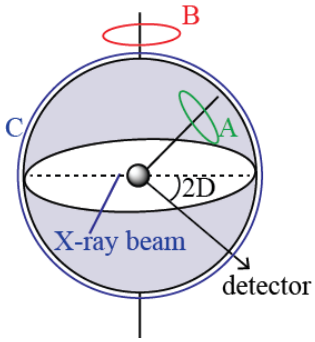

Figure 2.17 A four-circle diffractometer where A, B, C and D are the orientations of the components, and where each reflection (*hkl*) (*vide infra*) is monitored.

Advances in the X-ray field have made it semi-automated. A computer may control and rotate the crystal to detect diffractions, and to measure its intensity, as well as

background noise. There is also an automatic indexing to help systematize determination of the crystal structure.[78]

X-ray scattering is caused by the oscillation of incoming electromagnetic waves of electrons at the atom depending on the number of electrons the nucleus has. Scattering will be stronger for heavier nuclei (more valence electrons). X-rays detect all atoms except hydrogens (only one electron).

When a crystal is subject to X-rays, the interference of resulting scattered reflections causes a phenomenon called diffraction. Bragg's law of XRD (see Figure 2.18) is evidence for the periodic structure of the crystal containing stacks of reflecting lattice planes. Bragg's law states that scattering X-rays are separated by a distance *d* and the wavelength of radiation, λ, follows Equation 2.50 below:

$$\lambda = 2dsin\theta_c \quad [2.49]$$

where θ_c is the glancing angle.[79,77] The primary use of Bragg's law is the determination of spacing between the layers in the lattice (*vide infra*).

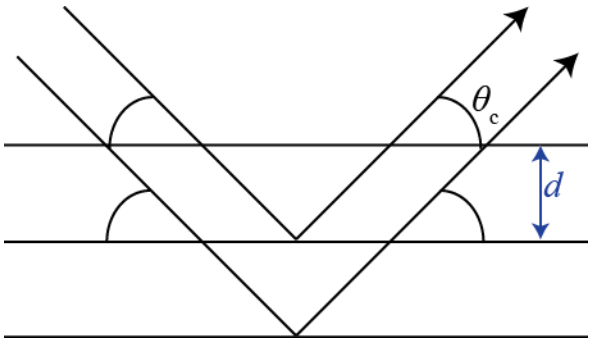

Figure 2.18 Bragg's law, reflection.

2.3.6 *Lattice and Crystal System*

A basic crystal structure is defined by space lattice patterns, which are three-dimensional infinite sequences of lattice points surrounded by identical neighbours. The unit cell of a crystal structure is the fundamental parallel-sided unit that contains the repeating pattern by translational motion; lengths are denoted by a_c, b_c and c_c and angles by α_c, β_c, and γ_c. Crystal structures are classified into seven systems (Table 2.1) based on the rotational symmetry elements that the unit cell possesses, and are further classified into fourteen distinct lattices in three-dimensional space known as the Bravais lattices[7] depicted in Figure 2.19.

Table 2.1 The seven crystal systems.

System	Essential Symmetries	The 14 Bravais Lattices[a]			
Triclinic	None	*P*			
Monoclinic	1 C_2 axis	*P*	*C*		
Orthorhombic	3 $\perp$ C_2 axis	*P*	*C*	I_c	*F*
Rhombohedral	1 C_3 axis	*R* or *P*			
Tetragonal	1 C_4 axis	*P*		I_c	
Hexagonal	1 C_6 axis	*P*			
Cubic	4 C_3 axis in a T_d arrangement	*P*		I_c	*F*

[a] Figure 2.19 depicts the 14 lattice systems with their different crystal axes. In the illustrations, (*P*) indicates a primitive or simple unit cell, (*C*) indicates a base-centered cell unit with two lattice points on two opposite faces, (I_c) indicates a body-centered unit cell and (*F*) indicates a face-centered unit cell.

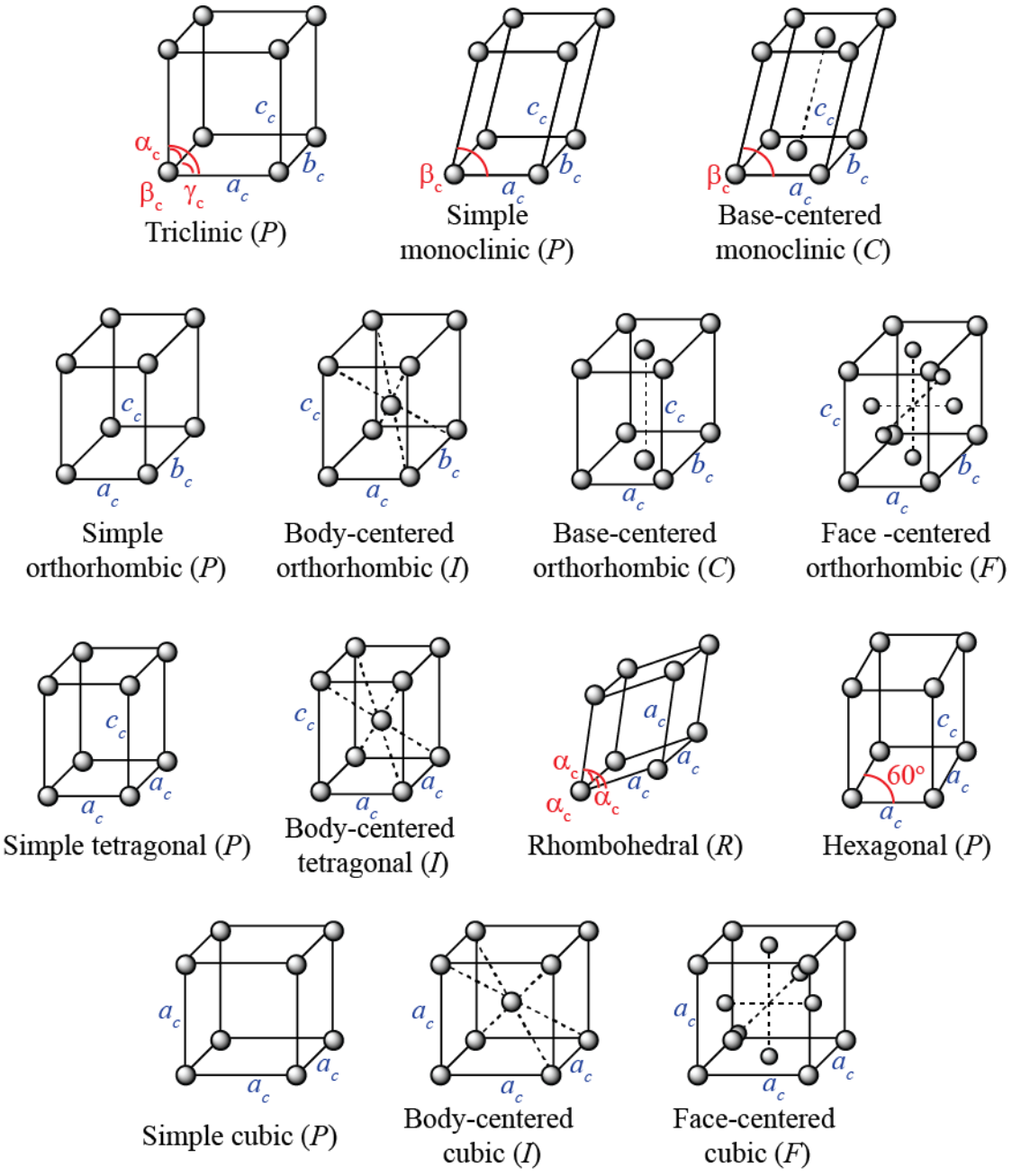

Figure 2.19 The crystal systems and the Bravais Lattice.

Miller indices (*hkl*) are used to identify the spacing and directions of different planes in the lattice of the crystal, where the points at the reciprocals of the fractional intercepts

intersection of the a_c, b_c, c_c axes of the unit cell form a plane.[80] Figure 2.20 illustrates the relationship between these planes and axes of a unit cell and to dimension, h_c.

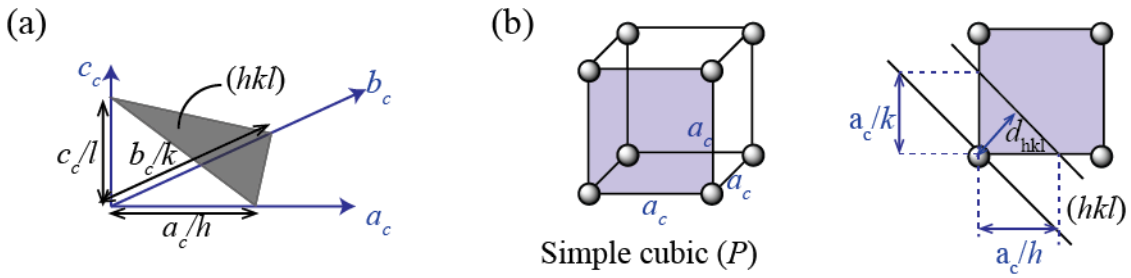

Figure 2.20 Miller indices (a) and spacing in a unit cell example for simple cubic (b).

Since X-ray scattering is caused by the oscillation of incoming electromagnetic waves at the nucleus, that electron density is employed to solve the detailed structure of a crystal from its primary unit cell. A structure factor, F_{hkl}, is first calculated and is defined below in Equation 2.52:

$$F_{hkl} = \sum_j f_j e^{i\varphi_{hkl(j)}}, \varphi_{hkl_{(j)}} = 2\pi(h_{xj} + k_{yj} + l_{zj}) \quad [2.50]$$

The intensity of a reflection (*hkl*) is proportional to $|F_{hkl}|^2$.[81] In a second time, once the structure factor is known, the electron density ρ(r) in the unit cell can be determined by Equation 2.53:

$$\rho(r) = \frac{1}{V}\sum_{hkl} F_{hkl} e^{-2\pi i(h_x + k_y + l_z)} \quad [2.51]$$

where V is the volume and Equation 2.52 is the Fourier synthesis. In some cases, phase problems are encountered. The resulting non-centrosymmetric unit cells are in that case solved with the Patterson synthesis.[81] The final step is the structure refinement, where the

parameters are adjusted systematically to give the best fit between observed and calculated diffracted intensities.

These crystal systems are further classified into *space groups*. A space group is a classification according to symmetry operations arising from translation through space, where the infinite array of points is indistinguishable from before the symmetry operation.[82] These are the well-known point group symmetry operations such as the proper (C_n) and improper (S_n) *n*-fold rotation about an axis, the reflection in a mirror plane (σ_{mp}), and the inversion (*i*).[7] Translational elements allow two additional types of symmetry operations: screw axes and glide plane operations.[7] All of the space groups defining crystal structures have been tabulated and made available by the International Union of Crystallography (IUCr).[83,84] The asymmetric unit is the smallest part of the space group necessary to build the whole space by using symmetry operations.

2.3.7 *Powder X-ray Diffraction*

Powder X-ray diffraction (PXRD) is a useful alternative to single X-ray crystallography when a single crystal of suitable quality and size cannot be grown. The resulting diffractogram is a combination of diffraction lines with specific intensities and positions that contains the same information obtained from a single crystal experiment, but is compressed into one dimension. The positions of the diffractions' maxima depend on the periodicity of the structure; the relative intensities depend on the distribution of the scattering material.[85] It is possible but quite complicated to obtain the crystal structure from a PXRD because overlapping peaks hide much important information. One of the main uses of PXRD is to verify the presence of a single phase or multiple phases in the bulk

material by comparing the diffractogram with diffraction patterns stored in large data banks. Well over half a million substances have been indexed and recorded by the International Centre for Diffraction Data (ICDD).[86] PXRD is used to verify bulk material purity and is shown throughout this work.

The diffraction maxima intensity is characterized by a set of Miller indices and is defined by a scattering vector $\boldsymbol{H}$ in reciprocal space ($\boldsymbol{H} = h\boldsymbol{a}_c + k\boldsymbol{b}_c + lc_c$, where $\boldsymbol{a}_c$, $\boldsymbol{b}_c$ and c_c are the reciprocal lattice vectors); the structure factor $F(\boldsymbol{H})$ is related to the electron density in the unit cell defined as:

$$F(H) = |F(H)| \exp\big(i\alpha(H)\big) = \int \rho(r) exp[2\pi i H \cdot r] dr \quad [2.52]$$

where $\boldsymbol{r}$ is the vector $\boldsymbol{r} = a_c x + b_c y + c_c z$ in the lattice (a_c, b_c, c_c are the lattice vector defining the periodicity in the crystal structure), the structure factor $|F(\boldsymbol{H})|$ is its amplitude, and $\alpha(\boldsymbol{H})$ is its phase. The X-ray crystal structure may be elucidated with the Patterson synthesis such as was described in section 2.3.2. More on the subject of solving structures from PXRD may be obtained from the references Harris[85] as well as Rissanen and Gavezzotti.[82]

Powder diffractometers use a Bragg-Brentano parafocusing instrument, where radiation from the monochromator deviates from the high-intensity K_α radiation and the X-rays converge into a knife slit and then diverge onto the specimen. Scattered X-rays from the flat sample converge at the receiving slit and are received at a solid detector. It is at the detector (which rotates) that the sample will be subject to the $\theta/2\theta$ scanning mode.

Diverse elements can affect the measurements. Precautions must be taken when preparing the sample and acquiring the diffractogram. For example, the sample must be

flat and crushed into a fine powder to avoid preferred orientation and to observe a statistical distribution of the peak positions and intensities.[87] Temperature may change the structure to a polymorphic form, which would be revealed by new peaks in the diffractogram. It is observed that crystals produce sharp X-ray diffraction peaks whereas amorphous materials such as glass or polymers will produce few diffraction peaks with maxima and diffuse backgrounds. This explains the long experimental times encountered for the halogen bonded compounds (polymeric 1D to 2D networks materials) to obtain useful diffractograms with high-intensity peaks.

2.4 THESIS MOTIVATION

2.4.1 *Nuclei of Interest*

In the present dissertation, new techniques are developed for the application of SSNMR to provide insight into the halogen bonding were developed. XRD and SSNMR have been used to characterize successfully a series of new halogen bonded compounds exhibiting interactions between the *iconic* halogen bond donor,[88] diiodobenzene (*p*-$C_6F_4I_2$, *o*-$C_6F_4I_2$, *p*-$C_6H_4I_2$) and various halogen bond acceptors. The nuclei directly involved in the non-covalent interaction were probed with SSNMR. This will permit the elucidation of the three-dimensional structure of the halogen bonded materials. Benchmark SSNMR data of halogen bonded compounds could be a useful tool for structure determination when crystal structures are unavailable.

Some of the important nuclear properties of the nuclei observed in this dissertation are presented in Table 2.2. Some are referred to as *exotic* nuclei because, as will be

discussed, they have particular nuclear properties, which make them difficult to study using NMR.

Table 2.2 Nuclear properties of the nuclei studied in this work.

nucleus	^{1}H	^{13}C	^{14}N	^{15}N	^{31}P	^{77}Se	^{35}Cl	^{37}Cl	^{79}Br	^{81}Br
I	1/2	1/2	1	1/2	1/2	1/2	3/2	3/2	3/2	3/2
Natural abundance/ %	99.99	1.07	99.63	0.37	100.00	7.63	75.78	24.22	50.69	49.31
γ/ 10^7 rad s^{-1} T^{-1}	26.75	6.73	1.93	-2.71	10.84	5.13	2.62	2.18	6.73	7.25
$\nu_L(B_o = 9.4\ T)$ / MHz	400.22	100.66	28.93	-40.58	162.16	76.68	39.26	32.68	100.62	108.46
Q / mbarn[a]	0	0	20.4	0	0	0	-81.65	-64.35	313	262

[a]The Q values are from Pyykkö.[89]

^{13}C is known to be a low-abundance nucleus (n.a. 1.07%), so in order to observe the complete CS tensor for the carbon of interest, isotope labelling must sometimes be employed since SSNMR enhancement methods are not enough to improve S/N. The same is true for the ^{15}N nucleus which has an even lower natural abundance (n.a. 0.37%), where the observation of the isotropic peak at fast spinning speeds combined with CP enhancement experiment will require long experimental time (overnight). For some SSNMR experiments in this work, the nucleus of interest was enriched with isotope labeling ^{15}N. In other experiments, quadrupolar ^{14}N (I = 1 and Q = 20.4 mbarn) static SSNMR spectra were acquired instead, as its natural abundance is extremely high (n.a. 99.63 %). However, for low gamma quadrupolar nuclei ($\gamma < 1.93 \cdot 10^7$rad s^{-1}T^{-1}), the use of the National ultrahigh-field NMR facility for solids (21.1 T) is necessary to increase sensitivity.

SSNMR of the 100% naturally abundant ^{31}P nuclei, which has a high Larmor frequency (ν_L (B_o = 9.4 T) = 162.16 MHz), provides a large amount of information since the complete CS tensor may be acquired at the moderate field of 9.4 T. It is also possible to observe J-coupling when the interaction is present. The exotic ^{77}Se nucleus (n.a. 7.63 %) is known for large CSA[90] and long T_1 relaxation times[91,92] and ^{77}Se SSNMR[93] provides a

particularly sensitive probe of molecular structure as it exhibits a large chemical shift range of over 3000 ppm.[94,95]

Moreover, presented in this study are the complete $^{35/37}$Cl (I = 3/2) and $^{79/81}$Br (I = 3/2) SSNMR spectra of the halides directly involved in the XB interaction, recorded at two fields (9.4 T and 21.1 T) using either WURST-QCPMG or solid-echo type experiments combined with the VOCS method. These quadrupolar nuclei require ultra-high magnetic fields to increase sensitivity when acquiring their SSNMR spectra. Chlorine, when combined with a large Q moment, provides challenges for acquiring nice spectra: it is a low-gamma nucleus with two isotopes, ^{35}Cl (Q = -81.65 mbarn, n.a. 75.78 %, $\gamma = 2.62 \cdot 10^7$rad s^{-1}T^{-1}) and ^{37}Cl (Q = -64.35 mbarn, n.a. 24.22 %, $\gamma = 2.18 \cdot 10^7$rad s^{-1}T^{-1}). Chlorine-35 usually affords nicer line shapes due to its higher natural abundance. Bromine also has two NMR-active nuclei ^{79}Br (Q = 313 mbarn, n.a. 50.69 %, $\gamma = 6.73 \cdot 10^7$rad s^{-1}T^{-1}) and ^{81}Br (Q = 262 mbarn, n.a. 49.31 %, $\gamma = 7.25 \cdot 10^7$rad s^{-1}T^{-1}), which yield ultra-wideline spectra due to their very large Q moment values. When studying halogen bonded systems with SSNMR, the much-diluted quantity of nuclei probed by unit of volume adds a level of difficulty. The latter Chapters of this work will show how these issues have been mitigated. Halogen SSNMR spectroscopy has proven to be an excellent tool to characterize halogen bonding interactions, as the NMR parameters are very sensitive to a local halogen bonding environment.

2.4.2 *Motivation*

Since NMR has proven to be a useful characterization method of other non-covalent interaction, such as into hydrogen bonding,[96,97,98, 99] cation-π interactions,[100, 101] and CH/π

interactions, [102] for example, it has sparked the interest to apply this to halogen bonds. As will be unraveled in the following Chapters, SSNMR has proven to provide fundamental insight into the XB phenomenon.

A previous study in our group considered halides involved in weak halogen bonding directly using chlorine, bromine, and iodine SSNMR in a series of haloanilium halides.[103] The ^{81}Br QI, isotropic CS, and CS span all proved to vary slightly as a function of the strength of the halogen bonding interaction. One difficulty encountered in that study was the simultaneous presence of halogen bonds and hydrogen bonds to halide ions, thereby complicating the interpretation of results solely in terms of the halogen bonding environment. The XB compounds presented in this thesis are devoid of hydrogen bonds and are considered to possess moderately strong halogen bonds when their R_{XB} values are considered (ranging between 0.79 and 0.93).

Single X-ray crystallography is an effective characterization tool that succeeds in elucidating the three-dimensional structure of many solids, but sometimes other methods are necessary. For example, XRD is not a suitable method for determining the positions of hydrogens in a lattice, since it requires a single crystal to characterize the structure; if disorder is present, or an amorphous system, or a powder state, it cannot be characterized by this method. Therefore, in this study the initial motivation was to use SSNMR to characterize the halogen bonding interaction so that when a single crystal is not possible, SSNMR is a potential solution.

As was demonstrated in the previous theoretical sections of this Chapter, NMR interactions are influenced by the distribution of electrons about the nucleus. The NMR parameters are sensitive to chemical differences at the nucleus of interest. A main task was

to measure accurately all of the NMR interactions (CS tensor, *J*-coupling, R_{DD}, EFG tensor) for the nuclei involved in halogen bonding.

SSNMR methods were chosen over solution as they provide unique insights into halogen bonds and provide several advantages:

- Competing halogen bonding interactions between the solvent and the halogen bond donor are absent
- Powdered samples are used (no need for a crystalline sample or single crystal)
- Complete NMR tensors may be measured instead of only their isotropic values
- Quadrupolar NMR is possible in the solid state, where $I > 1/2$ represent three-quarters of the NMR-active nuclei in the periodic table[104]

The NMR interactions studied were then correlated with the specific structural feature of the halogen bonding environment (bond length, XB angles, etc.). For this reason, X-ray crystallography is a complementary tool for this work: it provides the benchmark data of the structural properties of the new XB compounds studied here. Furthermore, computational chemistry will permit the experimental results to be corroborated by theoretical results and will permit the visualization of the EFG and CS tensor components with respect to the molecular frame. Equally important, computational chemistry will provide a means of understanding the correlation between the NMR observables and the halogen bonding interaction by using an MO interpretation.

In this dissertation, a combination of experimental and theoretical approaches have been carefully applied to arrive at a successful correlation between various fundamental

NMR interactions in the halogen bonding environment, and they will be demonstrated thoroughly in the following Chapters.

2.5 REFERENCES FOR CHAPTER 2

[1] W. Pauli, (1925), *Z. Phys.*, 31, 373.

2 W. Gerlach, O. Stern, (1922), *Z. Phys.*, 9, 349.

3 P. A. M. Dirac, (1928), *Proc. R. Soc. London, Ser. A*, 117, 610.

4 P. A. M. Dirac, (1928), *Proc. R. Soc. London, Ser. A.*, 118, 351.

5 M. H. Levitt, M. H. Levitt, (2001), *Magnetism, Spin Dynamics Basics of Nuclear Magnetic Resonance* (pp.23-42), Southampton, UK, John Wiley and Sons, Ltd.

6 P. Zeeman, (1897), *Nature*, 55, 347.

7 P. Atkins, J. de Paula, (2006), *Physical Chemistry 8 edition*, New York, NY, Oxford University Press.

8 Z. Yao, H.-T. Kwak, D. Sakellariou, L. Emsley, P. J. Grandinetti, (2000), *Chem. Phys. Lett.*, 327, 85.

9 J. Keeler, (2005), *The Vector Model, Understanding NMR Spectroscopy* (pp.51-77), Chichester, UK, John Wiley and Sons, Ltd.

10 F. A. L. Anet, D. J. O'Leary, (1991), *Concepts Magn. Reson.*, 3, 193.

11 J. B. Robert, L. Wiesenfeld, (1982), *Physics Report*, 86, 363.

12 J. Herzfeld, A. E. Berger, (1980), *J. Chem. Phys.*, 73, 6021.

13 J. Mason, (1993), Solid State Nucl. Magn. Reson., 2, 285.

14 R. K. Harris, (1998), *Solid State Nucl. Magn. Reson.*, 10, 177.

15 C. J. Jameson, (1998), *Solid State Nucl. Magn. Reson.*, 11, 265.

16 G. B. Arfken, (1985), *Mathematical Methods for Physicists*, New York, NY, Academic Press.

17 P. Grondana, A. C. Olivieri, (1993), *Concepts in Magn. Reson.*, 5, 319.

18 M. J. Duer, I. Farnan, (2002), *Quadrupolar Coupling: It's Measurements and Uses, Solid-State NMR Spectroscopy Principles and Applications* (pp. 179-215), M. J. Duer (Ed.), Cambridge, UK, Blackwell Science Ltd.

19 K. Eichele, R. E. Wasylishen, (2009), *WSolids1: Solid-State NMR Spectrum Simulation Package, v.1.19.11*, Tübingen, Germany, Universität Tübingen.

20 R. W. Schurko, S. Wi, L. Frydman, (2002), *J. Phys. Chem. A*, 106, 51.

21 C. M. Widdifield, A. D. Bain, D. L. Bryce, (2011), *Phys. Chem. Chem. Phys.*, 13, 12413.

22 F. A. Perras, C. M. Widdifield, D. L. Bryce, (2012), *Solid State Nucl. Magn. Reson.*, 45-46, 36.

23 M. H. Levitt, (2008), *Spin Dynamics. Basics of Nuclear Magnetic Resonance*, Southampton, UK, John Wiley & Sons.

24 C. P. Slichter, (1978), *Principles of Magnetic Resonance 2nd Edition*, P. Fulde (Ed.), New York, NY, Springer-Verlag.

25 K. Eichele, R. E. Wasylishen, (1992), *Solid State Nucl. Magn. Reson.*, 1, 159.

26 M. J. Duer, (2002), *Dipolar Coupling: It's Measurements and Uses, Solid-State NMR Spectroscopy Principles and Applications* (pp. 111-178), M. J. Duer (Ed.), Cambridge, UK, Blackwell Science Ltd.

27 F. A. Perras, D. L. Bryce, (2014), *J. Phys. Chem. Lett.*, 5, 4049.

28 J. Keeler, (2005), *Setting the Scene, Understanding NMR spectroscopy* (pp.5-24), Chichester, UK, John Wiley and Sons, Ltd.

29 P. A. Keifer, (1998), *Concepts in Magn. Reson.*, 11, 165.

30 M. H. Levitt, (2001), *Fourier Transform NMR, Spin Dynamics Basics of Nuclear Magnetic Resonance* (pp.81-108), Southampton, UK, John Wiley and Sons, Ltd.

31 J. Keeler, (2005), *Fourier Transformation and Data Processing, Understanding NMR Spectroscopy* (pp.5-24), Chichester, UK, John Wiley and Sons, Ltd.

32 M. J. Duer, (2002), *Essential Techniques for Spin-1/2 Nuclei*, *Solid-State NMR Spectroscopy Principles and Applications* (pp. 73-110), M. J. Duer (Ed.), Cambridge, UK, Blackwell Science Ltd.

33 E. R. Andrew, A. Bradbury, R. G. Eades, (1958), *Nature*, 182, 1659.

[34] I. J. Lowe, Phys. (1959), *Rev. Lett.*, 2, 285.

35 S. P. Brown, L. Emsley, (2014), *Solid-State NMR In Handbook of Spectroscopy 2nd edition*, G. Gauglitz, T. Vo-Dinh (Eds.), Weinheim, Germany, Wiley.

36 A. Samoson, E. Kunkla, E. Lippmaa, (1982), *J. Magn. Reson.*, 49, 350.

37 F. Bloch, (1958), *Phys. Rev.*, 111, 841.

38 A. E. Bennett, C. M. Rienstra, M. Auger, K. V. Lakshmi, R. G. Griffin, (1995), *J. Chem. Phys.*, 103, 6951.

39 B. M. Fung, A. K. Khitrin, K. Ermolaev, (2000), *J. Magn. Reson.*, 142, 97.

40 A. Pines, M. G. Gibby, J. S. Waugh, (1972), *J. Chem. Phys.*, 56, 1776.

41 E. O. Stejskal, J. Schaefer, J. S. Waugh, (1977), *J. Magn. Reson.*, 28, 105.

42 F. A. Perras, J. Viger-Gravel, K. M. N. Burgess, D. L. Bryce, (2013), *Solid State Nucl. Magn. Reson.*, 51-52, 1.

43 S. E. Ashbrook, M. J. Duer, (2006), *Concepts Magn. Reson. Part A*, 28, 183.

44 A. J. Vega, (1992), *Solid State Nucl. Magn. Reson.*, 1, 17.

45 C. Fernandez, M. Pruski, (2012), *Topics Curr. Chem.*, 306, 119.

46 M. J. Duer, (2002), *NMR Techniques for Studying Molecular Motions in Solids*, *Solid-State NMR Spectroscopy Principles and Applications* (pp. 240-279), M. J. Duer (Ed.), Cambridge, UK, Blackwell Science Ltd.

47 E. L. Hahn, (1950), *Phys. Rev.*, 80, 580.

48 I. Solomon, (1958), *Phys. Rev.*, 110, 61.

49 I. D. Weisman, L. H. Bennett, (1969), *Phys. Rev.*, 181, 1341.

50 P. R. Bodart, J.-P. Amoureux, Y. Dumazy, R. Lefort, (2000), *Mol. Phys.*, 98, 1545.

51 D. Massiot, I. Farnan, N. Gauthier, D. Trumeau, A. Trokiner, J. P. Coutures, (1995), *Solid State Nucl. Magn. Reson.*, 4, 241.

52 R. Bhattacharyya, L. Frydman, (2007), *J. Chem. Phys.*, 127, 1945031.

53 Ē. Kupče, R. Freeman, (1996), *J. Magn. Reson., Ser. A*, 118, 299.

54 L. A. O'Dell, (2013), *Solid State Nucl. Magn. Reson.*, 55-56, 28.

55 L. A. O'Dell, R. W. Schurko, (2008), *Chem. Phys. Lett.*, 464, 97.

56 J. T. Cheng, P. D. Ellis, (1989), *J. Phys. Chem.*, 93, 2549.

57 S. Adiga, D. Aebi, D. L. Bryce, (2007), *Can. J. Chem.*, 85, 496.

58 G. E. Scuseria, V. N. Staroverov, (2005), *Progress in the Development of Exchange-*Correlation Functionals, *Theory and Applications of Computational Chemistry*: *The First Forty Years 1st Edition* (pp. 663-724), Amsterdam, Kingdom of the Netherlands, Elsevier Science.

59 M. J. Frisch, G. W Trucks, H. B. Schlegel, G. E. Scuseria, M. A. Robb, J. R. Cheeseman, G Scalmani, V. Barone, B. Mennucci, G. A. Petersson, H. Nakatsuji, M. Caricato, X. Li, H. P. Hratchian, A. F. Izmaylov, J. Bloino, G. Zheng, J. L. Sonnenberg, M. Hada, M Ehara, K. Toyota, R. Fukuda, J. Hasegawa, M. Ishida, T. Nakajima, Y. Honda, O. Kitao, H. Nakai, T. Vreven, J. A. Jr. Montgomery, J. E. Peralta, F. Ogliaro, M. Bearpark, J. Heyd, E. Brothers, K. N. Kudin, V. N. Staroverov, R. Kobayashi, J. Normand, K. Raghavachari, A. Rendell, J. C. Burant, S. S. Iyengar, J. Tomasi, M. Cossi, N. Rega, N. J. Millam, M. Klene, J. E. Knox, J. B. Cross, V. Bakken, C, Adamo, J. Jaramillo, R. Gomperts, R. E. Stratmann, O. Yazyev, A. J. Austin, R. Cammi, C. Pomelli, J. W. Ochterski, R. L. Martin, K. Morokuma, V. G. Zakrzewski, G. A. Voth, P. Salvador, J. J. Dannenberg, S. Dapprich, A. D. Daniels, Farkas, J. B. Foresman, J. V. Ortiz, J. Cioslowski, D. J. Fox, *Gaussian 09 Revision A.02*, (2009), Gaussian, Inc., Wallingford, CT.

60 A. D. Becke, (1993), *J. Chem. Phys.*, 98, 5648.

61 J. M. Tao, J. P. Perdew, V. N. Staroverov, G. E. Scuseria, (2003), *Phys. Rev. Lett.*, 91, 146401.

62 E. J. Baerends, J. Autschbach, A. Bérces, F. M. Bickelhaupt, P. M. Boerrigter *et al.* (2010) *Amsterdam Density Functional Software ADF2009.01 SCM*; Amsterdam, The Netherlands, Theoretical Chemistry, Vrije Universiteit: http://www.scm.com/.

63 E. van Lenthe, E. J. Baerends, J. G. Snijders, (1993), *J. Chem. Phys.*, 99, 4597.

64 E. van Lenthe, E. J. Baerends, J. G. Snijders, (1994), *J. Chem. Phys.*, 101, 9783.

65 E. van Lenthe, E. J. Baerends, J. G. Snijders, (1999), *J. Chem. Phys.*, 110, 9943.

66 J. Autschach, Z. Zheng, R. W. Schurko, (2010), *Concepts Magn. Reson., Ser. A*, 36, 84.

67 J. Autschbach, T. Ziegler, (2004), *Relativistic Calculations of Spin-Spin Coupling Constants of Heavy Nuclei, Calculation of NMR and EPR Parameters: Theory and Applications* (pp.249-264), M. Kaupp, M. Bühl, V. G. Malkin (eds.), Weinheim, Germany, Wiley-VCH.

68 J. Autschbach, (2012), *J. Chem. Phys.*, 136, 150902.

69 Y. Nomura, Y. Takeuchi, N. Nakagawa, (1969), *Tetrahedron Lett.*, 639.

70 E. D. Glendening, J. K. Badenhoop, A. E. Reed, J. E. Carpenter, J. A. Bohmann, C. M. Morales, F. Weinhold, (2001), *NBO 5.0*, Madison, WI, Theoretical Chemistry Institute, University of Wisconsin; http://www.chem.wisc.edu/~nbo5.

71 J. P. Perdew, K. Burke, M. Ernzerhof, (1996), *Phys. Rev. Lett.*, 77, 3865.

72 J. P. Perdew, K. Burke, M. Ernzerhof, (1997), *Phys. Rev. Lett.*, 78, 1396.

73 C. J. Pickard, F. Mauri, (2001), *Phys. Rev. B*, 63, 245101.

74 S. J. Clark, M. D. Segall, C. J. Pickard, P. J. Hasnip, M. I. J. Probert, K. Refson, M. C. Payne, (2005), *Z. Kristallogr.*, 220, 567.

75 J. R. Yates, C. J. Pickard, F. Mauri, (2007), *Phys. Rev. B*, 76, 024401.

76 C. J. Pickard, F. Mauri, (2004), *Calculations of Magnetic Resonance Parameters in Solids and Liquids Using Periodic Boundary Conditions, Calculation of NMR and EPR Parameters : Theory and Applications* (pp.265-278), M. Kaupp, M. Bühl, V. G. Malkin (eds.), Weinheim, Germany, Wiley-VCH.

77 W. H. Bragg, W. L. Bragg, (1915), *X rays and Crystal Structure*, London, UK, G. Bell and Sons, Ltd.

78 F. H. Allen, (2002), *Acta Crystallogr., Sect. B: Struct. Sci.*, 58, 380.

79 M. F. C. Ladd, R. A. Palmer, (2013*), Structure Determination by X-ray Crystallography: Analysis by X-rays and Neutrons*, Ney York, NY, Springer Science.

80 Y. Waseda, E. Matsubara, K. Shirada, (2011), *Geometry of Crystals, X-ray diffraction crystallography: Introduction, Examples and Solved Problems* (pp.21-66), New York, NY, Springer Berlin Heidelberg.

81 Y. Waseda, E. Matsubara, K. Shirada, (2011), *Diffraction from Polycrystalline Samples and Determination of Crystal Structures, X-ray diffraction crystallography: Introduction, Examples and Solved Problems* (pp.107-167), New York, NY, Springer Berlin Heidelberg.

82 K. Rissanen, A. Gavezzotti, (2012), *Chapter 2 Lattices and Space-Group Theory, Theory Advanced X-ray Crystallography* (pp.51-110), New York, NY, Springer-Verlag Berlin Heidelberg.

83 T. Hahn, (1996), *International tables for crystallography, vol A, 4th edn.*, Dordrecht. Kluwer Academic.

84 N. F. M. Henry, K. Lonsdale K (eds) (1965), *International tables for X-ray crystallography, volume I*, Birmingham, UK, Kynoch Press.

85 K. D. M. Harris, (2012), *Topp. Curr. Chem.*, 315, 133.

86 http://www.icdd.com/education/xrd.htm.

87 W. Parrish, T. C. Huang, (1983), *Adv. X-ray Anal.*, 26, 35.

88 R. W. Troff, T. Mäkelä, F. Topić, A. Valkonen, K. Raatikainen, K. Rissanen, (2013), *Eur. J. Org. Chem.*, 1617.

89 P. Pyykkö, (2008), *Mol. Phys.*, 106, 1965.

90 M. J. Collins, C. I. Ratcliffe, J. A. Ripmeester, (1986), *J. Magn. Reson.*, 68, 172.

91 W. H. Dawson, J. D. Odom, (1977), *J. Am. Chem. Soc.*, 99, 8352.

92 J. D. Odom, W. H. Dawson, P. D. Ellis, (1978), *J. Am. Chem. Soc.*, 101, 5815.

93 B. A. Demko, R. E. Wasylishen, (2009), *Prog. Nucl. Magn. Reson. Spectrosc.*, 54, 208.

94 H. Duddeck, (1995), Prog. Nucl. Magn. Reson. Spectrosc., 27, 1.

95 H. Duddeck, (2004), *Annu. Rep. NMR Spectrosc.*, 52, 105.

96 I. Alkorta, J. Elguero, G. S. Denisov, (2008), *Magn Reson Chem*, 46, 599.

97 A. E. Aliev, (2004), *Probing Hydrogen Bonding in Solids Using Solid State NMR Spectroscopy*, *Struct. Bond*, 108, 1.

98 E. Brunner, U. Sternberg, (1998), *Prog. Nucl. Magn. Reson. Spectrosc.*, 32. 21.

99 G. Wu, C. J. Freure, E. Verdurand, (1998), *J. Am. Chem. Soc.*, 120, 13187.

100 D. L. Bryce, S. Adiga, E. K. Elliott, G. W. Gokel, (2006), *J. Phys. Chem. A*, 110, 13568.

101 P. K. Lee, R. P. Chapman, L. Zhang, J. Hu, L. J. Barbour, E. K. Elliott, G. W. Gokel, D. L. Bryce, (2007), *J. Phys. Chem. A*, 111, 12859.

102 M. J. Plevin, D. L. Bryce, J. Boisbouvier, (2010), *Nat. Chem.*, 2, 466.

103 R. J. Attrell, C. M. Widdifield, I. Korobkov, D. L. Bryce, (2012), *Cryst. Growth Des.*, 12, 1641.

104 R. E. Wasylishen, S. E. Ashbrook, S. Wimperis, (2012) *NMR of Quadrupolar Nuclei in Solid Materials*, Chichester, UK, John Wiley and Sons.

3 SSNMR STUDY OF HALOGEN BOND DONORS IN C-I···X⁻ MOTIFS

3.1 INTRODUCTION

As mentioned in Chapter 2, NMR has proven to be an excellent tool for the characterization of hydrogen bonding in solution and solids.[1] Following suit, ^{1}H NMR has also been used for the study of halogen bond formation. This was observed by a CS change for the methylene protons of CH_2Cl_2, CH_2Br_2, and CH_2I_2 and the haloformic protons ($CHCl_3$, $CHBr_3$, and CHI_3) in the presence of various amines, ethers, and non-polar electron-rich solvents.[2, 3] Resnati and co-workers also used multinuclear solution NMR to demonstrate the presence of XB between quinuclidine and 1-iodoperfluoropropane.[4] The ^{1}H and ^{13}C NMR spectra showed changes in the CS of the interacting compounds relative to the isolated components. Additional evidence of a C—I···N electrostatic interaction originated from ^{19}F (I = 1/2, n.a. 100 %) and ^{14}N NMR spectra, where chemical shifts changed by several ppm upon complexation. Metrangolo and co-workers used ^{19}F NMR to quantify the halogen bonding interaction in various halo-perfluorocarbons and heteroatom-containing hydrocarbons by correlating the solvent's electron donor ability to chemical shifts.[5] The Taylor group has also used ^{19}F NMR in titration experiments to determine the strength of the halogen bonding interaction in solution.[6]

Our group is interested in the study of the XB via SSNMR, where solvent effects are absent, and complete NMR interaction tensors may afford additional insight into the XB phenomenon. In the present work, the compounds have been designed such that only halogen bonding is present between halides and covalently-bonded iodine, and any possible competing effects of hydrogen bonding are absent. This will facilitate the elucidation of a relationship between halogen bonding environment and NMR parameters.

The proposed IUPAC definition of halogen bonding states that changes in magnetic resonance parameters may accompany the formation of a halogen bond.[7] Understanding what drives the change in the chemical shift when XB occurs motivates this work. In solution, ^{13}C NMR has been used to probe XB, and there have been strong correlations between the electron-donor ability of the solvent and the chemical shift.[8,9,10] In the solid state, it is more difficult to observe the resonance of the covalently-bonded carbon involved in halogen bonding interactions due to the strong residual dipolar interactions with the halogen nucleus[11, 12] and long relaxation times. Our present approach involves a combination of XRD, multi-field SSNMR, and computational analysis. In this study, the single-crystal X-ray structures and ^{13}C SSNMR spectra of five halogen bonded compounds constructed from *p*-DITFB and ammonium or phosphonium halide (X^- = Cl, Br) salts of the form RNX and RPX, where R = *n*-Bu_4 or $EtPh_3$ are reported. The compounds depicted in Figure 3.1 have the following formulas: [(*n*-Bu_4NCl)(*p*-DITFB)] (**1**), [(*n*-Bu_4PCl)(*p*-DITFB)] (**2**), [(*n*-Bu_4NBr)(*p*-DITFB)] (**3**), [(*n*-Bu_4PBr)(*p*-DITFB)] (**4**), [($EtPh_3PBr)_2$(*p*-DITFB)] (**5**). Compounds **1** and **3** were previously reported by Abate *et al*.; however, the structure solved by our group for **3** is slightly different (*vide infra*).[13] The crystallographic structure of each compound will be discussed with an emphasis on the subtle differences in the various halogen bonding networks. There will also be a comparison between the ^{13}C CPMAS SSNMR spectra of the XB compounds to its starting material, *p*-DITFB. Properly describing the NMR parameters in these compounds involves many challenges which will be discussed (*vide infra*); the ZORA-DFT approach is employed which allows for the treatment of scalar and spin-orbit relativistic effects.

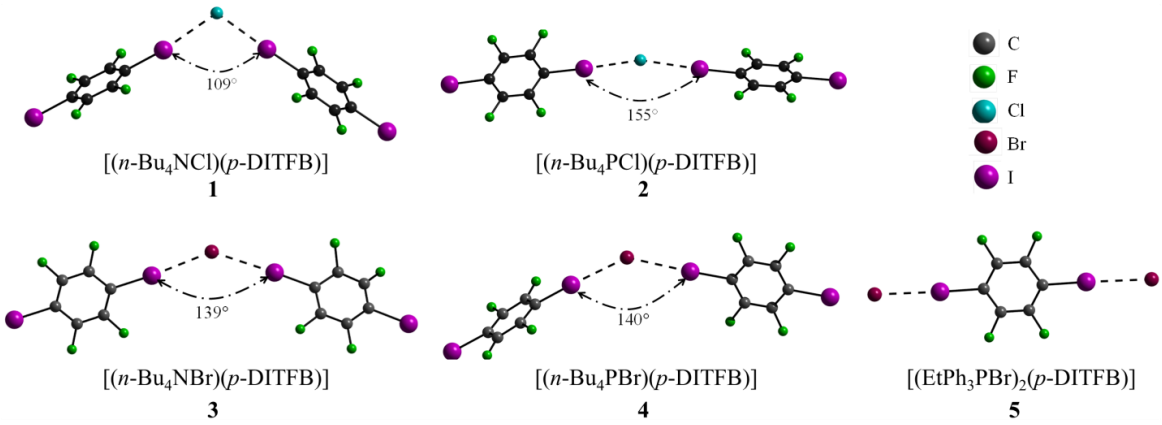

Figure 3.1 Halogen bonding contacts in compounds **1** to **5** with the corresponding formula and compound number. In compounds **1** to **4**, the halide interacts with two crystallographically distinct iodines, whereas in compound **5** the bromide interacts with one. Cations are omitted for clarity.

3.2 EXPERIMENTAL SECTION

3.2.1 *Sample Preparation*

All ammonium and phosphonium salts of the form RNX and RPX, where R = *n*-Bu_4 or $EtPh_3$ and X = Cl or Br, were purchased from Aldrich and used without further purification. Compounds **1** and **4** were prepared according to previously reported literature[13] but using a different solvent, dichloromethane. Compounds **2**, **3**, and **5**, were all prepared by dissolving equimolar amounts of R_4NX or R_4PX with *p*-DITFB, in a minimum amount of dichloromethane. Vials containing the solutions were then placed into a closed jar containing mineral oil and left to evaporate until the desired compound crystallized.

3.2.2 *X-ray Crystallography*

Data collection results for compounds **1**, **2**, **3**, **4**, and **5** represent the best data sets obtained in several trials for each sample. The crystals were mounted on thin glass fibers using paraffin oil. Mounted crystals were cooled by a stream of dry air to 200.15 °K prior

to data collection. Data were collected on a Bruker AXS KAPPA single crystal diffractometer equipped with a sealed Mo tube source (wavelength 0.71073 Å) and APEX II CCD detector. Raw data collection and processing were performed with the APEX II software package from BRUKER AXS.[14] Diffraction data for **1**, **2**, **4**, and **5** were collected with a sequence of 0.5° ω scans at 0, 120, and 240° in φ. Diffraction data for **3** were collected with a sequence of 0.5° ω scans at 0, 90, 180 and 270° in φ due to the lower quality of the crystal and weaker diffraction intensity to provide adequate data coverage. Initial unit cell parameters were determined from 60 data frames collected for different sections of the Ewald sphere. Semi-empirical absorption corrections based on equivalent reflections were applied.[15] Systematic absences in the diffraction data set and unit cell parameters were consistent with the monoclinic *C*2/*c* (№15) space group for compound **4**, monoclinic $P2_1/n$ (№14) for compound **5**, monoclinic $P2_1/c$ (№14) for compounds **1** and **2**, and orthorhombic *Pccn* (№56) for compound **3**. Solutions in the centrosymmetric space groups for all compounds yielded chemically reasonable and computationally stable results of refinement. The structures were solved by direct methods, completed with difference Fourier synthesis, and refined with full-matrix least-squares procedures based on F^2. These are further explained in the structure refinement section.

All hydrogen atoms were treated as idealized contributions. All scattering factors are contained in several versions of the SHELXTL program library, with the latest version used being v.6.12.[16] Crystallographic data and selected data collection parameters are reported in Table 3.1.

Table 3.1 Crystallographic Data and Selected Data Collection Parameters

compound	**2**	**3**	**4**	**5**
empirical formula	$C_{22}H_{36}ClF_4I_2P$	$C_{22}H_{36}BrF_4I_2N$	$C_{44}H_{72}Br_2F_8I_4P_2$	$C_{23}H_{20}BrF_2IP$
formula weight / g/mol	696.730	724.23	1482.38	572.17
crystal size/ mm	0.17 x 0.15 x 0.14	0.18 x 0.13 x 0.11	0.17 x 0.12 x 0.11	0.31 x 0.19 x 0.19
crystal system	monoclinic	orthorhombic	monoclinic	monoclinic
space group	$P2_1/c$	$Pccn$	$C2/c$	$P2_1/n$
Z	4	8	4	4
a/ Å	14.4599(2)	48.3095(10)	49.7447(10)	10.8351(3)
b/Å	14.9417(2)	8.7022(2)	8.4785(2)	11.9074(3)
c/ Å	15.0638(2)	13.6477(3)	14.1541(3)	17.0179(4)
α/ °	90	90.00	90.00	90
β/ °	117.6830	90.00	104.1190(10)	92.3430(10)
γ/ °	90	90.00	90.00	90
Volume / $Å^3$	2882.06(7)	5737.5(2)	5789.3(2)	2175.35(10)
calculated density/ mg/m^3	1.606	1.677	1.701	1.747
absorption coefficient/ mm^{-1}	2.364	3.620	3.641	3.405
F(000)	1368	2816	2880	1116
Θ range for data collection/ °	2.05 to 28.31	1.69 to 28.26	1.69 to 28.33	2.10 to 28.33
limiting indices	-19 <= h <= 19, -19 <= k <= 19, -20 <= l <= 19	-64 <= h <= 53, -11 <= k <= 11, -18 <= l <= 18	-66 <= h <= 64, 0 <= k <= 11, 0 <= l <= 18	-14 <= h <= 14, -14 <= k <= 15, -22 <= l <= 19
reflections collected/unique	62401 / 7118	58424 / 7074	15069 / 7049	23686 / 5372
R (int)	0.0186	0.0297	0.0000	0.0233
completeness to Θ = 28.32/ %	99.1	99.2	97.6	98.9
max and min transmission	0.7331 and 0.6894	0.6916 and 0.5619	0.6902 and 0.5765	0.5639 and 0.4183
data/restraints/parameters	7118 / 75 / 298	7074 / 244 / 319	7049 / 221 / 347	5372 / 0 / 254
goodness-of-fit on F^2	1.027	1.122	1.002	1.045
final R indices [I > 2α(I)]	R1 = 0.209, wR2 = 0.0492	R1 = 0.0668 wR2 = 0.1844	R1 = 0.0429 wR2 =0.1057	R1 = 0.0167 wR2 =0.0452
R indices (all data)	R1 = 0.269, wR2 = 0.0537	R1 = 0.0742 wR2 = 0.1888	R1 =0.0570 wR2 = 0.1136	R1 = 0.0190 wR2 =0.0464
largest diff peak/hole/ $e \cdot Å^{-3}$	0.671 and -0.714	1.001 and -1.481	1.007 and -1.448	0.346 and -0.650

Additional information on X-ray structure refinement

Structures of **1**, **3**, **4**, and **5** contain molecules of *p*-DITFB located on the inversion center. During the refinement of the structure for compound **2**, unusually large thermal motion parameters for several atoms in the *n*-Bu chains of the phosphonium cation suggested positional disorder. Disorder was modeled for the last two carbon atoms in the aliphatic chains and occupancy factors for both disorder models were refined to a 50/50

ratio for both disordered fragments. Similar disorder was discovered for the aliphatic chains of the cations in the structures of **3** and **4**. Similar models of the disorder for two tail carbon atoms of two *n*-Bu residues were refined with occupancy factors of 50/50 and 45/55 for compound **3**. The structure of compound **4** was refined with occupancy factors of 67/33 and 50/50 for disorder models similar to those described for **2** and **3**. The structures **3** and **4** contain disordered molecules of *p*-DITFB located on the inversion center. In both cases, disorder was modeled as a rotation of the aryl ring around the I - I axis. In the case of **4**, the rotational angle was found to be 48.67(3.02)◦ whereas for **3** this angle was found to be 25.20(2.66)◦, describing two disordered positions of the aryl rings. In order to improve the refinement results, obtain acceptable thermal motion parameters, and retain desirable molecular geometry, several sets of restraints were applied during the refinement of both structures. During the data collection for **4** it was discovered that crystal contained two non-merohedrally twinned domains. Twinning issues were resolved by integrating the data with two independent orientation matrices and performing the refinement using the HKLF 5 reflection intensities file. Refinement of the domain contributions yielded a twinning ratio of 48.3%.

3.2.3 *^{13}C Solid-State NMR Spectroscopy*

All compounds were ground into fine powders and packed in 4 mm outer diameter (o.d.) zirconia rotors. Data were acquired at the University of Ottawa using a 9.4 T ($\nu_L(^{13}C)$ = 100.6 MHz) wide-bore magnet equipped with a Bruker Avance III 400 console and a 4 mm Bruker triple resonance MAS probe. Data were also acquired at the National Ultrahigh-Field NMR Facility for Solids in Ottawa using a 21.1 T ($\nu_L(^{13}C)$ = 226.3 MHz) standard-

bore magnet equipped with a Bruker AVANCE II 900 console and a double-resonance MAS probe.

9.4 T Data. ^{13}C SSNMR spectra were collected using CPMAS. Experimental setup and pulse calibration were performed using the recommended IUPAC standard for ^{13}C (I = 1/2), solid glycine (δ(^{13}C=O) = 176.4 ppm with respect to TMS).[17] For compounds **1**, **2**, **5** and **3**, **4** the recycle delays and contact times were optimized to 13 s and 5 s, and 3 ms and 5 ms, respectively. The proton π/2 pulse was set to 3.50 μs in all cases, and the MAS frequencies were 8 kHz with the exception of **5** where 7.5 kHz was used. The number of scans varied for each compound, from a few hundred to 4k, and the experiments were run until a reasonable signal-to-noise ratio was obtained. Total experimental times ranged from 64 min to 15 h. In the case of *p*-DITFB, a rotor-synchronized Hahn-echo (*i.e.* π/2-τ_1-π-τ_2-acq)[18] MAS experiment was used. Pulse calibration was performed on the secondary reference adamantane (δ(^{13}C) = 38.55 and 29.50 ppm relative to TMS). The spinning speed was set to 8 kHz, while the recycle delay and π/2 pulse length were 20 s and 2.75 μs, respectively. TPPM ^{1}H decoupling was used for all experiments.[19] Line broadening was also used in the processing of the data and varied from 25 to 100 Hz.

21.1 T Data. The same method was used at this field for the acquisition of the ^{13}C SSNMR spectra as was done at 9.4 T. The MAS frequency was set to 18 kHz. The following parameters were used for the CPMAS experiments: recycle delay of 10 s, contact time of 3 ms and π/2 pulse length of 2.50 μs. The number of scans varied for each compound, ranging from 256 to 1024. As for the Hahn-echo MAS experiment (*p*-DITFB), a total of 4k scans were collected using a recycle delay equal to 10 s and a π/2 pulse length of 5 μs.

All NMR data were processed with Bruker TopSpin 3.0 software. The FIDs acquired using a Hahn-echo experiment for *p*-DITFB were left shifted an appropriate number of data points to the top of the echo. The number of distinct $\delta_{iso}(^{13}C)$ values for carbon atoms directly bonded to iodine atoms was determined independently from the X-ray crystal structures (one value for each magnetically distinct carbon site). Simulations of the MAS NMR spectra were carried out using WSolids1[20] through manual iteration using the appropriate number of $\delta_{iso}(^{13}C)$ values, and apodization. The precision in the reported $\delta_{iso}(^{13}C)$ values was assessed through simultaneous iterative fitting of the ^{13}C MAS NMR spectra obtained at both 21.1 and 9.4 T. Stack plots of the experimental and simulated spectra were prepared using DMFIT (v.2011).[21]

3.2.4 *Computational Details*

Cluster models centered on the halide ion involved in halogen bonding were generated using the X-ray crystal structures' atomic coordinates (models used are depicted in Figure 3.1). The structure of Chaplot *et al*. was used for *p*-DITFB.[22] The ^{13}C magnetic shielding tensors were calculated with the ADF software (version 2009.01).[23] Two sets of calculations were carried out: one set including scalar and spin-orbit relativistic effects using the ZORA, and the other set omitting relativistic effects. The PBE or revPBE, were the GGA exchange-correlation functional used in combination with the ZORA/TZP basis set. Some calculations were done with additional diffuse functions on the halide ions. For compounds **3** and **4**, disorder in the aromatic rings was eliminated by using an average structure of optimized C and F coordinates. The calculations were performed using the High-Performance Virtual Computing Laboratory (HPCVL). Magnetic shielding tensors

were converted to chemical shift tensors using the following equation: $\delta_{ij} = \frac{\sigma_{ref} - \sigma_{ij}}{1 - \sigma_{ref}}$ (where σ_{ref} = 184.1 ppm for carbon[24], δ_{ij} is the chemical shift tensor component, and σ_{ij} is the magnetic shielding tensor component).

3.3 Results And Discussion

3.3.5 *X-ray Crystal Structures*

Single-crystal X-ray crystallography was used to characterize the novel halogen bonded compounds **2**, **3**, **4**, and **5**. Relevant crystallographic data are presented in Table 3.1. Halogen bonding interactions are considered to be present when the distance between the halogen (*i.e.*, iodine) and the halide (*i.e.*, X^- = Cl^-, Br^-), $d_{I\cdots X}$, is shorter than the sum of their Van der Waals (VdW) radii (1.75, 1.85, 1.98 Å for Cl, Br, I,[25] and 1.81, 1.96, 2.20 Å for Cl^-, Br^-, and I^-, respectively[26]). The ratio of the short intermolecular contact distance and the sum of the VdW radii (d_{VdW}) is presented as the normalized distance parameter, $R_{XB} = d_{I\cdots X}/\Sigma d_{VdW}$, and is useful to describe the short contacts (*i.e.*, R_{XB} = 1 is a weak to non-existent XB).[27] Furthermore, the carbon-iodine bond length, $d_{C\cdots I}$, will change for each halogen bonded compound largely as a consequence of the non-covalent interaction. As described in the proposed IUPAC definition of XB, the length of the R—X covalent bond usually increases upon XB formation.[7] A further point is that the XB interaction has been observed to be almost linear in the case of a nucleophile interacting with an RX molecule. The halide will often align itself at an angle, $\theta_{C\cdots I\cdots X^-}$, that varies between 160 and 180°. These intermolecular contact distances and angles are reported in Table 3.2 for the compounds of interest as well as other geometrical information pertaining to their halogen bonding environments. Compounds **1** and **3** have been reported previously and discussed

thoroughly in the context of halogen bonding by Abate *et al.*[13] Similar compounds have previously been discussed in terms of halogen bonding by Triguero *et al.*, where 1,3,5-trifluoro-2,4,6-triiodobenzene is co-crystallized with *n*-Bu_4NX or *n*-Bu_4PX (X = Cl^-, Br^-).[28] Grebe *et al.* report donor-acceptor compounds involving Ph_4PX or Me_4NX (X = Cl^-, Br^-) and *p*-DITFB.[29] Hence, in this section our new crystal structures are briefly described and analyzed in terms of how they compare with previously reported crystallographic data. The halogen bonding motifs observed here are reminiscent of some of those reported for artificial anion receptors and related complexes.[30]

Table 3.2 Selected Intermolecular Contact Distances and Angles[a]

	compound	#I	$d_{I—C}$ /Å[b]	$d_{I\cdots X}$ /Å	R_{XB}[c]	$\theta_{C—I\cdots X}$ /°	$\theta_{I\cdots X\cdots I}$ /°
1	[(*n*-Bu_4NCl)(*p*-$C_6F_4I_2$)][d]	1	2.107	2.988	0.79	178.1	109.1
		2	2.096	3.104	0.82	170.2	
2	[(*n*-Bu_4PCl)(*p*-$C_6F_4I_2$)]	1	2.095	3.038	0.80	175.3	155.6
		2	2.102	2.976	0.79	176.9	
3	[(*n*-Bu_4NBr)(*p*-$C_6F_4I_2$)]	1	2.112	3.168	0.80	175.3	139.2
		2	2.096	3.232	0.82	177.9	
4	[(*n*-Bu_4PBr)(*p*-$C_6F_4I_2$)]	1	2.105	3.189	0.81	176.8	140.9
		2	2.099	3.196	0.81	177.7	
5	[($EtPh_3PBr)_2$(*p*-$C_6F_4I_2$)]	1	2.108	3.148	0.80	175.5	—

[a] See also models in Figure 3.1. [b] Experimental values determined by X-ray crystallography. [c] R_{XB}, normalized distance parameter, $R_{XB} = d_{I\cdots X}/\Sigma d_{VdW}$, where $d_{I\cdots X}$ is the shortest contact distance between the halogen and the halide and d_{VdW} is the sum of their Van der Waals radii (1.98 Å for I, and 1.81, 1.96 Å for Cl^- and Br^-, respectively). [d] This compound was previously reported by Abate e*t al.*[13]

Compound **1** exhibits the same unit cell parameters and halogen bonding environment as previously reported;[13] the chlorides enable the formation of long chains by interacting with iodines from two different *p*-DITFB molecules (see Figure 3.1). As for **3**, Abate *et al*. have solved a different structure that crystallizes in the monoclinic space group *C*2/*c*. Presently, co-crystallization of *n*-Bu_4PCl and *p*-$C_6F_4I_2$ in a different solvent (dichloromethane) afforded **3**, but which packs in the orthorhombic **P**ccn space group. The

main difference between this polymorph and the previously reported one is disorder of the aromatic ring in the *ac* plane (Figure 3.2). Compound **2** packs in the same space group and crystal system as compound **1** ($P2_1/c$). Compound **4** also packs in a monoclinic crystal system, but in a different space group ($P2_1/n$). Similarly to compound **3**, the aromatic ring in the *ac* plane in **4** exhibits disorder (see Figure 3.3).

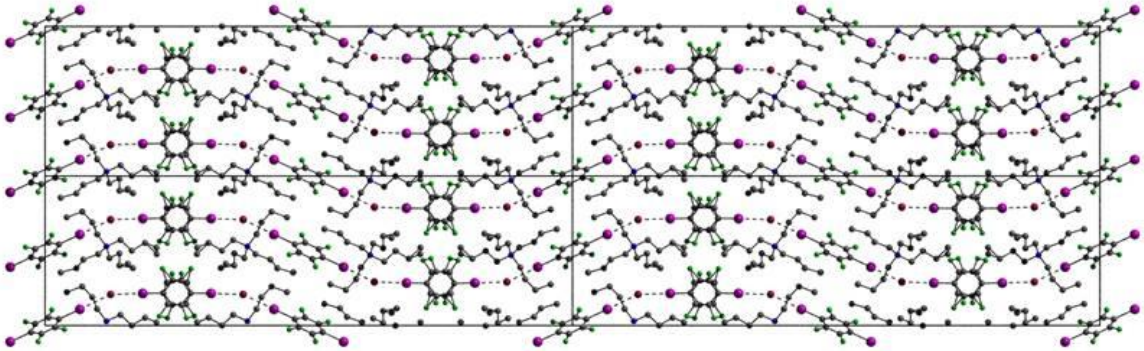

Figure 3.2 2 x 2 x 2 cell of compound **3** shown along the *b* axis. The *p*-$C_6F_4I_2$ molecules form polymeric chains with a bridging bromide. Those chains alternate with rows of cations (*n*-Bu_4N^+) along the *b* axis. There is disorder at the end of the butyl chains. Hydrogens are omitted for clarity.

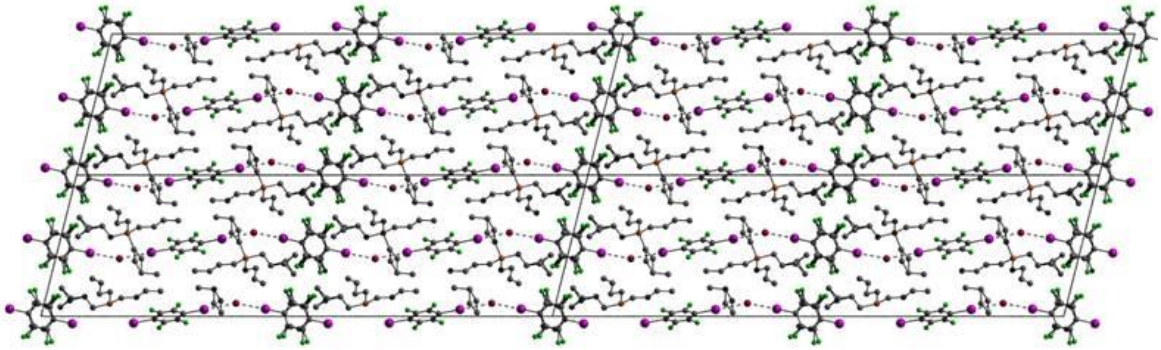

Figure 3.3 2 x 2 x 2 cell of compound **4** shown along the *b* axis. The *p*-$C_6F_4I_2$ molecules form polymeric chains with a bridging bromide. Those chains alternate with rows of cations (*n*-Bu_4N^+) along the *b* axis. There is disorder at the end of the butyl chains. Hydrogens are omitted for clarity.

In all of the halogen bonded compounds reported here with the exception of **5**, the two iodines of *p*-DITFB act as acceptors of electron density, and they form almost linear C—I···X^- arrangements with the donor of electron density (*i.e.*, Cl^- or Br^-). The C—I···X^- angles range from 170.2 to 178.1° for compounds **1** to **4**, and their normalized distance parameter, R_{XB}, values range between 0.79 and 0.82 (see Table 3.2). Hence, these compounds can be classified as having moderately strong halogen bonding interactions, since the short linear contacts, $d_{I—X}$, observed are ~ 20% shorter than their VdW radii. These XB compounds form polymeric anionic zigzag chains with halide bridges and have different coordination angles. The I···Cl^-···I angles are 109.1° and 155.6° for **1** and **2** respectively, and the I···Br^-···I angles are 139.2° and 140.9° for **3** and **4**, respectively (see Figure 3.1). In these compounds, the two iodines which interact with the halide are crystallographically non-equivalent. Similar halogen bonding environments were also observed by Grebe *et al.*, where the zigzag chains for [(Me_4NCl)(*p*-DITFB)] and (Me_4N)[(*p*-$C_6F_4I_2$)Br] · CH_3CN had, however, more acute angles, $\theta_{I\cdots Cl^-\cdots I}$ = 77.2° and $\theta_{I\cdots Br^-\cdots I}$ = 74.3°.[29] Furthermore, Abate *et al.* found an almost identical I···Br^-···I angle for compound **3** (138.4°).[13]

The crystal packing is similar for compounds **1** and **2**. The rows of polymeric chains between the halide and the *p*-DITFB molecules are separated by a row of cations. This is observed along the *a* axis for compounds **1** and **2**, as depicted in Figures 3.4 and 3.5, respectively (Figures along different axis are also present in Appendix A). Also, the butyl chains in compound **2** exhibit some disorder. In contrast to **1** and **2**, the polymeric chains in **3** and **4** formed by the two molecules of *p*-DITFB bridged by a bromide are not in the same plane; the non-disordered aromatic ring *p*-DITFB is in the *ab* plane, oriented almost

perpendicular to the disordered aromatic ring. The cations, *n*-Bu_4N^+ or *n*-Bu_4P^+, and bromide anions alternate in columns along the *b* axis, (Figure 3.2 and 3.3).

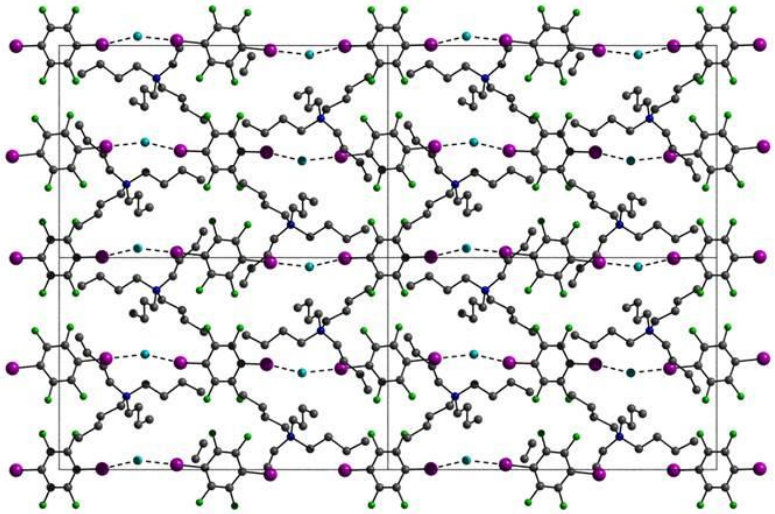

Figure 3.4 2 x 2 x 2 cell of compound 1 along the *a* axis. The *p*-$C_6F_4I_2$ molecules form polymeric chains with a bridging chloride. Those chains alternate with rows of cations (*n*-Bu_4N^+) along the *a* axis. Hydrogens are omitted for clarity.

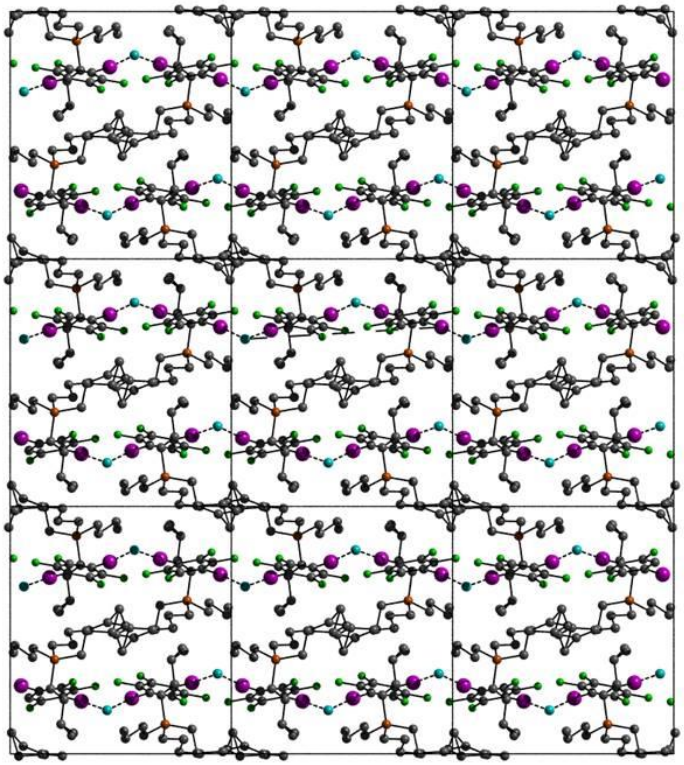

Figure 3.5 3 x 3 x 3 cell of compound 2 shown along the *a* axis. The *p*-$C_6F_4I_2$ molecules form polymeric chains with a bridging chloride. Those chains alternate with rows of cations (*n*-Bu_4N^+) along the *a* axis. There is disorder at the end of the butyl chains. Hydrogens are omitted for clarity.

Finally, compound **5** is formed between $EtPh_3PBr$ and *p*-$C_6F_4I_2$, resulting in $[(EtPh_3PBr)_2$(*p*-DITFB)] which crystallizes in a monoclinic system with a $P2_1/n$ space group. The bromide anion acts as a terminal donor, forming a dianionic $[Br\cdots I—C_6F_4—I\cdots Br]^{2-}$ species (see Figure 3.1). This scaffold has been observed previously by Grebe *et al*. in the compounds $(Ph_4P)_2[(p\text{-}C_6F_4I_2)Cl_2]\cdot 4CH_2Cl_2$ and $(Ph_4P)_2[(p\text{-}C_6F_4I_2)Br_2]\cdot 4CH_2Cl_2$.[29] Rows of $EtPh_3P^+$ cations alternate with rows of $[Br\cdots I—C_6F_4—I\cdots Br]^{2-}$ moieties along the *b* axis, (Figure 3.6). Also, a view of the unit cell of **5** shows that the cations are associated two by two into an inversion-centered phenyl embrace motif. Triguero *et al*. observed the same pattern in $(Ph_4P)[(sym\text{-}C_6F_3I_3)Br]$[28] and mention that it is

a recurrent motif for Ph_3PR derivatives.[31, 32] Again, the bromide adopts characteristic XB by forming systematic strong ~ 180° I···Br^- contacts (R = 0.80 and $\theta_{C—I\cdots Br^-}$ = 175.5°).

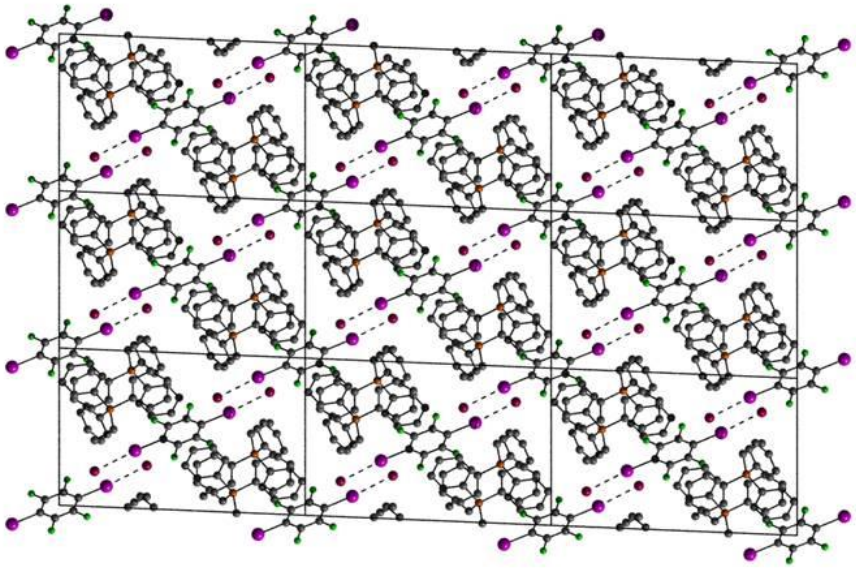

Figure 3.6 3 x 3 x 3 cell of compound 5 shown along the *b* axis. The rows of $EtPh_3P^+$ cations alternate with rows of $[Br\cdots I—C_6F_4—I\cdots Br]^{2-}$ moieties. The ethyltriphenylphosphonium cations are associated two by two into the inversion centered phenyl embrace motif. Hydrogens are omitted for clarity.

3.3.6 *Solid-State NMR Spectroscopy: ^{13}C Chemical Shifts*

Presented in Figure 3.7 are sections of the ^{13}C CPMAS NMR spectra corresponding to the covalently bonded C—I regions for solid powdered samples of **1** to **5**, and for *p*-DITFB. Such spectra are challenging to acquire with a good signal-to-noise ratio given the lack of directly bonded protons on the carbons of interest, the directly bonded iodine, the nearby fluorines, and long relaxation times. The ^{13}C chemical shifts for each of the compounds considered in this work are summarized in Table 3.3. These were obtained by a simultaneous simulation of each of the spectra acquired at both 9.4 and 21.1 T magnetic field strengths, shown in Figure 3.7 (g-l) and (a-f), respectively. The full ^{13}C CPMAS

SSNMR spectra for compounds **1** to **5** and for *p*-DITFB acquired at both fields may be found in Figure 3.8 and 3.9. The assignments of their chemical shifts are tabulated in Table 3.4 and follow the labelling depicted in Figure 3.10.

Table 3.3 Calculated and Experimental ^{13}C Isotropic Chemical Shifts of Carbon Covalently Bonded to Iodine

	compound	$\delta_{iso}(^{13}C)$ exp. / ppm[a]	$\delta_{iso}(^{13}C)$ calc. / ppm[b]
	p-$C_6F_4I_2$	76.50(0.50)	72.12
1	[(*n*-Bu_4NCl)(*p*-$C_6F_4I_2$)]	83.92(0.01)	114.17
		80.64(0.02)	85.22
2	[(*n*-Bu_4PCl)(*p*-$C_6F_4I_2$)]	81.75(0.45)	94.74
		83.65(0.15)	98.21
3	[(*n*-Bu_4NBr)(*p*-$C_6F_4I_2$)]	84.72(0.10)	92.95
		81.84(0.01)	69.53
4	[(*n*-Bu_4PBr)(*p*-$C_6F_4I_2$)]	83.80(0.06)	117.66
		83.00(0.02)	67.54
5	[($EtPh_3PBr$)$_2$(*p*-$C_6F_4I_2$)]	84.50(0.25)	95.62

[a] Experimental ^{13}C isotropic chemical shift of the carbon covalently bonded to iodine. In parentheses are the errors assessed from WSolids1 simulations. [b] DFT calculated $\delta_{iso}(^{13}C)$ including scalar and spin-orbit relativistic effects using ZORA as implemented in ADF. The revPBE exchange-correlation functional was used with the ZORA/TZP basis set, plus extra diffuse functions on the halide ion (ADF AUG directory).

Several important points can be made concerning the ^{13}C CP MAS SSNMR spectra. The use of the 21.1 T instrument allows for improved precision of the ^{13}C chemical shifts since the residual dipolar coupling (RDC) between ^{13}C and quadrupolar halogen nuclides (*i.e.*,^{127}I) decreases significantly at such a field, [33] and this is observed by a decrease in the line widths (80 to 200 Hz) of the resonances compared to the ones observed at 9.4 T (137 to 289 Hz). Residual dipolar coupling was satisfactorily accounted for with the use of apodization, as no specific asymmetric broadening or splitting patterns attributable to RDC were observed. This approach was validated by the consistent field-independent chemical shift values obtained in both applied magnetic fields. From the crystal structures, two

resonances are expected in **1**, **2**, **3**, and **4** for the carbons bonded to iodine whereas in **5** only one is anticipated. The spectra acquired at 21.1 T are consistent with the expected number of C—I resonances in all compounds with an increase in spectral resolution when compared to data acquired at 9.4 T. One particularly clear and unambiguous aspect of the spectra in Figure 3.7 is that an increase in $\delta_{iso}(^{13}C)$ is observed for the C—I resonance in the presence of halogen bonding relative to pure *p*-DITFB (76.50(0.50) ppm). These range from 80.64(0.02) ppm for **1** to 84.72(0.10) ppm for **3**. The fact that these chemical shifts are substantially lower than those typically observed for aromatic carbons is due to a well-known relativistic spin-orbit-induced heavy atom substituent effect caused by the covalently bonded iodine.[34]

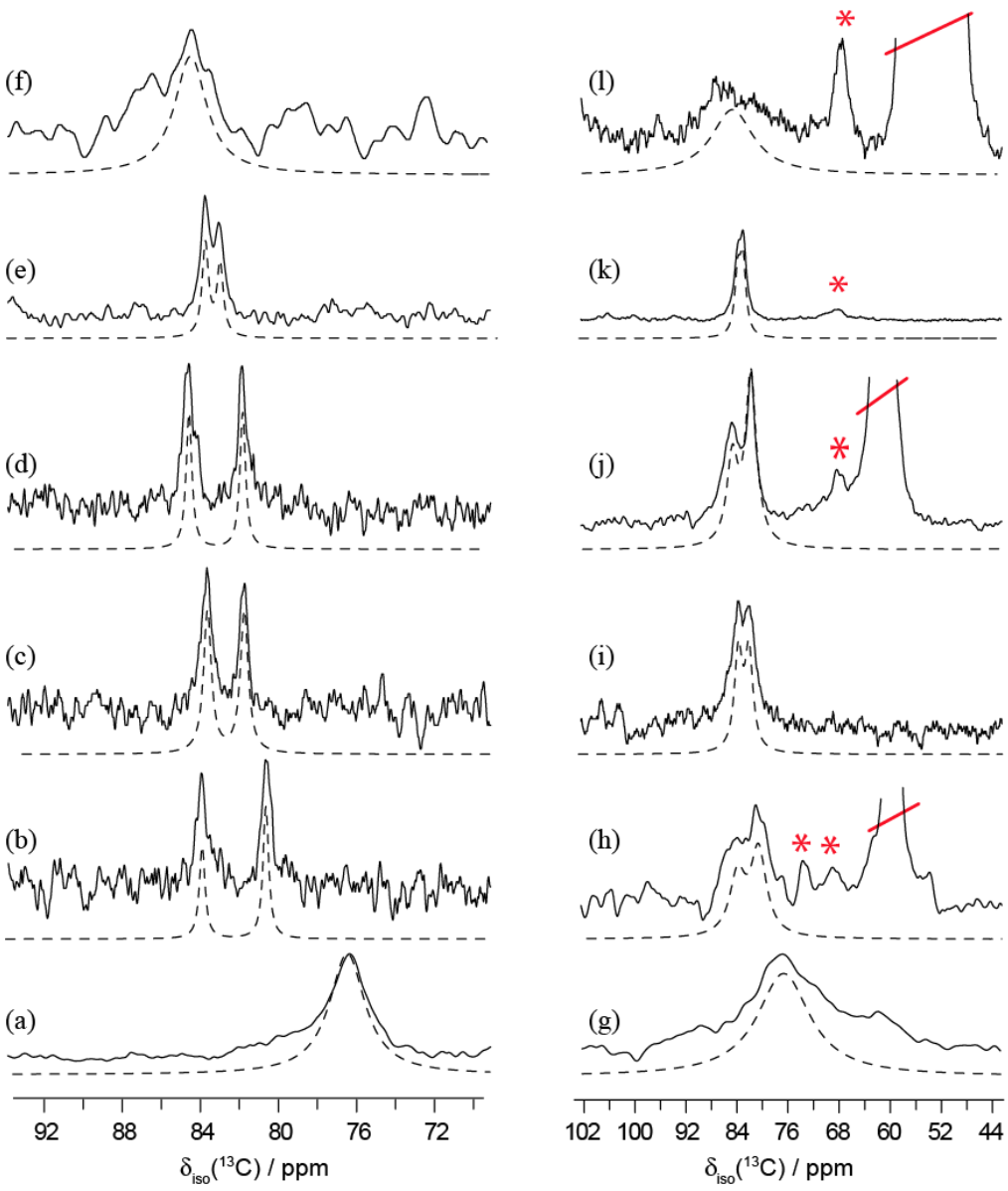

Figure 3.7 Experimental (solid line) and simulated (dashed line) ^{13}C CPMAS SSNMR spectra for the region of the carbon covalently bonded to iodine. The spectra on the left were recorded at 21.1 T with a MAS speed of 18 kHz and correspond to *p*-DITFB (a), **1** (b), **2** (c), **3** (d), **4** (e), and **5** (f). The right column corresponds to the spectra recorded at 9.4 T with a spinning speed of 8 kHz, where the spinning sidebands are indicated by a red asterisk and carbon atoms from the butyl chains are cut with a red dash. The spectra correspond to *p*-DITFB (g), **1** (h), **2** (i), **3** (j), **4** (k), and **5** (l).

It is of interest to further understand why changes in the value of $\delta_{iso}(^{13}C)$ occur for the C—I carbons in the presence of halogen bonding, relative to *p*-DITFB alone, where such an interaction is absent. It was mentioned in the previous section that the geometry of the halogen bond is different in each of the compounds studied. Firstly, the value of δ_{iso} for the ^{13}C directly bonded to the iodine involved in halogen bonding was plotted as a function of the strength of the XB by using the normalized distance parameter, R_{XB}. No clear correlation could be distinguished for the series of XB compounds presented here. Secondly, the C—I distances, $d_{C—I}$, are different for each of the halogen bonded compounds, and this distance is one possible indicator of halogen bonding.[7] When the values of $\delta_{iso}(^{13}C)$ are plotted as function of their respective C—I distances, a good exponential correlation is observed ($R^2 = 0.9613$, see Figure 3.8). An exponential is used to fit the data, since in principle as the bond length becomes infinitely long, the CS value observed would be constant (however, the physical meaning of this value is unclear). A linear fit which excludes the datum for the non-halogen bonded *p*-DITFB is reasonable as well (Figure 3.8). It is critical to note here that the assignments of the two values of $\delta_{iso}(^{13}C)$ to the two different crystallographic sites in a particular compound were determined independently from ZORA-DFT calculations (*vide infra*). There is no obvious way to do this experimentally, and therefore the correlation presented in Figure 3.8 should be considered as an experimental correlation established with the aid of computation. Small cluster models of the halogen bonding environment were used for the calculations, as shown in Figure 3.1. The calculated values of $\delta_{iso}(^{13}C)$ are presented in Table 3.3. In most cases it can be seen that when the C—I distance increases, the value of $\delta_{iso}(^{13}C)$ will also increase, perhaps since the spin-orbit effect is reduced. It is also interesting to mention that,

consistent with this interpretation, *p*-DITFB has the most shielded carbon CS (76.50(0.50) ppm) and shortest $d_{C—I}$ (blue diamond in Figure 3.8).

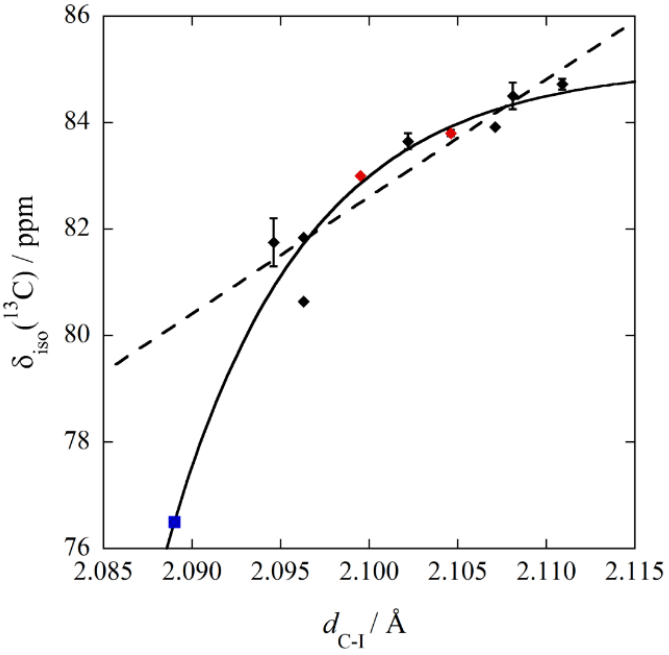

Figure 3.8 Plot of experimental values of $\delta_{iso}(^{13}C)$ as a function of the corresponding carbon-iodine distance, $d_{C—I}$, for carbons directly bonded to iodine. The values of $\delta_{iso}(^{13}C)$ are taken from Table 3.3 and the values of $d_{C—I}$ are tabulated in Table 3.2. The black diamonds represent the halogen bonded compounds **1**, **2**, **3**, and **5** and the blue square represents *p*-DITFB. The red diamonds represent compound **4**, where the assignment is ambiguous; they could be very well be assigned in reverse order from the ZORA DFT cluster model calculations. Some of the experimental vertical error bars are within the size of the symbols. The best fit represented by a black line is an exponential function: $\delta_{iso}(^{13}C) = 8.5629 \times (1\text{-}\exp(-128.96\ \Delta\ d)) + 76.5$, Pearson correlation coefficient $R^2 = 0.9613$, where $\Delta d = d_{C—I(XB\ compound)} - d_{C—I(p\text{-}DITFB)}$. A linear fit to the data for the halogen bonded complexes (blue square excluded from fit) is described by: $\delta_{iso}(^{13}C) = 220.15d\text{-}379.71$, $R^2 = 0.859$.

To our knowledge, this is the first time this trend correlating the values of $\delta_{iso}(^{13}C)$ to the C—I distance in halogen bonds has been reported in the solid state. Indeed, difficulties in observing such shifts and interpreting them have been described previously in the

literature. Efforts by Bouchmella and co-workers on the acquisition of ^{13}C CPMAS NMR spectra for halogen bonded compounds of imidazolyl-containing haloalkenes and haloalkynes have been reported.[11] Unfortunately, they were unable to observe the chemical shifts of the carbons bonded to iodine experimentally. Our observations are consistent with previous reports of ^{13}C chemical shifts in solution. Goroff and coworkers demonstrated that there is a measurable change in carbon resonances associated with the carbons bonded to iodine due to halogen bonding interactions with the solvent in diiodohexatriyne and diiodooctatetrayne.[8] These changed from 0.9 ppm in $CDCl_3$ to 14.6 ppm in DMSO for C_6I_2 and from 1.9 ppm in $CDCl_3$ to 17.9 ppm in DMSO for C_8I_2. This phenomenon is well known for iodoalkynes, were the carbon in iodophenylacetylene has a chemical shift of 6.1 ppm in $CDCl_3$ and 20 ppm in pyridine-d_5.[9,10] However, Glaser, Kaupp and co-workers have eloquently described the challenges in understanding such changes, particularly in solution, where spin-orbit effects and coordination shifts may nearly cancel each other out, making trends difficult to identify experimentally.[35]

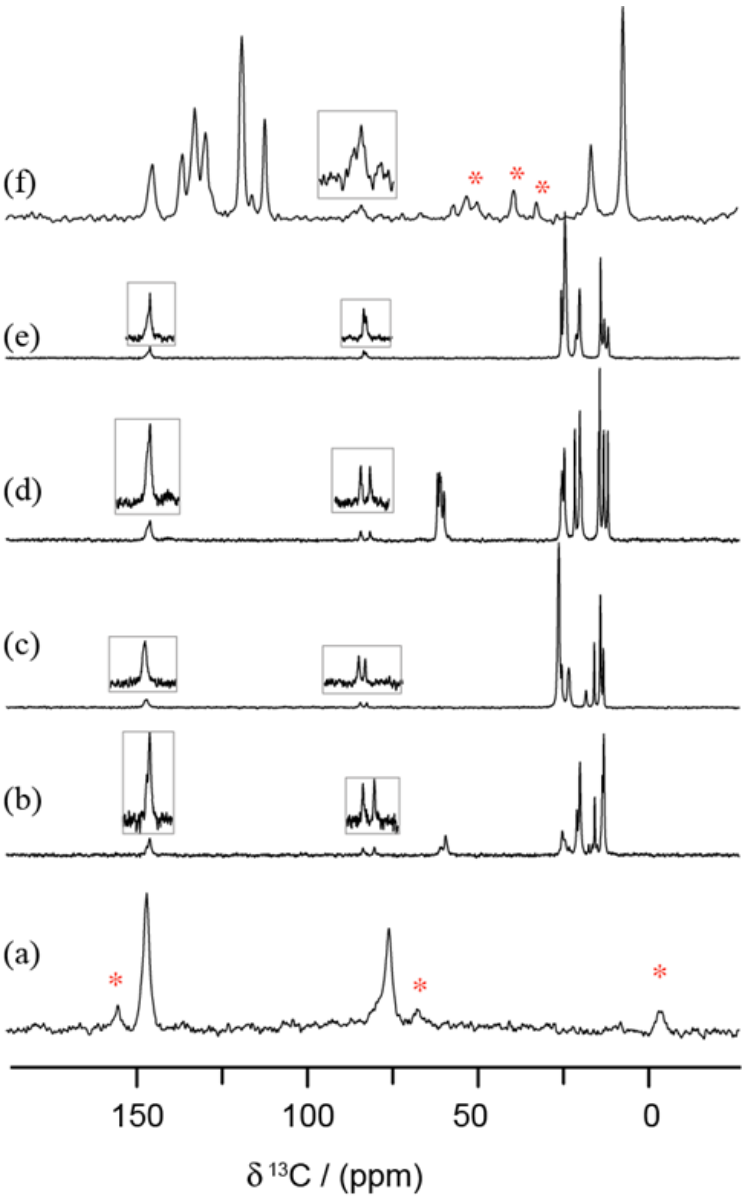

Figure 3.9 ^{13}C CPMAS SSNMR spectra acquired at 21.1 T of (a) *p*-DITFB, (b) **1**, (c) **2**, (d) **3**, (e) **4**, and (f) **5**. The insets show vertical expansions (4x). The asterisks denote spinning sidebands.

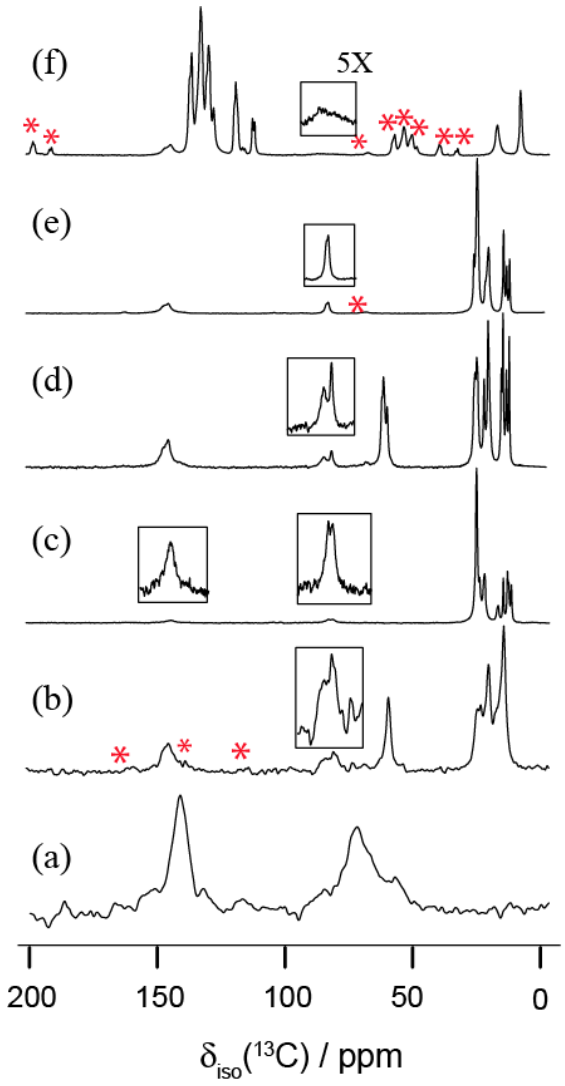

Figure 3.10 ^{13}C CPMAS SSNMR spectra acquired at 9.4 T of (a) *p*-DITFB, (b) **1**, (c) **2**, (d) **3**, (e) **4**, and (f) **5**. The insets show vertical expansions (4x, except for (f)). The asterisks denote spinning sidebands.

*Table 3.4 Experimental $\delta_{iso}(^{13}C)$ (ppm) of p-DITFB and compounds **1** to **5**[a]*

compound					C—I a, d	C—F b, c, e, f
p-DITFB					76.50	147.3
	CH_2 j ,k , r, s	CH_2 h, m, p, u	CH_2 i, l, q, t	CH_3 g, n, o, v		
1	61.5-58.8	24.0-26.0	21.6-19.6	16.0, 14.4-13.0	83.92 80.64	148.0- 145.5
2	26.2-24.5	23.1-22.1	18.1-17.2	15.5-12.2	81.75 83.65	147.4- 145.2
3	62.5-60.0	26.2-24.6	22.9, 20.7-19.8	14.9, 14.6, 13.5, 12.2	84.72 81.84	147.2- 145.7
4	26.1-24.7	23.1-22.2	18.1-15.2	13.4-12.5	83.80 83.00	
	CH_3 g CH_2 h	CH_2 i	CH j, k, l			
5	7.9 17.2	112.7,116.5, 120.3- 118.4	j, 131.3-129.3 k, 134.5-132.1 l, 138.5-135.9		84.50	147.2- 145.0

[a] ^{13}C CS assignment follows scheme depicted in Figure 3.11.

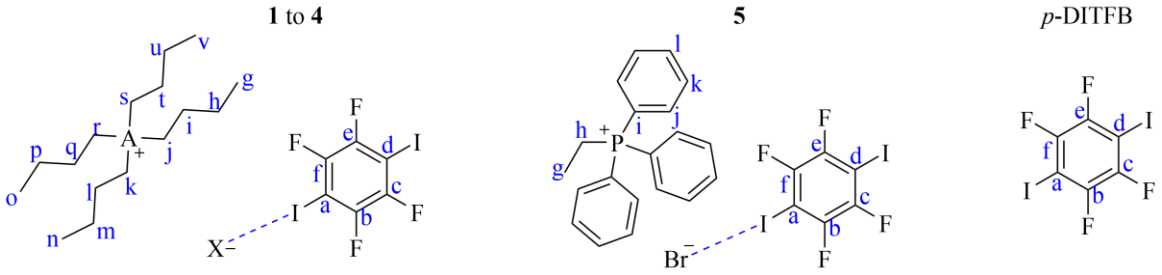

Figure 3.11 Labelling scheme used for attributing the $\delta_{iso}(^{13}C)$ values of XB compounds **1** to **5** and starting material *p*-DITFB, where A is either P or N and X is Cl or Br.

3.3.7 *ZORA DFT Calculations of ^{13}C Magnetic Shieldings and Chemical Shifts*

The challenges associated with chemical shift calculations for ^{13}C bonded to heavy atoms have been discussed in the literature.[34,35] ZORA-DFT computed ^{13}C—I chemical shifts for the compounds of interest are reported in Table 3.3. While the calculations provide chemical shifts which are significantly lower than those of aromatic carbons lacking a bonded iodine, the computed values of $\delta_{iso}(^{13}C)$ generally overestimate the

experimental data by tens of ppm. Calculations of these data are quite challenging for various reasons, and there are several possible explanations for the deviation between experiment and theory. For example, the cluster models used here do not allow for a full treatment of the effect of the ions in the crystal lattice on the computed NMR parameters. The GIPAW DFT method[36] does allow for calculations using periodic boundary conditions; however, it was concluded that the inclusion of relativistic effects via ZORA is more important for the present compounds (see Table A1, Appendix A). It would be desirable to be able to include periodic boundary conditions as well as ZORA relativistic effects; while this is an ongoing area of research,[37] it is beyond our current computational capabilities. Furthermore, in general it is known that the treatment of relativistic effects as well as the relative roles of dispersion and electrostatics in the XB are challenging for current computational methods.[38] On balance, the approach used here is a reasonable one given the various competing factors involved and the computational tools available.

Given the relatively poor absolute agreement between the experimental and calculated shifts shown in Table 3.3, I sought to confirm the experimentally observed trend (Figure 3.8) by attempting to reproduce the *trend* computationally, without focus on the precise magnitudes of the computed shifts. Additional calculations of ^{13}C chemical shifts were therefore performed on cluster models involving a molecule of *p*-DITFB halogen-bonded through one iodine to a chloride ion (see Figure A3, Appendix A). Two different systematic studies were performed. First, the short contact between the chloride and iodine was increased systematically from R_{XB} = 0.79 to 0.98, while the C—I distance and the halogen bonding angle, $\theta_{C—I\cdots Cl^-}$ were kept fixed at 2.096 Å and 180°, respectively. Shown in Figure 3.12 is an inverse linear correlation between the increasing strength of the XB

interaction and the calculated values of $\delta_{iso}(^{13}C)$ of the carbon covalently bonded to iodine. In Figure 3.12(a), scalar and spin-orbit relativistic effects are included in the calculations using ZORA, since spin-orbit-induced effects are expected in the presence of iodine.[34] In Figure 3.12(b), the same plot is presented without the incorporation of relativistic effects. Therefore, a second-order polynomial is used to best fit the data ($R^2 = 1$). The general trend is the same in both cases: an increase in XB strength is accompanied by an increase in chemical shift. The shaded areas in the plots are representative of the strength of the XB in the compounds presented in this study (R_{XB} = 0.79 to 0.82). A 6 ppm change is observed over this range when relativistic effects are incorporated in the calculations, and a 3 ppm change is observed for the non-relativistic calculations. Both sets of data are consistent with experiment, where a 4 ppm range is observed for $\delta_{iso}(^{13}C)$. Recall, however, that a clear correlation between $\delta_{iso}(^{13}C)$ and R_{XB} was not observed experimentally. Therefore, a second series of calculations was performed where the C—I distance was increased from 2.094 to 2.110 Å (representing the range of C—I bond length observed by XRD in our series of XB compounds) by increments of 0.002 Å and the normalized distance parameter, R_{XB}, was fixed at 0.81 with a linear C—I···Cl^- angle. Linear correlations are observed between the values of $\delta_{iso}(^{13}C)$ and the C—I bond length (Figure 3.12 with (b) and without (c) scalar and spin-orbit relativistic effects). In both cases, there is a ~1 ppm increase in $\delta_{iso}(^{13}C)$ when increasing the C—I bond length, and the same general trends are observed whether relativistic effects are included or not. However, the inclusion of scalar and spin-orbit relativistic effects in the calculations results in a decrease in the value of $\delta_{iso}(^{13}C)$ by 25 ppm relative to the non-relativistic results (~105 ppm vs ~130 ppm). Relativistic ZORA-

DFT calculations reproduce better the observed magnitudes of the chemical shifts of carbon covalently bonded to iodine.

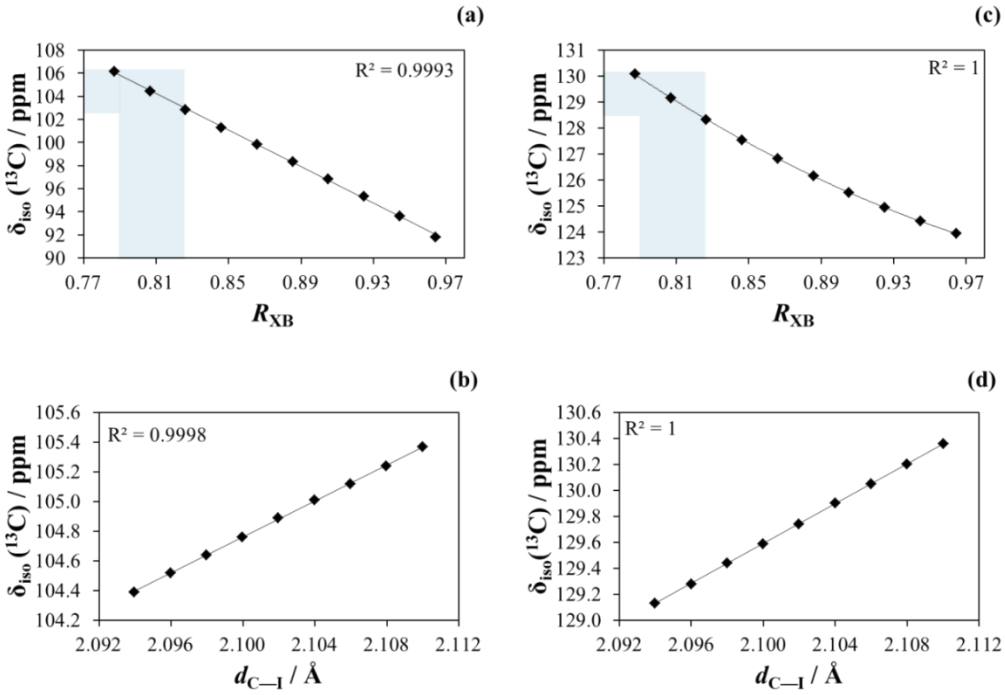

Figure 3.12 Calculated ^{13}C isotropic chemical shift of the carbon covalently bonded to iodine in a cluster model involving *p*-DITFB and chloride, using ZORA DFT implemented in ADF (GGA PBE and ZORA/TZP basis set). Plot (a and c) corresponds to $\delta_{iso}(^{13}C)$ in function of decreasing halogen bond strength (from R_{XB} = 0.79 to 0.98), where the value of $\theta_{C—I\cdots Cl^-}$ is fixed to 180°. The shaded areas represent the range of observed R_{XB} values for the halogen bonded compounds reported herein (R_{XB} = 0.79 to 0.82). In (a), scalar and spin-orbit relativistic effects are calculated using ZORA and in (c) no relativistic effects are included. Plots (b and d) correspond to $\delta_{iso}(^{13}C)$ as a function of increasing distance between the carbon and covalently bond iodine ($d_{C—I}$), where the halogen bond strength is held constant to 0.81 and $\theta_{C—I\cdots Cl}$ is linear. Scalar and spin-orbit relativistic effects are implemented using ZORA in (b) and not in (d). Solid lines are of best linear fit, except in the case of (c) where a second-order polynomial is used. The lines of best fit are as follows: (a) $\delta_{iso}(^{13}C) = -77.961R_{XB} + 168.43$, (b) $\delta_{iso}(^{13}C) = 60.75(d_{C—I}) - 22.814$, (c) $\delta_{iso}(^{13}C) = 64.21R_{XB}^2 - 148.25R_{XB} + 207.56$ and the linear fit would be $\delta_{iso}(^{13}C) = -33.96R_{XB} + 156.92$, Pearson correlation coefficient $R^2 = 0.9902$; (d) $\delta_{iso}(^{13}C) = 76.75(d_{C—I}) - 31.585$.

ZORA-DFT calculations and experiments both suggest that an increase in the C—I bond length correlates with an increase in the ^{13}C chemical shift for C—I groups involved in halogen bonds. While experimentally it was observed that increases in the C—I bond length correlate best in an inverse exponential manner with $\delta_{iso}(^{13}C)$, a linear trend is observed using ZORA-DFT. It is reasonable to suggest that this might be due to the constraints of the model. For example, the XB strength is fixed to R_{XB} = 0.81 in the calculations whereas experimentally, when the halogen bond strength increases, the C—I bond length simultaneously increases. This might also help to explain the 1 ppm change observed computationally versus the 4 ppm change observed experimentally for $\delta_{iso}(^{13}C)$ over the same range of C—I bond lengths. However, even though the calculated chemical shifts are overestimated, the overall trend is the one observed experimentally: an increase in the C—I bond length will result in a higher chemical shift of the carbon resonance involved in the XB interaction.

3.4 CONCLUSIONS

The preparation of a series of compounds have been reported exhibiting halogen bonding between *p*-diiodotetrafluorobenzene and halide anions, and characterized by close linear contacts. The XB compounds have been studied by XRD and ^{13}C solid-state magnetic resonance spectroscopy. X-ray diffraction revealed similarities and differences in the halogen bonding motifs for halides described by Abate *et al.*,[13] Triguero *et al.*,[28] and Grebe *et al.*[29] In particular, the halides are ditopic and form long polymeric chains with I···X$^-$···I angles ranging from 109.1 to 140.9° for compounds **1** to **4**. The bromine anion in compound **5** forms halogen bonds with one iodine, forming [Br···I—C_6F_4—I···Br]$^{2-}$ moieties.

For compounds **1** to **5**, the solid-state ^{13}C chemical shifts increase by several ppm relative to the pure non-halogen-bonded *p*-DITFB component. Recalling the provisional IUPAC definition of the XB interaction (R—X···Y—Z), the halogen bond may lead to characteristic changes in the NMR signals of R—X. In this study, the value of $\delta_{iso}(^{13}C)$ is correlated to the halogen bonding environment, as quantified by the carbon-iodine bond length. As the C—I distance increases, the chemical shift also increases. Correlations with the value of the normalized distance parameter, R_{XB}, were not observed experimentally; this may be in part due to the fact that both chloride and bromide electron donors are considered within the same data set. ZORA-DFT calculations of the ^{13}C chemical shift carried out on a cluster model reproduced the experimental trend as the carbon-iodine distance was varied. The inclusion of scalar and spin-orbit relativistic effects in the calculations resulted in a decrease in the computed values of $\delta_{iso}(^{13}C)$ of about 25 ppm. It is clear that there is further room for improvement in the calculation of magnetic shielding tensors in halogen-bonded systems where relativistic effects are important. This combined experimental-theoretical study has demonstrated that carbon-iodine-halide halogen bonding interactions are reflected in the ^{13}C chemical shifts, thereby providing an example of the utility of NMR methods in characterizing halogen bonding interactions in the solid state.[39]

3.5 REFERENCES FOR CHAPTER 3

1 (a) A. E. Aliev, K. D. M. Harris, (2004), *Probing Hydrogen Bonding in Solids Using Solid State NMR Spectroscopy*, D. M. P. Mingos (Ed.), *Supramolecular Assembly via Hydrogen Bonds, Structure and Bonding*, 108, 1. (b) S. Grzesiek, F. Cordier, V. Jaravine, M. Barfield, (2004), *Prog. Nucl. Magn. Reson. Spectrosc.*, 45, 275. (c) G. Wu, C. J. Freure, E. Verdurand, (1998), *J. Am. Chem. Soc.*, 120, 13187.

2 J. F. Bertrán, M. Rodríguez, (1980), *Org. Magn. Reson.*, 14, 244.

3 J. F. Bertrán, M. Rodríguez, (1979), *Org. Magn. Reson.*, 12, 92.

4 M. T. Messina, P. Metrangolo, W. Panzeri, E. Ragg, G. Resnati, (1998), *Tet. Lett.*, 39, 9069.

5 P. Metrangolo, W. Panzeri, F. Recupero, G. Resnati, (2002), *J. Fluor. Chem.*, 114, 27.

6 M. G. Sarwar, B. Dragisic, L. J. Salsberg, C. Gouliaras, M. S. Taylor, (2010), *J. Am. Chem. Soc.*, 132, 1646.

7 G. R. Desiraju, P. S. Ho, L. Kloo, A. C. Legon, R. Marquardt, P. Metrangolo, P. A. Politzer, G. Resnati, K. Rissanen, (2013), *Pure Appl. Chem.*, 85, 1711.

8 K. Gao, N. S. Goroff, (2000), *J. Am. Chem. Soc.*, 122, 9320.

9 P. D. Rege, O. L. Malkina, N. S. Goroff, (2002), *J. Am. Chem. Soc.*, 124, 370.

10 J. A. Webb, J. E. Klijn, P. A. Hill, J. L. Bennett, N. S. Goroff, (2004), *J. Org. Chem.*, 69, 660.

11 K. Bouchmella, S. D. Dutremez, B. Alonso, F. Mauri, C. Gervais, (2008), *Cryst. Growth. Des.*, 8, 3941.

12 R. K. Harris, A. C. Olivieri, (1992), *Prog. Nucl. Magn. Reson. Spectrosc.*, 24, 435.

13 A. Abate, S. Biella, G. Cavallo, F. Meyer, H. Neukirch, P. Metrangolo, T. Pilati, G. Resnati, G. Terraneo, (2009), *J. Fluor. Chem.*, 130, 1171.

14 Bruker AXS: Bruker Suite, version 2008/3, (2008), Madison, WI, USA Bruker AXS Inc.

15 G. M. Sheldrick, (2008), SADABS *Bruker AXS area detector scaling and absorption* version 2008/1, Germany University of Göttingen.

16 G. M. Sheldrick, (2008), *Acta Crystallogr., Sect. A: Found. Crystallogr.*, 64, 112.

17 W. L. Earl, D. L. VanderHart, (1982), *J. Magn. Reson.*, 48, 35.

18 S. R. Hartmann, E. L. Hahn, (1962), *Phys. Rev.*, 128, 2042.

19 A. E. Bennett, C. M. Rienstra, M. Auger, K. V. Lakshmi, R. G. Griffin, (1995), *J. Chem. Phys.*, 103, 6951.

20 K. Eichele, R. E. Wasylishen, (2001), *WSOLIDS NMR Simulation Package* version 1.20.15, Halifax, NS, Dalhousie University.

21 D. Massiot, F. Fayon, M. Capron, I. King, S. Le Calvé, B. Alonso, J.-O. Durand, B. Bujoli, Z. Gan, G. Hoatson, (2002), *Magn. Reson. Chem.*, 40, 70.

22 S. L. Chaplot, G. J. McIntyre, A. Mierzejewski, G. S. Pawley, (1981), *Acta Crystallogr.,Sect.B: Struct. Sci.*, 37, 2210.

23 Amsterdam Density Functional Software ADF2009.01 SCM, (2010) Amsterdam, The Netherlands, Theoretical Chemistry, Vrije Universiteit: http://www.scm.com/.

24 A. K. Jameson, C. J. Jameson, (1987), *Chem. Phys. Lett.*, 134, 461.

25 A. Bondi, (1964), *J. Phys. Chem.*, 68, 441.

26 R. D. Shannon, (1976), *Acta Crystallogr., Sect. A: Found. Crystallogr.*, 32, 751.

27 J. P. M. Lommerse, A. J. Stone, R. Taylor, F. H. Allen, (1996), *J. Am. Chem. Soc.*, 118, 3108.

28 S. Triguero, R. Llusar, V. Polo, M. Fourmigué, (2008), *Cryst. Growth Des.*, 8, 2241.

29 J. Grebe, G. Geiseler, K. Harms, K. Dechnicke, (1999), *Z. Naturforsch.*, 54b, 77.

30 (a) M. G. Chudzinski, C. A. McClary, M. S. Taylor, (2011), *J. Am. Chem. Soc.*, 133, 10559; (b) E. Dimitrijević, O. Kvak, M. S. Taylor, (2010), *Chem. Commun.*, 46, 9025; (c) M. G. Sarwar, B. Dragisic, S. Sagoo, M. S. Taylor, (2010), *Angew. Chem. Int. Ed.*, 49, 1674; (d) P. Metrangolo, T. Pilati, G. Terraneo, S. Biella, G. Resnati, (2009), *CrystEngComm*, 11, 1187.

31 I. Dance, M. Scudder, (1996), *Chem. Eur. J.*, 2, 481.

32 I. Dance, M. Scudder, (1995), *J. Chem. Soc., Chem. Commun.*, 1039.

33 V. V. Terskikh, S. J. Lang, P. G. Gordon, G. D. Enright, J. A. Ripmeester, (2009), *Magn. Reson. Chem.*, 47, 398.

34 M. Kaupp, O. L. Malkina, V. G. Malkin, P. Pyykkö, (1998), *Chem. Eur. J.*, 4, 118.

35 R. Glaser, N. Chen, H. Wu, N. Knotts, M. Kaupp, (2004), *J. Am. Chem. Soc.*, 126, 4412.

36 (a) C. J. Pickard, F. Mauri, (2001), *Phys. Rev. B*, 63, 245101. (b) J. R. Yates, C. J. Pickard, F. Mauri, (2007), *Phys. Rev. B*, 76, 024401. (c) M. Profeta, F. Mauri, C. J. Pickard, (2003), *J. Am. Chem. Soc.*, 125, 541. (c) S. J. Clark, M. D. Segall, C. J. Pickard, P. J. Hasnip, M. I. J. Probert, K. Refson, M. C. Payne, (2005), *Z. Kristallogr.*, 220, 56.

37 D. Skachkov, M. Krykunov, T. Ziegler, (2011), *Can. J. Chem.*, 89, 1150.

38 (a) K. E. Riley, P. Hobza, Cryst. Growth Des., 2011, 11, 4272. (b) K. E. Riley, P. Hobza, (2008), *J. Chem. Theory Comput.*, 4, 232.

39 (a) J. Autschbach, T. Ziegler, (2000), *J. Chem. Phys.*, 113, 936. (b) J. Autschbach, T. Ziegler, (2000), *J. Chem. Phys.*, 113, 9410. (c) R. M. Dickson, T. Ziegler, (1996), *J. Phys. Chem.*, 100, 5286. (d) J. Khandogin, T. Ziegler, (1999), *Spectrochim. Acta Part A*, 55, 607.

4 SSNMR AND NLMO STUDY OF QUADRUPOLAR HALOGEN BOND ACCEPTORS IN C-I···X⁻···I-C MOTIFS

4.1 INTRODUCTION AND OBJECTIVES

Let's recall a feature from the IUPAC definition of XB that states "the X···Y halogen bond usually leads to characteristic changes in the NMR signals of R—X and Y—Z.[1] As was previously stated in the introduction of Chapter 3, such changes were observed in ^{1}H,[2] ^{13}C,[3] and ^{19}F NMR studies in solution.[134,135] Erdélyi has used NMR to demonstrate elegantly that symmetric halogen bonding is preferred in solution in certain $[N\text{-}X^{-}N]^{+}$ systems.[4] In the solid state, Weingarth and co-workers have determined N···I distances from ^{15}N-^{127}I dipolar coupling interactions through rotary resonance recoupling ^{15}N SSNMR experiments.[5] As well other studies conducted in our group,[6,7] have observed significant changes in the CS tensors and C_Q of the nuclei involved in the halogen bond compared to the starting material which is devoid of the non-covalent interaction with multinuclear solid-state magnetic resonance ($^{14/15}$N, $^{35/37}$Cl, $^{79/81}$Br, and ^{127}I).[8,9,10,11,12,13,14,15]

One of the open questions in characterizing halogen bonds concerns the understanding of how the NMR parameters of the nuclei involved in halogen bonds, particularly the halogens themselves, may be more rigorously related to (1) the local XB geometry and (2) the local electronic structure; more specifically, the MOs involved in the halogen bond.

In the present study, novel complexes have been synthesized to have moderately strong halogen bonds specifically, with R_{XB} values ranging between 0.79 and 0.91. In addition, these co-crystals were designed to be devoid of competing interactions such as hydrogen bonding. The compounds used in this study contain iodoperfluorobenzenes,

"now considered to be the 'iconic' halogen bond donors",[16] co-crystallized with different ammonium or phosphonium halide XB acceptors. In addition to characterization by XRD, comprehensive multinuclear solid-state magnetic resonance spectroscopic studies are reported. The origins of the observed NMR parameters, such as the quadrupolar coupling constant, C_Q, and asymmetry parameter, η_Q, are further examined with NLMO analyses.[17,18] NLMO analyses provide direct insight into the relationship between structure and spectral parameters by allowing one to identify contributions of individual occupied MOs to the NMR interaction tensors.[19] This work, therefore, combines experimental and theoretical methods to provide insight into the relationship between the geometry and electronic structure of halogen bonds and their corresponding spectroscopic observables.

4.2 EXPERIMENTAL SECTION

4.2.1 *Sample Preparation*

Starting materials were purchased from Sigma-Aldrich and were used without further purification. At room temperature, equimolar amounts of either *p*-DITFB, *o*-DITFB, or *p*-diiodobenzene (*p*-DIB) were dissolved in dichloromethane with an ammonium or phosphonium salt, (*n*-Bu_4PCl, *n*-Bu_4PBr, *n*-Bu_4NBr, Ph_4PCl, $EtPh_3PBr$) yielding the following halogen-bonded co-crystals: [(*n*-Bu_4NCl)(*p*-DITFB)] **1**[43], [(*n*-Bu_4PCl)(*p*-DITFB)] **2**, [(*n*-Bu_4PBr)(*p*-DITFB)] **3**, [(*n*-Bu_4NBr)(*p*-DITFB)] **4**, [($EtPh_3PBr$)(*p*-DITFB)] **5**, [(Ph_4PCl)(*p*-DITFB)] **6**, [($EtPh_3PBr$)$_2$(*p*-DIB)] **7**, [(*n*-Bu_4PCl)(*o*-DITFB)] **8**, [(*n*-Bu_4PBr)(*o*-DITFB)] **9**, [(Ph_4PCl)(*o*-DITFB)]·(CH_2Cl_2)$_2$ **10**. The preparation and crystal structures of some of the halogen-bonded compounds containing *p*-

DITFB were previously reported.[43] The numbering used for the compounds is summarized in Table 4.1 below.

Table 4.1 Halogen Bonded Compounds and Labelling.

compound	*n*-Bu_4NX (X = Cl^-, Br^-)	*n*-Bu_4PX (X = Cl^-, Br^-)	Ph_4PCl	$EtPh_3PBr$
p- DITFB	[(*n*-Bu_4NCl)(*p*-$C_6F_4I_2$)] **1**	[(*n*-Bu_4PCl)(*p*-$C_6F_4I_2$)] **2**	[(Ph_4PCl)(*p*-$C_6F_4I_2$)] **6**	[($EtPh_3PBr$)$_2$(*p*-$C_6F_4I_2$)] **5**
	[(*n*-Bu_4NBr)(*p*-$C_6F_4I_2$)] **4**	[(*n*-Bu_4PBr)(*p*-$C_6F_4I_2$)] **3**		
o- DITFB		[(*n*-Bu_4PCl)(*o*-$C_6F_4I_2$)] **8**	[(Ph_4PCl)(*o*-$C_6F_4I_2$)]·(CH_2Cl_2)$_2$ **10**	
		[(*n*-Bu_4PBr)(*o*-$C_6F_4I_2$)] **9**		
p- DIB				[($EtPh_3PBr$)$_2$(*p*-$C_6H_4I_2$)] **7**

Crystals of compounds **6** and **8** were obtained by slow evaporation from a minimum amount of dichloromethane. Crystals of compounds **9** and **10** were obtained using a slow diffusion method. The compounds were dissolved in a minimum amount of dichloromethane and placed in a vial which was then placed in a jar containing hexane and sealed.

4.2.2 *Single Crystal X-ray Diffraction*

Data collection results for compounds **1-5** are reported in Chapter 3 section 3.2.2. Data collection results for compounds **6**, **7**, **8**, **9**, **10**, and *o*-DITFB represent the best data sets obtained in several trials for each sample. The crystals were mounted on thin glass fibers using paraffin oil. Prior to data collection, crystals were cooled to 200.15 K. Data were collected on a Bruker AXS SMART single crystal diffractometer equipped with a sealed Mo tube source (wavelength 0.71073 Å) APEX II CCD detector. Raw data collection and processing were performed with the APEX II software package from BRUKER AXS.[20]

Diffraction data for **6**, **7**, **8**, **9**, and *o*-DITFB were collected with a sequence of 0.5° ω scans at 0, 120, and 240° in φ. In order to ensure adequate data redundancy, diffraction data for **10** were collected with a sequence of 0.5° ω scans at 0, 90, 180 and 270° in φ due to their lower symmetry. Initial unit cell parameters were determined from 60 data frames with a 0.3° ω scan, each collected for different sections of the Ewald sphere. Semi-empirical absorption corrections based on equivalent reflections were applied.[21] Systematic absences in the diffraction dataset and unit cell parameters were consistent with triclinic $P\bar{1}$ (№2) for compound **10**, monoclinic $P2_1/c$ (№14) for compounds **8** and **9**, monoclinic $P2_1/n$ (№14) for compound **7** and *o*-DITFB, and monoclinic $C2/c$ (№15) for compound **6**. Solutions in centrosymmetric space groups for all compounds yielded chemically reasonable and computationally stable results of refinement. The structures were solved by direct methods, completed with difference Fourier synthesis, and refined with full-matrix least-squares procedures based on F^2. Further PXRD experimental information and diffractograms are given in Appendix B.

For compound **10**, thermal motion parameters for atoms of two partially occupied CH_2Cl_2 solvent molecules suggested a positional disorder not related to the symmetry elements. Disorder was successfully modeled; however, the set of geometrical (SADI) and thermal motion (SIMU, DELU) restraints were applied to achieve acceptable molecular geometries and thermal motion values. Disordered fragment occupancies were refined with satisfactory results at 25%: 25% for both CH_2Cl_2 solvent molecules.

In the structural models of **8**, **9**, **10**, and *o*-DITFB, all molecular fragments of the structures are located in general positions (i.e., not on symmetry elements). In the structure of **6**, two molecules of *p*-$C_6I_2F_4$ are located on two different inversion centers whereas all

the other structural fragments are situated in general positions. Similarly, one molecule of *p*-$C_6I_2H_4$ in the structure of **7** also occupies an inversion center with the rest of the moieties located in general positions. In structural models for all compounds, hydrogen atoms were located from the differences in Fourier maps. However, after initial positioning, all hydrogen atoms were constrained to suitable geometries and subsequently treated as idealized contributions during the refinement. All scattering factors are contained in several versions of the SHELXTL program library, with the latest version being used (6.12).[22]

4.2.2.1 *Comments on the X-ray structure of **6** and **8***

In the case of **6**, two out of four arene molecules are located on an inversion center. Upon inspection of the bond distances, it was found that one of the carbon – iodine bonds is noticeably shorter than all other bonds of this type in the structure. However, upon closer investigation of the thermal motion parameters for the atoms of the tetrafluorodiiodobenzene molecules with unusually short bonds, it was discovered that the arene molecules exhibit minor positional disorder. This disorder could be described as a minor rotation of the molecule in the plane of aromatic ring with the pivot point located on the iodine atom opposed to the unusually short bond. Unfortunately, the disorder was not prominent enough to be successfully resolved. An attempt to treat the disorder by splitting the locations of above-mentioned molecule into two positions and refining the occupancies did not lead to a significant improvement of the overall quality of the structure. Moreover, introduction of several restraints was necessary to obtain satisfactory geometrical and thermal motion parameters. After careful consideration, an undesirable decrease in the data-to-parameters ratio due to the disorder modeling outweighed the slight increase in the

quality of the model. Therefore, the disorder modeling with occupation refinement was removed from the final structure.

Diffraction data for compound **8** were collected to 0.75 Å resolution; however, due to small crystal size and weak diffraction it was discovered that both R(int) and R(sigma) exceed 35% for the data below 0.95 Å resolution. Based on the R(sigma) value, data were truncated to 0.90 Å resolution for refinement. Refinement of the structural model demonstrated good agreement of the stronger reflections with the predicted theoretical values, with $R_1 = 0.0607$ and $wR_2 = 0.1203$ for all the reflections with $I > 2\sigma(I)$. It should be noted that for weak reflections, both R_1 and wR_2 values increase moderately. However, such an increase can be explained by weak diffraction at high angles and higher resolution cut off at 0.90 Å. Thermal motion parameters for the carbon atoms of the butyl chains of the *n*-Bu_4P^+ fragments suggest symmetry unrelated positional disorder. Due to untreated disorder, thermal motion parameter values are more pronounced than for the all the other atoms in the crystal structure. Modelling of the disorder would require the introduction of additional refinement parameters as well as geometry and thermal motion restraints. Despite the disorder, the structural fragments that define the halogen-halide interaction within the structure are refined with acceptable positional precision and thermal motion parameter values. Considering all of the above and in order to conserve an acceptable data-to-parameters ratio for the rather large asymmetric unit, the structure was refined without modelling the disorder. It should be understood that unusually large thermal motion parameters for the *n*-Bu_4P^+ fragments are responsible for the apparent shortening of C(sp3) – C(sp3) bonds, and this may be considered as a crystallographic artifact.

4.2.3 *Solid-State NMR Spectroscopy*

Carbon-13 and chlorine-35/37 SSNMR experiments were carried out on a 400 MHz (B_0 = 9.4 T) Bruker Avance III wide-bore spectrometer equipped with a triple resonance 4 mm MAS probe and a 5 mm solenoid probe, respectively. ^{13}C, $^{35/37}$Cl, and $^{79/81}$Br SSNMR experiments were also carried out at the National Ultrahigh-field NMR Facility for Solids in Ottawa using a 21.1 T Bruker Avance II spectrometer equipped with either a Bruker 4 mm double-resonance MAS probe for ^{13}C or a home-built 5 mm solenoid probe for $^{35/37}$Cl and $^{79/81}$Br. Samples were powdered and packed in 4 mm o.d. zirconium oxide rotors for ^{13}C experiments, and in 5 mm glass tubes for static $^{35/37}$Cl and $^{79/81}$Br experiments. Further experimental information is given in Appendix B.

4.2.3.1 *^{13}C SSNMR*

Ramped amplitude ^{13}C CPMAS NMR[23] spectra were collected with SPINAL64 ^{1}H decoupling[24] for all samples containing protons at two fields, 9.4 T and 21.1 T (^{13}C Larmor frequencies of 100.613 MHz and 226.338 MHz, respectively). Chemical shifts were referenced to solid glycine (δ_{iso}(^{13}C=O) 176.4 ppm with respect to TMS). The $\pi/2$ pulse length and contact times were 3.5 μs and 3 ms or 5 ms at 9.4 T, and 2.5 μs and 3 ms at 21.1 T. Recycle delays ranged from 5 to 15 s. A single-channel rotor synchronized Hahn-echo experiment (*i.e.*, $\pi/2$-τ_1-π-τ_2-acq) was used for the acquisition of the spectrum of *o*-DITFB.

4.2.3.2 *$^{35/37}$Cl SSNMR*

Chlorine chemical shifts and pulse widths were calibrated using the $^{35/37}$Cl NMR signal of KCl powder (δ_{iso}(KCl(s)) = 8.54 ppm with respect to 0.1 M NaCl in D_2O). The CT-selective pulse widths were scaled by 1/2(I + ½). Spectra were collected under stationary conditions at two fields (ν_L(^{35}Cl) = 39.204 MHz at 9.4 T and 88.194 MHz at 21.1

T; $\nu_L(^{37}Cl)$ = 32.634 MHz at 9.4 T and 73.412 MHz at 21.1 T). At 9.4 T, WURST-QCPMG[25] experiments combined with proton CW decoupling to acquire $^{35/37}Cl$ NMR spectra in combination with VOCS method (100 kHz steps) were advantageous at 9.4 T as the nuclei of interest are dilute in the halogen-bonded complexes ($^{35/37}Cl$ ranges from 6.29 to 33.1 mg/cm^3) and the spectra are broad.[26] A 50 μs WURST pulse with 500 kHz bandwidth sweeping from high to low frequency was used with pulse powers optimized experimentally (see Appendix B). The spikelet separation was set to 5 kHz by setting the echo duration to 106 μs with pulse ring-down times of 20 μs; 128 echoes were acquired in every scan. The recycle delays used for these compounds varied between 2 and 4 s. At 21.1 T, $^{35/37}Cl$ SSNMR signals were acquired using an echo (*i.e.*, $\pi/2$-τ_1-$\pi/2$-τ_2-acq)[27] pulse sequence combined with the VOCS method and CW proton decoupling. Typical acquisition parameters were CT-selective $\pi/2$ pulse lengths of 4 μs, spectral windows of 500 kHz, τ_1 values of 45 μs, pulse delays of 1 or 2 s, and 14k to 32k scans per piece.

4.2.3.3 $^{79/81}Br$ SSNMR

Experimental setup, pulse calibration, and referencing were done using solid KBr (δ_{iso}(KBr(s)) = 54.51 ppm with respect to 0.03 M NaBr in D_2O). The Larmor frequencies for bromine were $\nu_L(^{79}Br)$ = 225.518 MHz and $\nu_L(^{81}Br)$ 243.094 MHz at 21.1 T. The CT-selective $^{79/81}Br$ pulses were 1.5 μs for the Solomon echo experiment used to acquire the SSNMR spectra. A recycle delay of 0.2 s, spectral window of 2 MHz, and transmitter offsets of 500 kHz were used. τ_1 varied between 18 and 175 μs, and each piece was collected with 14k to 24k scans.

4.2.3.4 *Spectral Simulation and Processing*

All NMR data were processed with Bruker TopSpin 3.0 software. Echoes were left-shifted where required. The WURST-QCPMG spectra were processed in magnitude mode. The first echo of each of the ^{37}Cl WURST-QCPMG datasets was omitted due to probe ringing. No apodization is used when processing these spectra. For the VOCS method, each piece is processed identically, and co-added together to yield the final spectrum. Simulations were performed with WSolids1[28] and DMFIT (v.2011).[29] Simulations of ^{13}C NMR spectra included chemical shifts, line broadening, and the appropriate number of crystallographic sites determined by X-ray crystallography. Stack plots of the experimental and simulated spectra were prepared using DMFIT. Further information is given in the Appendix B.

4.2.4 ***Computational Details***

Models were generated from X-ray crystal structure atomic coordinates for each halogen-bonded compound using one halide ion and the nearest interacting (*p*- or *o*)-DITFB or *p*-DIB molecule(s) (see Figure 4.1).

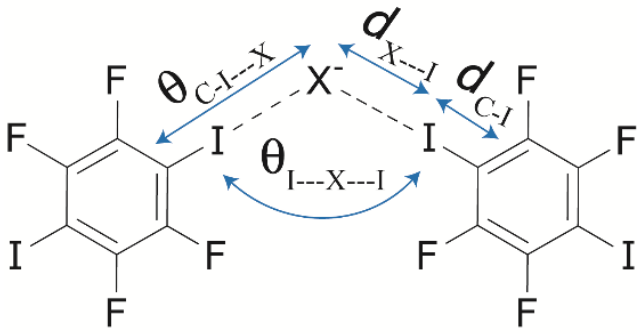

Figure 4.1 General halogen bonding motif (X = Cl or Br) for **1**, **2**, **3**, **4**, **8**, and **9**.

Only for Cl2 (site A) of **6** were the diiodotetrafluorobenzenes replaced by iodotrifluoromethane molecules to ensure convergence. The positions of the fluorine atoms in that model were optimized in Gaussian09[30] (B3LYP/3-21G). The NLMOs, EFG and MS tensors were calculated with the ADF program. Scalar and spin-orbit relativistic effects were included using the ZORA. The exchange-correlation functional GGA revPBE of Zhang and Yang is used for all calculations.[31] The basis sets used for all atoms were Slater-type triple-zeta with polarization functions. A diffuse function was included in the basis set for the halide ion (i.e., AUG/ATZP)[32], whereas the basis set used for all the other atoms was relativistically optimized (i.e., ZORA/TZP).[33]

The EFG and shielding tensors contained in the output files were analyzed using a modified version of the EFGShield program.[34] Magnetic shielding constants were converted to chemical shifts according to the formula $\delta_{ij} = \frac{\sigma_{ref} - \sigma_{ij}}{1 - \sigma_{ref}}$, where σ_{ref} is the absolute shielding constant of a reference compound (184.1 ppm for ^{13}C in TMS;[35] 974 ppm for $^{35/37}Cl$ in infinitely dilute $Cl^-(aq)$).[36] The concentration of 0.1 M NaCl in D_2O[37]

and the significant isotope shift of ~5 ppm caused by D_2O[38] is accounted for in order to properly compare the calculated and experimental $\delta_{iso}(^{35/37}Cl)$ values.

4.3 RESULTS AND DISCUSSION

4.3.1 *X-ray Crystal Structures and Halogen Bond Geometry*

Summarized in Table 4.2 are the crystallographic data for the new XB compounds and in Table 4.3 are the relevant halogen bonding distances, $d_{I\cdots X^-}$, and angles, $\theta_{C—I\cdots X^-}$, as well as the I···X$^-$···I angles ($\theta_{I\cdots X^-\cdots I}$) for the compounds studied presently (see Figure 4.1). Also presented in Table 4.3 are the carbon-iodine bond lengths, which have been demonstrated to increase upon XB formation.[1] The crystal structures for XB compounds **1**, **2**, **3**, **4**, and **5** show a range of Cl$^-$···I and Br$^-$···I halogen bond environments and have been discussed previously.[40] The discussion below will therefore focus on crystallographic aspects of the new XB compounds. Their local halogen bonded environment are shown in Figure 4.2. Also shown in Table 4.3 are the normalized distance parameters, R_{XB} (vdW radii (1.98 Å for covalent I, and 1.81 and 1.96 Å for Cl$^-$ and Br$^-$, respectively[26]), which range from 0.79 (**1**) to 0.91 (**7**). These values indicate the presence of moderately strong (**1**) to weak (**5**) halogen bonds. Very strong halogen bonds can have R_{XB} values as low as 0.69.[39,1] All of the reported compounds exhibit near-linear halogen bonds, with angles ranging from 167.6º to 179.4º for $\theta_{C—I\cdots Cl^-}$, and 170.7º to 178.2º for $\theta_{C—I\cdots Br^-}$.

Table 4.2 Crystallographic Data and Selected Data Collection Parameters

compound	**6**	**7**	**8**	**9**	**10**[a]
empirical formula	$C_{42}H_{20}ClF_{12}I_6P$	$C_{46}H_{44}Br_2I_2P_2$	$C_{66}H_{108}Cl_3F_{12}I_6P_3$	$C_{22}H_{36}BrF_4I_2P$	$C_{31}H_{22}Cl_3F_4I_2P$
formula weight	1580.40	1072.37	2090.18	741.19	861.60
crystal size, mm	0.21 x 0.17 x 0.15	0.24 x 0.20 x 0.17	0.27 x 0.23 x 0.11	0.24 x 0.18 x 0.10	0.21 x 0.14 x 0.14
crystal system	monoclinic	monoclinic	monoclinic	monoclinic	triclinic
space group	*C* 2/*c*	$P2_1/n$	$P2_1/c$	$P2_1/c$	$P\bar{1}$
Z	8	2	4	4	2
a, Å	18.5756(2)	9.24230(10)	13.4256(3)	13.1132 (4)	11.8135(2)
b, Å	19.3258(2)	12.5396(2)	25.3718(6)	15.1457(5)	12.8379(3)
c, Å	26.4008(3)	18.5824(3)	25.3449(6)	14.4157(5)	13.4744(3)
α, °	90.00	90	90	90.00	92.2880(10)
β, °	99.1840(10)	98.3230(10)	98.915(2)	98.7470(10)	114.0890(10)
γ, °	90.00	90	90	90.00	104.8300(10)
volume, $Å^3$	9356.08(18)	2130.92(5)	8529.0(3)	2829.78(16)	1779.12(7)
R_1 (ref)	0.0366	0.0228	0.1716	0.0289	0.0390
wR_2 (ref)	0.0763	0.0520	0.1541	0.0604	0.1208

[a] **10** is a solvate.

Table 4.3 Selected Intermolecular Contact Distances, Angles, and Halogen Bonding Environment Surrounding the Halides in Halogen-Bonded Compounds[a]

compound	#I	$d_{I—C}$ /Å	$d_{I\cdots X^-}$ /Å	R^b	$\theta_{C—I\cdots X^-}$ /°	$\theta_{I\cdots X^-\cdots I}$ /°	$I_x\cdots X^-\cdots I_y$
1[c]	1	2.1071	2.988	0.79	178.1	109.1	$I_1\cdots Cl^-\cdots I_2$
	2	2.0963	3.104	0.82	170.2		
2[c]	1	2.0946	3.038	0.80	175.0	155.7	$I_1\cdots Cl^-\cdots I_2$
	2	2.1022	2.976	0.79	177.0		
3[c]	1	2.1046	3.189	0.83	176.8	140.9	$I_1\cdots Br^-\cdots I_2$
	2	2.0995	3.196	0.83	177.7		
4[c]	1	2.1121	3.166	0.83	175.3	139.2	$I_1\cdots Br^-\cdots I_2$
	2	2.0963	3.236	0.84	177.9		
5[c]	1	2.1081	3.147	0.82	175.5	—	
6 Cl1	1	2.0931	3.204	0.85	174.4	91.6	$I_1\cdots Cl^-\cdots I_2$
	2	2.0952	3.240	0.86	167.6	75.7	$I_2\cdots Cl^-\cdots I_3$
Cl2	3	2.0653	3.332	0.88	174.6	100.4	$I_1\cdots Cl^-\cdots I_3$
	4	2.0872	3.191	0.85	179.4	176.3	$I_4\cdots Cl^-\cdots I_5$
	5	2.0944	3.204	0.85	176.1		
	6	2.0925	3.204	0.85	174.5		
7	1	2.1125	3.472	0.91	170.7	—	
8 Cl1	1	2.1152	3.157	0.84	175.8	112.0	$I_3\cdots Cl^-\cdots I_2$
	2	2.0965	3.088	0.82	175.3	144.5	$I_1\cdots Cl^-\cdots I_6$
Cl2	3	2.1173	3.115	0.83	178.0	123.4	$I_5\cdots Cl^-\cdots I_4$
	4	2.115	3.150	0.83	174.9		
Cl3	5	2.0948	3.052	0.81	169.6		
	6	2.0874	3.062	0.81	176.8		
9	1	2.1085	3.347	0.87	174.6	80.4	$I_1\cdots Br^-\cdots I_2$
	2	2.1047	3.269	0.85	174.1		
10[d]	1	2.1058	3.132	0.83	177.4	120.1	$I_1\cdots Cl^-\cdots I_2$
	2	2.1065	3.152	0.83	176.1		

[a]Refer to Figure 4.1 for information on the reported angles and distances. [b]R_{XB}, normalized distance parameter, $R_{XB} = d_{I\cdots X^-}/\Sigma d_{VdW}$, where $d_{I\cdots X}$ is the shortest contact distance between the halogen and the halide and d_{VdW} is the sum of their van der Waals radii (1.98 Å for I, and 1.81, 1.96 Å for Cl^- and Br^-, respectively).[42] [c]Crystal structure reported in ref. [40] [d]Disordered solvate (DCM).

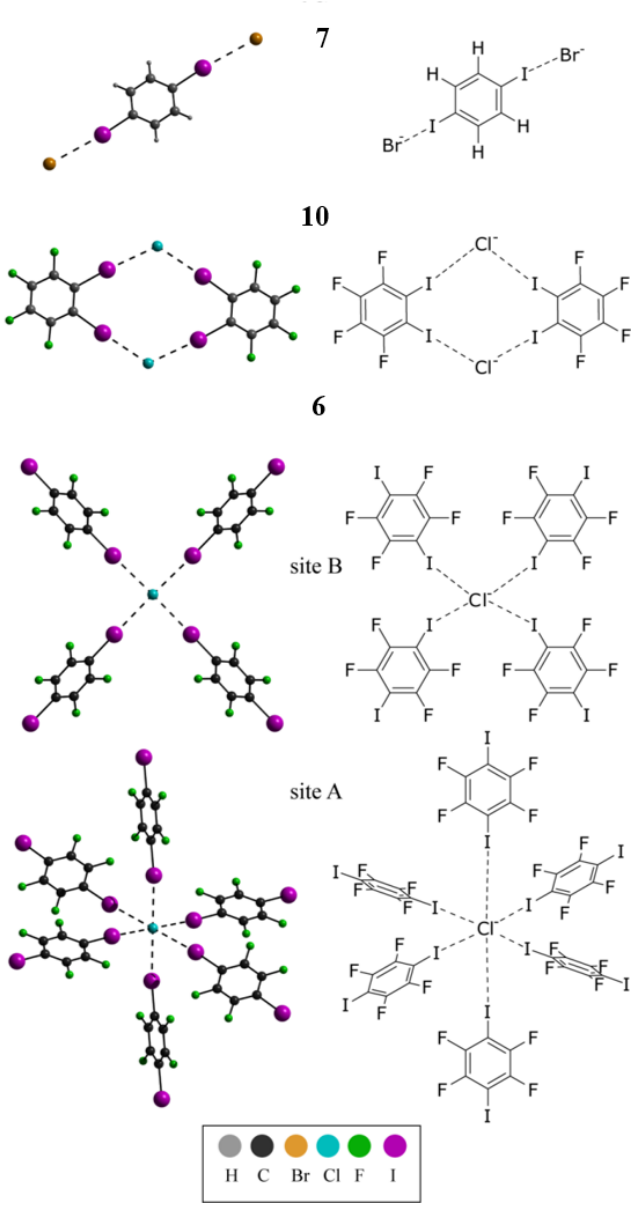

Figure 4.2 Local halogen bonding geometries for some of the compounds studied in this work, from XRD (left), and corresponding molecular structure schemes (right). Each atom is color coded: iodine is violet, chlorine is turquoise, bromine is orange, fluorine is green, carbon is black, and hydrogen is gray. Relative atom sizes are based on their relative van der Waals' radii. See angles and bond distances in Table 4.3. **6** has two crystallographically distinct chloride sites, where the symmetry about site A and B are almost perfectly octahedral and square planar, respectively. **7** exhibits dianionic species of the form $[Br\cdots I–C_6H_4–I\cdots Br]^{2-}$. Cations are not shown.

7 exhibits the same dianionic motif ($[Br\cdots I—C_6H_4—I\cdots Br]^{2-}$) as the previously described compound **5**[40] (see Figure 4.2), as well as the same space group and crystal system ($P2_1/n$ and monoclinic). **7** is the only reported compound in this study where the halogen donor molecule is *p*-diiodobenzene, and exhibits the weakest XB interaction with an R_{XB} value of 0.91. This is attributed to the fact that protons are less electron-withdrawing than fluorine; this leads to the formation of a smaller σ-hole to interact with the halogen bond acceptor (Br^-).[41] A super cell may be viewed in Figure 4.3, where it is observed that the dianionic species form discrete entities in alternating rows with PPh_3Et^+ cations which are associated two-by-two into an inversion-centered phenyl embrace motif. This motif has been observed for bulky phosphonium salts (i.e., Ph_3PR) derivatives[42], and was also observed in compound **5**.[40]

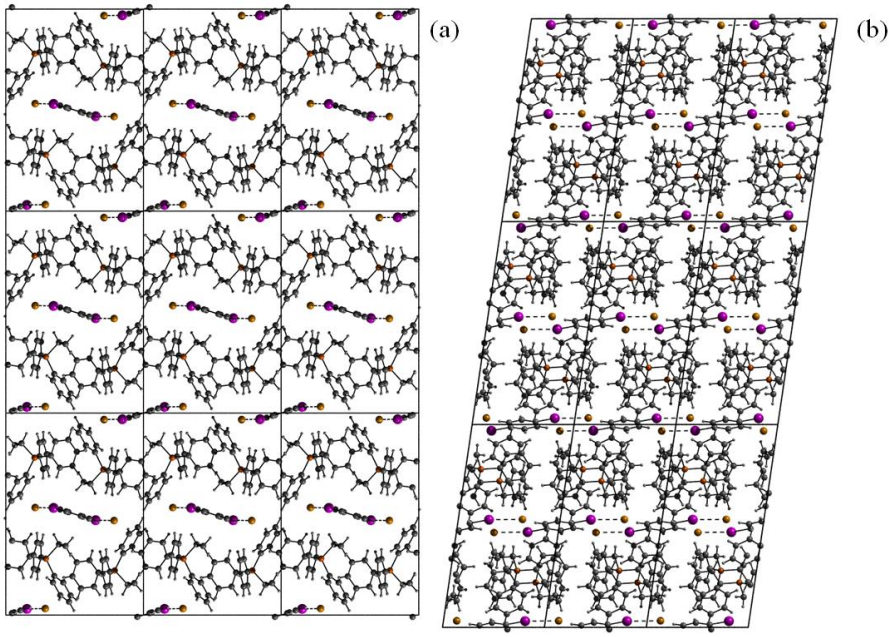

Figure 4.3 3 x 3 x 3 super cell of **7**. The dianionic species $[Br\cdots I—C_6H_4—I\cdots Br]^{2-}$ is between rows of $EtPh_3P^+$ cations along the a axis in (a) and along the *b* axis in (b). Also in (b) the cations are associated two by two into an inversion-centered phenyl embrace motif.

Halogen-bonded compounds **8** and **9** form one-dimensional architectures as shown in Figure 4.4. Each halogen bond acceptor (Cl^- or Br^-) interacts with two iodine atoms, forming polymeric anionic zigzag chains as described for compounds **1**, **2**, **3**, and **4**[40] and by Abate *et al.*[43] Interestingly, for **8** there are three crystallographically distinct chloride ion sites; the environment surrounding each halide is quite different, with I···Cl^-···I angles of 112.0°, 144.5°, and 123.4° for Cl1, Cl2, and Cl3, respectively. One bromide site is present in **9** and the I···Br^-···I angle is rather acute, 80.4°. Such acute angles have been observed previously by Grebe *et al.* in similar compounds.[44] Both **8** and **9** pack in the monoclinic crystal system with the $P2_1/c$ space group. Figure 4.5 and 4.6 show the packing diagrams for compounds **8** and **9**, respectively.

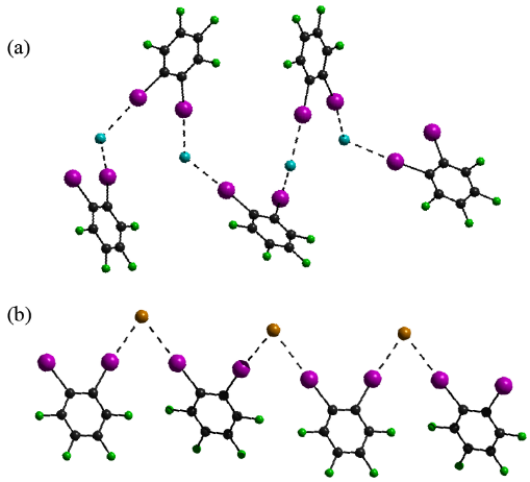

Figure 4.4 XB compounds **8** (a) and **9** (b) form one dimensional chains in the crystal lattice. The halogen bond acceptor (Cl^- or Br^-) forms short contacts with two iodines from different DITFB molecules in a polymeric manner.

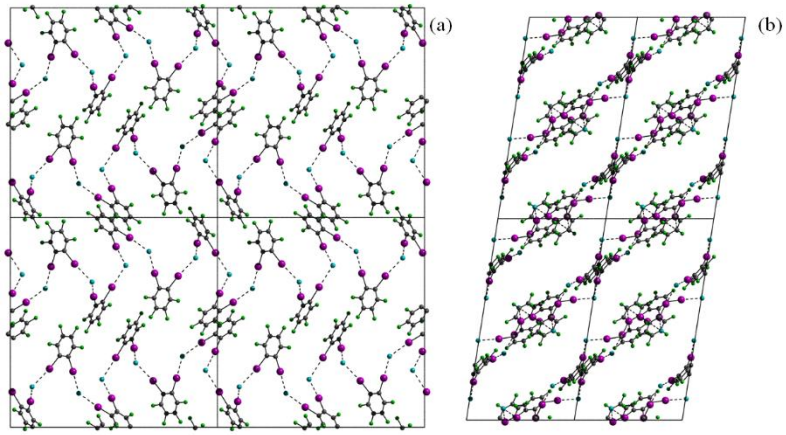

Figure 4.5 (a) 2 x 2 x 2 super cell of **8** shown along the *a* axis where hydrogen atoms and *n*-Bu_4P^+ cations are not shown for clarity. Along the b axis it is possible to see that the cations form rows between the aromatic *o*-DITFB molecules, in the empty space as seen in (b).

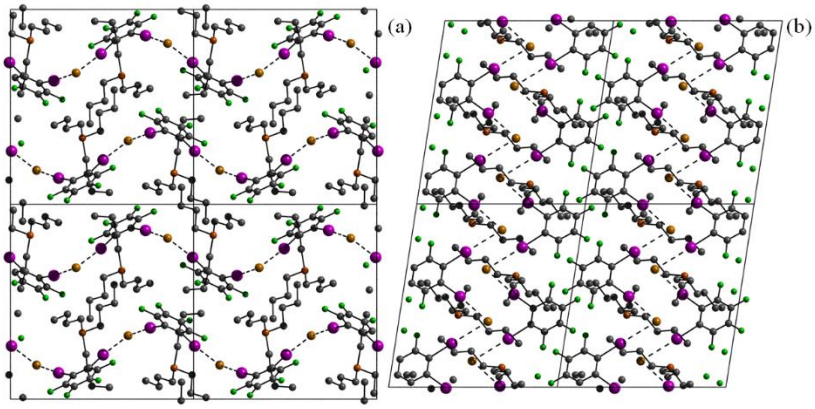

Figure 4.6 (a) 2 x 2 x 2 super cell of **9** shown along the *a* axis. Hydrogen atoms are not shown for clarity. Rows of the polymeric anionic zigzag chains can be observed along the *a* axis, and the *n*-Bu_4P^+ cations are between the rows formed by these chains. (b) View along the *b* axis.

Compound **10** packs in the triclinic crystal system and $P\bar{1}$ space group. Two molecules of *o*-DITFB and two chlorides interact together as shown in Figure 4.2, where two halogen bond donors (I) interact with one halogen bond acceptor (Cl^-), forming a I···Cl^-

···I angle of 120.1°. In the unit cell along the *c* axis, there are two halogen-bonded complexes forming a row. These rows are separated by PPh_4^+ cations associated two-by-two into an inversion-centered phenyl embrace motif (Figure 4.7), as observed for **5** and **7**.[42,40] Dichloromethane molecules crystallize in the unit cell.

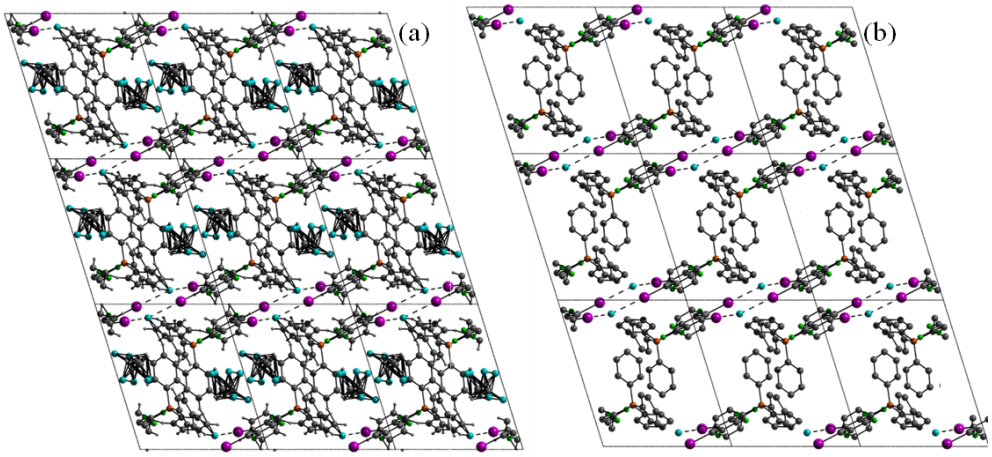

Figure 4.7 (a) 3 x 3 x 3 super cell of compound **10** viewed along the *c* axis. In (b), the disordered DCM molecules and all hydrogen atoms have been removed for clarity.

Finally, in **6** ([(Ph_4PCl)(*p*-DITFB)]) there are two unique chloride sites in the crystal structure with two very different halogen bonding environments and crystal networks. The first chloride site is at the centre of a distorted square planar motif, where four different XB donor molecules interact with a single chloride anion (see Figure 4.2). These form infinite one-dimensional networks along the *c* axis (see Figure 4.8). The second chloride site sits at the centre of a distorted octahedron by interacting with six iodine atoms (Figure 4.2), and forms a secondary intrinsic two-dimensional network (see Figure 4.8). In **6**, when observing both chloride sites, they alternate rows along the *b* axis (Figure 4.8). Looking at

the overall structure along the c axis, the Ph_4P^+ cation forms columns with the halide, which alternates rows with *p*-DITFB molecules.

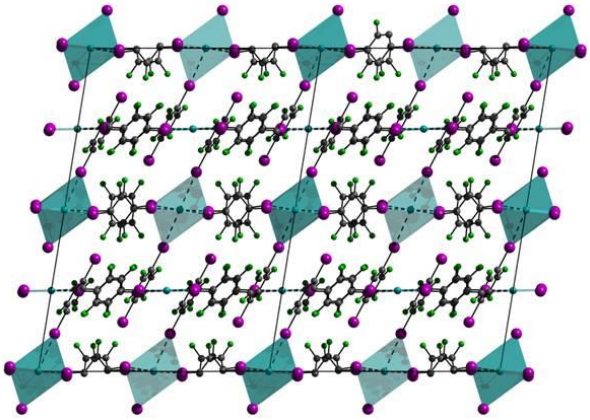

Figure 4.8 Double x cell of **6** shown along the *b* axis (C*2/c* space group). Hydrogen atoms are omitted for clarity.

The C-H hydrogen atoms in the onium counterions are well-removed from the halide ions' coordination sphere in all compounds. Aliphatic CH-chloride contacts typically cluster around 2.39 Å,[45] whereas most of the shortest H-anion distances in the compounds studied here are around 3 Å.

4.3.2 *Solid-State NMR Spectroscopy: Correlation of NMR Data with Local Structure*

4.3.2.1 *^{13}C NMR*

The ^{13}C CPMAS NMR spectra of **6**, **7**, **8**, and **9**, corresponding to the region of the carbons covalently bonded to iodine are shown in Figure 4.9. Analogous spectra of the pure non-halogen-bonded aromatic compounds (*o*-DITFB, *p*-DITFB, *p*-DIB) are also shown. The chemical shifts, which were obtained by simultaneously fitting the spectra at magnetic fields of 9.4 and 21.1 T, are summarized in Table 4.4. The full ^{13}C CPMAS NMR spectra and chemical shift assignments may be found in Appendix B. As previously

described,[40] such spectra are challenging to acquire due to possible relaxation caused by to the directly bonded iodine, nearby fluorines causing dipolar broadening, and distant protons rendering CP inefficient. The use of a 21.1 T spectrometer was essential to resolve some of the chemical shifts observed for the carbons involved in the weak XB interaction. The residual dipolar coupling (RDC) between a spin-½ nucleus such as ^{13}C and a quadrupolar nucleus such as ^{127}I is reduced at higher magnetic fields, as is apparent when the line widths observed at 9.4 T are compared to those measured at 21.1 T (~125 vs ~90 Hz). No splitting or asymmetric broadening attributable to RDC is observed, and spectra at both fields were fit with consistent chemical shift values. A calculation using typical parameters for the ^{127}I-^{13}C dipolar coupling constant (657 Hz) and the ^{127}I quadrupolar coupling constant (1000 MHz) gives a residual dipolar coupling constant of about -1.1 kHz at 21.1 T. A spectral simulation based on these values shows that a fully ^{127}I-coupled ^{13}C multiplet line shape should span about 12 ppm at 21.1 T, suggesting that the ^{13}C line shapes obtained presently are at least partly ^{127}I-self-decoupled.

Table 4.4 Experimental ^{13}C Isotropic Chemical Shifts of Carbons Covalently Bonded to Iodine.

	compound	δ_{iso} (^{13}C) / ppm[a]
	o-$C_6F_4I_2$	92.6(1.3)
	p-$C_6H_4I_2$	97.1(2.6)
6[b]	[(Ph_4PCl)(*p*-$C_6F_4I_2$)]	80.2(1.5)
7	[($EtPh_3PBr$)$_2$(*p*-$C_6H_4I_2$)]	99.5(0.5)
8[b]	[(*n*-Bu_4PCl)(*o*-$C_6F_4I_2$)]	102.5(0.3)
		101.4(0.3)
		100.2(0.5)
		97.9(0.2)
9	[(*n*-Bu_4PBr)(*o*-$C_6F_4I_2$)]	98.6(0.4)
		101.4(0.4)

[a]Experimental ^{13}C isotropic chemical shift of the carbon covalently bonded to iodine. In parentheses are the errors, which are equal to the line width at half height. [b]For **8** and **6**, six distinct carbon sites are expected for each, from X-ray crystallography.

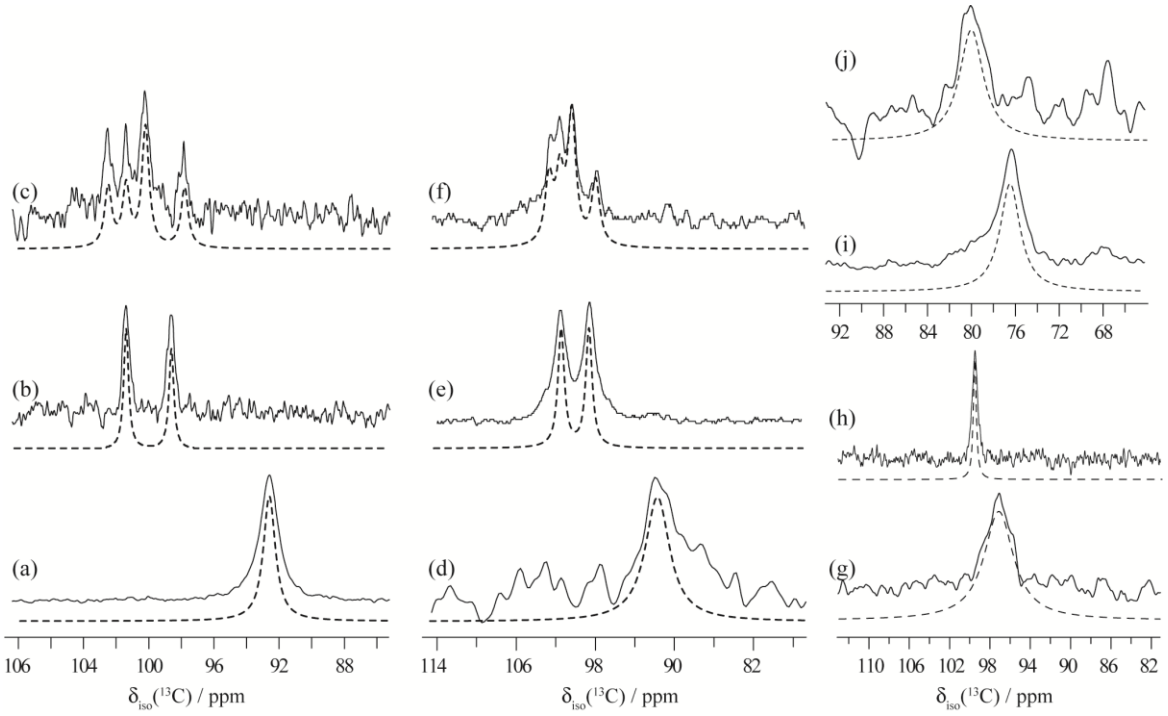

Figure 4.9 Selected regions of the experimental (solid line) and simulated (dashed line) ^{13}C CPMAS SSNMR spectra of (a, d) *o*-DITFB, (b, e) **9,** (c, f) **8** recorded at 21.1 T (left, (a)-(c)) and 9.4 T (middle, (d) – (f)); (g) *p*-DIB, (h) **7,** (i) *p*-DITFB (this spectrum was also shown in ref. 40), and (j) **6**, recorded at 21.1 T (right). In the case of **8**, intensities of the lines in the simulations were adjusted to match the experimental data. This accounts in an ad hoc manner for partial overlap of unresolved resonances and possible small differences in site intensities due to differential cross-polarization efficiencies.

Higher ^{13}C chemical shifts are observed to generally correlate with longer C—I bonds in the halogen-bonded *o*-DITFB compounds. The values of $\delta_{iso}(^{13}C)$ for the C—I carbons in **9** (98.6(0.4) and 101.4(0.4) ppm) and **8** (102.5(0.3), 101.4(0.3), 100.2(0.5), 97.9(0.2) ppm), are all significantly larger than that for pure *o*-DITFB where no XB is present, 92.6(1.3) ppm. This is consistent with the trend noted for halogen-bonded *p*-DITFB

compounds.[40] The substantially lower chemical shift observed for the carbon bonded to iodine compared to the typical chemical shift of carbons in aromatic rings is due to a relativistic spin-orbit-induced heavy atom substituent effect; the magnitude of the relativistic shift is largely due to the magnitude of the spin-orbit splitting of the heavy atom and tends to increase with the valence s orbital character of the observed nucleus.[46] However, a precise correlation between $d_{C—I}$ and $\delta_{iso}(^{13}C)$ values cannot be established for the halogen-bonded *o*-DITFB compounds since for two out of the four compounds studied here, not all the isotropic peaks of the different crystallographically distinct carbons are resolved. In the case of **8**, six non-equivalent carbons are expected from the crystal structure and only four resonances are resolved in the NMR spectra at both fields (Figure 4.9(c,f)).

The ^{13}C resonance of the halogen-bonded complex **7** is more deshielded ($\delta_{iso}(^{13}C)$ = 99.5(0.5) ppm) when compared to pure *p*-DIB (Figure 4.9(g,h)) (97.1(2.6) ppm). In this example, the increase in chemical shift upon halogen bonding may be clearly correlated to an increased carbon iodine distance ($d_{C—I}$ = 2.09635 and 2.1125 Å, for *p*-DIB and **7** respectively) measured from X-ray since only one distinct carbon site is present for both the XB compound and the starting material.

Compound **6** should have a total of six distinct carbon sites which are involved in halogen bonds. In spectra recorded at fields of 9.4 and 21.1 T, only one very broad peak is observed; hence, none of the chemical shifts can be resolved (Figure 4.9(j)). However, it is clear that the carbon isotropic chemical shift of the halogen-bonded complex is deshielded with respect to *p*-DITFB, as was previously observed for **1**, **2**, **3**, **4**, and **5**.[40] This follows the overall trend even though a site-specific correlation with the six different C—I distances cannot be established.

4.3.2.2 $^{79/81}Br$ NMR

Compounds with a bromide anion as halogen bond acceptor have been characterized with $^{79/81}$Br SSNMR at 21.1 T (see Figure 4.10 and 4.11). The bromine NMR parameters summarized in Table 4.5 were obtained by simultaneously simulating the NMR spectra of both bromine isotopes when possible. These spectra span several MHz due to second-order quadrupolar broadening. Incorporating CSA is important in order to obtain the correct simulations of the $^{79/81}$Br spectra. Figure B7 in the Appendix B highlights the mismatch between experimental and simulated spectra when CSA is omitted from the fits. Attempts to acquire these spectra at moderate magnetic fields of 9.4 T or 11.75 T were impractical due to the combined effect of the large breadth of the spectra and because the bromide concentration is quite low for $^{79/81}Br^-$, ranging from 23 mg/cm^3 (**9**) to 64 mg/cm^3 (**7**).

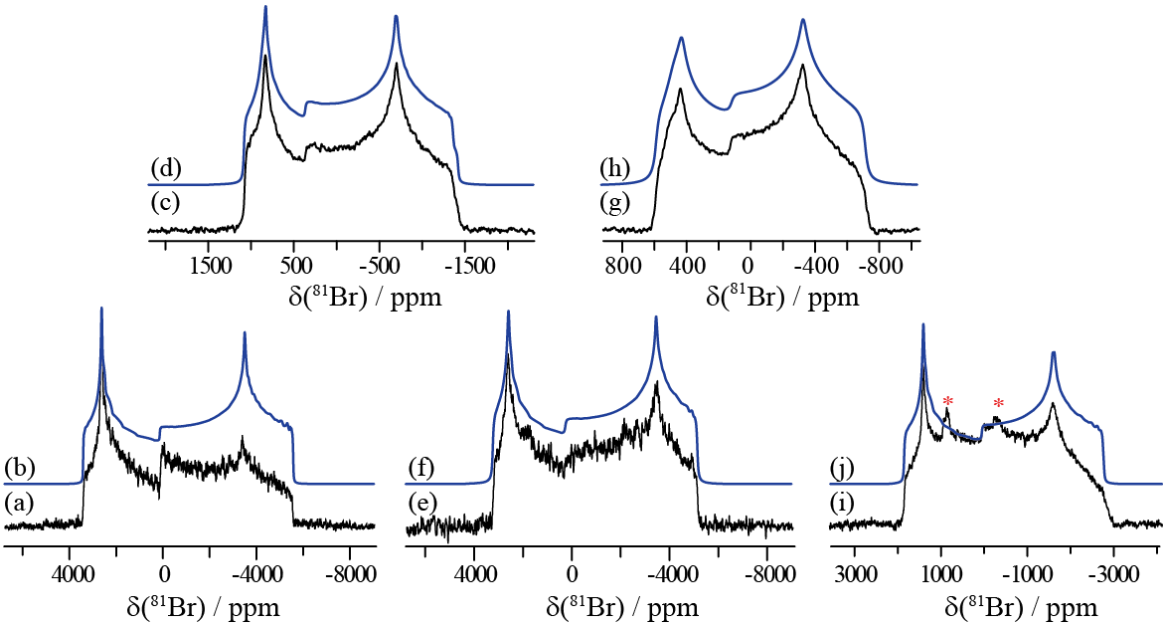

Figure 4.10 ^{81}Br SSNMR spectra of stationary powdered halogen-bonded compounds acquired at 21.1 T. Experimental spectra are shown in (a) **4**, (c) **9**, (e) **3**, (g) **7**, (i) **5**, and their respective simulated spectra are in (b), (d), (f), (h), and (j). Asterisks in (i) mark an impurity.

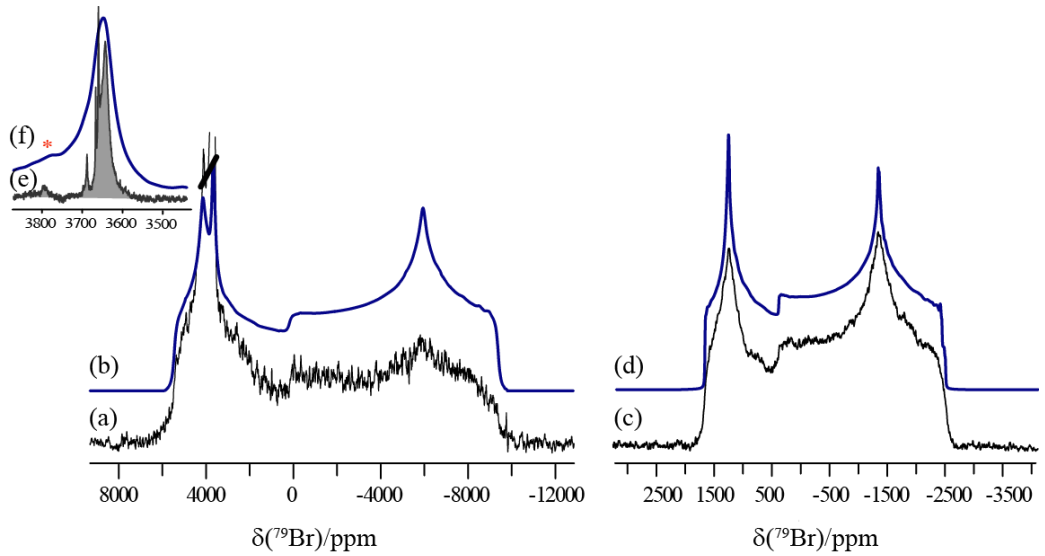

Figure 4.11 ^{79}Br static SSNMR spectra of powdered halogen bonding compounds acquired at B_o = 21.1 T using VOCS methodology and a solid-echo experiment. Experimental spectrum of (a) **4** and (c) **9**, where (b) and (d) show their simulated spectra, respectively. The red dash in (a) indicates the observed ^{13}C peak in the ^{79}Br spectrum. The inset (f) shows the high-frequency discontinuity of the ^{79}Br spectrum of **4**. In (e) is the same region of the ^{79}Br spectrum recorded with a single pulse experiment with proton decoupling, where the carbon peaks are resolved.

The ^{81}Br quadrupolar coupling constants for this series of halogen-bonded compounds vary from 21.5(0.1) MHz for **7** to 58.0(0.2) MHz for **4**. These values are an order of magnitude greater than the values for the pure bromide starting materials, i.e., ammonium or phosphonium bromide salts.[8, 47] Generally, less symmetric electronic environments will correlate with larger C_Q values. They are in the same range (C_Q(^{81}Br) = 12.3 to 45.3 MHz) as the values reported for halogen-bonded haloanilium halides by Attrell *et al.*[15] The ^{81}Br isotropic chemical shifts are within the known range for bromides,[6] ranging from 140(10) ppm to 350(5) ppm, and the CS tensor spans range from less than 50 ppm to 320(20) ppm.

Compounds **4** and **3** are isostructural and feature polymeric anionic chains with $\theta_{I\cdots Br^-\cdots I}$ angles of 139.2° and 140.9°, respectively. Two polymorphs are known for **4**: that

of Metrangolo *et al.*[43] crystallizes in a *C*2/*c* space group whereas our group reported a *Pccn* space group.[40] Compound **3** also packs in the *C*2/*c* space group. These halogen-bonded compounds are characterized by similar ^{81}Br EFG tensor parameters (Table 4.5): $|C_Q(^{81}Br)|$ values of 58.0(0.2) and 57.0(0.2) MHz and η_Q values of 0.22(0.01) and 0.19(0.01) for **4** and **3**, respectively. At higher magnetic field, bromine CSA contributes significantly to the NMR line shapes (Figure 4.10 (a) and (e); the span, Ω, is 255(20) ppm for **4** and 110(10) ppm for **3**; see also Figure B7, Appendix B). The halogen-bonded compound **9** also forms polymeric anionic zigzag chains, but with acute I···Br$^-$···I angles (80.4°) and packs in the $P2_1/c$ space group. Qualitatively, this compound gives a much narrower ^{81}Br NMR line shape which is quantified by a $|C_Q(^{81}Br)|$ value of 30.8(0.1) MHz (Figure 4.10(c)). This value may be related to the local halogen bonding environment (*vide infra*). Bromine CSA parameters for **9** are in between the values reported for **3** and **4**, e.g., a span, Ω, of 192(10) ppm. To improve the precision of the reported quadrupolar and CS tensor parameters, ^{79}Br NMR spectra of compounds **4** and **9** were also acquired and are shown in the Figure 4.11.

Table 4.5 Experimental ^{81}Br EFG and CS Tensor Parameters for Halogen-Bonded Compounds[a]

	$\lvert C_Q(^{81}Br)\rvert$ / MHz[b]	η_Q	δ_{iso} / ppm	Ω / ppm	κ	α / °	β / °	γ / °
3	57.0(0.2)	0.19(0.01)	310(10)	110(10)	0.9(0.3)	0(0)	20(10)	90(0)
4	58.0(0.2)	0.22(0.01)	250(6)	255(20)	1.0(0.2)	0(0)	0(0)	90(20)
5	21.5(0.1)	0.32(0.01)	140(10)	115(15)	-0.9(0.2)	90(2)	0(5)	30(5)
7	40.7(0.1)	0.26(0.01)	210(10)	320(20)	0.9(0.1)	0(20)	5(1)	90(40)
9	30.8(0.1)	0.27(0.01)	256(4)	192(10)	0.0(0.1)	34(4)	82(2)	12(2)

[a] Error bounds are given in parentheses. [b] While C_Q may take any real value, only $|C_Q|$ can be measured from conventional SSNMR experiments.

Two dianionic bromide-containing species, **5** and **7**, are isostructural and pack in the same space group, $P2_1/n$. Their ^{81}Br NMR spectra are shown in Figure 4.10(i, g). As

stated above, compound **7** exhibits a much weaker halogen bond compared to **5**. This difference is reflected in their respective ^{81}Br EFG and CSA parameters. For example, the value of $|C_Q(^{81}Br)|$ for **7**, 21.5(0.1) MHz, is half the value observed for **5**, 40.7(0.1) MHz. The smaller value of C_Q for **7** may be qualitatively rationalized by considering that the bromide anion in this compound is much further removed from the nearby iodine, and its local electronic environment more closely approximates that of an isolated Br^- anion for which the value of C_Q is zero. The asymmetry parameters are similar, with values of 0.26(0.01) and 0.32(0.01) for **5** and **7**, respectively. Also, the more weakly halogen-bonded complex **7** has a smaller bromine chemical shift (140(10) ppm) and span (115(15) ppm) compared to **5** (δ_{iso} = 210(10) ppm and Ω = 320(20)ppm), corroborating the trend reported by Attrell *et al.*[15]

4.3.2.3 $^{35/37}Cl$ SSNMR

Presented in Figures 4.12 and 4.13 are the $^{35/37}$Cl NMR spectra (21.1 T) of the halogen-bonded complexes in which the halogen bond acceptor is a chloride anion. The spectra acquired at 9.4 T for ^{35}Cl and ^{37}Cl using the WURST-QCPMG pulse sequence are also shown in Figures 4.41 and 4.15, respectively. The ^{35}Cl EFG and CS tensor parameters are presented in Table 4.6 and were obtained by simultaneously modeling the NMR spectra of both chlorine isotopes' spectra at two magnetic fields.

Table 4.6 Experimental ^{35}Cl EFG and CS tensor Parameters for Halogen-Bonded Compounds.[a]

	$\lvert C_Q(^{35}Cl)\rvert$ / MHz	η_Q	δ_{iso} / ppm	Ω / ppm	κ	α / °	β / °	γ / °
1	5.43(0.05)	1.00(0.01)	117(3)	94(4)	-0.3(0.2)	0(5)	0(8)	106(4)
2	10.42(0.04)	0.07(0.01)	132(4)	180(15)	0.85(0.10)	35(30)	2(2)	45(20)
6[c] site 1	3.66(0.10)	0.38(0.04)	177(8)	60(15)	-0.4(0.2)	120(20)	106(16)	35(10)
site 2	6.85(0.10)	0.12(0.02)	98(4)	96(10)	0.0(0.2)	0(10)	90(10)	40(10)
8[b] site 1	4.57(0.20)	1.00(0.04)	112(10)	<20	-	-	-	-
site 2	8.22(0.30)	0.12(0.04)	148(20)	<30	-	-	-	-
site 3	7.15(0.05)	0.70(0.04)	135(20)	<50	-	-	-	-
10	6.77(0.20)	0.44(0.04)	94(10)	60(20)	1.00(0.04)		5(4)	

[a] Error bounds are given in parentheses. See also footnotes b and c of Table 3.4. [b] Three crystallographically distinct chlorine sites are determined from the XRD structure. The asymmetry parameter is characteristic of the halogen bonding environment, and each site may be assigned to the corresponding chloride. Details of the assignment are in the main text. No CSA is incorporated in these fits to avoid over-interpretation of the NMR spectrum. [c] Two crystallographically distinct chlorine sites are present in the crystal structure of **6**. The chloride in the pseudo-O_h geometry was assigned as Cl1, as the C_Q is the smaller which is expected for a quadrupolar nucleus in a symmetric environment. The second site has a larger C_Q value, in agreement with its square planar geometry.

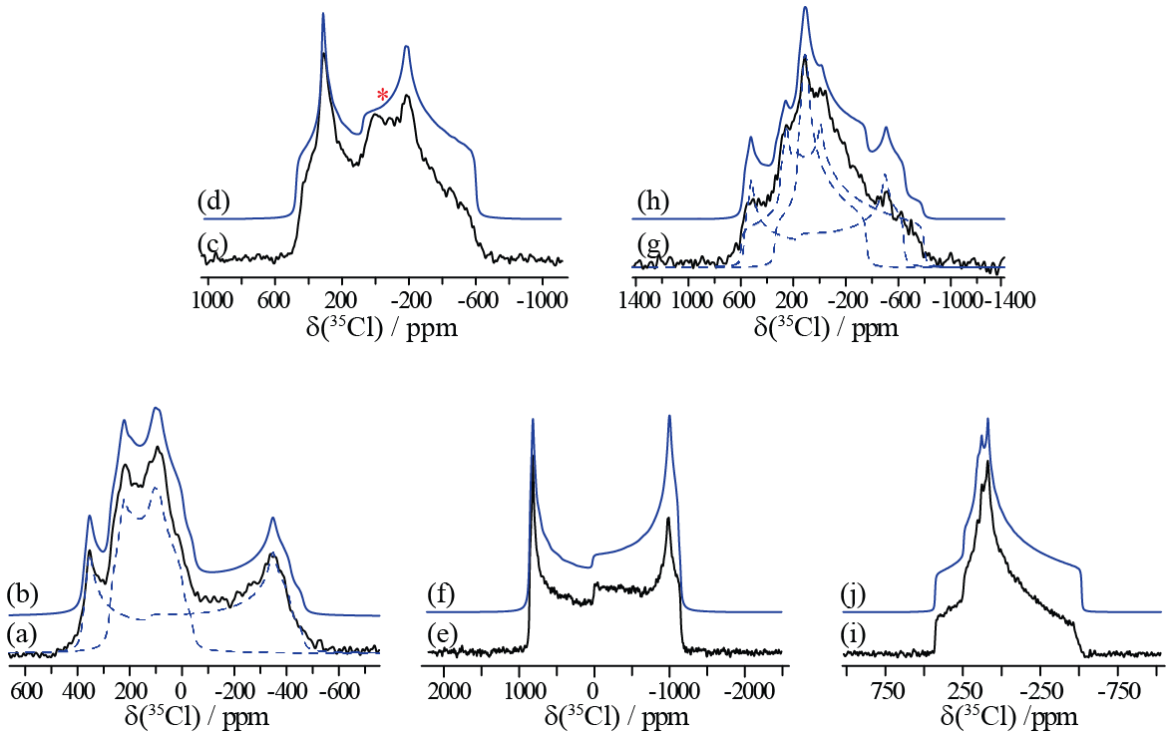

Figure 4.12 ^{35}Cl SSNMR spectra of static powdered halogen-bonded compounds acquired at 21.1 T. Experimental spectra are shown in (a) **6**, (c) **10**, (e) **2**, (g) **8**, (i) **1** and their simulated spectra are in (b), (d), (f), (h), and (j), respectively. Residual Ph_4PCl in (c) is marked by a red asterisk. There are two crystallographically distinct sites in compound **6** (a), and three crystallographically distinct sites in **8** (g); (simulations shown with dashed lines).

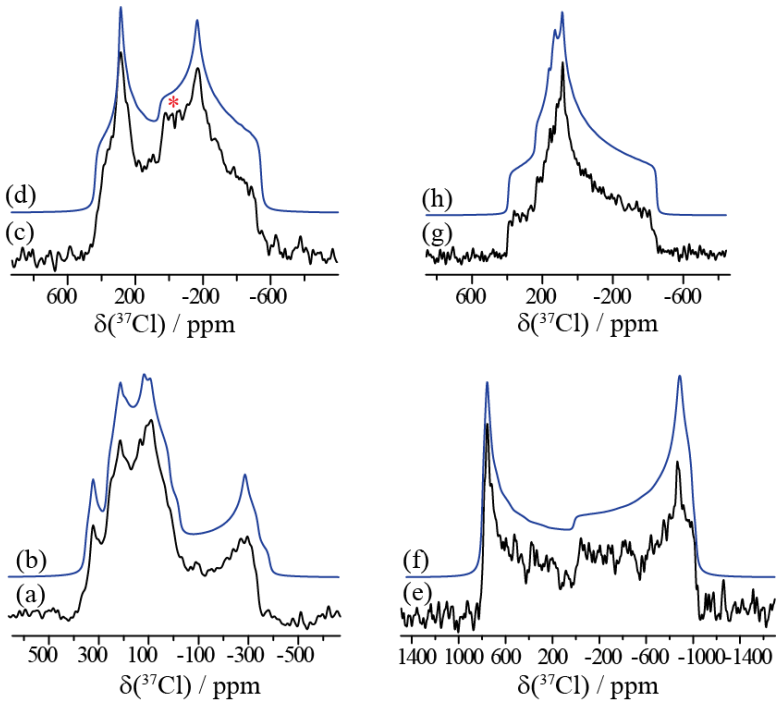

Figure 4.13 ^{37}Cl static SSNMR spectra of powdered halogen bonding compounds acquired at B_0 = 21.1 T using VOCS methodology and a solid-echo experiment. Experimental spectra are shown in (a) **6**, (c) **10**, (e) **2**, (g) **8** and their simulated spectra are in (b), (d), (f), and (h), respectively. Residual Ph_4PCl is marked by an asterisk in (a).

The ^{35}Cl quadrupolar coupling constants range from 3.66(0.10) MHz for **6** to 10.42(0.04) MHz for **2**. The largest of these values is slightly greater than that observed previously[15] for more weakly halogen-bonded compounds. The chloride compounds in this study are moderately strongly halogen-bonded with R_{XB} values ranging from 0.79 to 0.87. The asymmetry parameters vary across the entire range of possible values, from 0.07(0.01) for **2** to 1.00(0.01) for **1**. All spectra of the halogen-bonded complexes were simulated with CSA, where the effect is more prominent at 21.1 T; however, due to the small magnitude of the anisotropies and small overall range in their values, no clear correlation with any structural element is noted. The chlorine isotropic chemical shifts range from 98(4) ppm

for **6** to 148(20) ppm for **8** and the span from 60(15) ppm for **6** to 180(15) ppm for **2,** which are within the known range of values for chloride ions in non-symmetric environments.[6,12,48,49]

The chlorine EFG tensor parameters may be related to the chloride anion halogen bonding environment and to the local electronic structure (*vide infra*). First, consider the spectrum of **6**, where two crystallographically non-equivalent chlorine sites are present, shown in Figure 4.12 (a). From the NMR line shape, the two different sites are clearly differentiated as shown by the spectral deconvolution. It is possible to resolve multiple sites from a spectrum of quadrupolar nuclei as the quadrupolar coupling constant is dependent on the coordination environment. When the coordination environment surrounding the nuclide is spherically symmetric, the C_Q will be null and any divergence from that symmetry will cause an increase in C_Q.[50] In **6**, chlorine site 1 (Cl1) is in a nearly octahedral geometry according to the X-ray crystal structure. This site may be assigned to the narrower ^{35}Cl NMR powder pattern with the smaller $|C_Q(^{35}Cl)|$ value of 3.66(0.10) MHz. The second chlorine site is in a pseudo-square planar geometry and may be assigned to the broader ^{35}Cl line shape characterized by a quadrupolar coupling constant of 6.85(0.10) MHz (this assignment is supported by DFT calculations, *vide infra*).

Compounds **1**, **2**, and **8** have similar halogen bonding environments where one chloride anion interacts with two iodine atoms, thereby forming infinite linear polymeric anionic chains. **1** and **2** have very similar structures and only differ by their cation, either being *n*-Bu_4N^+ or *n*-Bu_4P^+ respectively; they additionally pack in the same space group $P2_1/c$. This change in cation is accompanied by a change in the angle surrounding the halide, $\theta_{I\cdots Cl^-\cdots I}$ = 109.1° for **1** and 155.7° for **2**. This interesting feature in their structures

might explain the very different line shapes observed for these halogen-bonded compounds (see Figure 4.12 (e) and (i)) as will be demonstrated through the NLMO analysis, *vide infra*. The $|C_Q(^{35}Cl)|$ value for **1** (5.43(0.05) MHz) is about half that for **2** (10.42(0.04) MHz). Even more intriguing, the asymmetry parameters takes on two limiting values where in **1** two spectral discontinuities ('horns') collapse with an η_Q value equal to one (1.00(0.01)) and for **2**, two distinct horns may be observed where the asymmetry parameter approaches zero (0.07(0.01)).

Compound **8** exhibits three crystallographically distinct chloride sites in the unit cell. They all have similar halogen bonding environments, where one chloride anion interacts with two halogen bond donors, forming a one-dimensional network (Figure 4.4). However, from the ^{35}Cl NMR spectrum (see Figure 4.12 (g)), it is not directly obvious how to assign the three powder patterns to the three crystallographic sites (*vide infra*).

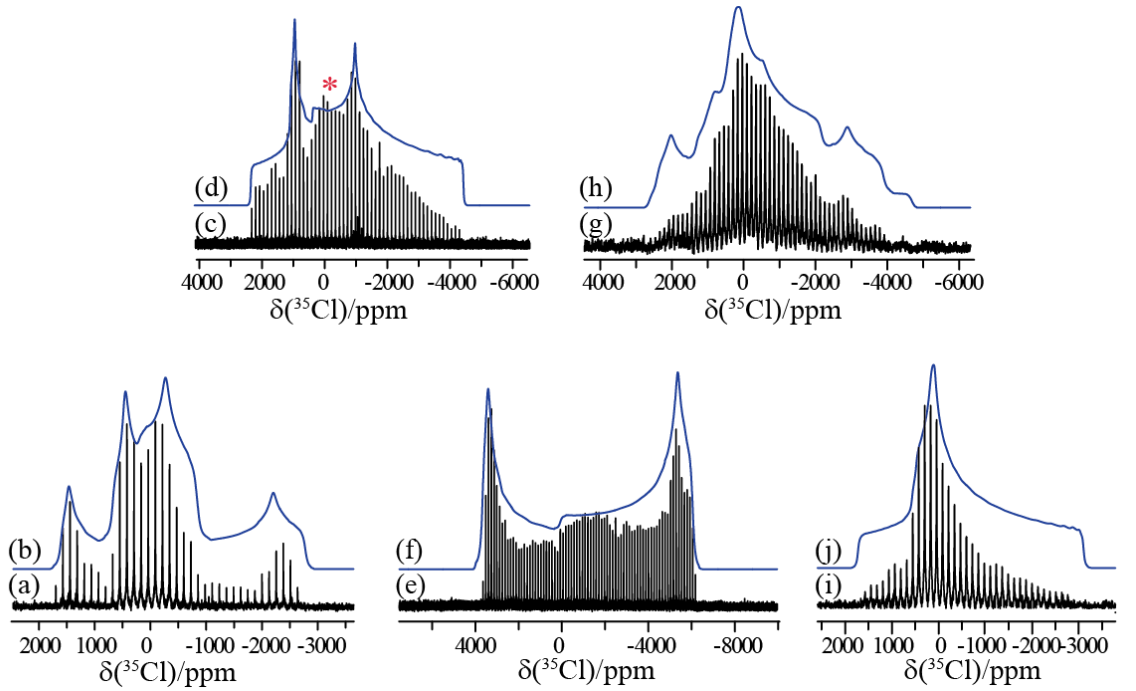

Figure 4.14 ^{35}Cl static SSNMR spectra of powdered halogen bonding compounds acquired at B_0 = 9.4 T using VOCS methodology and a WURST-QCPMG experiment. Experimental spectra: (a) **6**, (c) **10**, (e) **2**, (g) **8**, and (i) **1**. Simulations are shown in (b), (d), (f), (h), and (j), respectively. Residual Ph_4PCl is marked with an asterisk in (c). There are two crystallographically distinct sites in compound **6** and three distinct chlorine sites for compound **8**.

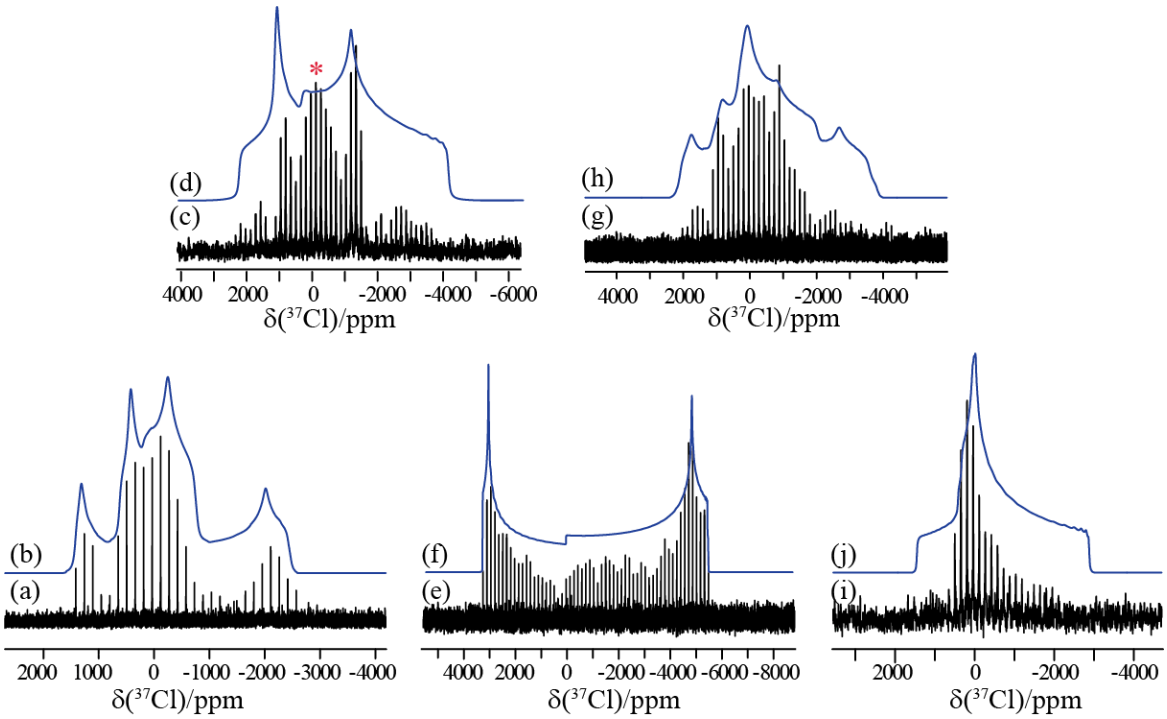

Figure 4.15 ^{37}Cl static SSNMR spectra of powdered halogen bonding compounds acquired at B_0 = 9.4 T using VOCS methodology and a WURST-QCPMG experiment. Experimental spectra: (a) **6**, (c) **10**, (e) **2**, (g) **8**, and (i) **1**. Simulations are shown in (b), (d), (f), (h), and (j), respectively. Residual Ph_4PCl is marked with an asterisk in (c). There are two crystallographically distinct sites in compound **6** and three distinct chlorine sites for compound **8**. Clearly, experimental and simulated line shapes do not show all the same discontinuities due to the low sensitivity of ^{37}Cl particularly at this magnetic field strength.

4.3.3 *Discussion: NLMO Analysis of the Halide Quadrupolar Coupling Tensors in the Context of the Experimental NMR and X-ray Data*

The origins of the quadrupolar interaction at the halide nuclei as a result of the formation of a halogen bond may be intuitively grasped by considering a standard molecular orbital diagram (Figure 4.16(a); after Pinter *et al.*[51]). Interaction of a halide lone pair (represented here by a p orbital) with the σ* orbital of the carbon-iodine bond results in a

halogen bond. It is the polarization of this same p orbital which gives rise to the quadrupolar interaction at the halide nucleus.

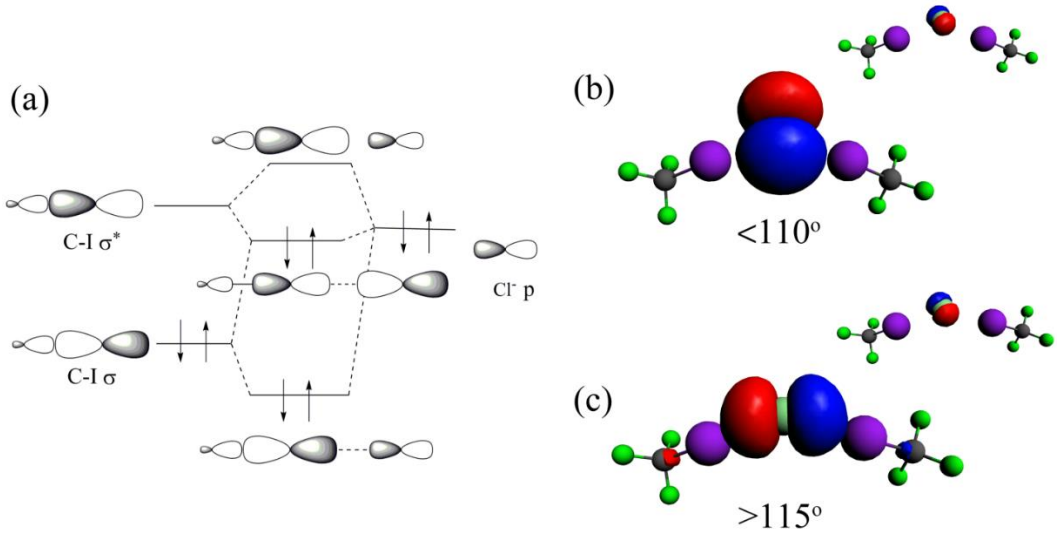

Figure 4.16 Left: (a) Simplified molecular orbital diagram for a halogen bond between a C-I moiety and a chloride ion (after Pinter *et al.*[51]). Right: NLMO contributions to the largest principal component of the ^{35}Cl EFG tensor in a model halogen bonded system ($F_3C—I\cdots Cl^-\cdots I—CF_3$). In (b) the lone pair orbital for chloride is represented for $I\cdots Cl^-\cdots I$ angles less than or equal to 110° and the inset is the representation of the less important core orbital NLMO. In (c) is the chlorine lone pair orbital for $\theta_{I\cdots Cl\cdots I} \geq 115°$ and in the inset the core orbital is presented. The lone pair orbitals dominate the resulting EFG.

While this qualitative picture is useful, ZORA DFT computations were carried out to provide more theoretically rigorous insight into the relationship between the halogen bond acceptors' local environment and the observed NMR parameters. The calculations are used to analyze the contributions of key molecular orbitals to the halide EFG tensors, through an NLMO analysis.[17,18,19] The theoretical basis of this analysis has been described and applied by Autschbach *et al.*[17] One of this method's advantages is that it provides

interpretation of the NMR parameters in terms of orbitals which are familiar to chemists (e.g., lone pairs, bonding orbitals, and core functions). Here, a model comprised of two molecules of iodotrifluoromethane halogen-bonded with a chloride anion, where the I···Cl^-···I angle was varied between 85 and 180° in 5° increments, was employed. The calculated value of V_{33} was chosen for more in-depth analysis as it determines the value of the chlorine quadrupolar coupling constant. The major NLMO contributions to $V_{33}(^{35}Cl)$ as core and lone-pair orbitals are presented in the Appendix B.

Plotted in Figure 4.18(a) are the calculated ^{35}Cl principal components of the EFG tensor as a function of the I···Cl^-···I angle. A change in sign of the principal components, V_{11} and V_{33}, is evident for angles exceeding the tetrahedral angle of about 110°. From the calculations it is possible to determine the orientation of the EFG tensor, which has been plotted in Figure 4.17 for three I···Cl^-···I angles of interest: 110, 115, and 180 degrees. At $\theta_{I\cdots Cl^-\cdots I} = 110°$, the eigenvector corresponding to V_{33} lies in the I···Cl^-···I plane and bisects the $\theta_{I\cdots Cl^-\cdots I}$ angle. Around 115°, the eigenvector reorients to lie close to the I···Cl^- internuclear vector, and finally at 180° it is completely aligned with the I···Cl^-···I axis.

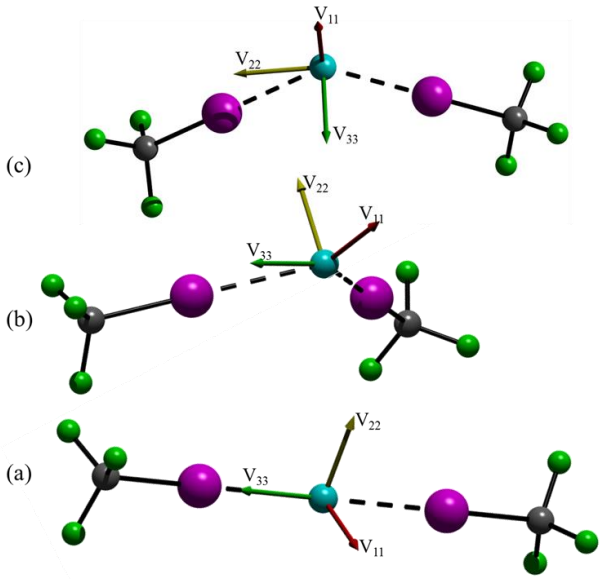

Figure 4.17 The ^{35}Cl EFG tensor orientations in a model halogen bonded system (CF_3—I···Cl^-···I—CF_3) at different angles: (a) 180° , (b) 115° and (c) 110° respectively. The chlorine, iodine, carbon, and fluorine atoms are represented in blue, purple, gray, and green respectively.

When the NLMO contributions to V_{33} are examined, two main types of MOs centred on the chloride anion dominate: core orbitals and lone pair orbitals. From the plot shown in Figure 4.18(b), one can see that the contributions from the sum of the chloride core orbitals are minor (black line) and do not vary significantly between 80 and 180°. The same can be observed qualitatively from a plot of these core orbitals (Figure 4.16). Conversely, the contributions to V_{33} from the sum of the chloride ion lone pair NLMOs are more important: the same change in sign is observed between the angles 110 and 115° as for V_{33} (black squares). Additional details as well as each contributing lone pair orbital have been tabulated and plotted in the Appendix B. Examination of the lone pair NLMO which largely determines the value of V_{33} in Figure 4.16(b, c) reveals that the main contributing orbital changes at ~115°. At 115° and for larger angles, the principal axis of the orbital is aligned

with the iodine atom; this corresponds to the localized orbital which is responsible for the halogen bond. To put this in the context of more familiar orbital types, consider again the MO diagram in Figure 4.16(a) which depicts explicitly the chloride p-orbital involved in the halogen bond. This p-orbital may be readily identified with the p-type NLMO resulting from our DFT calculations and shown in Figure 4.16(c), thus providing an intuitive understanding of the connection between the simple MO diagram, the NLMO analysis, and the resulting NMR parameters.

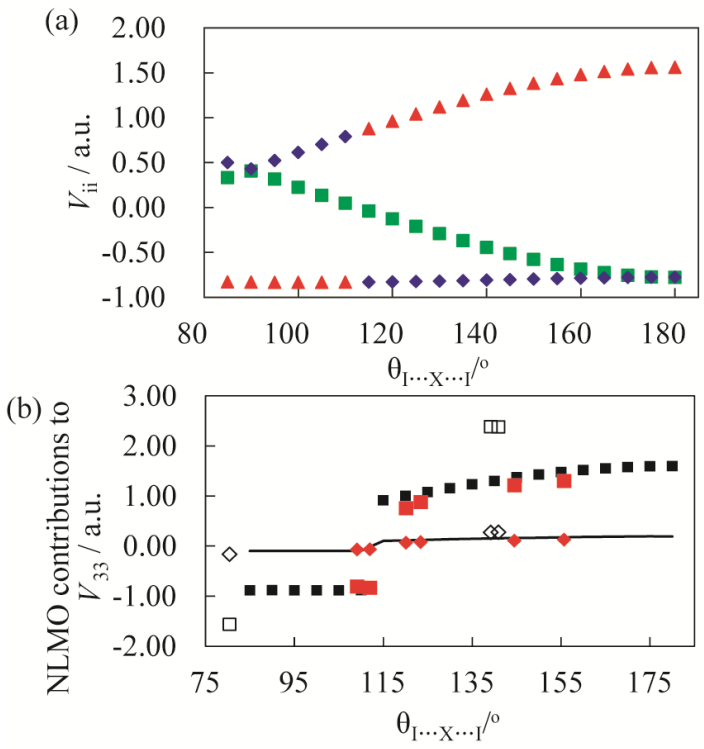

Figure 4.18 (a) Plot of the calculated EFG tensor components (where V_{33} are the red triangles, V_{22} are the green squares and V_{11} are the blue diamonds, with $V_{33} \geq V_{22} \geq V_{11}$) for ^{35}Cl in a F_3C—I···Cl^-···I—CF_3 model system where the I···Cl^-···I angle is varied. In (b) the NLMO contributions to the largest principal component V_{33} are plotted as a function of $\theta_{I\cdots Cl^-\cdots I}$ where the solid black squares represent the contributions from the chlorine lone pair orbitals and the black line represents the contributions from the chlorine core orbitals. Overlaid on this plot are the values of the calculated contributions for the experimental halogen-bonded complexes (values from Table 4.7). In red are data for the chloride compounds (squares: lone pair NLMOs; diamonds: core NLMOs), showing excellent agreement with the data for the model system. The corresponding data for the bromide compounds are shown as empty squares and diamonds; as expected, the values are larger than those for chloride due to differences in geometry, unit cell volume, and Sternheimer antishielding factor.

Additionally, when the I···Cl^-···I angle approaches linearity there is an increase in the contribution from the sum of the chloride lone pair orbitals to V_{33}, since there is a greater degree of halogen bonding which further distorts this 'p' orbital. Hence, the main

contribution from the chloride lone pair orbital after 115° is proposed to be the orbital that dictates the value of the chlorine quadrupolar coupling constant, the orbital may also be visualized as participating in electron donation to the σ-hole characteristic of the halogen bond. In the limit of an idealized model system, this interpretation of the value of C_Q can thus be taken as a measure of the halogen bonding interaction.

To validate the above hypothesis, the same NLMO analysis of V_{33} was conducted for each of the halogen-bonded complexes studied experimentally (**4**, **3**, **9** for bromide and **1**, **2**, **8**, **10** for chloride; see Table 4.7). When the halogen-bonded environment is comprised of two XB donors (iodine) interacting with a halide (I···X$^-$···I motif), the same contributions are observed from the core and lone pair orbitals for the halide as were observed for the model system discussed above. Examination of the results plotted in Figure 4.18(b) shows that the calculated contributions for the halogen-bonded compounds follow the same trend for chloride (red) and bromide (black outline; the values are larger for this nuclide), and also follow the general trend established for the iodotrifluoromethane model. A change in sign is observed around 110 to 115° from the contributing lone pair orbitals (squares) to V_{33} and a linear trend is observed for the contribution of the core orbital (diamonds) to V_{33}. The two dianionic species **5** and **7** have additional minor contributions from iodine lone pair orbitals to V_{33}. Compound **6** has a different geometry. Its main contribution to V_{33} is from the chloride core and lone pair orbitals. The octahedral site in **6** also has a very minor contribution from the iodine lone pair.

Table 4.7 Analysis of Calculated Chlorine EFG Tensor NLMO Contributions to the Largest Principal Component (V_{33}) in Halogen-Bonded Compounds.

compound		core (Cl^-)	lone pair (Cl^-)	lone pair (I)[a]	Sum[b]	V_{33}
1		-0.070	-0.809		-0.879	-0.831
2		0.128	1.301		1.429	1.337
3		0.277	2.381		2.658	2.452
4		0.271	2.383		2.654	2.456
5		0.247	2.127	-0.106	2.268	2.165
6	site 1	0.029	0.262	-0.042	0.249	0.245
	site 2	-0.098	-0.999		-1.097	-0.968
7		0.116	0.876	-0.074	0.918	0.840
8	site 1	-0.068	-0.832		-0.900	-0.848
	site 2	0.108	1.215		1.323	1.246
	site 3	0.079	0.882		0.961	0.898
9		-0.165	-1.567		-1.732	-1.581
10		0.067	0.757	-0.035	0.789	0.764

[a] Blank lines indicate that contributions are less than 5% of the sum. [b] Sum of 'core' and 'sum(LP)'. Values obtained in this way differ from the total calculated V_{33} (final column) because not all of the contributions are printed.

Finally, similar plots were prepared for the experimental values of V_{33} as a function of the I···X^-···I angle determined from X-ray crystallography for the halogen-bonded complexes in this study (Figure 4.19(b)). Satisfyingly, when the I···X^-···I angle increases, the largest principal component of the halide EFG tensor also increases. This is in agreement with the computational study discussed above. The calculated asymmetry parameters are plotted as a function of the I···X^-···I angle extracted from the NLMO EFG tensor study in Figure 4.19(a). The plot forms a bell shape over the range 80° to 180°. Overlaid on the same plot are the experimental values of the asymmetry parameters of the halogen-bonded complexes as a function of their experimentally determined I···X^-···I angles. Data for the chloride and bromide compounds both follow the predicted trend.

From this conclusions can be drawn: the experimentally observed asymmetry parameters are largely determined by the I···X$^-$···I angles, as suggested by ZORA DFT.

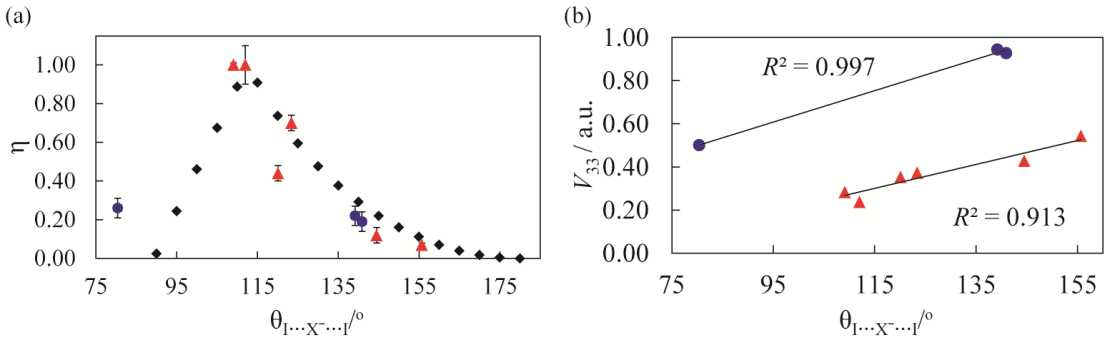

Figure 4.19 (a) Plot of quadrupolar asymmetry parameter versus I···Cl$^-$···I angle. The black diamonds represent the calculated values for ^{35}Cl in a F_3C—I···Cl$^-$···I—CF_3 model system. The red triangles and blue circles represent the experimental values for ^{35}Cl and ^{81}Br, respectively. (b) Plot of experimentally determined values of the largest component of the EFG tensor for ^{35}Cl (red triangles) and ^{81}Br (blue circles) versus the value of the I···Cl$^-$···I angle for compounds where two iodines interact with one halide anion. Solid lines show the best linear fit; $V_{33}(^{81}\text{Br}) = 0.0073(\theta_{\text{I}\cdots\text{Br}^-\cdots\text{I}}) - 0.0084$ and $V_{33}(^{35}\text{Cl}) = 0.0056(\theta_{\text{I}\cdots\text{Cl}^-\cdots\text{I}}) - 0.3383$.

A simple picture explaining the reasons behind this may be gleaned from a re-inspection of the data in Figure 4.16 and 4.17. When the I···X$^-$···I angle is zero, the asymmetry parameter is zero due to the cylindrical I···X$^-$···I symmetry, with the largest, unique EFG tensor component (V_{33}) oriented along the symmetry axis of the two halogen bonds. The chloride p orbital is oriented along this same axis and contributes to the electric field gradient in that direction. Similarly, when the I···X$^-$···I angle is 90° (the other limiting case), the V_{33} component lies perpendicular to the plane containing those three atoms, and the remaining components lying in the plane (V_{11} and V_{22}) are equal due to symmetry, resulting again in an asymmetry parameter of zero. For all intermediate angles, the values of V_{11} and V_{22} will not be equal due to the lower symmetry of the molecule, and the resulting

asymmetry parameter will be non-zero. The asymmetry parameter reaches a maximum value of unity when the I···X$^-$···I angle is near the tetrahedral angle and the EFG tensor component V_{22} lies close to one of the iodine-chloride internuclear vectors (Figure 4.17).

Once this dependence on the local structure surrounding the halide was understood it was possible to successfully simulate the ^{35}Cl NMR spectrum for compound **8**, [(n-Bu$_4$PCl)(*o*-DITFB)], where three distinct chloride ion sites are present. The I···Cl$^-$···I angles allowed for a good prediction of the asymmetry parameters for the three sites. For chloride site 1 $\theta_{I\cdots Cl^-\cdots I}$ = 112.0° the η_Q is 0.94(0.02), whereas the second chloride site has a much larger angle ($\theta_{I\cdots Cl^-\cdots I}$ = 144.5°) and the value of η_Q is 0.14(0.04). The third chloride site has an I···Cl$^-$···I angle in between those for the two other sites (123.4°) and η_Q is 0.72(0.10). This is a satisfying example of how the halogen bonding environment surrounding the halide is manifested in the NMR parameters, and highlights the advantages of a combined experimental-theoretical approach to evaluate the NMR parameters when there are multiple non-equivalent sites in the sample of interest where site assignment may be ambiguous. In addition to the fundamental insights provided by this analysis, value also lies in the extension of the spectroscopic and computational methods employed herein to characterize halogen-bonded complexes where diffraction methods may not be amenable.

Given the clear-cut dependence of the halide quadrupolar asymmetry parameter on the I···Cl$^-$···I angle in halogen-bonded systems, it is of interest to compare this result to similar findings available for hydrogen bonds. The ^{2}H asymmetry parameters for deuterons in hydrogen bonds are known to deviate somewhat from zero for non-linear geometries,[52] but the dependence on structure can be complicated.[53] However, deuterons are electron acceptors in hydrogen bonds, whereas halide ions in halogen bonds are electron donors. A

more apposite discussion is then of ^{17}O quadrupolar asymmetry parameters in hydrogen bonds of the form –N-H ⋯ O=C, where the oxygen acts as the electron donor. Wu and co-workers have demonstrated that $\eta(^{17}O)$ decreases as $r_{N\cdots O}$ increases in hydrogen-bonded amides.[54] They have also shown that $\eta(^{17}O)$ correlates with the hydrogen bond strength in a series of nucleic acid bases.[55] The full bell-shaped dependence noted presently for the halide quadrupolar asymmetry parameter is not seen for typical hydrogen bonds, likely simply due to constraints on possible hydrogen bond geometries relative to what is seen for halogen bonds. Interestingly, however, Smith and co-workers reported[56] that computed ^{17}O EFG tensor orientations change with the strength of the hydrogen bond, analogously to what has been noted for halogen bonds in this work (Figure 4.17).

Additional computations resulted in the NMR parameters for ^{13}C, $^{35/37}Cl$, and $^{79/81}Br$ of the XB compounds studied experimentally. The calculated NMR parameters are summarized in Table 4.8 and 4.9 for chlorine and bromine, respectively. The models used consist of the simple halogen bonding environment surrounding the halide (see Figure 4.2).

Table 4.8 Calculated ^{35}Cl EFG and CS Tensor Parameters for Halogen-Bonded Compounds[a]

	C_Q(^{35}Cl) / MHz	η_Q	δ_{iso} / ppm[c]	Ω / ppm	κ	α / °	β / °	γ / °
1	15.76	0.69	233	313	0.03	272	89	357
2	-25.36	0.18	197	480	0.95	37	1	79
6 site 1	-4.67	0.43	186	88	0.01	28	1	79
site 2	18.38	0.02	215	239	-0.99	183	90	3
8 site 1	16.03	0.84	245	406	-0.12	271	90	1
site 2	-23.60	0.23	212	495	0.68	320	1	146
site 3	-17.01	0.83	240	442	0.10	30	2	241
10	-14.42	0.63	106	198	0.82	280	1	79

[a] Relativistic scalar ZORA calculation using the revPBE exchange-correlation functional and the all electron basis set: ZORA/TZP. [b]A simple formula relates the shielding component to the chemical shift (CS, $\delta_{ij} = \frac{\sigma_{ref}-\sigma_{ij}}{1-\sigma_{ref}}$) component when a suitable shielding reference exists, σ_{ref} = 974 ppm in the case of chlorine. [57] To properly compare the calculated and experimental δ_{iso} values, the concentration of 0.1 M NaCl in D_2O, which is negligible [58] and the significant isotope shift of ~5 ppm due to D_2O must be account for.[59]

Table 4.9 Calculated ^{81}Br EFG and MS Tensor Parameters for Halogen-Bonded Compounds[a]

	$\lvert C_Q(^{81}Br)\rvert$ / MHz	η_Q	σ_{iso} / ppm	Ω / ppm	κ	α / °	β / °	γ / °
3	149.88	0.32	2397.5	889	0.70	161	3	294
4	145.96	0.34	2433.8	870	0.65	158	2	293
5	132.18	0.04	2520.9	1031	0.93	151	1	210
7	51.26	0.01	2997.1	410	0.95	76	4	292
9	-96.16	0.19	2368.9	492	-0.63	61	86	180

[a] Relativistic scalar ZORA calculation using the revPBE exchange-correlation functional and the all-electron basis set: ZORA/TZP.

The ^{13}C chemical shifts are overestimated by the calculations, consistent with our previous report on *p*-DITFB complexes (see Appendix B for full ^{13}C resonance assignments).[40] Nevertheless, in cases where distinct carbon resonances were observed experimentally, assignments to particular crystallographic sites were possible on the basis

of differences in the carbon-iodine bond lengths. The calculations similarly overestimate the halide quadrupolar coupling parameters and show correlations of varying quality (Figure 4.20). Multiple reasons may explain this inability to reproduce the experimental values precisely. For one, DFT calculations are performed in the gas phase and use a simple cluster model whereas the compounds of interest crystallize in the solid state. A full treatment of the effect of the ions in the crystal lattice on the computed NMR parameters is possible with the gauge-including projector-augmented wave (GIPAW) DFT method[60] for calculations using periodic boundary conditions; however, for the present work many of the unit cells are too large for us to carry out such computations. Furthermore, I was interested in the NLMO analysis offered with the ZORA DFT method. The inclusion of relativistic effects via ZORA is important for computing the ^{13}C magnetic shielding tensors for carbon atoms bonded to iodine. Our calculations are carried out at 0 K while the X-ray and NMR data are acquired at higher temperatures. This may also contribute to the discrepancies between the experimental and calculated values shown in Figure 4.20.

Since there is no single generally available computational approach at present which will simultaneously properly account for all of the above-mentioned issues, compromises were made in choosing the best approach to address the problem at hand. The priorities for this study ((i) the ability to carry out an NLMO analysis to gain insight into the relationship between the halogen bond and the NMR observables and (ii) a proper consideration of relativistic effects on the NMR parameters) meant that the ZORA DFT method offered the best compromise.

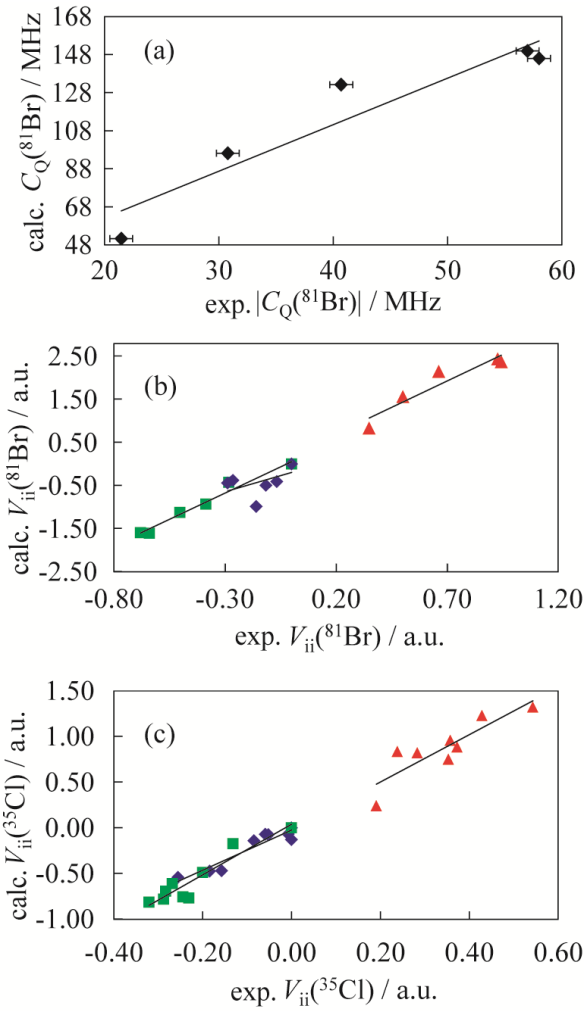

Figure 4.20 Plots of calculated versus experimental EFG tensors for bromine (a, b) and chlorine (c). The principal components V_{33}, V_{22}, and V_{11} are represented by the red triangles, green squares, and blue diamonds, respectively. Solid lines represent the best linear fit: (a) C_Q(calc.) = 2.4446 C_Q(exp.) + 13.423, R^2 = 0.8933 (b) calc.(V_{11}) = 1.4926exp.(V_{11}) – 0.1952, R^2 = 2.2722, calc.(V_{22}) = 2.413exp.(V_{22}) – 0.0548, R^2 = 0.9765, calc.(V_{33}) = 2.4446exp.(V_{33}) – 0.2185, R^2 = 0.8955; (c) calc.(V_{11}) = 2.1957exp.(V_{11}) – 0.0235, R^2 = 0.8826, calc.(V_{22}) = 2.7712exp.(V_{22}) – 0.041, R^2 = 0.8826, calc.(V_{33}) = 2.5907exp.(V_{33}) – 0.0148, R^2 = 0.7080.

4.4 CONCLUSIONS

A multifaceted study of halogen bonds has been presented. New halogen-bonded compounds without competing hydrogen bonds were prepared and characterized with X-ray crystallography and multinuclear magnetic resonance spectroscopy (^{13}C, $^{35/37}$Cl, $^{79/81}$Br). These iodobenzene-onium halide co-crystals exhibit C-I$\cdots$X$^-$ distances and angles which allow them to be classified as moderately strong halogen-bonded compounds as quantified by their reduced distance parameters, $R_{XB,}$ of 0.79 to 0.91. The main conclusions of this study are as follows:

- From ^{13}C CPMAS SSNMR, an increase in the chemical shift is observed for the *ipso* C—I carbon of the halogen *o*-diiodotetrafluorobenzene bonded complexes when compared to the starting materials; ^{13}C chemical shifts are therefore diagnostic of the strength of the halogen bond.
- From halogen SSNMR studies of a larger series of co-crystals, the NMR parameters of chloride and bromide anions were correlated to the local halogen bonding environment. For example, octahedral and square planar chloride ion coordination environments are clearly differentiated on the basis of their ^{35}Cl nuclear quadrupolar coupling constant. For C-I$\cdots$X$^-\cdots$I-C systems, the value of the halogen quadrupolar coupling constant correlates with the strength of the halogen bond.
- A NLMO DFT study afforded further chemical insight into the relationship between the quadrupolar NMR parameters of the halide ions, their local halogen bond environment, and an intuitive molecular orbital picture. The value of the quadrupolar coupling constant and the quadrupolar asymmetry parameter were found to be well correlated with the I$\cdots$X$^-\cdots$I angle. Furthermore, this dependence

could be explained, via both an NLMO analysis and a simple canonical MO picture, as arising largely from the contribution of a lone pair-type orbital centered on the halide ion. The experimental asymmetry parameters follow the DFT trend and are highly correlated to the $I\cdots X^{-}\cdots I$ angle.

- The correlations noted between the halide quadrupolar coupling parameters and the local halogen bond geometry are in qualitative agreement with the limited corresponding data available for the comparable electron donors in hydrogen bonds (i.e., ^{17}O quadrupolar parameters for oxygen); however the data for halogen bonds cover a broader range of geometries.

Overall, this work contributes to a chemically intuitive understanding of the connection between the geometry and electronic structure of halogen bonds and various NMR parameters with the aid of NLMO analysis. The experimental and computational methods employed here, as well as the insights gained, set the stage and hold promise for studying more complex halogen bond environments, such as those found in biomolecules,[61] gels,[83] receptors,[135] MOF-like framework materials,[85] and other systems where diffraction methods may provide an incomplete picture.

4.5 REFERENCES FOR CHAPTER 4

1 G. R. Desiraju, P. S. Ho, L. Kloo, A. C. Legon, R. Marquardt, P. Metrangolo, P. A. Politzer, G. Resnati, K. Rissanen, (2013), *Pure Appl. Chem.*, 85, 1711.

2 J. F. Bertrán, M. Rodríguez, (1979), *Org. Magn. Reson.*, 12, 92.

3 (a) P. D. Rege, O. L. Malkina, N. S. Goroff (2002), *J. Am. Chem. Soc.*, 124, 370. (b) J. A. Webb, J. E. Klijn, P. A. Hill, J. L. Bennett, N. S. Goroff, (2004), *J. Org. Chem.*, 69, 660.

4 (a) A.-C. C. Carlsson, J. Gräfenstein, A. Budnjo, J. L. Laurila, J. Bergquist, A. Karim, R. Kleinmaier, U. Brath, M. Erdélyi, (2012), *J. Am. Chem. Soc.*, 134, 5706. (b) A.-C. C. Carlsson, M. Uhrbom, A. Karim, U. Brath, J. Gräfenstein, M. Erdélyi, (2013), *CrystEngComm*, 15, 3087.

5 M. Weingarth, N. Raouafi, B. Jouvelet, L. Duma, G. Bodenhausen, K. Boujlel, B. Schöllhorn, P. Tekely, (2008), *Chem. Commun.*, 5981.

6 R. P. Chapman, C. M. Widdifield, D. L. Bryce, (2009), *Prog. Nucl. Magn. Reson. Spectrosc.*, 55, 215.

7 D. L. Bryce, C. M. Widdifield, R. P. Chapman, R. J. Attrell, (2011), *Chlorine, Bromine, and Iodine Solid-State NMR*, R. E. Wasylishen, S. E. Ashbrook, S. Wimperis (Eds.), *NMR of Quadrupolar Nuclei in Solid Materials*, Chichester, UK, John Wiley and Sons.

8 K. M. N. Burgess, I. Korobkov, D. L. Bryce, (2012), *Chem. Eur. J.*, 18, 5748.

9 R. P. Chapman, D. L. Bryce, (2009), *Phys. Chem. Chem. Phys.*, 11, 6987.

10 C. M. Widdifield, D. L. Bryce, (2010), *J. Phys. Chem. A.*, 114, 2102.

11 F. A. Perras, D. L. Bryce, (2012), *Angew. Chem. Int. Ed.*, 124, 4303.

12 H. Hamaed, J. M. Pawlowski, B. F. T. Cooper, R. Fu, S. H. Eichhorn, R. W. Schurko, (2008), *J. Am. Chem. Soc.*, 130, 11056.

13 B. Alonso, T. Mineva, P. Innocenzi, G. Trimmel, K. Stubenrauch, I. Melnyk, Y. Zub, F Fayon, P. Florian, D. C. R. Massiot, (2010), *Chimie*, 13, 431.

14 C. M. Widdifield, G. Cavallo, G. A. Facey, T. Pilati, J. Lin, P. Metrangolo, G. Resnati, D. L. Bryce, (2013), *Chem. Eur. J.*, 19, 11949.

15 R. J. Attrell, C. M. Widdifield, I. Korobkov, D. L. Bryce, (2012), *Cryst. Growth Des.*, 12, 1641.

16 R. W. Troff, T. Mäkelä, F. Topić, A. Valkonen, K. Raatikainen, K. Rissanen, K. (2013), *Eur. J. Org. Chem.*, 1617.

17 J. Autschbach, S. Zheng, R. W. Schurko, (2010), *Concepts Magn. Reson. Part A*, 36, 84.

18 L. A. O'Dell, R. W. Schurko, K. J. Harris, J. Autschbach, C. I. Ratcliffe, (2011), *J. Am. Chem. Soc.*, 133, 527.

19 A. J. Rossini, R. W. Mills, G. A. Briscoe, E. L. Norton, S. J. Geier, I. Hung, S. Zheng, J. Autschbach, R. W Schurko, (2009), *J. Am. Chem. Soc.*, 131, 3317.

20 APEX Software Suite v.2010, (2005), Madison, WI, Bruker AXS.

21 R. Blessing, (1995), *Acta Crystallogr., Sect. A: Found. Crystallogr.*, 51, 33-38.

22 G. M. Sheldrick, (2008), *Acta Crystallogr., Sect. A: Found. Crystallogr.*, 64, 112-122.

23 (a) G. Metz, X. Wu, S. O. Smith, (1994), *J. Magn. Reson. Series A*, 110, 219. (b) J. Schaefer, E. O. Stejskal, (1976), *J. Am. Chem. Soc.*, 98, 1031.

24 B. M. Fung, A. K. Khitrin, K. Ermolaev, (2000), *J. Magn. Reson.*, 142, 97.

25 L. A. O'Dell, R. W. Schurko, (2008), *Chem. Phys. Lett.*, 464, 97.

26 D. Massiot, I. Farnan, N. Gautier, D. Trumeau, A. Trokiner, J. P. Coutures, (1995), *Solid State Nucl. Magn. Reson.*, 4, 241.

27 (a) I. Solomon, (1958), *Phys. Rev.* 110, 61. (b) I. D. Weisman, L. H. Bennett, (1969), *Phys. Rev.*, 181, 1341. (c) P. R. Bodart, J. –P. Amoureaux, Y. Dumazy, R. Lefort, (2000), *Mol. Phys.*, 98, 1545.

28 K. Eichele, R. E. Wasylishen, (2001), *WSOLIDS1 NMR Simulation Package* version 1.20.15, Tübingen, Germany Universitat Tübingen.

29 D. Massiot, F. Fayon, M. Capron, I. King, S. Le Calvé, B. Alonso, J. –O. Durand, B. Bujoli, Z. Gan, G. Hoatson, G. (2002), *Magn. Reson. Chem.*, 40, 70.

30 M. J. Frisch, G. W Trucks, H. B. Schlegel, G. E. Scuseria, M. A. Robb, J. R. Cheeseman, G Scalmani, V. Barone, B. Mennucci, G. A. Petersson, H. Nakatsuji, M. Caricato, X. Li, H. P. Hratchian, A. F. Izmaylov, J. Bloino, G. Zheng, J. L. Sonnenberg, M. Hada, M Ehara, K. Toyota, R. Fukuda, J. Hasegawa, M. Ishida, T. Nakajima, Y. Honda, O. Kitao, H. Nakai, T. Vreven, J. A. Jr. Montgomery, J. E. Peralta, F. Ogliaro, M. Bearpark, J. Heyd, E. Brothers, K. N. Kudin, V. N. Staroverov, R. Kobayashi, J. Normand, K. Raghavachari, A. Rendell, J. C. Burant, S. S. Iyengar, J. Tomasi, M. Cossi, N. Rega, N. J. Millam, M. Klene, J. E. Knox, J. B. Cross, V. Bakken, C, Adamo, J. Jaramillo, R. Gomperts, R. E. Stratmann, O. Yazyev, A. J. Austin, R. Cammi, C. Pomelli, J. W. Ochterski, R. L. Martin, K. Morokuma, V. G. Zakrzewski, G. A. Voth, P. Salvador, J. J. Dannenberg, S. Dapprich, A. D. Daniels, Farkas,

J. B. Foresman, J. V. Ortiz, J. Cioslowski, D. J. Fox, (2009), *Gaussian 09*, Revision A.02, Wallingford, CT, Gaussian Inc.

31 Y. Zhang, W. Yang, (1998), *Phys. Rev. Lett.*, 80, 890.

32 D. P. Chong, (2005), *Mol. Phys.*, 103, 749.

33 E. van Lenthe, E. J. J. Baerends, (2003), *J. Comput. Chem.*, 24, 1142.

34 S. Adiga, D. Aebi, D. L. Bryce, (2007), *Can. J. Chem.*, 85, 496.

35 A. K. Jameson, C. J. Jameson, (1987), *Chem. Phys. Lett.*, 134, 461.

36 M. Gee, R. E. Wasylishen, A. Laaksonen, (1999), *J. Phys. Chem. A*, 103, 10805.

37 C. Deverell, R. E. Richards, (1969), *Mol. Phys.*, 16, 421.

38 A. Loewenstein, M. Shporer, (1968), *J. Chem. Soc., Chem. Comm.*, 214.

39 (a) K. Raatikainen, K. Rissanen, (2011), *CrystEngComm*, 13, 6972. (b) M. T. Johnson, Z. Džolić, M. Cetina, O. F. Wendt, L. Öhrström, K. Rissanen, (2012), *Cryst. Growth Des.*, 12, 362.

40 J. Viger-Gravel, S. Leclerc, I. Korobkov, D. L. Bryce, (2013), *CrystEngComm*, 15, 3168.

41 T. Clark, M. Hennemann, J. S. Murray, P. Politzer, (2007), *J. Mol. Model*, 13, 291.

42 (a) I. Dance, M. Scudder, (1996), *Chem. Eur. J.*, 2, 481. (b) I. Dance, M. Scudder, (1995), *J. Chem. Soc., Chem. Commun.*, 1039.

43 A. Abate, S. Biella, G. Cavallo, F. Meyer, H. Neukirch, P. Metrangolo, T. Pilati, G. Resnati, G. Terraneo, (2009), *J. Fluorine Chem.*, 130, 1171.

44 J. Grebe, G. Geiseler, K. Harms, K. Dehnicke, (1999), *Z. Naturforsch.*, 54b, 77.

45 G. R. Desiraju, T. Steiner, (1999), *The Weak Hydrogen Bond In Structural Chemistry and Biology, IUCr Monographs on Crystallography 9*, Oxford, UK, Oxford University Press.

46 M. Kaupp, O. L. Malkina, V. G. Malkin, P. Pyykkö, (1998), *Chem. Eur. J.*, 4, 118.

47 P. G. Gordon, D. H. Brouwer, J. A. Ripmeester, (2010), *ChemPhysChem*, 11, 260.

48 C. M. Widdifield, R. P. Chapman, D. L. Bryce, (2009), *Ann. Rep. Nucl. Magn. Reson. Spectrosc.*, 66, 195.

49 R. P. Chapman, J. R. Hiscock, P. A. Gale, D. L. Bryce, (2011), *Can. J. Chem.*, 89, 822.

50 A. P. M. Kentgens, (1997), *Geoderma*, 80, 271.

51 B. Pinter, N. Nagels, W. A. Herrebout, F. De Proft, (2013), *Chem. Eur. J.*, 19, 519.

52 T. L. Brown, L. G. Butler, D. Y. Curtin, Y. Hiyama, I. C. Paul, R. B. Wilson, (1982), *J. Am. Chem. Soc.*, 104, 1172.

53 C. A. Michal, J. C. Wehman, L. W. Jelinski, (1996), *J. Magn. Reson., Ser. B*, 111, 31.

54 K. Yamada, S. Dong, G. Wu, (2000), *J. Am. Chem. Soc.*, 122, 11602.

55 G. Wu, S. Dong, R. Ida, N. Reen, (2002), *J. Am. Chem. Soc.*, 124, 1768.

56 A. Wong, K. J. Pike, R. Jenkins, G. J. Clarkson, T. Anupõld, A. P. Howes, D. H. G. Crout, A. Samoson, R. Dupree, M. E. Smith, (2006), *J. Phys. Chem. A*, 110, 1824.

57 M. Gee, R. E. Wasylishen, A. Laaksonen, (1999), *J. Phys. Chem. A*, 103, 10805.

58 C. Deverell, R. E. Richards, (1969), *Mol. Phys.*, 16, 421.

59 A. Loewenstein, M. Shporer, (1968), *J. Chem. Soc., Chem. Comm.*, 214.

60 (a) C. J Pickard, F. Mauri, (2001), *Phys. Rev. B*, 63, 245101. (b) J. R. Yates, C. J. Pickard, F. Mauri, (2007), *Phys. Rev. B*, 76, 024401. (c) M. Profeta, F. Mauri, C. J. Pickard, (2003), *J. Am. Chem. Soc.*, 125, 541. (c) S. J. Clark, M. D. Segall, C. J. Pickard, P. J. Hasnip, M. I. J. Probert, K. Refson, M. C Payne, (2005), *Z. Kristallogr.*, 220, 567.

61 M. Carter, A. R. Voth, M. R. Scholfield, B. Rummel, L. C. Sowers, P. S. Ho, (2013), *Biochemistry*, 52, 4891.

5 STUDY OF C-I···P=SE HALOGEN BOND MOTIFS BY SSNMR COMBINED WITH AN NLMO ANALYSIS

5.1 INTRODUCTION AND OBJECTIVES

The impact that NMR spectroscopy has had on the characterization and understanding of hydrogen bonds in solution and the solid state paved the way for study of another non-covalent interaction, the halogen bond. Carlsson *et al.* have elegantly probed the symmetry of halogen bonds in solution using NMR chemical shifts.[1] Yan *et al.* have recently studied the possible application of σ-hole···Cl^- bonds in separation science using ^{19}F NMR titration experiments in solution.[2] Our group has recently reported SSNMR studies of halogen-bonded complexes and demonstrated the relationships between various NMR observables and the halogen bond geometry and environment (Chapter 3 and 4).[3,4,5,6] For instance, ^{13}C chemical shifts of the ipso C-I carbon in diiodoperfluorobenzene-halide complexes exhibiting halogen bonds were shown to be sensitive to the C-I bond length, which in turn is a measure of the extent of halogen bonding in the C-I···X^- motif.[4] Chlorine-35/37, bromine-79/81, and iodine-127 SSNMR spectroscopies of halogen-bonded anions have revealed the sensitivity of the nuclear quadrupolar coupling tensors to the halogen bond environment.[5,6]

The study of hydrogen bonds (e.g., N-H···O=C in proteins) by NMR spectroscopy took a quantum leap forward with the successful measurement and interpretation of indirect nuclear spin-spin (*J*) couplings across and within such bonds, in solution and in the solid state.[7, 8, 9, 10] For example, Limbach and co-workers have examined such couplings experimentally and computationally in small molecules.[11,12] *J*-couplings have also been

measured in van der Waals' complexes[13] and have been used to characterize CH-π interactions.[14]

J-couplings are present in principle between the various nuclei involved in a halogen bond. To our knowledge, however, *J*-coupling constants have not been measured experimentally for halogen bonds. Computed *J*-coupling constants for model systems in the gas phase have been reported, and these suggest that non-negligible one-bond and two-bond couplings are possible and that there is a dependence on the local geometry.[15] A multinuclear SSNMR study is reported here of phosphine selenide-iodofluorobenzene complexes exhibiting P=Se···I halogen bonds. *J*-couplings measured between ^{31}P and ^{77}Se (both spin-1/2 nuclides) are shown to be sensitive to the presence and geometry of the halogen bond between the P=Se and I-C moieties. ^{77}Se and ^{31}P chemical shift tensors are also measured experimentally and interpreted in relation to halogen bonding. Related work has demonstrated the sensitivity of $J(^{77}\text{Se},^{31}\text{P})$ coupling to selenium-cadmium interactions in solutions containing phosphine selenides and cadmium complexes.[16,17] Our data are interpreted in the context of single-crystal and PXRD data and DFT calculations. An NLMO[18] DFT analysis of the $J(^{77}\text{Se}, ^{31}\text{P})$ coupling constants provides insight into the connection between the experimental observables and the electronic structure. Such analyses have been applied to study magnetic shielding tensors, electric field gradient tensors, and *J*-couplings in a variety of systems.[19,20,21,22]

5.2 EXPERIMENTAL SECTION

5.2.1 *Sample Preparation*

Iodobenzene derivatives (*p*-$C_6F_4I_2$, *o*-$C_6F_4I_2$) and triphenylphosphine selenide (Ph_3PSe) were purchased from Aldrich and used without further purification. *sym*-$C_6F_3I_3$ was acquired from Alfa Aesar and used as received. Compounds (Ph_3PSe)(*p*-DITFB) **11** and (Ph_3PSe)(*o*-DITFB) **12** were prepared according to the literature.[23] The syntheses of **11** and **12** were scaled to yield 150 to 200 mg of the desired product for SSNMR studies. *o*- or *p*-DITFB (0.1295 g, 0.32 mmol) was mixed with Ph_3PSe (0.1100 g, 0.32 mmol) in a small vial and dissolved in a minimum amount of dichloromethane at room temperature. The mixture was left to evaporate slowly, yielding **11** and **12**. Compound (Ph_3PSe)(*sym*-$C_6F_3I_3$) **13** was prepared by dissolving equimolar amounts of Ph_3PSe (0.0787 g, 0.23 mmol) with *sym*-$C_6F_3I_3$ (0.1175 g, 0.23 mmol) in a minimum amount of dichloromethane. A vial containing the solution was then left at room temperature until the desired compound crystallized, (**13**). All samples were prepared at natural isotopic abundance. Their local halogen bonded environment is depicted in Figure 5.1.

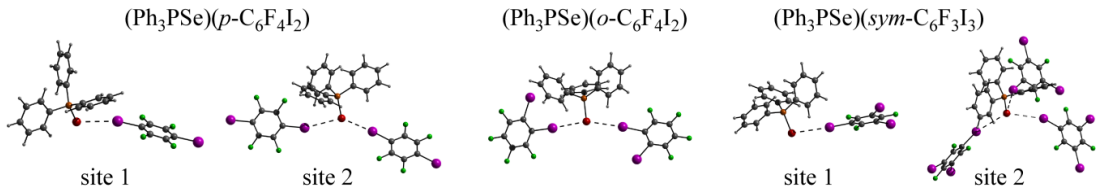

Figure 5.1 Local halogen bonding geometries for compounds (Ph_3PSe)(*p*-DITFB) **11**, (Ph_3PSe)(*o*-DITFB) **12**, and (Ph_3PSe)(*sym*-$C_6F_3I_3$) **13** studied in this work, from XRD. See angles and bond lengths in Table 5.2. Compounds **11** and **13** have two crystallographically distinct selenium and phosphorus sites each. Each atom is colour-coded: selenium (red), phosphorus (orange), carbon (grey), iodine (purple), fluorine (green) and hydrogen (white).

5.2.2 *Single-Crystal X-ray Crystallography*

Data collection results for compounds **11**, **12**, and **13** represent the best data sets obtained in several trials for each sample. The crystals were mounted on thin glass fibers using paraffin oil. Mounted crystals were cooled by a stream of dry air to 200.15 K prior to data collection. Data were collected on a Bruker AXS KAPPA single crystal diffractometer equipped with a sealed Mo tube source (wavelength 0.71073 Å) and APEX II CCD detector. Raw data collection and processing were performed with the APEX II software package from BRUKER AXS.[24] Diffraction data for **11**, **12**, and **13** were collected with a sequence of 0.5° ω scans at 0, 120, and 240° in φ. Unit cell parameters for **11** were verified to be consistent with the literature.[23] Systematic absences in the diffraction data set and unit cell parameters were consistent with the monoclinic $P2_1/n$ space group for compounds **12** and **13**. Solutions in centrosymmetric space groups for all compounds yielded chemically reasonable and computationally stable results of refinement. The structures were solved by direct methods, completed with difference Fourier synthesis, and refined with full-matrix least-squares procedures based on F^2. All hydrogen atoms were treated as idealized contributions. All scattering factors are contained in several versions of the SHELXTL program library, with the latest version used being 6.12.[25] Crystallographic data and selected data collection parameters are reported in Table 5.1.

Table 5.1 Crystallographic Data and Selected Data Collection Parameters

compound	**12**	**13**
empirical formula	$C_{24}H_{15}F_4I_2PSe$	$C_{48}H_{30}F_6I_6P_2Se_2$
formula weight / g/mol	743.09	1701.98
crystal size/ mm	0.28 x 0.19 x 0.17	0.22 x 0.14 x 0.13
crystal system	monoclinic	monoclinic
space group	*P* $2_1/n$	*P* $2_1/n$
Z	4	4
a/ Å	13.7022(3)	28.1286(7)
b/Å	12.7689(3)	9.4276(3)
c/ Å	13.9386(3)	23.3606(7)
α/ °	90	90
β/ °	101.2140(10)	93.1692(16)
γ/ °	90	90
Volume / $Å^3$	2392.16(9)	5085.92(27)
calculated density/ Mg/m^3	2.063	2.223
absorption coefficient/ mm^{-1}	4.259	5.214
F(000)	1400	3152
Θ range for data collection/ °	1.91 to 28.33	1.764 to 30.535
limiting indices	-18 <= h <= 18, -17 <= k <= 17, -17 <= l <= 18	-29 <= h <= 32, -13 <= k <= 13, -33 <= l <= 32
reflections collected/unique	31024/5895	77460
R (int)	0.0187	0.0297
completeness to Θ = 28.32/ %	98.9	99.4
max and min transmission	0.5313 and 0.3818	0.550 and 0.393
data/restraints/parameters	5895/0/289	15250 /0 /577
goodness-of-fit on F^2	1.049	1.017
final R indices [I > 2*α*(I)]	R1 = 0.0164, wR2 = 0.0416	R1 = 0.0287 wR2 = 0.0641
R indices (all data)	R1 = 0.0179, wR2 = 0.0424	R1 = 0.0379 wR2 = 0.0681
largest diff peak/hole/ e· $Å^{-3}$	0.407 and -0.757	1.625 and -2.108

5.2.3 ***Powder X-ray Diffraction***

Sample purity and identity were verified by X-ray powder diffraction analysis. All experiments were carried out using a Rigaku Ultima IV instrument at room temperature (298 ± 1 K) with Cu $K\alpha_1$ radiation (λ = 1.54060 Å). All experiments were carried out with 2θ ranging between 5 and 50° in increments of 0.02° at a rate of 0.6° per minute. Simulations of patterns from single crystal results were generated using Mercury software available from the CCDC and were compared to those observed for bulk reaction products.

5.2.4 *Solid-State NMR Spectroscopy*

All compounds were ground into fine powders and packed in 4 mm o.d. zirconia rotors. Data were acquired at the University of Ottawa using either a 9.4 T ($\nu_L(^{13}C)$ = 100.6 MHz, $\nu_L(^{31}P)$ = 161.976 MHz, $\nu_L(^{77}Se)$ = 76.311 MHz) magnet equipped with a Bruker Avance III 400 console and a 4 mm Bruker triple resonance MAS probe or a 11.75 T ($\nu_L(^{13}C)$ = 125.758 MHz, $\nu_L(^{31}P)$ = 202.456 MHz, $\nu_L(^{77}Se)$ = 95.382 MHz) Bruker Avance 500 wide bore spectrometer equipped with a 4 mm triple resonance MAS probe. Some data were also acquired at the National Ultrahigh-Field NMR Facility for Solids in Ottawa using a 21.1 T ($\nu_L(^{77}Se)$ = 171.668 MHz) standard-bore magnet equipped with a Bruker AVANCE II 900 console and a double-resonance MAS probe.

Spectra for ^{13}C, ^{31}P, and ^{77}Se were collected under CPMAS conditions[26] with proton decoupling. Experimental setup and pulse calibration were performed using solid glycine for ^{13}C ($\delta_{iso}(^{13}C{=}O)$ = 176.4 ppm with respect to TMS),[27,28] solid diammonium selenate ($(NH_4)_2SeO_4$) for ^{77}Se (δ_{iso} = 1040.2 ppm with respect to $Se(CH_3)_2(l)$),[29] and ammonium dihydrogen phosphate for ^{31}P ($NH_4H_2PO_4$, δ_{iso} = 0.81 ppm with respect to H_3PO_4 in 85% D_2O).[30]

5.2.4.1 ^{13}C SSNMR.

Recycle delays were 35, 10, and 15 s respectively for **11**, **12**, and **13**. The proton $\pi/2$ pulse and contact time were set to 3.25 or 3.50 μs and 2 ms, respectively, in all cases. MAS frequencies varied between 8 and 10 kHz.

5.2.4.2 *^{31}P SSNMR.*

^{31}P SSNMR experiments used a recycle delay of 6 s at 9.4 T and 30 s at 11.75 T. The proton π/2 pulse length was optimized to 2.50 or 3.00 μs at 9.4 T and 4.50 μs at 11.75 T. The contact time was 5 ms and 2 ms at 9.4 and 11.75 T, respectively. MAS frequencies varied between 2.1 kHz and 10 kHz.

5.2.4.3 *^{77}Se SSNMR.*

For ^{77}Se NMR experiments, the recycle delays were 34 s, 20 s, and 30s for compounds **11**, **12**, **13**, respectively. The ^{1}H π/2 pulse length used for the CP experiments was typically 3.75 μs at 9.4 T. The proton π/2 pulse lengths used at 11.75 and 21.1 T were 2.8 and 4.0 μs, respectively. The contact time was typically 20 ms.

Spectra were simulated using WSOLIDS[31] and SIMPSON.[32] Additional experimental details may be found in Appendix C.

5.2.5 ***Computational Details***

Cluster models were generated using the X-ray crystal structures' atomic coordinates and are depicted in Figure 5.1. The structure of Codding and Kerr[33] was used for Ph_3PSe. ^{31}P and ^{77}Se magnetic shielding tensors were calculated with the ADF software[3450] or Gaussian09[51] software. The positions of the hydrogen atoms in the models were optimized prior to NMR calculations. For the DFT calculations performed with Gaussian09 software, the TPSS functional[35] and 6-311G** basis set were used.

For all calculations using ADF, scalar relativistic effects were included via the ZORA.[36] All contributions to the J tensor were included in the calculations. NLMO

analyses were performed with the NBO 5.0 code[37] in ADF[18,50] and were visualized with the program adfview. The revised PBE[38] GGA exchange-correlation functional was used with the ZORA triple zeta basis set for magnetic shielding and J tensor calculations. Additionally the meta-GGA TPSS functional was used for a second set of *J*-coupling calculations. These calculations were performed using the High-Performance Virtual Computing Laboratory (HPCVL).

A simplified model was prepared for the calculations on site 2 of compound **13**. In this model, the *sym*-$C_6F_3I_3$ molecules were replaced by CF_3I and the positions of all other atoms were fixed while the new fluorine positions were optimized before proceeding to the magnetic shielding and *J*-coupling calculations. Also, a systematic study was performed on a small cluster model of $(CH_3)_3PSe\cdots ICF_3$ were the Se···I distance was varied systematically by increments of 0.04 Å between 3.40 (R_{XB} = 0.85) and 3.66 Å (R_{XB} = 0.92). For each calculation, the model was geometry optimized while keeping the Se···I distance fixed. With the converged geometry, the *J*-coupling calculation combined with the NLMO analysis was then performed, as well as the magnetic shielding tensor calculations. Note that the halogen bond geometry itself is not optimized computationally in any of the present calculations.

The computed magnetic shielding tensors were analyzed using the EFGShield program.[39] Magnetic shielding tensors were converted to chemical shift tensors using the following equation: $\delta_{ij} = \frac{\sigma_{ref} - \sigma_{ij}}{1 - \sigma_{ref}}$ (where σ_{ref} = 2069 ppm for selenium in $Se(CH_3)_2$(l)[40] and where σ_{ref} = 331.51 ppm for phosphorus in H_3PO_4 (85% D_2O)[41]). The ADF output files from the *J*-coupling calculations were analyzed to select the NLMOs with large contributions to the

isotropic *J*-coupling constant. The sum of the Lewis and non-Lewis terms are reported for the largest contributions.

5.3 RESULTS AND DISCUSSION

5.3.6 *The Structures of (Ph$_3$PSe)(o-DITFB) and (Ph$_3$PSe)(sym-TITFB)*

Co-crystallization of triphenylphosphine selenide (Ph_3PSe) and iodobenzene derivatives (*o*- or *p*-$C_6F_4I_2$ and *sym*-$C_6F_3I_3$ which are also referred to as DITFB and TITFB, respectively) yielded two novel co-crystals exhibiting halogen bonds, (**12**) and (**13**), and (**11**) which was previously reported by Arman *et al.*[23] The relevant halogen bond distances, $d_{I\cdots Se}$, angles, $\theta_{C—I\cdots Se}$, and I···Se···I angles ($\theta_{I\cdots Se\cdots I}$), as well as $R_{XB'}$ carbon-iodine bond lengths ($d_{I—C}$), phosphorus-selenium bond lengths ($d_{P=Se}$), and P=Se···I angles ($\theta_{P=Se\cdots I}$) are given in Table 5.2. Summarized in Table 5.1 are the crystallographic data for compounds **12** and **13**.

Table 5.2 Selected halogen bond intermolecular contact distances and angles.[a]

		$d_{I—C}$ /Å	$d_{I\cdots Se}$ /Å	R_{XB}[b]	$\theta_{C—I\cdots Se}$ /°	$d_{P=Se}$/Å	$\theta_{P=Se\cdots I}$ /°	$\theta_{I\cdots Se\cdots I}$ /°	R_{DD}[d] / Hz
Ph_3PSe		-	-	-	-	2.1080	-	-	995
		-	-	-	-	2.1074	-	-	996
11	Site 1	2.092	3.4224	0.86	166.5	2.1070	112.6	-	997
	Site 2	2.082	3.4944	0.88	171.4	2.1270	113.0	126.0	969
		2.078	3.6841	0.93	154.9	-	88.9	-	
12	Site 1	2.0986	3.4014	0.85	175.2	2.1320	104.0	139.8	962
		2.1034	3.5863	0.90	174.7	-	91.9	-	
13	Site 1	2.0949	3.5528	0.89	166.8	2.1190	104.6	-	980
	Site 2	2.0901	3.5027	0.88	162.5	2.1252	107.3	118.6	972
		2.0886	3.6024	0.91	159.2	-	91.3	-	
		2.0842	3.9227	0.99	159.7	-	155.3	-	

[a] See models in Figure 5.1. Experimental values determined by single-crystal X-ray crystallography. [b] $R_{XB} = d_{X\cdots Y}/\Sigma d_{VdW}$, the ratio of the distance between the halogen (i.e., I) and the electron donor (i.e., Se) to the sum of their van der Waals radii (1.98 Å for I and 2.00 Å for Se). [42] [c] Arman *et al.*[23] [d] ^{77}Se-^{31}P dipolar coupling constant, $R_{DD} = (\frac{\mu_o}{4\pi})(\frac{\gamma_I \gamma_S h}{4\pi^2})\langle r_{IS}^{-3}\rangle$, where μ_o is the permeability constant, γ_I and γ_S are the magnetogyric ratios of the coupled spins *I* and *S* (i.e., ^{31}P and ^{77}Se) and $\langle r_{IS}^{-3}\rangle$ is the motionally-averaged inverse cube of the distance between the coupled nuclei.

The X-ray crystal structure of **11** was verified to match that reported previously.[23] The halogen bond environments in **11** may be described as follows: there are two different selenium sites and both engage in halogen bonding with iodine. Interactions at one of the sites (labelled site 2 in Figure 5.1) result in infinite chains along the *a* axis involving one halogen bond acceptor (i.e., Se) and two halogen bond donors from different *p*-DITFB molecules. Selenium atoms in the other distinct site (labelled site 1 in Figure 1) interact

with one iodine atom and the result is discrete halogen-bonded entities rather than infinite chains.

One polymorph of compound **12** has been previously reported;[23] however, in this work a different polymorph is reported, which crystallizes in the $P2_1/n$ space group (Table 5.1). The polymorph synthesized in this work features discrete halogen-bonded entities; the selenium atom forms short contacts with two iodine atoms (R_{XB} = 0.85 and 0.90) from different arene molecules with a I···Se···I angle of 138.8°. The C—I···Se angles are nearly linear (175.2° and 174.7°). The local structural motif is shown in Figure 5.1. The extended crystal network is shown in Figure 5.2.

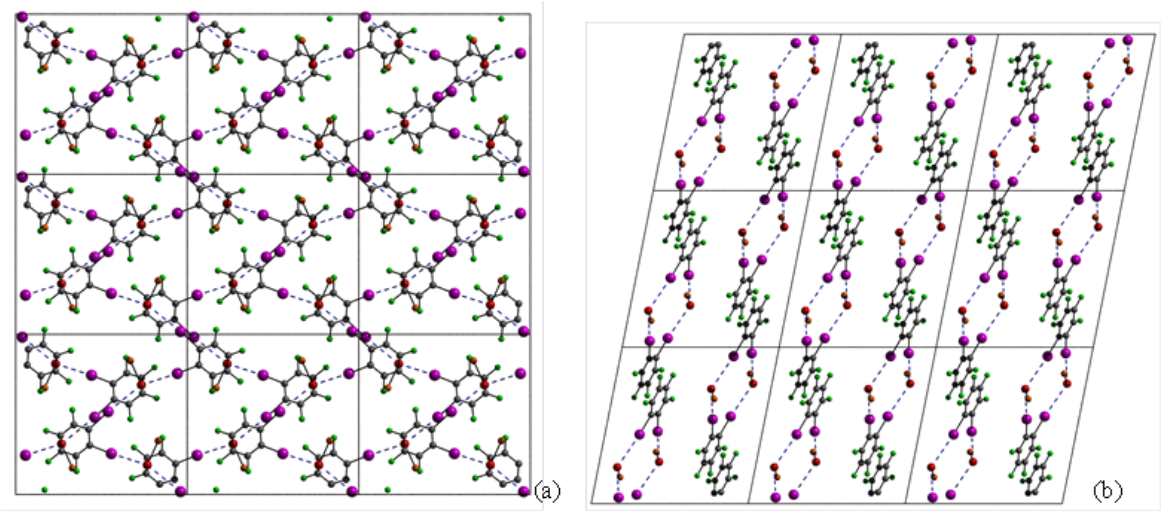

Figure 5.2 Crystal packing of **12** in a 3 x 3 x 3 super cell viewed along the *a* axis (a) and *b* axis (b). In (b) the extended network are observed. The phenyl rings on P are omitted to more clearly show the network.

Compound **13** crystallizes in the $P2_1/n$ space group. This halogen-bonded compound has two crystallographically distinct P=Se environments (see Figure 5.1). The first selenium atom interacts with a single iodine atom (R_{XB} = 0.89; $\theta_{C—I\cdots Se}$ = 166.8°),

resulting in discrete entities in the crystal lattice (see Figure 5.3). The second crystallographically distinct type of selenium atom is surrounded by three iodine atoms from different *sym*-TITFB molecules as depicted in Figure 5.1. The values of R_{XB} for each of the three Se···I contacts are 0.88, 0.91, and 0.99, respectively. This indicates that the third contact hardly constitutes a halogen bond (i.e., an R_{XB} value of 1 implies that the atoms in question are no closer than the sum of their van der Waals' radii). The two iodine atoms involved in halogen bonding with Se form a I···Se···I angle of 118.6°. These interactions at the second selenium site result in polymeric zigzag chains along the *b* axis (Figure 5.3).

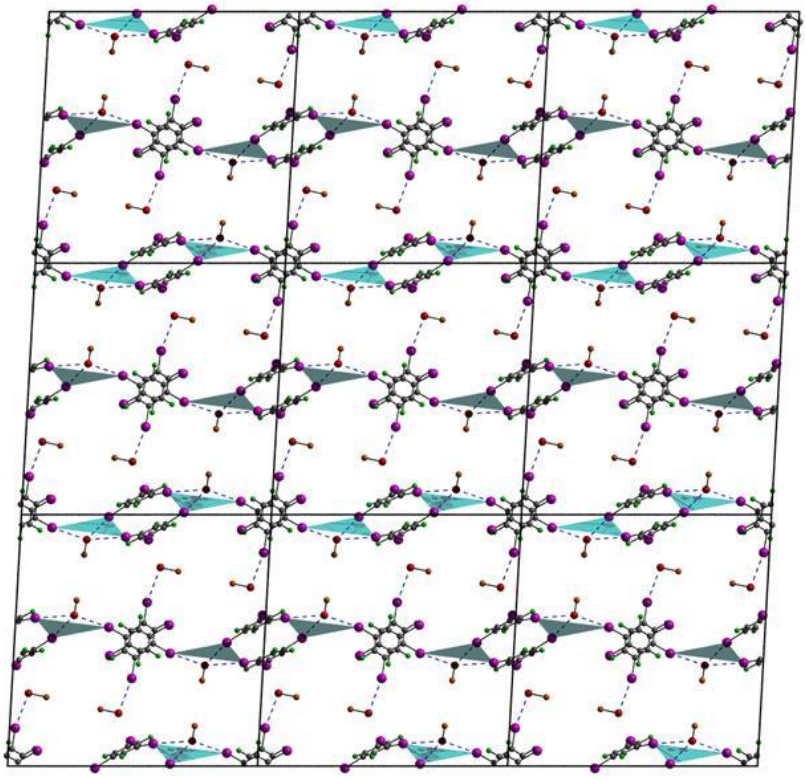

Figure 5.3 Crystal packing of a 3 x 3 x 3 unit cell for **13** along the *b* axis. There are two crystallographically unique selenium sites in **13**. One is highlighted by the blue surface of a polyhedron which forms a one dimensional zigzag chain along the *b* axis. The second site is within a discrete entity between the zigzag chains. The phenyl rings on P are omitted for clarity.

5.3.7 *Initial Characterization*

To verify the phase purity of **11**, **12**, and **13** upon grinding of the crystals for SSNMR spectroscopy, PXRD experiments are performed, which provided diffractograms in good agreement with those predicted from the single-crystal X-ray crystal structures (Figure 5.4).

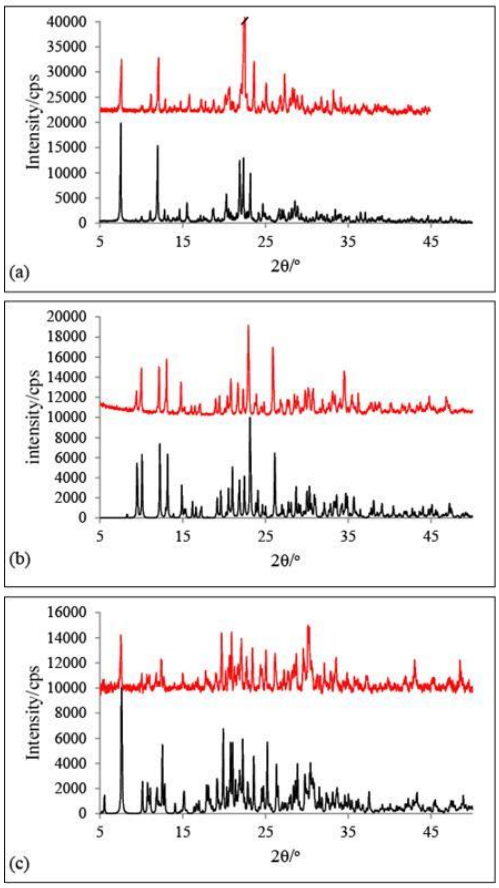

Figure 5.4 Experimental PXRD patterns (red trace) for (a) (Ph_3PSe)(*p*-DITFB), (b) (Ph_3PSe)(*o*-DITFB), (c) (Ph_3PSe)(*sym*-TITFB) along with simulations in black based on single crystal X-ray data. All experiments were carried out using a Rigaku Ultima IV instrument with 2θ ranging between 5 and 50° in increments of 0.02° at a rate of 0.6° per minute. Simulations were generated using Mercury software available from the CCDC.

^{13}C CPMAS SSNMR spectra (see Figure 5.5) also suggest the formation of halogen bonds in the structures. As expected, the chemical shifts of the carbon atoms covalently bonded to iodine (C-I) are quite shielded due to the relativistic spin-orbit-induced 'heavy-

atom light-atom' (HALA) effect caused by the covalently bonded iodine.[43] The average values for **11**, **12**, and **13** are 73.4, 97.6, and 65.3 ppm, respectively. These chemical shifts differ from those of the parent iodobenzenes (e.g., 76.5 ppm for solid *p*-DITFB[4] and 64.0 ppm for *sym*-TITFB[44] (in chloroform-*d*)). All three compounds have more than one crystallographically distinct C-I site (four for **11**, two for **12**, and five for **13**) but only one broad ^{13}C NMR peak is observed in each case. This is due to spectral overlap and possible line broadening due to the nearby iodine and fluorine nuclei. For example, a residual ^{127}I-^{13}C dipolar coupling of -2.4 kHz at 9.4 T is expected on the basis of a one-bond ^{127}I-^{13}C dipolar coupling constant of 657 Hz and a typical C_Q(^{127}I) of 1000 MHz.

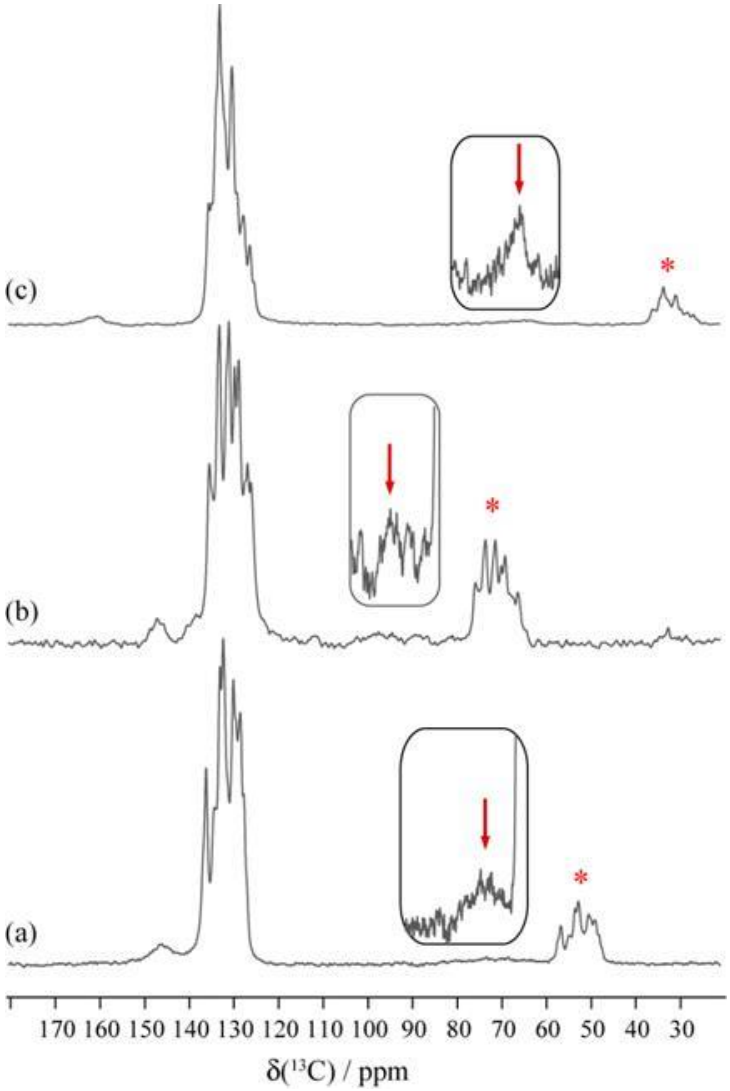

Figure 5.5 Experimental ^{13}C CPMAS SSNMR spectra acquired at 9.4 T are presented for (a) (Ph_3PSe)(*p*-DITFB) with a MAS rate of 8 kHz, (b) (Ph_3PSe)(*o*-DITFB) with a MAS rate of 5 kHz, and (c) (Ph_3PSe)(*sym*-TITFB) with a MAS rate of 10 kHz. Red asterisks indicate spinning sidebands and the inset shows a vertical expansion of the C-I region. The peaks of interest, particularly in (b), were further identified by experiments at different MAS rates.

5.3.8 *^{31}P and ^{77}Se SSNMR spectroscopy of halogen-bonded compounds*

The ^{31}P and ^{77}Se CPMAS SSNMR spectra of triphenylphosphine selenide have been thoroughly investigated by Demko *et al.*[45] as well as Grossmann et al.[46] The latter study

was performed on a Ph_3PSe sample which was 70% isotopically enriched in ^{77}Se, resulting in spectra with excellent signal-to-noise. The ^{31}P and ^{77}Se data from these previous studies are used for comparison with the data obtained for halogen-bonded compounds **11**, **12**, and **13** (see Tables 5.3 and 5.4). All compounds in the present study were investigated at natural isotopic abundance.

Table 5.3 Experimental ^{31}P CS tensor parameters.[a]

	compound		δ_{iso} / ppm	Ω / ppm	κ
	Ph_3PSe[b]	site 1	35.90	161	0.47
		site 2	41.90	144	0.39
11	$(Ph_3PSe)(p\text{-}C_6F_4I_2)$	site 1	34.25(0.10)	134(4)	0.53(0.10)
		site 2	34.25(0.10)	134(4)	0.53(0.10)
12	$(Ph_3PSe)(o\text{-}C_6F_4I_2)$	site 1	31.85(0.13)	112(2)	1.00(0.15)
13	$(Ph_3PSe)(sym\text{-}C_6F_3I_3)$	site 1	35.82(0.10)	133(3)	0.45(0.03)
		site 2	34.00(0.10)	112(2)	0.46(0.01)

[a] Error bounds are given in parentheses. [b] Previously reported by Demko *et al.*[45] and Grossmann *et al.*[46]

Table 5.4 Experimental ^{77}Se CS tensor parameters and $J(^{77}Se, ^{31}P)$ values.[a]

compound		δ_{iso} / ppm	Ω / ppm	κ	$J(^{77}Se, ^{31}P)$ / Hz	R_{eff} / Hz[c]
Ph_3PSe	site 1	-257	221	-0.58	-733[b]	695
	site 2	-242	247	-0.62	-736[b]	696
11	site 1	-220	160(15)	1.0(0.2)	-725(25)	697
	site 2	-163	260(30)	0.2(0.2)	-663(38)	669
12	site 1	-158	170(5)	1.0(0.2)	-626(2)	729
13	site 1	-188	350(20)	0.25(0.20)	-717(17)	680
	site 2	-140	250(15)	0.35(0.20)	-641(25)	672

[a] Error bounds are given in parentheses. Errors in the isotropic chemical shifts are 1 ppm or less. [b] CS tensors and $J(^{77}Se, ^{31}P)$ previously reported.[45,46] [c] See main text for further explanation.

Presented in Figure 5.6 are the ^{31}P CPMAS NMR spectra of compounds **11**, **12**, and **13** obtained in an applied magnetic field of 9.4 T. Analogous data obtained at 11.75 T are provided in Figure 5.7. The isotropic chemical shifts, span, and skew are presented in Table 5.3. The total range of chemical shifts observed is from 31.85 ppm in **12** to 41.90 ppm in site 2 of Ph_3PSe. Two crystallographically distinct phosphorus sites are expected for **11**;

however, only one is resolved in the ^{31}P SSNMR spectrum. It is noted that there is a small but consistent decrease in the ^{31}P chemical shifts in the halogen-bonded compounds relative to both sites in Ph_3PSe where halogen bonding is absent. Similarly, the ^{31}P chemical shift tensor spans are smaller in the halogen-bonded complexes (ranging from 112 to 134 ppm) relative to both sites in Ph_3PSe (144 and 166 ppm). The span (Ω) is a measure of the degree of anisotropy of the chemical shift tensor and a smaller span reflects a small change in the electronic structure of the P=Se bond in the halogen-bonded complexes.

Also shown in Figure 5.6 are expansions of the centreband where the *J*-coupling between ^{31}P and ^{77}Se may be observed in the satellite peaks (note that the natural abundance of ^{77}Se is 7.63%). The values obtained from these spectra are consistent with those obtained from the corresponding ^{77}Se CPMAS NMR spectra of the same compounds (see Table 5.4); however, analysis of the latter spectra (*vide infra*) allows for improved precision since the effects of the coupling are clearly seen in the main peaks rather than in low-intensity satellites which partially overlap with the main peaks.

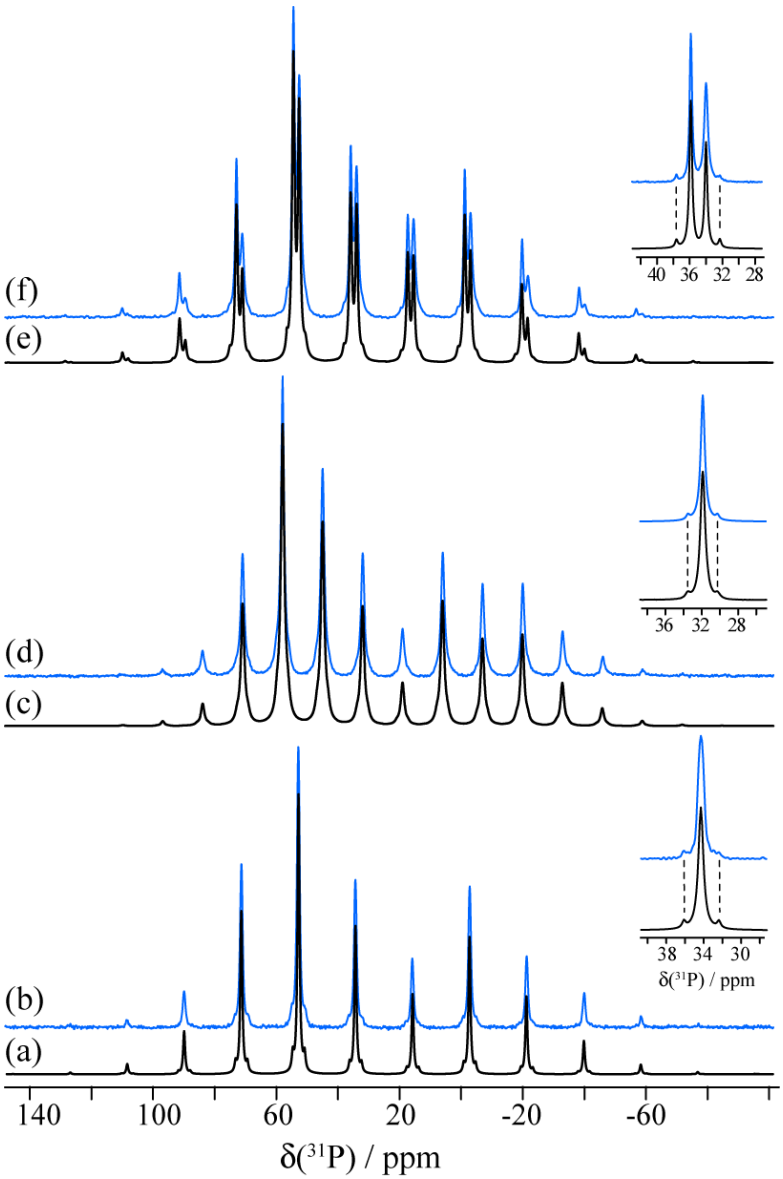

Figure 5.6 Experimental ^{31}P CPMAS SSNMR spectra (blue) acquired at 9.4 T for (b) **11** (MAS 3 kHz), (d) **12** (MAS 2.1 kHz), and (f) **13** (MAS 3 kHz). Their respective simulated spectra are shown in black ((a), (c), (e)). Each inset shows the centreband and the ^{77}Se-^{31}P satellites due to *J*-coupling (B_0 = 11.75 T). The top inset for compound **13** shows evidence of *J*-coupling for both crystallographically distinct Se-P sites.

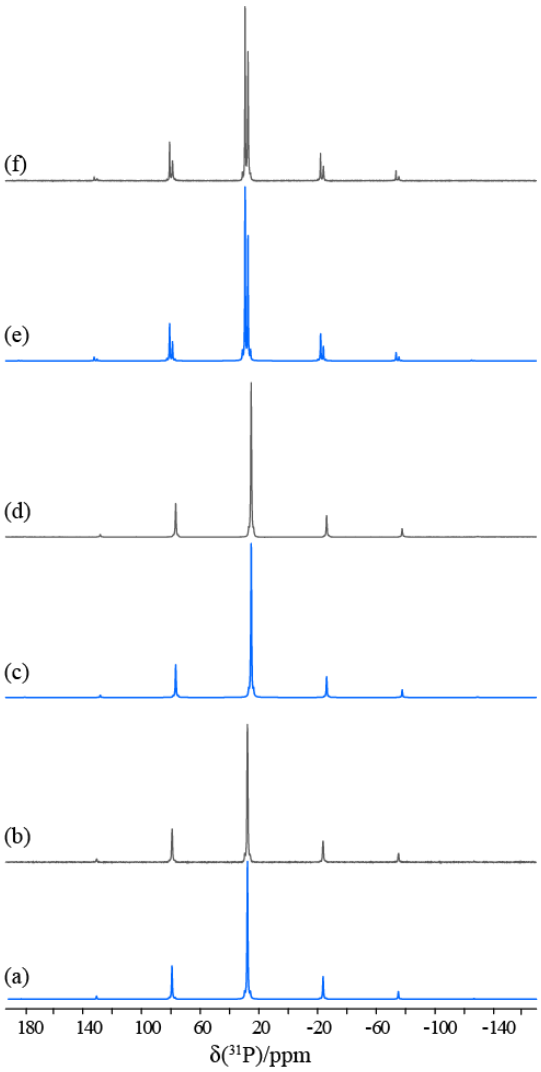

Figure 5.7 Experimental ^{31}P CPMAS SSNMR spectra acquired at 11.75 T with a spinning frequency of 10 kHz are presented for (b) **11**, (d) **12**, (f) **13**. Their respective simulated spectra are shown in blue ((a), (c) and (e)).

Shown in Figures 5.8, 5.9, and 5.11 are the ^{77}Se CPMAS SSNMR spectra of **11**, **12**, and **13** recorded at 9.4 T with two different spinning frequencies. Spectral fitting at two MAS frequencies, as well as at more than one applied magnetic field strength (at least 9.4 T and 11.75 T), allows for the measurement of the isotropic $J(^{77}\text{Se}, ^{31}\text{P})$ coupling and the ^{77}Se chemical shift tensor magnitude. Simulations also included the direct dipolar coupling

between ^{77}Se and ^{31}P ($R_{DD} = (\mu_0/4\pi)(\gamma_{^{77}Se}\gamma_{^{31}P}\hbar/2\pi)\langle r^{-3}\rangle$ where r is the distance between the spins), as well as contributions from the anisotropic part of the $\ddot{\mathbf{J}}$ tensor (ΔJ).[47,48,49] The ^{77}Se CS tensor parameters and J-coupling values are presented in Table 5.4 and were obtained by simultaneously modeling the NMR spectra obtained at both MAS frequencies and in both applied magnetic fields. For **12**, three magnetic fields were used to model the NMR spectra (Figure 5.10 for ^{77}Se CPMAS SSNMR spectra acquired at 11.75 and 21.1 T). Fitting was done in a manual iterative fashion, by cycling between the various spectra until a self-consistent set of parameters was determined. Error estimates were obtained through this process as well. Errors in $J(^{77}Se, ^{31}P)$ are larger than those which would be obtained from signal-to-noise or digital resolution estimates on a single spectrum.

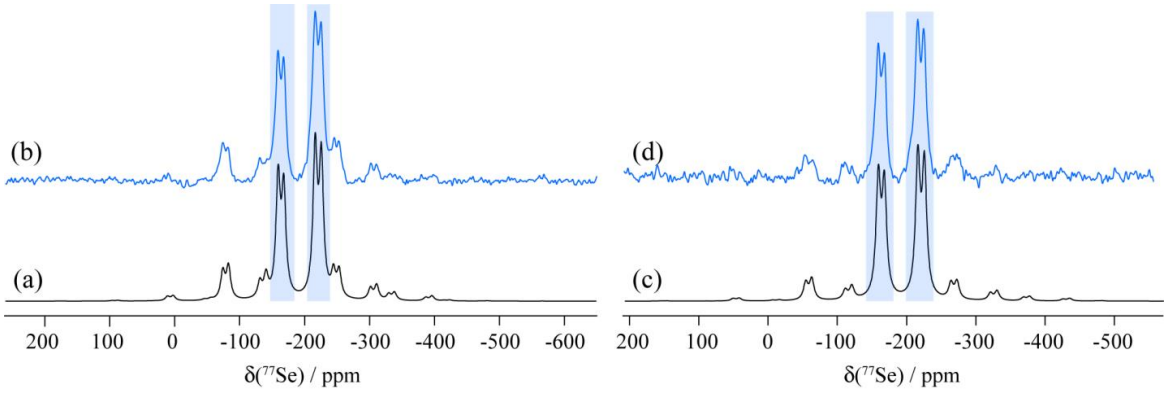

Figure 5.8 Experimental ^{77}Se CPMAS SSNMR spectra acquired at 9.4 T with MAS rates of 6.5 kHz (b) and 8 kHz (d) for compound **11**. Simulations are shown in black. The centrebands for each of the two crystallographically distinct sites are highlighted in blue bars. Each of these is split into a doublet due to $J(^{77}Se, ^{31}P)$ coupling.

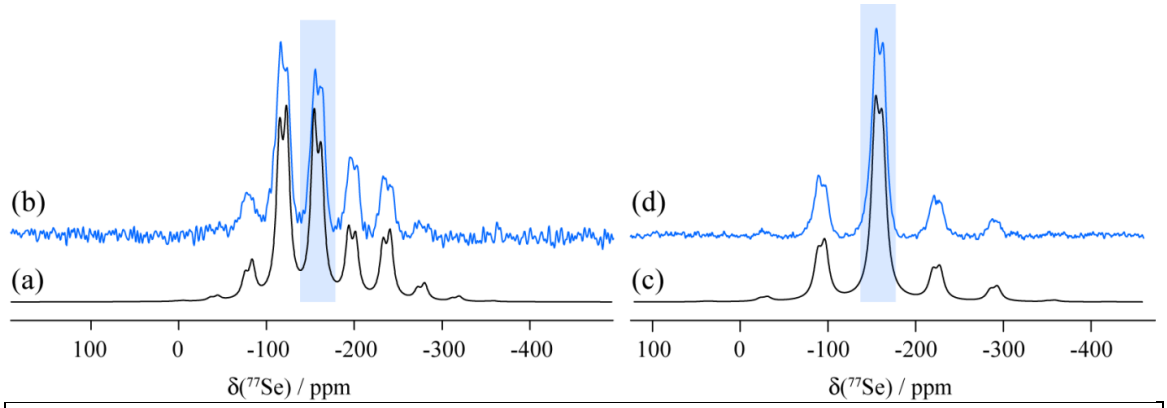

Figure 5.9 Experimental ^{77}Se CPMAS SSNMR spectra acquired at 9.4 T with MAS rates of 3 kHz (b) and 5 kHz (d) for compound **12**. Simulations are shown in black ((a) and (c)). The centrebands, highlighted in blue bars, are split into doublets due to $J(^{77}\text{Se}, ^{31}\text{P})$ coupling. Small differences in the relative intensities of some of the peaks in the experimental and simulated spectra have been observed previously (see e.g,. Figures 6 and 9 of reference 45). Additionally, dipolar coupling to ^{19}F and ^{127}I may serve to further broaden and alter spectral intensities in the present work. From the crystal structure, the values of $R_{DD}(^{127}\text{I},^{77}\text{Se})$ for the two shortest contacts are 118 and 101 Hz; the largest value of $R_{DD}(^{77}\text{Se},^{19}\text{F})$ is 431 Hz.

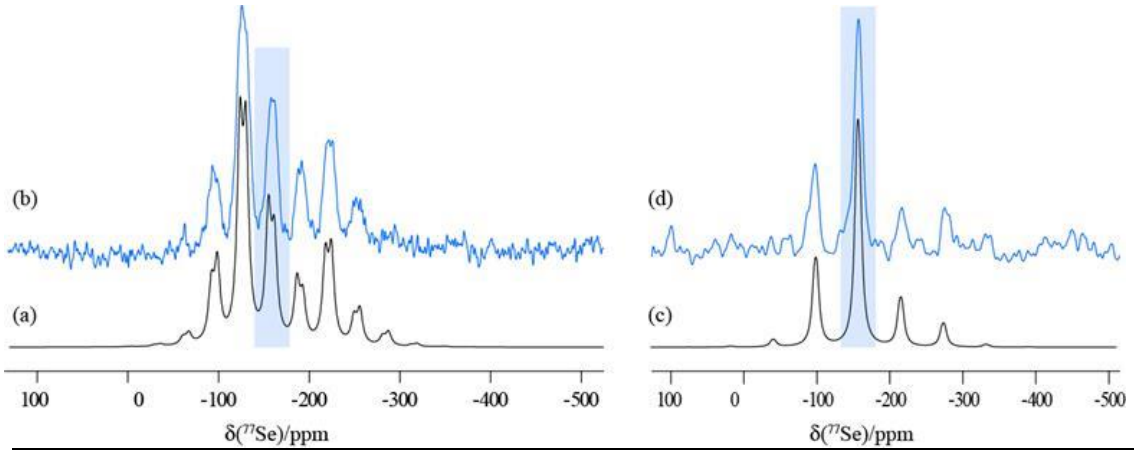

Figure 5.10 Experimental ^{77}Se CPMAS SSNMR spectra of (Ph_3PSe)(*o*-DITFB) acquired at 11.75 T with a spinning frequency of 3 kHz (b) and at 21.1 T with a spinning frequency of 10 kHz (d). Their respective simulated spectra are in black ((a) and (c)). A long relaxation time constant (T_1) hindered the acquisition of a spectrum with good signal-to-noise at 21.1 T in a reasonable time.

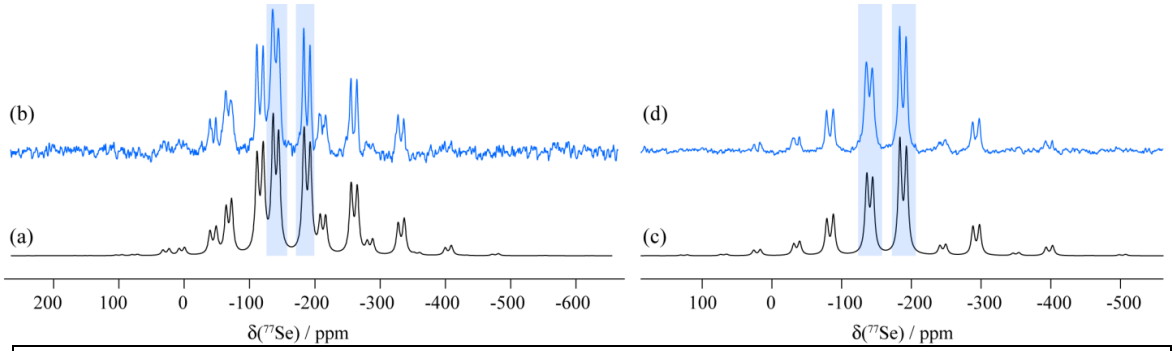

Figure 5.11 Experimental ^{77}Se CPMAS SSNMR spectra acquired at 9.4 T at a MAS rate of 5.5 kHz (b) and 8 kHz (d) for compound **13**. Simulations are shown in black ((a) and (c)). The centrebands, highlighted in blue bars, are split into doublets due to $J(^{77}\text{Se}, ^{31}\text{P})$ coupling. The relative intensities of sites 1 and 2 were adjusted to be ~1:1.2 for the best fit to experiment; attributable to differential cross-polarization efficiencies.

Such spectra were difficult to acquire due to the presence of the nearby fluorines and protons (dipolar coupling), long ^{1}H relaxation times, as well as the halogen-bonded iodines (residual dipolar coupling), which resulted in broad lines particularly in **12**. For all compounds, the $J(^{77}\text{Se}, ^{31}\text{P})$ coupling is resolved and ranges between -626(2) Hz for (Ph_3PSe)(*o*-DITFB) and -725(25) Hz for (Ph_3PSe)(*p*-DITFB). It is important to note here that the assignments of the two different $J(^{77}\text{Se}, ^{31}\text{P})$ coupling values to their different crystallographic P=Se sites in a particular compound were determined independently from the ZORA-DFT calculations (*vide infra*).

R_{DD} and ΔJ cannot be separated in an NMR experiment; an effective direct dipolar coupling describes the effects of both: $R_{eff} = R_{DD} - \Delta J/3$. For spectral simulation, the values used for R_{DD} were calculated from the X-ray crystal structures (see Table 5.2) and ΔJ values were estimated at 900 Hz, which is the approximate value observed for various organophosphine selenides.[45] The R_{eff} values shown here were fixed for spectral

simulations rather than determined from the experimental MAS spectra because simulations of the latter were not sensitive enough to the value of ΔJ to be able to determine values with high precision. The ^{77}Se-^{31}P dipolar and ^{77}Se chemical shift tensors were set to be coincident in all spectral simulations (δ_{33} aligned with the internuclear vector). The sign of $J(^{77}\text{Se}, ^{31}\text{P})$ was identified as being negative through the spectral simulations (which depend on the relative signs of $J(^{77}\text{Se}, ^{31}\text{P})$ and $R_{\text{eff}}(^{77}\text{Se}, ^{31}\text{P})$) and was corroborated with DFT computations (*vide infra*) and previous literature reports.[45]

The isotropic selenium chemical shifts increase in the presence of a halogen bond with iodine relative to those for the non-halogen-bonded Ph_3PSe (-257 and -242 ppm for its two crystallographic sites). The $\delta_{iso}(^{77}\text{Se})$ values for compounds **11**, **12**, and **13** range from -140 ppm for site 2 of compound **13** to -220 ppm for site 2 in compound **11**. When the values of $\delta_{iso}(^{77}\text{Se})$ are plotted as a function of their respective P=Se distances, a linear correlation is observed (Figure 5.12 (a)). An analogous trend was observed for the ^{77}Se chemical shifts of selenocyanate anions halogen-bonded with *p*- or *o*-DITFB, where the value of $\delta_{iso}(^{77}\text{Se})$ increases in a halogen-bonded environment.[3] Furthermore, DFT calculations on a $(CH_3)_3P{=}Se\cdots ICF_3$ cluster model revealed the same trend; the $\delta_{iso}(^{77}\text{Se})$ value increases when the P=Se bond length increases, *vide infra*. The anisotropy of the ^{77}Se chemical shift tensor does not conclusively differentiate between Ph_3PSe and the halogen-bonded compounds.

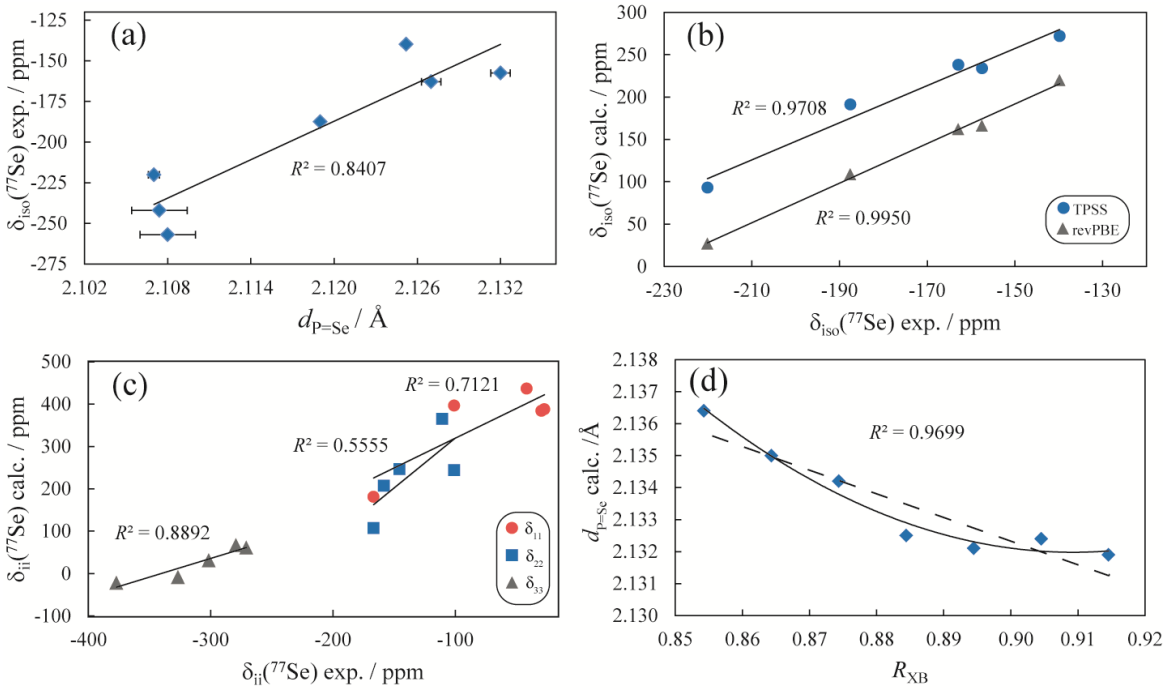

Figure 5.12 (a) Experimental $\delta_{iso}(^{77}Se)$ values as a function of the experimental P=Se bond lengths for the compounds in Table 5.2 ($\delta_{iso}(^{77}Se)^{exp.} = 3924 d_{P=Se} - 8505$ ppm, $R^2 = 0.8407$). In (b) and (c) are plots of calculated versus experimental chemical shift tensor parameters for selenium. Solid lines represent the best linear fit: (b, TPSS) $\delta_{iso}^{calc.} = 2.1919\ \delta_{iso}^{exp.} + 586.08$ ppm, (b, revPBE) $\delta_{iso}^{calc.} = 2.3368\ \delta_{iso}^{exp.} + 542.34$ ppm and (c, TPSS) $\delta_{11}^{calc.} = 1.4071\ \delta_{11}^{exp.} + 460.28$ ppm, $\delta_{22}^{calc.} = 2.3579\ \delta_{22}^{exp.} + 555.75$ ppm and $\delta_{33}^{calc.} = 0.8816\ \delta_{33}^{exp.} + 300.06$ ppm. (d) Optimized $d_{P=Se}$ distances as function of R_{XB} for a cluster model comprised of $(CH_3)_3PSe\cdots ICF_3$ ($d_{P=Se}^{calc.} = 1.485(R_{XB})^2 - 2.701(R_{XB}) + 3.360$ ($R^2 = 0.9699$) or $d_{P=Se}^{calc.} = -0.0739 R_{XB} + 2.199$, $R^2 = 0.8642$).

5.3.9 *Chemical Shifts. DFT Computations and Correlation with Halogen Bond Geometry*

DFT calculations of ^{31}P and ^{77}Se magnetic shielding tensors were performed on cluster models involving the molecules which are halogen-bonded; the numerical results are summarized in Table 5.5 and 5.6. The X-ray crystal structure heavy-atom atomic coordinates (all atoms except hydrogen) were used for these models, shown in Figure 5.1.

Computations using either the revPBE functional and the ZORA/TZP basis set (including scalar relativistic effects), as implemented in the ADF software,[50] or the TPSS functional and the 6-311G** basis set as implemented in Gaussian 09[51] were used.

Table 5.5 Calculated ^{31}P Chemical Shift Tensors.

	compound		method[a]	δ_{iso} / ppm	Ω / ppm	κ
	Ph_3PSe	site 1	ZORA	48.1	203	0.57
		site 1	TPSS	19.7	208	0.68
		site 2	ZORA	43.8	200	0.51
		site 2	TPSS	20.6	207	0.63
11	(Ph_3PSe)(*p*-$C_6F_4I_2$)	site 1	ZORA	51.6	177	0.32
		site 1	TPSS	55.9	189	0.79
		site 2	ZORA	37.3	157	0.79
		site 2	TPSS	60.0	177	0.48
12	(Ph_3PSe)(*o*-$C_6F_4I_2$)	site 1	ZORA	46.5	143	0.82
		site 1	TPSS	57.5	161	0.87
13	(Ph_3PSe)(*sym*-$C_6F_3I_3$)	site 1	ZORA	61.7	179	0.68
		site 1	TPSS	62.3	176	0.71
		site 2	ZORA	57.0	159	0.65
		site 2	TPSS	55.5	149	0.74

[a.] ZORA indicates a GGA revPBE calculation including scalar relativistic effects carried out in ADF with the ZORATZP basis set. TPSS indicates a calculation carried out with the TPSS functional in Gaussian 09 with the 6-311G** basis set.

Table 5.6 Calculated ^{77}Se Chemical Shift Tensors and J(^{77}Se,^{31}P) Coupling Constants

	compound		method[a]	δ_{iso} / ppm	Ω / ppm	κ	$J(^{77}Se, ^{31}P)$ / Hz
	Ph_3PSe	site 1	ZORA	29.1	420	0.17	-689
		site 1	TPSS	-19.4	371	0.11	-645
		site 2	ZORA	37.5	436	0.28	-689
		site 2	TPSS	-21.6	383	0.26	-645
11	(Ph_3PSe)(*p*-$C_6F_4I_2$)	site 1	ZORA	27.0	224	-0.19	-678
		site 1	TPSS	93.4	189	0.22	-635
		site 2	ZORA	162.1	428	0.02	-628
		site 2	TPSS	238.0	405	0.06	-587
12	(Ph_3PSe)(*o*-$C_6F_4I_2$)	site 1	ZORA	166.2	365	0.14	-619
		site 1	TPSS	234.0	335	0.09	-579
13	(Ph_3PSe)(*sym*-$C_6F_3I_3$)	site 1	ZORA	108.8	428	0.14	-678
		site 1	TPSS	191.2	409	0.12	-616
		site 2	ZORA	219.9	326	0.85	-616
		site 2	TPSS	272.1	317	0.88	-573

[a]same note as table 5.5 and for *J*-couplings, TPSS indicates a calculation carried out in ADF with the TPSS functional and ZORATZP basis set, with scalar relativity.

In Figure 5.12(b,c) are plotted the calculated ^{77}Se isotropic chemical shift and chemical shift tensor components versus the experimental values. Even though the calculated values are larger than the experimental ones, the experimental trend is well-reproduced for $\delta_{iso}(^{77}Se)$ at both levels of theory; linear fits with correlation coefficients, R^2, of 0.9708 and 0.9950 are noted for the TPSS and revPBE functionals, respectively. The trends in the principal components of the ^{77}Se chemical shift tensor are reasonably well-reproduced, particularly in the case of the TPSS method and the δ_{33} component (see Figure 5.12(c)).

Generally, there are multiple factors which could contribute to the lack of a perfect correlation between the experimental and computed chemical shift tensor parameters. Firstly, cluster models do not allow for a full treatment of the effect of crystal packing on the computed NMR parameters. The gauge-including projector-augmented wave (GIPAW) DFT method[52] enables calculations using periodic boundary conditions; however, the volume of the unit cells (2392.2 Å^3 for **12** to 5085.9 Å^3 for **13**) of these compounds results in computational demands which are beyond our current capabilities. Additionally, several theoretical[53,54,55] reports describe the challenges in establishing the best ^{77}Se absolute shielding scale;[40] the selenium chemical shift range is over 3000 ppm and the shielding constants are subject to relativistic effects.[45,56]

The P=Se distance, $d_{P=Se}$, is different for each of the compounds studied here (Table 5.2). It is well known from the IUPAC definition that the distance R—X of the halogen bond donor tends to increase when involved in a halogen bond;[57] however, in this case the same type of change is also noted for the halogen bond acceptor, Y—Z (i.e., Se=P). As mentioned above, a plot of experimental $\delta_{iso}(^{77}Se)$ values vs $d_{P=Se}$ for the compounds studied

herein shows a reasonable linear correlation, with increased values of $d_{P=Se}$ corresponding to increased chemical shifts (Figure 5.12(a)). Weak inverse correlations of $\delta_{iso}(^{31}P)$ with $d_{P=Se}$ are also noted (see Figure 5.13(a)).

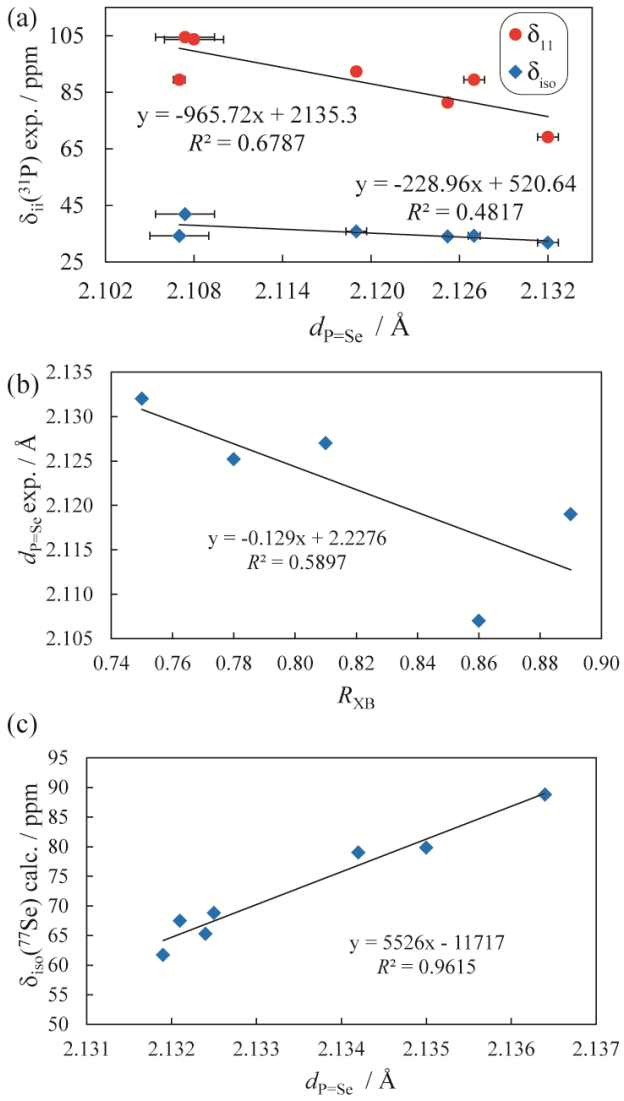

Figure 5.13 (a) Experimental ^{31}P chemical shifts as a function of the selenium-phosphorus distances, $d_{P=Se}$. (b) Selenium-phosphorus distances as a function of the cumulative halogen bond reduced distance parameter, R_{XB}. (c) ZORA calculated ^{77}Se isotropic chemical shifts as a function of $d_{P=Se}$. For (c), computations (ZORA revPBE) were performed on a cluster model ($(CH_3)_3PSe\cdots ICF_3$) where the I···Se distance was increased by increments of 0.04 Å between 3.40 (R_{XB} = 0.85) and 3.66 Å (R_{XB} = 0.92) and kept fixed while the model was geometry optimized.

This experimental observation was corroborated using ZORA calculations on the model halogen bonded complex $(CH_3)_3P{=}Se\cdots ICF_3$. The halogen bond distance ($d_{I\cdots Se}$) was

varied systematically between 3.40 (R_{XB} = 0.85) and 3.66 Å (R_{XB} = 0.92) in 0.04 Å increments. These R_{XB} values reflect the range observed experimentally. As can be seen in Figure 5.12(d), as the halogen bonding interaction is weakened, the optimal value of $d_{P=Se}$ decreases. When the calculated values of $\delta_{iso}(^{77}Se)$ are plotted as a function of $d_{P=Se}$, a linear correlation (R^2 = 0.9615) in accord with that observed experimentally is obtained (see Figure 5.13(c)).

5.3.10 *J(^{77}Se,^{31}P) Coupling in Halogen Bonds. Correlation with Structure and DFT NLMO Analysis*

Shown in Figure 5.14(a) is a plot of the calculated $J(^{77}Se, ^{31}P)$ coupling constants versus the experimentally measured values. For the calculations, two different cluster models were used. The first model (blue squares) consists of the halogen bond donor and acceptor molecules as depicted in Figure 5.1. The second model (black circles) consists only of $(arene)_3PSe$ molecules, omitting the halogen bond donor(s). By comparing the results of the two sets of revPBE calculations with the experimental data, one can assess the impact of the halogen bond to iodine on the values of $J(^{77}Se, ^{31}P)$. That is, are the values of $J(^{77}Se, ^{31}P)$ sensitive to the halogen bonding interaction? When the two linear fits are compared, it is seen that inclusion of the halogen bond donor(s) in the model results in a slope closer to unity (0.714 vs 0.315) and an increased correlation coefficient (R^2 = 0.9719 vs 0.8761). This suggests that indeed the halogen bond to selenium is manifested in the value of $J(^{77}Se, ^{31}P)$. Analysis of the analogous data obtained using the TPSS functional (Tables 5.5 and 5.6) also shows improved slopes (0.652 vs 0.306) and correlation coefficients (0.9371 vs 0.8832) when the halogen bond donors are included in the models. The root-mean-squared

deviation (RMSD) between the experimental and calculated data when the halogen bond donors are included is 37 Hz for the revPBE functional and 82 Hz for the TPSS functional.

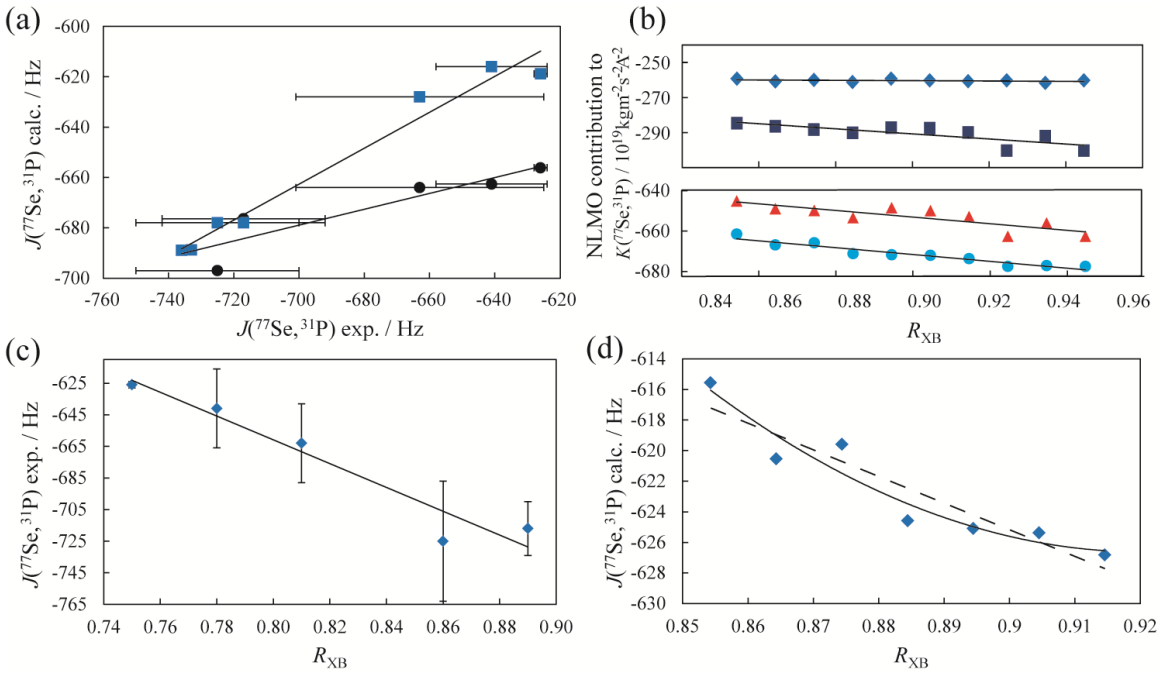

Figure 5.14 (a) Calculated versus experimental $J(^{77}Se, ^{31}P)$ coupling constants for the compounds in Table 5.4 (revPBE ZORA/TZP). Two models were used: blue squares account for the model where the molecule of the halogen bonding acceptor and donor are included and the black circles omit all halogen bond acceptor(s) in the model. The solid lines are linear fits: (a, blue squares) $J(^{77}Se,^{31}P)^{calc.} = 0.714\ J(^{77}Se,^{31}P)^{exp.} - 163$ Hz, $R^2 = 0.9719$, RMSD = 37 Hz, and (a, black circles) $J(^{77}Se,^{31}P)^{calc.} = 0.315\ J(^{77}Se,^{31}P)^{exp.} - 458$ Hz, $R^2 = 0.8761$. (b) Plot of the sum of Lewis and non-Lewis largest NLMO contributions to $J(^{77}Se,^{31}P)$ as a function R_{XB} for the $(CH_3)_3PSe\cdots ICF_3$ cluster model (Top: blue diamonds represent the Se=P bonding orbital ($K = -9.81\ R_{XB} - 251.5$) and black squares represent the selenium lone pair orbital ($K = -144.9\ R_{XB} - 160.4$). Bottom: red triangles represent the sum of the contributions from the selenium lone pair orbital, the phosphorus lone pair orbital, and the Se=P bonding orbital ($K = -163.9\ R_{XB} - 505.6$) while the turquoise circles represent the total coupling including all other minor contributions ($K = -169.6\ R_{XB} - 518.9$)). (c) Experimental $J(^{77}Se, ^{31}P)$ coupling constants for the compound in Table 4 as a function of R_{XB} ($J(^{77}Se,^{31}P)^{exp.} = -752.6\ R_{XB} - 58.77$ Hz, $R^2 = 0.9304$). (d) Calculated $J(^{77}Se, ^{31}P)$ coupling constants as a function of R_{XB} for the model compound $(CH_3)_3PSe\cdots ICF_3$ ($J(^{77}Se,^{31}P)^{calc.} = 2395.6\ (R_{XB})^2 - 4411.5(R_{XB}) + 1404.3$ Hz, $R^2 = 0.9699$ or $J(^{77}Se,^{31}P)^{calc.} = -174.15\ R_{RB} - 468.48$ Hz, $R^2 = 0.8702$.) For the R_{XB} values in (c), when more than one halogen bond donor interacts with the Se=P site, a cumulative value was used ($R_{XB} = 1 - (1-R_{XB}(donor1)) - (1-R_{XB}(donor2)) - \ldots$).

As shown in Figure 5.14(c), experimentally the $J(^{77}Se, ^{31}P)$ coupling magnitudes are observed to increase as the halogen bonds to selenium weaken. To account for multiple iodine halogen bond donors to a single selenium site, a cumulative R_{XB} value was used in this plot (i.e., R_{XB} = 1 - (1-R_{XB}(donor1)) - (1-R_{XB}(donor2)) - …). To further understand the origins of the variations in $J(^{77}Se,^{31}P)$ for halogen-bonded complexes, additional calculations were carried out, including a NLMO DFT study. This type of calculation allows one to analyze the contributions of key molecular orbitals to the *J*-coupling.[18,20] Calculations on a $(CH_3)_3PSe\cdots ICF_3$ cluster model reproduce the experimental correlation between $J(^{77}Se, ^{31}P)$ and R_{XB} (see Figure 5.14(d)).

An analysis of the largest NLMO contributions to the $J(^{77}Se,^{31}P)$ coupling values was conducted for the $(CH_3)_3PSe\cdots ICF_3$ cluster model as a function of the R_{XB} value. Three major contributions are seen to influence the *J*-coupling value: a selenium lone pair orbital (~43%)), the bonding P=Se orbital (~38 %) and the phosphorus core orbital (~15%). Figure 5.14 (b) shows how the first two of these contributions vary as a function of the R_{XB} value; it is clear that the variations in the contribution from the selenium core orbital determine the overall trend. The lower part of Figure 5.14(b) shows how the sum of the three most important contributions changes with the value of R_{XB} (red triangles) and how the sum of all contributions follows the same trend (turquoise circles).

Calculations for compounds **11**, **12**, and **13** demonstrate that the isotropic $J(^{77}Se,^{31}P)$ coupling constant originates largely from the ZORA analogue of the Fermi-contact spin-dipolar mechanism (~80%) with non-negligible contributions from the paramagnetic spin-orbit mechanism (~20%). Shown in Figure 5.15 are the NLMOs resulting in the largest contributions to the isotropic *J*-coupling. (Note that only the three largest contributions are

listed and for this reason the sums differ from 100%.) For Ph_3PSe and for the halogen-bonded compounds, the largest contribution to $J(^{77}Se,^{31}P)$ arises from the selenium lone pair orbital and its relative contribution is about ~57 % except for in compound **12** (81.7 %) and site 2 in **13** (81.7 %), which both have the smallest experimental *J*-coupling values (-626(2) Hz, -641(25) Hz for **12** and site 2 in **13**, respectively), the longest P=Se bonds (2.1320 Å and 2.1252 Å for **12** and site 2 in **13**, respectively), and the strongest halogen bonding interactions. The P=Se bonding orbital makes the second largest contribution to the *J*-coupling. The relative contributions are about 30 %, except again for the sites having the strongest halogen bonds, **12** (-16.9 %) and site 2 in **13** (-16.6 %). Percentage contributions are negative if they are opposite in sign to the sum of all other contributions and therefore serve to reduce the total value. Finally, another contribution to $J(^{77}Se,^{31}P)$ arises from the phosphorus core orbital or selenium core orbital. The NLMO contributions from the iodine lone pair are minor (~ 0.1 to 0.6 %; see Figure 5.16).

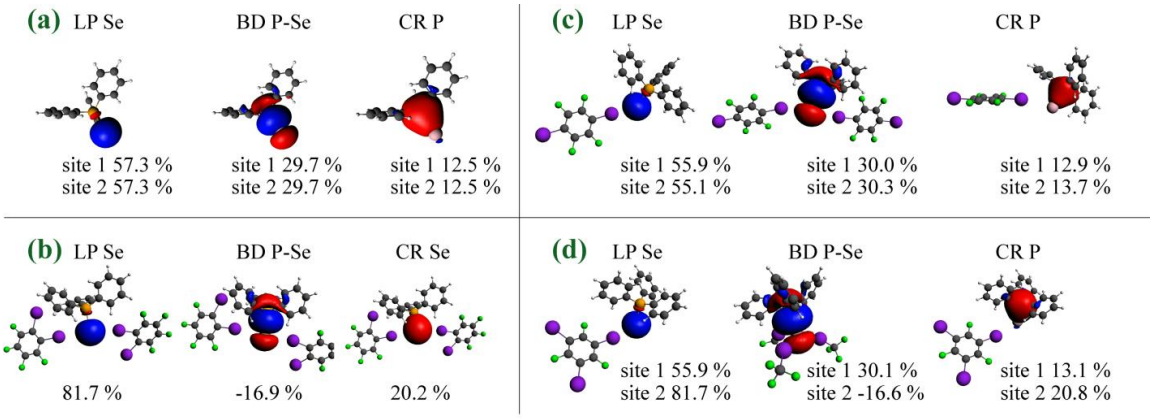

Figure 5.15 Selected NLMOs having the largest contributions to the isotropic $J(^{77}Se, ^{31}P)$ coupling values for halogen-bonded systems (**12** (b), **11** (c), **13** (d)) and Ph_3PSe (a). The percentages underneath the orbitals represent the contribution from the selenium lone pair (LP Se), the bonding orbital between P and Se (BD P-Se) orbital and the P core orbital (CR P) or Se core orbital (CR Se) to the isotropic *J*-coupling constant for each distinct selenium site. Note that the totals do not sum to 100% because only the largest contributions are shown.

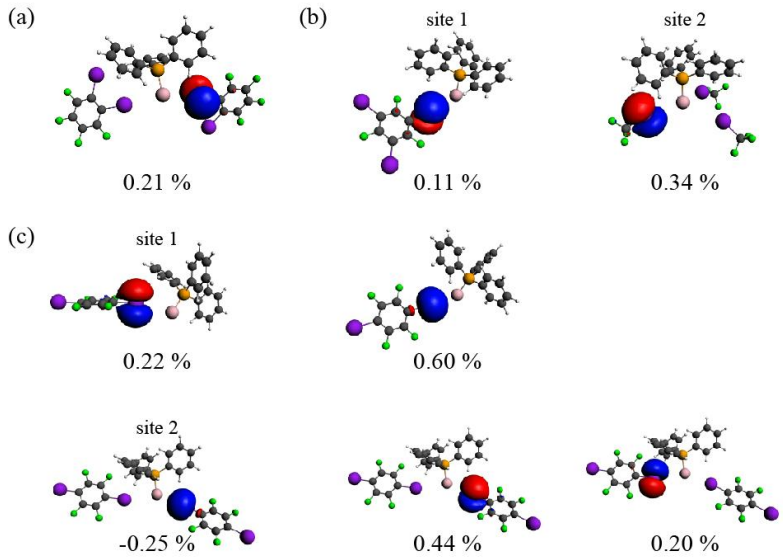

Figure 5.16 Iodine lone pair NLMOs having the next-largest contributions to the isotropic nuclear spin-spin $J(^{77}Se,^{31}P)$ coupling values in 2 (a), 3 (b), and 1 (c). The percentages underneath the orbitals represent the minor contributions to the $J(^{77}Se,^{31}P)$ coupling values for the XB systems.

5.4 CONCLUSIONS

A series of compounds featuring P=Se···I-C halogen bonds has been prepared and characterized by XRD and ^{31}P, ^{77}Se, and ^{13}C SSNMR spectroscopy. Phosphorus and selenium chemical shift tensors as well as $J(^{77}Se,^{31}P)$ coupling constants have been measured and interpreted with the aid of DFT computations. Informed by a comparison with pure triphenylphosphine selenide, the following conclusions are drawn:

- ^{77}Se isotropic chemical shifts increase due to halogen bonding with iodine, and correlate with the P=Se distance which in turn correlates inversely with the reduced halogen bond distance parameter R_{XB};
- $J(^{77}Se, ^{31}P)$ coupling constants increase in magnitude as the selenium-iodine halogen bonds weaken;
- computed $J(^{77}Se, ^{31}P)$ coupling constants improve relative to the experimental values when the iodinated halogen bond acceptor is included in the structural model used for the calculations, suggesting that $J(^{77}Se, ^{31}P)$ coupling constants are at least in part diagnostic of the halogen bond;
- an NLMO analysis provides insight into the orbitals which contribute to $J(^{77}Se, ^{31}P)$; for example, contributions from the selenium lone pair orbital tend to dominate both the magnitude and trends in $J(^{77}Se, ^{31}P)$, with the selenium-phosphorus bonding orbital being the second-largest contributor.

To our knowledge, this study represents the first systematic experimental examination of *J*-coupling constants within the halogen bond fragment R-X···Y-Z. It will be of interest in future work to examine *J*-couplings across the halogen bond, e.g., *J*(R, Y). The existence of such couplings and their value in understanding the halogen bond have been examined

computationally for small model systems;[15] however, experimental SSNMR measurements are likely to be challenging due to the NMR properties of the nuclei involved in typical halogen bonds and the probable small magnitude of the coupling constants.

5.5 REFERENCES FOR CHAPTER 5

1 A.-C. C. Carlsson, J. Gräfenstein, A. Budnjo, J. L. Laurila, J. Bergquist, A. Karim, R. Kleinmaier, U. Brath, M. Erdélyi, (2012), *J. Am. Chem. Soc.*, 134, 5706.

2 X. Q. Yan, X. R. Zhao, H. Wang, W. J. Jin, (2014), *J. Phys. Chem. B.*, 118, 1080.

3 J. Viger-Gravel, I. Korobkov, D. L. Bryce, (2011), *Cryst. Growth Des.*, 11, 4984.

4 J. Viger-Gravel, S. Leclerc, I. Korobkov, D. L. Bryce, (2013), *CrystEngComm*, 15, 3168.

5 R. J. Attrell, C. M. Widdifield, I. Korobkov, D. L. Bryce, (2012), *Cryst. Growth Des.*, 12, 1641.

6 C. M. Widdifield, G. Cavallo, G. A. Facey, T. Pilati, J. Lin, P. Metrangolo, G. Resnati, D. L. Bryce, (2013), *Chem. Eur. J.*, 19, 11949.

7 S. Grzesiek, F. Cordier, V. Jaravine, M. Barfield, (2004), *Prog. Nucl. Magn. Reson. Spectrosc.*, 45, 275.

8 A. J. Dingley, S. Grzesiek, (1998), *J. Am. Chem. Soc.*, 26, 8293.

9 S. P. Brown, M. Pérez-Torralba, D. Sanz, R. M. Claramunt, L. Emsley, (2002), *Chem. Commun.*, 1852.

10 Y.-X. Wang, J. Jacob, F. Cordier, P. Wingfield, S. J. Stahl, S. Lee-Huang, D. Torchia, S. Grzesiek, A. Bax, (1999), *J. Biomol. NMR*, 14, 181.

11 H. Benedict, I. G. Shenderovich, O. L. Malkina, V. G. Malkin, G. S. Denisov, N. S. Golubev, H.-H. Limbach, (2000), *J. Am. Chem. Soc.*, 122, 1979.

12 N. S. Golubev, I. G. Shenderovich, S. N. Smirnov, G. S. Denisov, H.-H. Limbach, (1999), *Chem. Eur. J.*, 5, 492.

13 M. P. Ledbetter, G. Saielli, A. Bagno, N. Tran, M. V. Romalis, (2012), *Proc. Natl. Acad. Sci. U. S. A.*, 109, 12393.

14 M. J. Plevin, D. L. Bryce, J. Boisbouvier, (2010), *Nat. Chem.*, 2, 466.

15 J. E. Del Bene, I. Alkorta, J. Elguero, (2008), *J. Phys. Chem. A*, 112, 7925.

16 R. Garcia-Rodríguez, H. Liu, (2014), *J. Phys. Chem. A*, 118, 7314.

17 P. A. W. Dean, M. K. Hughes, (1980), *Can. J. Chem.*, 58, 180.

18 J. Autschbach, (2007), *J. Chem. Phys.*, 127, 124106.

19 A. J. Rossini, R. W. Mills, G. A. Briscoe, E. L. Norton, S. J. Geier, I. Hung, S. Zheng, J. Autschbach, R. W. Schurko, (2009), *J. Am. Chem. Soc.*, 131, 3317.

20 S. Zheng, J. Autschbach, (2011), *Chem. Eur. J.*, 17, 161.

21 A. Sutrisno, A. Y. H. Lo, J. A. Tang, J. L. Dutton, G. J. Farrar, P. J. Ragogna, S. Zheng, J. Autschbach, R. W. Schurko, (2009), *Can. J. Chem.*, 87, 1546.

22 L. A. O'Dell, R. W. Schurko, K. J. Harris, J. Autschbach, C. I. Ratcliffe, (2011), *J. Am. Chem. Soc.*, 133, 527.

23 H. D. Arman, E. R. Rafferty, C. A. Bayse, W. T. Pennington, (2012), *Cryst. Growth Des.*, 12, 4315.

24 Bruker AXS: Bruker Suite, version 2008/3, (2008), Madison, WI, Bruker AXS Inc.

25 G. M. Sheldrick, (2008), *Acta Crystallogr., Sect. A: Found. Crystallogr.*, 64, 112.

26 J. Schaefer, E. O. Stejskal, (1976), *J. Am. Chem. Soc.*, 98, 1031.

27 W. L. Earl, D. L. VanderHart, (1982), *J. Magn. Reson.*, 48, 35.

28 A. K. Jameson, C. J. Jameson, (1987), *Chem. Phys. Lett.*, 134, 461.

29 M. J. Collins, C. I. Ratcliffe, J. A. Ripmeester, (1986), *J. Magn. Reson.*, 68, 172.

30 D. L. Bryce, G. M. Bernard, M. Gee, M. D. Lumsden, K. Eichele, R. E. Wasylishen, (2001), *Can. J. Anal. Sci. Spectrosc.*, 46, 46.

31 K. Eichele, WSolids1 ver. 1.20.21, (2013), Tübingen, Germany, Universität Tübingen.

32 M. Bak, J. T. Rasmussen, N. C. Nielsen, (2000), *J. Magn. Reson.*, 147, 296.

33 P. W. Codding, K. A. Kerr, (1979), *Acta Crystallogr., Sect. B: Struct. Sci.*, 35, 1261.

34 (a) G. Schreckenbach, T. Ziegler, (1995), *J. Phys. Chem.*, 99, 606. (b) S. K. Wolff, T. Ziegler, E. van Lenthe, E. J. Baerends, (1999), *J. Chem. Phys.*, 110, 7689.

35 J. M. Tao, J. P. Perdew, V. N. Staroverov, G. E. Scuseria, (2003), *Phys. Rev. Lett*., 91, 146401.

36 J. Autschbach, T. Ziegler, (2000), *J. Chem. Phys.*, 113, 936.

37 E. D. Glendening, J. K. Badenhoop, A. E. Reed, J. E. Carpenter, J. A. Bohmann, C. M. Morales, F. Weinhold, (2001), NBO version 5.0, Madison, WI, Theoretical Chemistry Institute, University of Wisconsin; http://www.chem.wisc.edu/~nbo5

38 (a) J. P. Perdew, K. Burke, M. Ernzerhof, (1996), *Phys. Rev. Lett.*, 77, 3865. (b) J. P. Perdew, K. Burke, M. Ernzerhof, (1997), *Phys. Rev. Lett.*, 78, 1396.

39 S. Adiga, D. Aebi, D. L. Bryce, (2007), *Can. J. Chem.*, 85, 496.

40 C. J. Jameson, A. K. Jameson, (1987), *Chem. Phys. Lett.*, 135, 254.

41 C. J. Jameson, A. DeDios, A. K. Jameson, (1990), *Chem. Phys. Lett.*, 167, 575.

42 (a) A. Bondi, (1964), *J. Phys. Chem.*, 68, 441. (b) R. D. Shannon, (1976), *Acta Crystallogr., Sect. A: Found. Crystallogr*., 32, 751.

43 (a) P. Pyykkö, A. Görling, N. Rösch, (1987), *Mol. Phys.*, 61, 195; (b) M. Kaupp, O. L. Malkina, V. G. Malkin, (1997), *Chem. Phys. Lett.*, 265, 55; (c) M. Kaupp, O. L. Malkina, V. G. Malkin, P. Pyykkö, (1998), *Chem. Eur. J.*, 4, 118.

44 R. D. Chambers, (1996), *J. Chem. Soc. Perkin Trans. 1: Organic and Bio-Organic Chemistry*, 14, 1659.

45 B. A. Demko, K. Eichele, R. E. Wasylishen, (2006), *J. Phys. Chem. A*, 110, 13537.

46 G. Grossmann, M. J. Potrzebowski, U. Fleischer, K. Krüger, O. L. Malkina, W. Ciesielski, (1998), *Solid State Nucl. Magn. Reson.*, 13, 71.

47 U. Haubenreisser, U. Sternberg, A.-R. Grimmer, (1987), *Mol. Phys.*, 60, 151.

48 H. Bai, R. K. Harris, (1992), *J. Magn. Reson.*, 96, 24.

49 D. L. Bryce, (2009), *Tensor Interplay*, R. K. Harris, R. E. Wasylishen, M. J. Duer (Eds.), *NMR Crystallography*, Chichester, UK, John Wiley and Sons Ltd.

50 (a) G. te Velde, F. M. Bickelhaupt, S. J .A. van Gisbergen, C. Fonseca Guerra, E. J. Baerends, J. G. Snijders, T. Ziegler, (2001), *J. Comp. Chem.*, 22, 931. (b) C. Fonseca Guerra, J. G. Snijders, G. te Velde and E. J. Baerends, (1998), *Theor. Chem. Acc.*, 99, 391. (c) E. J. Baerends *et al.* (2010), *Amsterdam Density Functional Software ADF2009.01 SCM*; Amsterdam, The Netherlands, Vrije Universiteit: http://www.scm.com/.

51 M. J. Frisch *et al.*, (2009), *Gaussian 09*, revision A.02, Wallingford, CT, Gaussian, Inc,.

52 (a) C. J. Pickard, F. Mauri, (2001), *Phys. Rev. B*, 63, 245101. (b) J. R. Yates, C. J. Pickard, F. Mauri, (2007), *Phys. Rev. B*, 76, 024401. (c) M. Profeta, F. Mauri, C. J. Pickard, (2003), *J. Am. Chem. Soc.*, 125, 541. (c) S. J. Clark, M. D. Segall, C. J. Pickard, P. J. Hasnip, M. I. J. Probert, K. Refson, M. C. Payne, (2005), *Z. Kristallogr.*, 220, 567.

53 J. Jokisaari, P. Lazzeretti, P. Pyykkö, (1988), *Chem. Phys.*, 123, 339.

54 M. Bühl, W. Thiel, U. Fleischer, W. Kutzelnigg, (1995), *J. Phys. Chem.*, 99, 4000.

55 G. Schreckenbach, Y. Ruiz-Morales, T. Ziegler, (1996), *J. Chem. Phys.*, 104, 8605.

56 W. Nakanishi, S. Hayashi, Y. Katsura, M. Hada, (2011), *J. Phys. Chem. A*, 115, 8721.

57 G. R. Desiraju, P. S. Ho, L. Kloo, A. C. Legon, R. Marquardt, P. Metrangolo, P. A. Politzer, G. Resnati, K. Rissanen, (2013), *Pure Appl. Chem.*, 85, 1711.

6 CHEMICAL SHIFT ANISOTROPY AND RESIDUAL DIPOLAR COUPLING AS CHARACTERIZATION PROPERTIES OF THIOCYANATE AND SELENOCYANATE HALOGEN BOND ACCEPTORS

6.1 INTRODUCTION

Recently, Cauliez *et al.* published a report on the thiocyanate anion as a polydentate halogen bond acceptor.[1] The compounds they studied had the form $(R_4NSCN)_x$ (*ortho- or para*- $C_6F_4I_2)_y$ and $(R_4NSCN)_x$(*sym*- $C_6F_3I_3)_y$. They determined that both the sulfur and nitrogen atoms of the thiocyanate moiety engaged in halogen bonding interactions as previously described by Bock and Holl for tetraiodoethylene, tetraiodothiophene, and *N*-methyltetraiodopyrrole.[2] However, Cauliez *et al.* observed C-S···I bond angles of about 90° as well as multiple iodines interacting with sulfur and strong deviations from linearity in the C≡N···I interactions (145-170°).[1] These interesting results prompted us to initiate an investigation of similar compounds, $(R_4NSCN)_x$(*p*-$C_6F_4I_2)_y$ and $(R_4NSeCN)_x$(*o*- or *p*-$C_6F_4I_2)_y$, with a focus on the potential information which may be available through SSNMR spectroscopy and on the interaction motifs of the selenocyanate ion versus the thiocyanate ion. Selenium has been observed to participate in halogen bonding in a mutant form of T4 lysozyme, selenoethers, and selenoamides.[3,45] With four readily observable NMR-active nuclei (^{13}C, $^{14/15}N$, and ^{77}Se) involved directly and indirectly in this non-covalent interaction in our compounds of interest, a good deal of information may potentially be gained from their CS tensors. SSNMR powder line shapes provide a wealth of structural information and insight into the interactions which are characteristic of a particular nuclear environment, such as dipolar coupling (R_{DD}) and chemical shift anisotropies (CSA).[6]

In the current work, the effect of halogen bonding on the compounds mentioned above using XRD, multinuclear solid-state magnetic resonance, and quantum chemistry

was investigated. Possible correlations between halogen bonding and the NMR parameters were described. Results are compared with those for simple thiocyanate and selenocyanate salts.

6.2 EXPERIMENTAL SECTION

6.2.1 *Sample Preparation*

n-Bu_4NSCN was purchased from Aldrich whereas ^{13}C isotopically enriched KSCN (99.99 %) and ^{15}N isotopically enriched KSCN (> 98 %) were purchased from ISOTEC and all compounds were used without further purification. Me_4NSCN, $Me_4NS^{13}CN$, $Me_4NSC^{15}N$ and Me_4NSeCN were synthesized according to published procedures.[7] Melting points were measured and found to be consistent with those previously reported[8] and crystal structures were also solved using single-crystal XRD. (*n*-Bu_4NSCN)(*p*-$C_6F_4I_2$) (**16**) was synthesized as described by Cauliez *et al.*[1] The halogenated compounds (Me_4NSCN)(*p*-$C_6F_4I_2)_2$ (**17**), (Me_4NSeCN)(*p*-$C_6F_4I_2)_2$ (**14**), and (Me_4NSeCN)(*o*-$C_6F_4I_2)_2$ (**15**) were synthesized by dissolving the relevant compounds in a minimum amount of warm EtOH (95%), using a warm water bath (50 °C). For each synthesis, two equivalents of *p*-DITFB or *o*-DITFB were mixed with one equivalent of $Me_4NS^{13}CN$, $Me_4NSC^{15}N$, or Me_4NSeCN, respectively.

6.2.1.1 *Synthesis of isotopically labelled compounds*

These compounds were synthesized according to a previously reported procedure.[9] Isotopically (^{13}C) enriched $Me_4NS^{13}CN$ was prepared, as shown in reaction 6.1, from a mixture of labelled 99.99 % $KS^{13}CN$ (106 mg) and KSCN in natural abundance (144 mg)

(total of 250 mg, 2.57 mmol, 1 eq) which was then mixed with tetramethylammonium chloride (375 mg, 3.42 mmol, 1.33 eq.) in dry MeCN (1.8 mL). The mixture was refluxed for an hour under an inert atmosphere. KCl precipitate was eliminated by filtration using a frit. The desired product was precipitated by adding diethyl ether dropwise to the filtrate. The flask was placed in an ice bath to induce crystallization of the desired compound. $Me_4NS^{13}CN$ (~42 % ^{13}C-labelled thiocyanate) was filtered and recrystallized from acetonitrile (slow evaporation). $Me_4NS^{13}CN$ was obtained in 60 % yield. Nitrogen-15 labelled $Me_4NSC^{15}N$ was prepared using the same procedure, however 1 g of KSCN was used (500 mg of labelled $KSC^{15}N$ combined with 500 mg KSCN, 10.3 mmol, 1 eq) and 1.5 g of Me_4NCl (13.69 mmol, 1.33 eq.) was added and refluxed in 4 mL of dry acetonitrile. This gave the desired product in 75 % yield (~ 50 % labelled $Me_4NSC^{15}N$). Me_4NSeCN, as shown in reaction 6.2, was prepared using the same protocol as stated above, however, KSeCN (3g, 20.82 mmol, 1 eq) was mixed with Me_4NCl (3.03 g, 27.70 mmol, 1.33 eq.) and refluxed in 10.5 mL of MeCN without the use of an inert atmosphere. Me_4NSeCN was isolated in 92 % yield. Melting points were consistent with those previously reported (Me_4NSCN m.p. 292- 297 °C; Me_4NSeCN m.p. 267-268 °C).[9] These compounds were used as is in the next step to prepare the halogen bonding complexes. Crystal structures of these compounds were solved with single crystal XRD, and their .cif files are reported in this work.

$$Me_4NCl_{(aq)} + KSCN_{(aq)} + MeCN_{(l)} \rightarrow \boldsymbol{Me_4NSCN_{(aq)}} + KCl_{(s)} + MeCN_{(l)} \quad [6.1]$$

$$Me_4NCl_{(aq)} + KSeCN_{(aq)} + MeCN_{(l)} \rightarrow \boldsymbol{Me_4NSeCN_{(aq)}} + KCl_{(s)} + MeCN_{(l)} \quad [6.2]$$

6.2.2 *X-ray Crystallography*

Crystal structures were collected at the University of Ottawa in the XRD Laboratory. Data collection results for compounds **14**, **15**, and **17** represent the best data sets obtained in several trials for each sample. The crystals were mounted on thin glass fibres using paraffin oil. Data for **17** were collected at 296.15 K. Crystals of the other two compounds were cooled to 200.15 K prior to data collection. Data were collected on a Bruker AXS SMART single crystal diffractometer equipped with a sealed Mo tube source (wavelength 0.71073 Å) APEX II CCD detector. Raw data collection and processing were performed with the APEX II software package from Bruker AXS.[10] Diffraction data for **14** and **17** were collected with a sequence of 0.5° ω scans at 0, 120, and 240° in φ. Diffraction data for **15** were collected with a sequence of 0.5° ω scans at 0, 90, 180, and 270° in φ due to the lower symmetry of the crystal unit cell to provide adequate data coverage. Initial unit cell parameters were determined from 60 data frames collected for different sections of the Ewald sphere. Semi-empirical absorption corrections based on equivalent reflections were applied.[11] Systematic absences in the diffraction data set and unit cell parameters were consistent with monoclinic *C*2/*c* (№15) for compound **17**, monoclinic $P2_1/n$ (№14) for compound **14**, and triclinic $P\bar{1}$ (№2) for compound **15**. Solutions in the centrosymmetric space groups for all compounds yielded chemically reasonable and computationally stable refinement results. All hydrogen atoms were treated as idealized contributions. All scattering factors are contained in several versions of the SHELXTL program library, with the latest version used being v.6.12.[12] Crystallographic data are reported in Table 6.1.

Table 6.1 Crystallographic data and selected data collection parameters

compound	**14**	**15**	**17**
empirical formula	$C_{17}H_{12}F_8I_4N_2Se$	$C_{17}H_{12}F_8I_4N_2Se$	$C_{17}H_{12}F_8I_4N_2S$
formula weight	982.85	982.85	935.95
crystal size, mm	0.20 x 0.17 x 0.17	0.27 x 0.17 x 0.17	0.24 x 0.17 x 0.13
crystal system	monoclinic	triclinic	monoclinic
space group	$P2_1/n$ (№14)	$P\bar{1}$ (№2)	$C2/c$(№15)
Z	4	2	4
a, Å	9.4954(3)	8.7214(7)	12.2784(3)
b, Å	24.6517(8)	11.0795(9)	9.0581(3)
c, Å	11.4085(4)	13.4793(11)	23.5345(6)
α, °	90	93.753(4)	90
β, °	103.240(1)	90.429(4)	94.268(2)
γ, °	90	97.315(4)	90
volume, Å^3	2599.49(15)	1288.95(18)	2610.22(13)
calculated density, Mg/m^3	2.511	2.532	2.382
absorption coefficient, mm^{-1}	6.260	6.313	4.920
F(000)	1784	892	1712
Θ range for data collection,	2.01 - 28.30	2.32 - 28.35	2.80 - 26.47
limiting indices	h = ±10, k = ±21, l =	h = ±11, k = ±14, l =	h = ±15, k = ±11, l =
reflections collected /	16$\bar{1}$48 / 6393	26$\bar{9}$61 / 6346	15$\bar{6}$07 / 2681
R(int)	0.0183	0.0262	0.0273
completeness to Θ = 28.32,	98.9	98.4	98.8
max. and min. transmission	0.4158 and 0.3674	0.4941 and 0.2906	0.5672 and 0.3847
data / restraints / parameters	6393 / 0 / 289	6346 / 0 / 289	2681 / 0 / 159
goodness-of-fit on F^2	1.018	1.073	1.022
final R indices [I>2σ(I)]	R_1 = 0.0276, wR_2 = 0.0621	R_1 = 0.0228, wR_2 = 0.0573	R_1 = 0.0289, wR_2 = 0.0760
R indices (all data)	R_1 = 0.0379, wR_2 = 0.0656	R_1 = 0.0255, wR_2 = 0.0588	R_1 = 0.0394, wR_2 = 0.0826
largest diff. peak/hole, e·Å^{-3}	0.477 / -0.946	0.907 / -1.382	0.555 / -0.646

6.2.2.1 *Refinement information*

The structures were solved by direct methods, completed with difference Fourier synthesis, and refined with full-matrix least-squares procedures based on F^2. In the structure of **17**, molecules of diiodotetrafluorobenzene are located on the inversion center, and the thiocyanate anion is located on 2-fold rotation axes and disordered over two positions by symmetry with 50 % : 50 % occupancies, and the tetramethylammonium cation

is located on the 2-fold axes. In the structures of **14** and **15**, all moieties are located in general positions. Both compounds **14** and **17** demonstrate enlarged thermal parameters for the carbon atoms of the tetramethylammonium groups. In the case of **17**, this increase of the thermal parameters is more pronounced, which can be explained by the higher data collection temperature. Attempts to treat the disorder by splitting the locations of above-mentioned carbon atoms on two positions each and refining the occupancies did not improve significantly the overall quality of the structure. The thermal parameters of the contributing disordered atoms were still exhibiting significant enlargement of one of the thermal parameters. After careful consideration, a decrease in the data to parameters ratio due to the disorder modeling was found to be more disadvantageous than the slight increase in the quality of the model. Therefore, the disorder modeling with occupation refinement was removed from the final structure.

6.2.3 ***Solid-State NMR Spectroscopy***

Static, MAS, CP, and Hahn-echo SSNMR experiments were used for the characterization of the halogenated compounds of the form $(R_4NeSCN)_x(o\text{- or } p\text{-}C_6F_4I_2)_y$ and $(R_4NSCN)_x(p\text{-}C_6F_4I_2)_y$ and the ammonium thiocyanate or selenocyanate salts of the form R_4NSCN or R_4NSeCN. Samples were powdered and packed in 7 and 4 mm o.d. zirconium oxide rotors.

6.2.3.1 *4.7 T Data.*

The majority of the SSNMR experiments for ^{13}C (ν_L = 50.307 MHz) were conducted on a Bruker Avance III 200 MHz wide bore spectrometer (4.7 T) equipped with

a 7 mm triple resonance HXY MAS probe or wideline probe. Experimental setup and pulse calibrations were performed using glycine, the standard for ^{13}C. The carbon chemical shifts were referenced to TMS by setting the chemical shift of the carbonyl peak of solid glycine to 176.4 ppm. [13]

A Hahn-echo (*i.e.* $\pi/2$-τ_1-π-τ_2-acq)[14] pulse sequence was used for the acquisition of a ^{13}C NMR spectrum of 99.9 % ^{13}C-enriched powdered KSCN under stationary conditions. Parameters used were: 4 μs 90° pulse length, 120 s recycle delay, and 1329 scans were collected for a total of 44 h of experimental time.

For CP experiments, the recycle delay used was 2 s for R_4NSCN and R_4NSeCN, and 14 s for the halogenated compounds. A contact time of 12 ms was optimized on Me_4NSCN. The proton 90° pulse lengths used were all ~3.5 μs. MAS spinning frequencies were 5 kHz. Total experimental time ranged from 1 h to 3 h for MAS experiments and 21 to 44 hours for static experiments. Proton decoupling using the SPINAL-64[15] method was applied during acquisition of the spectra of all samples.

6.2.3.2 *9.4 T Data.*

^{13}C (ν_L = 100.613 MHz), ^{77}Se (ν_L = 76.311 MHz), and ^{15}N (ν_L = 40.56 MHz) SSNMR experiments were carried out on a 400 MHz (B_0 = 9.4 T) Bruker Avance III wide-bore spectrometer equipped with a triple resonance 4 mm HXY MAS probe. Experimental setup and pulse calibration were performed using the recommended IUPAC standards for ^{13}C, ^{15}N, and ^{77}Se.[16,17] Nitrogen chemical shifts were referenced to NH_3 (*l*, 293 K) by setting the chemical shift of the ammonium peak in solid ammonium nitrate, $^{15}NH_4NO_3$, to 23.8 ppm.[16] Solid diammonium selenate, $(NH_4)_2SeO_4$, (δ_{iso} = 1040.2 ppm), was used to

reference the chemical shift of selenium with respect to $Se(CH_3)_2$ (*l*).[17] The contact times used for ^{13}C and ^{15}N CP experiments were optimized on labelled ^{13}C and ^{15}N Me_4NSCN and found to be 13 and 18 ms, respectively. For ^{77}Se NMR experiments, the recycle delay and contact time used were 5 s and 30 ms, respectively. The ^1H 90° pulse lengths used for the CP experiments were ~ 3 to 4 μs in all cases. Proton decoupling using the CW,[18] SPINAL-64,[15] or TPPM[19] methods was applied during acquisition of the spectra of all samples. In the case of ^{15}N, low decoupling powers were needed to observe the ammonium peak of the R_4NSCN (R= Me_4, *n*-Bu_4) and Me_4NSeCN salts; this is consistent with motion of the R_4N^+ groups.[20] For CPMAS experiments on ^{13}C and ^{15}N, the MAS spinning frequencies ranged between 2 and 8 kHz. For ^{77}Se, MAS frequencies ranged from 6 to 10 kHz. Total experimental time for ^{13}C CPMAS experiments varied between 15 minutes and 3 hours, and static experiments lasted 20 hours. Natural abundance ^{15}N experiments necessitated 12 to 44 hours for signal averaging, whereas ~50 % isotopically enriched samples needed one hour for Me_4NSCN to 40 hours for compound **17**. Experiment times for the ^{77}Se SSNMR experiments ranged from five minutes (Me_4NSeCN) to one day (**14** and **15**).

6.2.3.3 *Complementary data collected at 11.75 T*

Recording SSNMR data at more than one applied magnetic field can often increase the precision of the reported NMR parameters. ^{77}Se ($\nu_L(^{77}Se)$ = 95.382 MHz) and ^{15}N ($\nu_L(^{15}N)$ = 50.697 MHz) SSNMR experiments were carried out on a 500 MHz (B_0 = 11.75 T) Bruker AVANCE wide-bore spectrometer equipped with a 4 mm HXY MAS probe and 4 mm low-frequency double-resonance MAS probe for each nucleus, respectively. Experimental setup and pulse calibrations were performed using the recommended IUPAC

standards for ^{15}N and ^{77}Se nuclei as described in 9.4 T data section above.[21,22] The contact time and recycle delays used in ^{77}Se and ^{15}N CP experiments are the same values used on the 9.4 T spectrometer. The ^{1}H 90° pulse lengths used for the CP experiments were ~ 3 μs for ^{15}N and 5 μs for ^{77}Se. Proton decoupling using SPINAL64[23] or TPPM[24] was applied during acquisition of the spectra for all samples. The MAS frequencies used for ^{15}N are 2.5 kHz and 8 kHz. A total of 20 minutes or ~24 hours of experimental time was required for ^{15}N and ^{77}Se CPMAS experiments, respectively.

6.2.3.4 *21.1 T Data.*

^{14}N SSMNR experiments were performed on the 900 MHz (B_0 = 21.14 T) Bruker Avance II spectrometer at the National Ultrahigh-Field NMR Facility for Solids in Ottawa ($\nu_L(^{14}N)$ = 65.046 MHz) using a Bruker Avance II console and a 7.0 mm HX static probe built in-house. The WURST-QCPMG pulse sequence,[25] which combines the broadband excitation and refocusing capabilities[26] of frequency swept wideband, uniform rate, smooth truncation (WURST) pulses[27] with the signal enhancement of the quadrupolar Carr-Purcell-Meiboom-Gill (QCPMG) protocol was used.[28] For KSCN, the variable offset method was used with 100 kHz intervals and 10 pieces acquired, giving half of the spectrum. Each piece was collected with a spectral window of 2 MHz, 254 scans, and 64 echoes per scan. The parameters used were: 10 s recycle delay, 50 μs WURST pulse, 5 kHz spikelet separation.

6.2.3.5 *Spectral Processing and Simulation.*

NMR spectra were processed using the Bruker TopSpin 3.0 program. For variable offset spectra, the different pieces were co-added to produce the whole spectrum. Spectral

simulations were performed using WSOLIDS1,[29] which incorporates the space-tiling algorithm of Alderman *et al.*[30] The spinning sidebands observed in the CPMAS NMR spectra were analyzed to obtain the CSA using the procedure of Herzfeld and Berger[31] with the program HBA.[32] The fit was then verified and refined using WSOLIDS1. Stack plots were produced using DMFit2010.[33]

6.2.4 *Computational Details*

A model was generated from the X-ray crystal structure atomic coordinates for each halogenated compound using one SCN^- or $SeCN^-$ anion and the nearest interacting (*p* or *o*)-DITFB moieties, where the X-ray structure demonstrates characteristic halogen bonding distances and angles. ^{77}Se magnetic shielding tensors were calculated for those models with the Gaussian 09 program.[34] The hybrid DFT functional, B3LYP,[35] was used for all calculations. A study of different basis sets was conducted and 6-311++G** was found to provide the most reliable results. A smaller basis set was used for iodine (6-311G**).

The shielding tensors contained in the Gaussian 09 output files were analyzed using a modified version of the EFGShield program (version 1.1).[36] The absolute shielding scale for ^{77}Se was used to convert shielding constants to chemical shifts.[37]

6.3 Results and Discussion

6.3.5 *X-ray Crystal Structures*

The X-ray crystal structures of the halogen compounds **14**, **15**, **16**, and **17** were collected. The crystallographic data for the new compounds may be found in Table 6.1.

Halogen bonding interactions are inferred from the observed short interatomic distances when compared with the sum of the van der Waals radii (I···N: 3.68 Å, I···S: 3.72 Å, and I···Se: 3.98 Å) or with the sum of the non-isotropic radii of Nyburg and Faerman[38] (I···N: 3.36 Å, I···S: 3.79 Å, and I···Se: 3.91 Å). As mentioned, halogen bonding is a highly directional interaction; the thiocyanate anion demonstrates bidentate character with ~90° bond angles for I···S-C and angles of 145 to 170° for I···N-C.[2, 1] For selenocyanate, one may anticipate observing I···Se-C angles varying between 90° and 120° in halogen bonding interactions, as selenium is analogous to sulfur. Interatomic N···I, S···I, and Se···I distances as well as I···N-C, I···S-C, and I···Se-C angles are presented in Table 6.2 for each compound. A description of the solid state structural motifs and correlations to halogen bonding interactions follows.

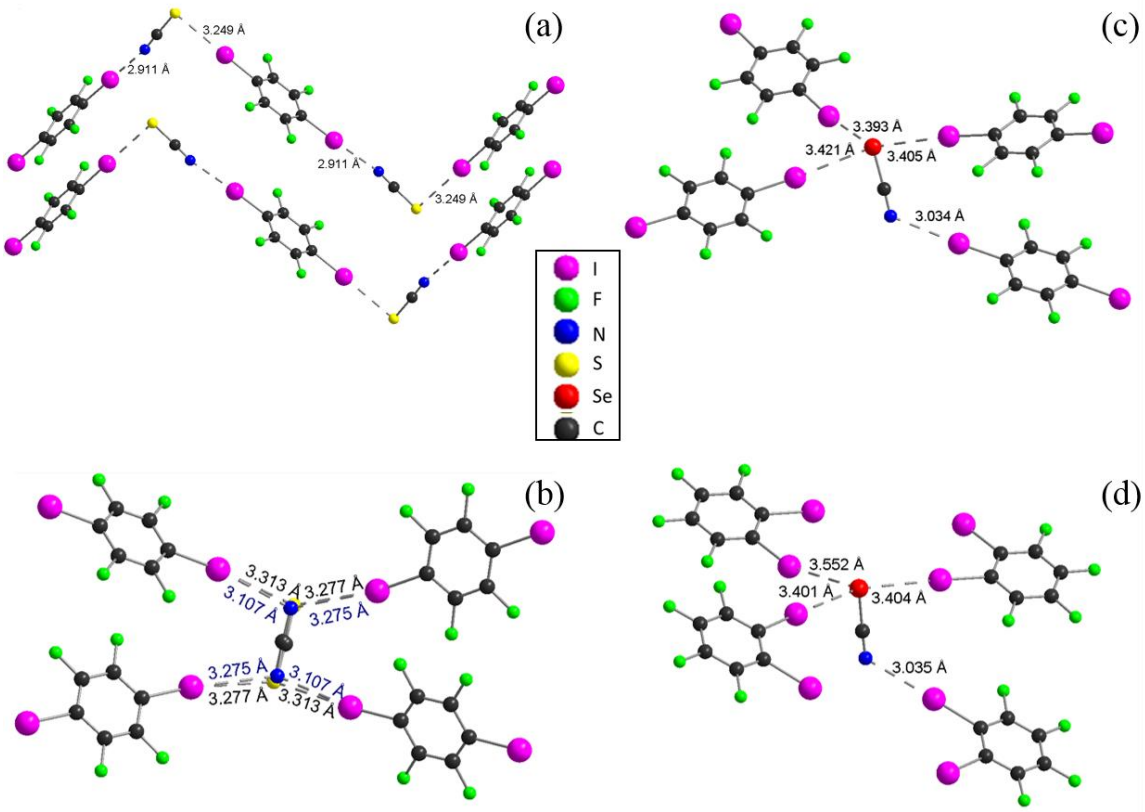

Figure 6.1 Halogen bonding environments around the thiocyanate and selenocyanate anions in compounds **14**-**17**. (a) A view of a chain formed by the bidentate anion SCN^- in compound **16**, (*n*-Bu_4NSCN)(*p*-$C_6F_4I_2$), along the *b* axis.[1] (b) Projection view along the *b* axis of the disordered compound **17**, (Me_4NSCN)(*p*-$C_6F_4I_2)_2$ (short contact distance in blue text corresponds to I-N and black corresponds to I-S) and (c) of one layer of **15**, (Me_4NSeCN)(*p*-$C_6F_4I_2)_2$ and (d) **14**, (Me_4NSeCN)(*o*-$C_6F_4I_2)_2$ showing the halogen bonds with $SeCN^-$. The R_4N^+ cations have been omitted for clarity.

Table 6.2 Selected intermolecular contact distances (Å) and angles (°)

compound	$d_{I\cdots N}$	R_{XB}	$\theta_{I\cdots NC}$	$d_{I\cdots Se}$	R_{XB}	$\theta_{I\cdots SeC}$
14	3.034	0.82	125.76	3.393	0.87	111.72
				3.421	0.88	83.91
				3.405	0.88	86.98
15	3.035	0.82	124.13	3.404	0.88	80.95
				3.552	0.92	89.95
				3.401	0.88	94.01
compound	$d_{I\cdots N}$	R_{XB}	$\theta_{I\cdots NC}$	$d_{I\cdots S}$	R_{XB}	$\theta_{I\cdots SC}$
16	2.911	0.79	169.19	3.249	0.88	87.51
17	3.275	0.89	114.11	3.277	0.88	104.23
	3.107	0.84	104.67	3.313	0.89	94.59

As mentioned, compound **16** has previously been characterized by Cauliez *et al.*;[1] the complex synthesized in our laboratory presents the same unit cell parameters. The halogen bonding occurring in this compound is consistent with that previously reported: the thiocyanate anion acts as a bidentate ligand forming long chains separated by the bulky tetrabutylammonium cation. The motif can be seen in Figure 6.1(a). The related compound **17** crystallizes in a monoclinic system with the *C*2/*c* space group. Disorder is present in the crystal structure, as the SCN^- anion may be aligned in two different directions. Figure 6.1(b) shows the two possible orientations thiocyanate can take in the unit cell. In one unit cell, the SCN^- ion is oriented in a unique direction and it is clear that either way the linear anion is placed, the I···N and I···S short contacts remain the same due to symmetry. It is the random position of SCN^- in the adjacent unit cell which could affect the NMR interaction tensors of the first SCN^- moiety; a broadened resonance could be observed in the ^{13}C and ^{15}N SSNMR spectra of **17** (*vide infra*). The *p*-$C_6F_4I_2$ molecules form unaligned columns along the *b* axis, and the cations (Me_4N^+) are located between those columns and

alternate with the SCN^- anion (Figure 6.2). Nitrogen and sulfur both interact with two iodines, as shown in Figure 6.1(b). In this compound, **17**, it is not clear if nitrogen is part of a halogen bond according to the definition, since the I···N-C angles are far from linear (114.1° and 104.7°). However, the interactions between iodine and nitrogen are not negligible (as inferred from the internuclear distances of 3.275 Å and 3.107 Å). In the case of sulfur, the interatomic distances ($d_{I\cdots S}$: 3.313 Å, 3.277 Å, and 3.313 Å) and angles ($\theta_{I\cdots S\text{-}C}$: 104.3° and 94.6°) are both typical of halogen bonding. The overall crystal packing motif for **17** is shown in Figure 6.2. Briefly, the packing consists of alternating layers of *p*-DITFB and charged moieties. The layers consisting of the charged species alternate between cation (Me_4N^+) and anion (SCN^-). In addition, the aromatic molecules are oriented in two different directions, which is concomitant with the halogen bonding interactions between the iodine and thiocyanate.

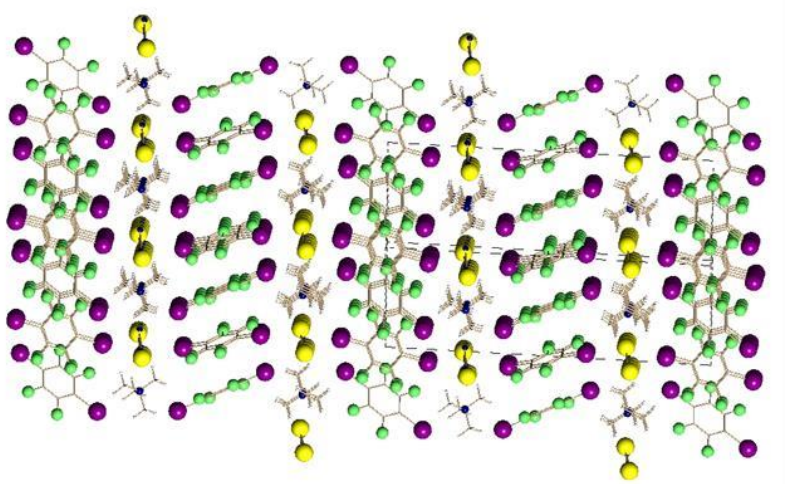

Figure 6.2 Compound **17** viewed along the *b* axis. The packing consists of alternating layers of *p*-DITFB and charged moieties. The layers consisting of the charged species alternate between cation (Me_4N^+) and anion (SCN^-). In addition, the aromatic molecules are oriented in two different directions, which is concomitant with the halogen bonding interactions between the iodine and thiocyanate.

Conversely, no orientational disorder of the selenocyanate anion is observed in the analogous $(Me_4NSeCN)(p\text{-}C_6F_4I_2)_2$, compound **14**, and indeed compounds **14** and **17** pack in different space groups (Table 6.1). Compound **14** crystallizes in the monoclinic system with the $P2_1/n$ space group. The $C_6F_4I_2$ molecules are aligned in columns along the *a* axis and are connected through the *b* axis by halogen bonding interactions. The cations (Me_4N^+) alternate with the $SeCN^-$ anion between the $C_6F_4I_2$ molecules (Figure 6.3). Out of the four halogen bonds per selenocyanate anion, three are interactions between iodine and selenium (a trifurcated bond), and one is between nitrogen and a single iodine (Figure 6.1(c)). Analogously, Cinčić *et al.* observed trifurcated bonds associated with four-centered interactions at the sulfur atom in metal bonded thiocyanate ions with I···S-C angles of 90°.[39] Cauliez *et al.* observed a similar phenomenon with thiocyanate in the compound

$(Et_4NSCN)_2(p\text{-}C_6F_4I_2)_5$, where the nitrogen interacts with two iodines, while the sulfur interacts with three iodines.[1] One may anticipate that selenocyanate may bind in a similar fashion to thiocyanate, since they are analogues. Again, compound **14** demonstrates strong halogen bonding type interactions, as characterized by short $d_{I\cdots Se}$ (3.393, 3.421, 3.405 Å) and $d_{I\cdots N}$ (3.034 Å) interatomic distances and typical halogen bonding angles involving selenium ($\theta_{I\cdots Se\text{-}C}$: 117.7°, 83.9°, 87.0°). Conversely, nitrogen behaves in a somewhat unexpected manner, where the I···N≡C angle observed (125.8°) deviates from what would be expected for a halogen bond with the SCN^- anion. Bock and Holl[2] and Cauliez *et al.*[1] have observed I···N≡C angles ranging between 145° and 170° and approximately 90° I···S-C angles.

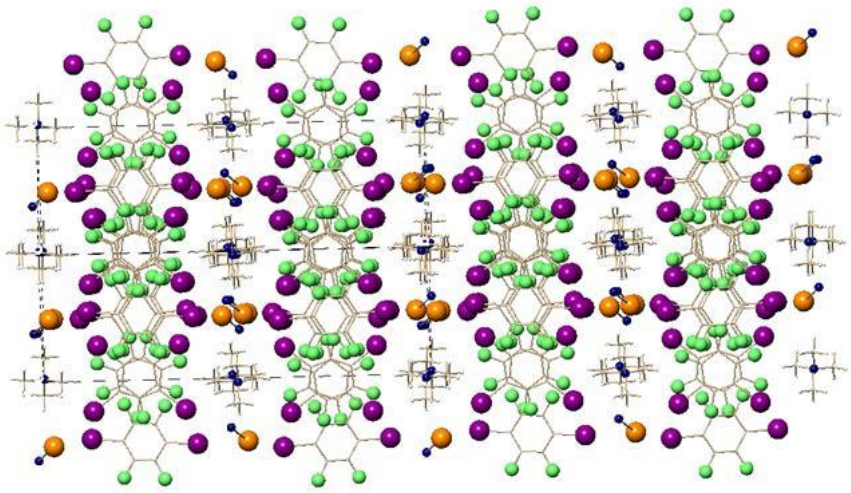

Figure 6.3 Packing of compound **14** along the *a* axis. The packing consists of alternating layers of *p*-DITFB and charged moieties. The layers consisting of the charged species alternate between cation (Me_4N^+) and anion ($SeCN^-$). The *p*-DITFB molecules form three types of unaligned columns, all with the iodine oriented toward the $SeCN^-$.

Finally, compound **15** is formed between Me_4NSeCN and *o*-$C_6F_4I_2$, resulting in $(Me_4NSeCN)(o\text{-}C_6F_4I_2)_2$. It crystallizes in a triclinic system with the $P\bar{1}$ space group. The selenium atom interacts with three iodines, forming a trifurcated bond, and nitrogen interacts with a single iodine, similar to what was observed for compound **14** (Figure 6.1(d)). The *o*-$C_6F_4I_2$ moieties pack in a staggered column. The Me_4N^+ cation and selenocyanate anion alternate between the *o*-$C_6F_4I_2$ moieties along the *c* axis (Figure 6.4). Again, the selenocyanate anion adopts specific motifs characterized by short 90° I···Se contacts and I···Se-C angles near 90° ($d_{I\cdots Se}$: 3.404, 3.552, 3.401 Å and $\theta_{I\cdots Se\text{-}C}$: 80.95°, 89.95°, and 94.01°), and a non-linear I···NC contact ($d_{I\cdots N}$: 3.035 Å $\theta_{I\cdots N\text{-}C}$: 124.13 °).

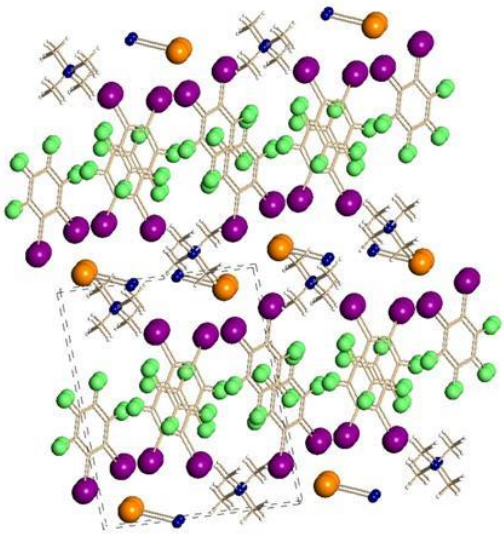

Figure 6.4 View of compound **15** along the *c* axis. The packing consists of alternating layers of *o*-DITFB and charged moieties. The layers consisting of the charged species alternate between cation (Me_4N^+) and anion ($SeCN^-$). There are three different types of unaligned of *o*-$C_6F_4I_2$ columns; each one has an iodine directed toward one of the two selenocyanate ions in that particular layer.

6.3.6 ***Solid-State NMR Spectroscopy***

6.3.6.1 *^{13}C and ^{15}N chemical shifts*

Presented in Figure 6.5 are the cyanate regions of the ^{15}N CPMAS NMR spectra of compounds **14** to **17** as well as simple KSCN, Me_4NSCN, *n*-Bu_4NSCN, and Me_4NSeCN salts for comparison. The isotropic chemical shifts are presented in Table 6.3, and range from 212.4 ppm for KSCN to 258.3 ppm for $(Me_4NSeCN)(o\text{-}C_6F_4I_2)_2$. Several important points can be made. First, it is observed that for the thiocyanate anion, the ^{15}N chemical shifts in general are somewhat sensitive to the identity of the counterion and to differences in crystal packing in the various compounds. For example, the chemical shifts for Me_4NSCN and *n*-Bu_4NSCN, which have similar ammonium counterions, are comparable (within 1.6 ppm). Second, it is clear that the selenocyanate nitrogen resonance is consistently shifted to higher frequency relative to thiocyanate nitrogens; this is consistent with previous reports, where Bernard *et al.*[47] observed an increase in the cyanate ^{15}N chemical shift in Me_4NSeCN compared to NH_4SCN of 44 ppm, and also compared two previous solution ^{15}N NMR studies of selenocyanate[40] and thiocyanate[41] ions and noted analogous increases of 30 ppm. It is also observed that the addition of a halogen bonding interaction to the thiocyanate nitrogen environment results in a small but measureable shift of the cyanate ^{15}N resonance to lower frequency; this shift is 4.5 ppm for the *n*-Bu_4NSCN / $(n\text{-}Bu_4NSCN)(p\text{-}C_6F_4I_2)$ pair and 2.5 ppm for the Me_4NSCN / $(Me_4NSCN)(p\text{-}C_6F_4I_2)_2$ pair. Conversely, for the selenocyanates, a small increase in the ^{15}N chemical shift is observed for the compounds exhibiting halogen bonding relative to Me_4NSeCN; the shift is 5.9 ppm for the Me_4NSeCN / $(Me_4NSeCN)(p\text{-}C_6F_4I_2)_2$ pair and 6.1 ppm for the Me_4NSeCN / $(Me_4NSeCN)(o\text{-}C_6F_4I_2)_2$ pair. It is not immediately clear why the shifts are in opposite

directions for the thiocyanate pairs compared to the selenocyanate pairs, and it is not possible to unequivocally attribute the shifts solely or directly to the presence of a halogen bonding interaction. Undoubtedly there is an interplay of competing factors which influence the observed shifts; for example, the direct effects of a halogen bonding interaction may compete with concurrent small structural changes in the ions (bond lengths and angles) and with changes in longer-range interactions (*i.e.*, different space groups and crystal packing effects). The promising conclusion from the ^{15}N NMR spectra, however, is that changes are observed in the spectra of compounds exhibiting halogen bonding to nitrogen relative to reference compounds where such interactions are absent. A final point of interest in these spectra is the much broader resonance (250 Hz line width at half-height) observed for $(Me_4NSCN)(p\text{-}C_6F_4I_2)_2$ relative to the other compounds.

Table 6.3 Experimental ^{13}C and ^{15}N chemical shift parameters for thiocyanate and selenocyanate compounds

compound	δ_{iso} (^{13}C)/ ppm	Ω(^{13}C) / ppm	κ(^{13}C)	δ_{iso} (^{15}N) / ppm	Ω(^{15}N) / ppm	κ(^{15}N)
KSCN[a]	139.2(0.4)	327(1)	0.95(0.4)	212.4(0.1)	410(10)	0.96(0.10)
n-Bu_4NSCN	129.4(0.3)	n/a	n/a	222.4(0.4)	n/a	n/a
16	129.8(0.6)	n/a	n/a	217.9(0.4)	n/a	n/a
Me_4NSCN[a]	128.5(0.1)	296(5)	1.00(0.10)	224.0(0.2)	420(10)	0.96(0.10)
17[a]	131.5(0.5)	302(4)	0.93(0.02)	221.5(0.5)	488(8)	0.94(0.40)
Me_4NSeCN[b]	118.5(0.1)	285(8)	0.98(0.01)	252.2(0.7)	439(10)	1.00(0.03)
14	113.4(0.4)	n/a	n/a	258.1(0.5)	n/a	n/a
15	116.1(0.7)	n/a	n/a	258.3(0.6)	n/a	n/a

[a] The thiocyanate groups in KSCN, Me_4NSCN and $(Me_4NSCN)(p\text{-}C_6F_4I_2)_2$ were isotopically enriched in ^{13}C or ^{15}N . All data in the the table are for the cyanate carbons and nitrogens only. [b] Span and skew values determined by Bernard *et al.*[47]

This is also observed in the ^{13}C NMR spectrum of the same compound (*vide infra*) and is consistent with the disorder of the thiocyanate ion noted from the X-ray crystallography studies (*vide supra*). To aid in confirming that the broadened peaks could be attributed to disorder, calculations (B3LYP/3-21G), were performed on the two closest isolated thiocyanate anions (5.8 Å between the two nitrogen atoms) from adjacent unit cells. Two environments were studied, where one SCN^- was kept in a fixed position and the second SCN^- was flipped in each of the two possible orientations. This rudimentary calculation permitted to see if one could expect a measurable chemical shift difference as a result of disorder. Calculations demonstrated that the magnetic shielding constant, σ_{iso}, varies by 1 ppm for ^{15}N. This is consistent with the breadth of the peak observed experimentally for ^{15}N.

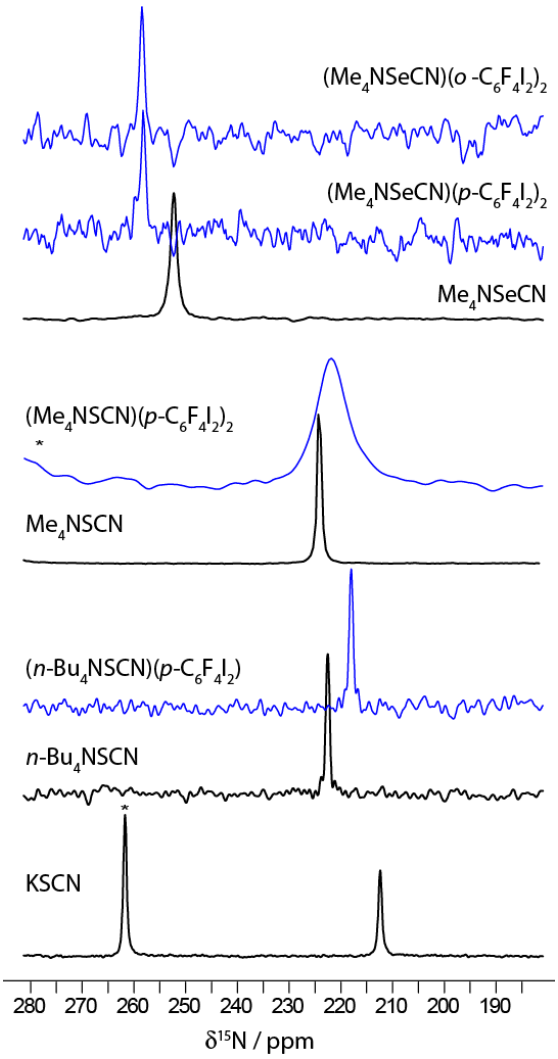

Figure 6.5 Experimental ^{15}N CPMAS SSNMR spectra acquired at 9.4 T of all SCN^- and $SeCN^-$ salts (black) studied as well as related halogen-containing complexes (blue). KSCN, Me_4NSCN, and **17** are 98 %, ~50 % and < 50 % labeled with ^{15}N thiocyanate, respectively. The ^{15}N spectra of the other compounds were acquired with ^{15}N in natural abundance. Spinning sidebands are represented by asterisks.

Since the isotropic chemical shift represents an average of the three principal components of the CS tensor, the possibility that more substantial changes in the tensor components were occurring in the presence of halogen bonding was explored. The

Me_4NSCN / $(Me_4NSCN)(p\text{-}C_6F_4I_2)_2$ pair was prepared with ^{15}N isotopic enrichment (~50 %) at the thiocyanate nitrogen and spinning sideband manifolds were obtained using CPMAS NMR. The spectra and their corresponding simulations are presented in Figure 6.6 and 6.7. Whereas the ^{15}N CS tensor span and skew remain constant within experimental error for the simple salts $KSC^{15}N$ (Figure 6.8(b)) and $Me_4NSC^{15}N$, a non-negligible increase in the span from 420 to 488 ppm is observed for the Me_4NSCN / $(Me_4NSCN)(p\text{-}C_6F_4I_2)_2$ pair. While this change must due to the change in environment around the thiocyanate nitrogen, it is difficult to interpret the results further in terms of halogen bonding, given the relatively small changes in each of the principal components of the CS tensor and also given the disorder of the SCN^- ion. Furthermore, it may be seen in Figure 3(d) that each of the spinning sidebands are broadened (250 Hz at half-height) for $(Me_4NSCN)(p\text{-}C_6F_4I_2)_2$ relative to those for Me_4NSCN (40 Hz at half-height), which may decrease the precision of the reported numbers for the former compound. The observed broadening, however, is again consistent with disorder of the SCN^- ions in $(Me_4NSCN)(p\text{-}C_6F_4I_2)_2$.

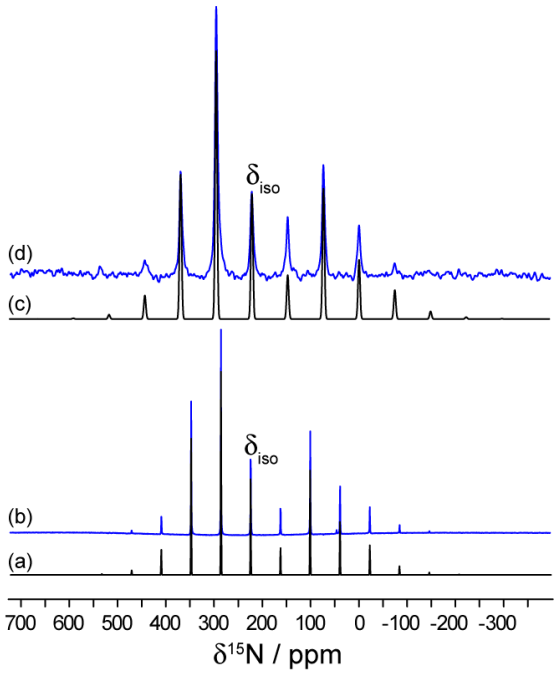

Figure 6.6 Experimental ^{15}N CPMAS SSNMR spectra acquired at 9.4 T for (b) Me_4NSCN (~50 % SCN^- labeled ^{15}N), (d) $(Me_4NSCN)(p\text{-}C_6F_4I_2)_2$ (< 50 % SCN^- labeled ^{15}N), and analytical simulations (a) and (c), respectively. Isotropic peaks are indicated (224.0 ppm and 221.5 ppm) with spinning frequencies of 2.5 kHz and 3.0 kHz for (b) and (d), respectively.

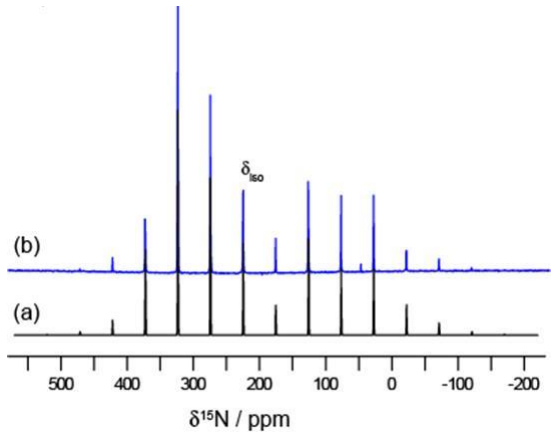

Figure 6.7 Experimental ^{15}N CPMAS SSNMR spectra acquired at 11.75 T for (b) Me_4NSCN (~50 % SCN^- labeled ^{15}N) and analytical simulations (a). Isotropic peak is indicated, 224.0 ppm, at a spinning frequency of 2.5 kHz.

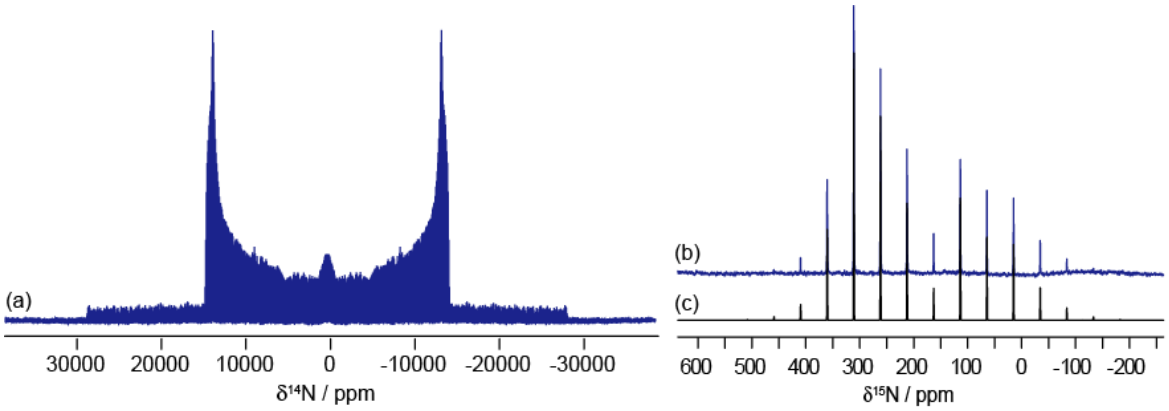

Figure 6.8 Experimental ^{14}N WURST-QCPMG SSNMR spectrum of KSCN acquired at 21.1 T (a). The ^{14}N spectrum was obtained by acquiring only half of the spectral region and symmetrizing it. This approach is only valid if the CSA is negligible compared to the breath of the of the spectrum. Experimental ^{15}N CPMAS SSNMR spectrum of labelled ^{15}N (98 %) KSCN acquired at 9.4 T (b) and simulated spectrum (c).

The cyanate carbon region of the ^{13}C CPMAS NMR spectra of compounds **14** to **17** as well as KSCN, Me_4NSCN, *n*-Bu_4NSCN, and Me_4NSeCN are shown in Figure 6.9. As for ^{15}N, changes in chemical shifts are small but measurable when comparing a simple salt to the analogous halogen-bonded compound. In direct opposition to the ^{15}N chemical shifts, the ^{13}C chemical shift for the thiocyanate ion *increases* slightly in the presence of halogen bonding, and the ^{13}C chemical shift for the selenocyanate ion *decreases* slightly in the presence of halogen bonding (Table 6.3). For example, for the Me_4NSCN/(Me_4NSCN)(*p*-$C_6F_4I_2$)$_2$) pair this shift is 3.0 ppm, and for the Me_4NSeCN / (Me_4NSeCN)(*p*-$C_6F_4I_2$)$_2$ pair it is 5.1 ppm. It is not surprising that the ^{13}C chemical shifts change minimally for a given pair of compounds since the carbon atom is in the centre of the thiocyanate and selenocyanate ions, and therefore is not directly interacting with a halogen atom.

Interestingly, Kargol *et al*. have observed with ^{13}C solution NMR a change in chemical shift in analogous coordinated thiocyanate and selenocyanate metal complexes.[42]

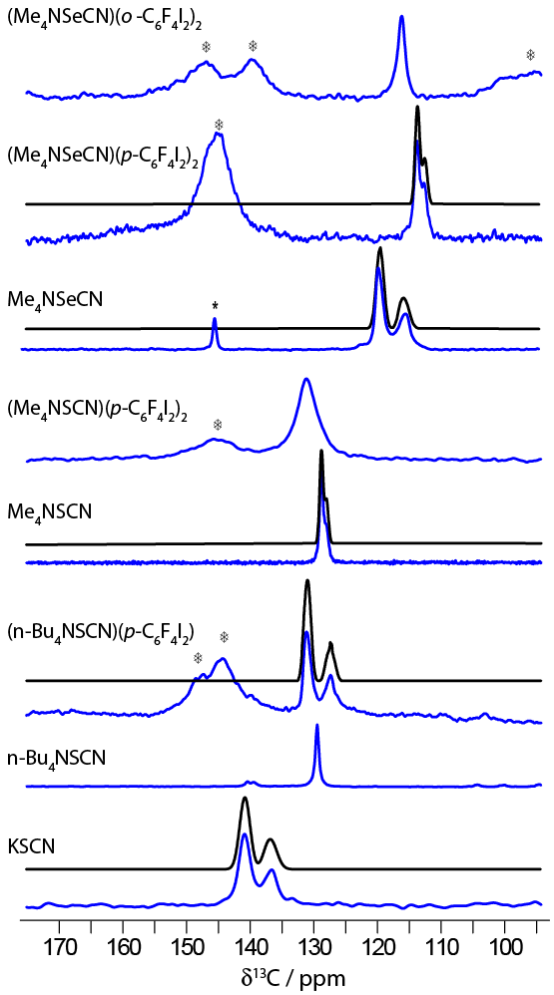

Figure 6.9 ^{13}C CPMAS SSNMR spectra (blue) of all R_4NSCN, R_4NSeCN and related halogen-containing complexes. Spinning sidebands are indicated with asterisks and the aromatic carbon resonances are indicated by snowflakes. Spectra were acquired at either 4.7 T (KSCN (99.99 % ^{13}C), Me_4NSCN (42 % ^{13}C), *n*-Bu_4NSCN, Me_4NSeCN) or 9.4 T (compounds **14**, **15**, **16**, and **17** (< 42 % ^{13}C)) using proton decoupling (SPINAL64). Residual dipolar coupling between ^{14}N (I = 1) and ^{13}C (I = 1/2) of SCN^- or $SeCN^-$ anion is observed for certain compounds. The simulations of the isotropic peak are done using WSOLIDS1 under the assumption of an infinite MAS rate (black). The values of $C_Q(^{14}N)$, R_{DD}, and the ^{13}C chemical shifts can be found in Tables 6.3 and 6.4.

6.3.6.2 *^{13}C-^{14}N Dipolar Coupling and Comments on ^{14}N SSNMR*

In 1982, Zumbulyadis and Gysling[43] reported an unusually narrow ^{13}C NMR spectrum for a static powdered sample of KSCN. The lack of a broad well-defined powder pattern was attributed to rapid motion of the thiocyanate ion; however, I suspect their sample was hydrated. In this work, the proper ^{13}C NMR spectrum was acquired for powdered KS^{13}CN (Figure 6.10) and fit it to determine the ^{13}C CS tensor parameters as well as the effective ^{14}N,^{13}C dipolar coupling constant and carbon-nitrogen bond length (Table 6.4). The analogous experiment was performed for isotopically enriched ($Me_4NS^{13}CN$)(*p*-$C_6F_4I_2)_2$, and the ^{14}N-^{13}C bond length was determined to be 1.25 Å, in excellent agreement with the X-ray value measured (1.242 Å) in this work. This suggests that the thiocyanate disorder in this compound is static rather than dynamic, as no averaging of the static dipolar coupling tensor is observed. Although ^{13}C isotopic enrichment of all compounds in this paper was beyond the scope of the current study, the good quality of the spectra and the quantitative agreement between NMR and X-ray methods for measuring selected internuclear distances demonstrates the potential of multinuclear solid-state magnetic resonance for further studies of halogen bonding interactions. This may be particularly useful in cases where single crystals or good quality diffraction data are difficult to obtain.

Table 6.4 Experimental cyanate ^{14}N,^{13}C dipolar couplings and cyanate ^{14}N quadrupolar coupling data obtained from solid-state NMR spectroscopy and X-ray data

		SSNMR		X-ray	
compound	C_Q (^{14}N) / MHz	R_{DD} / Hz	$r_{C\text{-}N}$ /Å[d]	R_{DD} / Hz	$r_{C\text{-}N}$ /Å
KSCN[a]	-2.43(0.01)	1246(12)	1.206	1458	1.144
n-Bu_4NSCN[c]	n/a	n/a	n/a	1462	1.143
16[c]	-1.75(0.05)	1514(10)	1.130	1514	1.130
Me_4NSCN[b]	-2.15(0.10)	1254(15)	1.203	1254	1.203
17[a]	unresolved	1125(10)	1.247	1140	1.242
Me_4NSeCN[a]	-2.60(0.20)	1180(30)	1.228	1538	1.113
14[b]	-2.55(0.20)	1428(7)	1.152	1428	1.152
15[c]	unresolved	n/a	n/a	1460	1.144

[a]These compounds have ^{13}C static SSNMR spectra; in these cases the dipolar coupling constant, R_{DD}, is directly extracted from the spectra. [b]Static ^{13}C SSNMR experiments on static samples were *not* carried out in these cases, therefore R_{DD} is fixed at the value determined from the crystal structure and the value of C_Q is determined from SSNMR with the angles $\beta = \alpha = 0°$. [c]No residual dipolar coupling is observed for these compounds in their ^{13}C CPMAS NMR spectra. [d] Distances are calculated under the assumption of negligible motional averaging of R_{DD}, and also under the assumption of a negligible indirect nuclear spin-spin coupling tensor anisotropy (ΔJ). For these reasons is it difficult to assign precise errors bars to the r_{CN} data.

There is a 2:1 doublet-like structure observed in most of the ^{13}C CPMAS NMR spectra (Figure 6.9). It is well-known that MAS does not entirely average the dipolar coupling between a spin-1/2 nucleus (such as ^{13}C) and a quadrupolar nucleus (such as ^{14}N) to zero.[44,45] For this reason, residual dipolar coupling (RDC) is often observed in the ^{13}C CPMAS NMR spectra of ^{13}C spins which are coupled to ^{14}N; this is the origin of the 2:1 doublets. Simulation of these line shapes[46] depends on the dipolar coupling constant between the two spins, the quadrupolar coupling constant (C_Q) of the ^{14}N, and the

orientation of the ^{14}N EFG with respect to the ^{14}N-^{13}C dipolar tensor. The frequency shift $\nu_I(m_S)$ is expressed in Equation (6.3),

$$\nu_I(m_I) = \frac{3R_{DD}C_Q^S}{20\,\nu_L^S}\left[\frac{S(S+1)-3m_I^2}{S(2S+1)}\right]\left[3cos^2\beta_D - 1 + 2\eta_Q^S sin^2\beta_D cos^2 2\alpha_D\right] \quad [6.3]$$

$$R_{DD} = \frac{\mu_0}{4\pi}\frac{\hbar\gamma_S\gamma_I\langle r^{-3}\rangle}{2\pi} \quad [6.4]$$

which depends on C_Q^S (the quadrupolar coupling constant of the coupled nucleus (S)), S is the spin of the coupled nucleus, ν_L^S is its Larmor frequency, m_I is the spin state of the coupled nucleus, the angles β_D, α_D are those which relate the dipolar principal axis system (PAS) to the EFG PAS, R_{DD} is the dipolar coupling constant (Equaiton 6.4) which depends on the motionally-averaged inverse cube of internuclear distance between the nuclei, h is the Planck constant, γ are the magnetogyric ratios, and μ_0 is the permeability constant. In the case of SCN^- and $SeCN^-$ ions, it is reasonable to assume that the largest component of the ^{14}N EFG tensor will be coincident with the unique component of the dipolar tensor since the ions maintain local pseudo-C_∞ symmetry in the complexes; hence, the angles α_D and β_D were fixed to zero. Furthermore, in many cases the R_{DD} may be calculated directly from the X-ray coordinates of the two coupled nuclei, *i.e.*, independently of the NMR experiment. However, the value R_{DD}(^{14}N,^{13}C) can be extracted from a ^{13}C spectrum of a stationary powdered sample (demonstrated in Chapter 2, section 2.1.3.3), for compound **17** and KSCN. This leaves the ^{14}N quadrupolar coupling constant and asymmetry parameter as the only unknown parameters, and it is clear that the asymmetry parameter must be close to zero for linear ions (and when $\beta_D = 0$, there is no spectral dependence on η_Q). The fits of the 2:1 doublets in the MAS NMR spectra therefore provide some new information on the value of C_Q(^{14}N). The data are presented in Table 6.4.

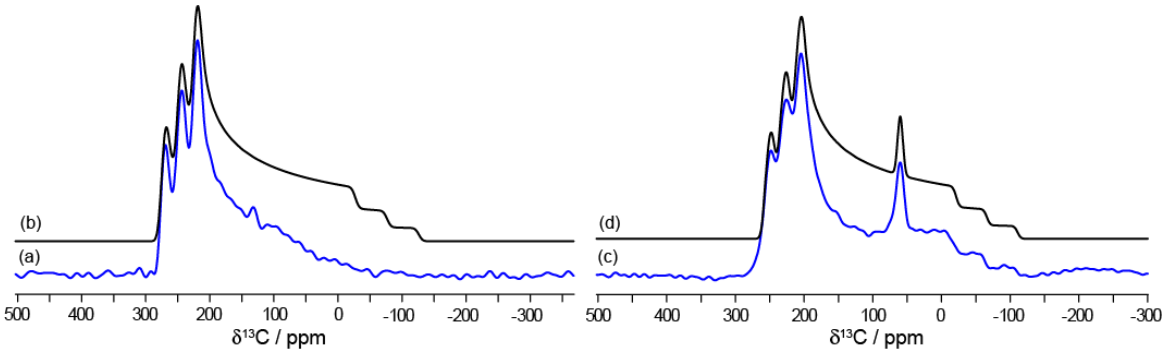

Figure 6.10 Experimental (a) and simulated spectra (b) of ^{13}C SSNMR KSCN (99.99 % ^{13}C) under stationary conditions using a Hahn echo (*i.e.* $\pi/2$-τ_1-π-τ_2-acq) pulse sequence. Experimental ^{13}C static CP SSNMR spectrum of < 42 % ^{13}C-enriched ($Me_4NS^{13}CN$)(*p*-$C_6F_4I_2$)$_2$ (c) and simulated spectrum (d). The peak at ~60 ppm corresponds to the methyl groups. Both ^{13}C SSNMR spectra were acquired at 4.7 T. Difficulties in observing the three 'step' discontinuities experimentally in (a) are attributed to anisotropic spin-lattice relaxation.

The measurement of a more complete set of $C_Q(^{14}N)$ values was pursued through the direct observation of the ^{14}N SSNMR spectra. A spectrum for KSCN was recorded and it was possible to determine that the value of $C_Q(^{14}N)$ was consistent with that obtained through the analysis of the residual dipolar coupling in the ^{13}C NMR spectrum (Figure 6.8(a)). Here, due to the breadth of the ^{14}N NMR spectrum, only half of the spectrum was acquired and symmetrization was used to produce the other half. This procedure assumes that the nitrogen CSA is negligible compared to the breadth of the ^{14}N powder pattern. As shown in the ^{15}N NMR spectrum in Figure 6.8(b), the nitrogen CSA is certainly measurable, but very small compared to the breadth of the ^{14}N powder pattern shown in Figure 6a. As a result, this measurement of $C_Q(^{14}N)$ for KSCN is not extremely precise, but useful to show consistency with the value inferred from the ^{13}C MAS NMR spectroscopy (*vide supra*). ^{14}N

WURST-QCPMG SSNMR experiments are technically challenging and importantly require a long enough ^{14}N T_2 relaxation time constant. Attempts to record ^{14}N WURST-QCPMG SSNMR spectra of *n*-Bu_4NSCN at 21.1 T and a larger series of the compounds in Table 6.4 at 9.4 and 11.7 T were unsuccessful and the lack of signal is attributable to a short ^{14}N T_2, likely due to molecular motion and/or due to ^{14}N-^{19}F and ^{14}N-^{127}I dipolar couplings which are absent in the model compound KSCN. Thus, while the ^{14}N quadrupolar coupling constant provides additional information on the nitrogen environment in thiocyanate and selenocyanate compounds, it is currently impractical to acquire these data for most of the compounds in Table 6.4 through direct wide-line ^{14}N NMR spectroscopy.

6.3.6.3 *^{77}Se SSNMR*

As discussed above, the X-ray crystal structures obtained for (Me_4NSeCN)(*p*-$C_6F_4I_2$)$_2$ and (Me_4NSeCN)(*o*-$C_6F_4I_2$)$_2$ feature a trifurcated halogen bonding interaction between each Se and three iodines, at distances less than the sum of their van der Waals radii and at angles near 90°. For these reasons, ^{77}Se CPMAS NMR experiments are employed to study the selenium environment in the halogen-bonded complexes, and compare the results to those for Me_4NSeCN and other benchmark data reported by Bernard *et al*.[47]

Shown in Figure 6.11 are the ^{77}Se CPMAS NMR spectra of Me_4NSeCN, (Me_4NSeCN)(*p*-$C_6F_4I_2$)$_2$, and (Me_4NSeCN)(*o*-$C_6F_4I_2$)$_2$ acquired at 9.4 T. The spectra acquired at 11.75 T of XB compounds are also shown in Figure 6.12. The spectra are of good quality and exhibit spinning sideband manifolds typical of a spin-1/2 nucleus. For

Me_4NSeCN, a span of the ^{77}Se CS tensor of 854 ppm is measured; axial symmetry of the tensor is also noted. The axial symmetry is consistent with the near-C_∞ symmetry of the $SeCN^-$ ion in this compound. The value for the span is consistent with the values reported for a series of similar selenocyanates by Bernard *et al*. Their work also showed that, although there are small variations in the ^{77}Se CS tensor principal components which may be correlated with changes in electronic structure, overall the values of Ω do not vary by more than 70 ppm for a $SeCN^-$ ion in a simple salt.[47]

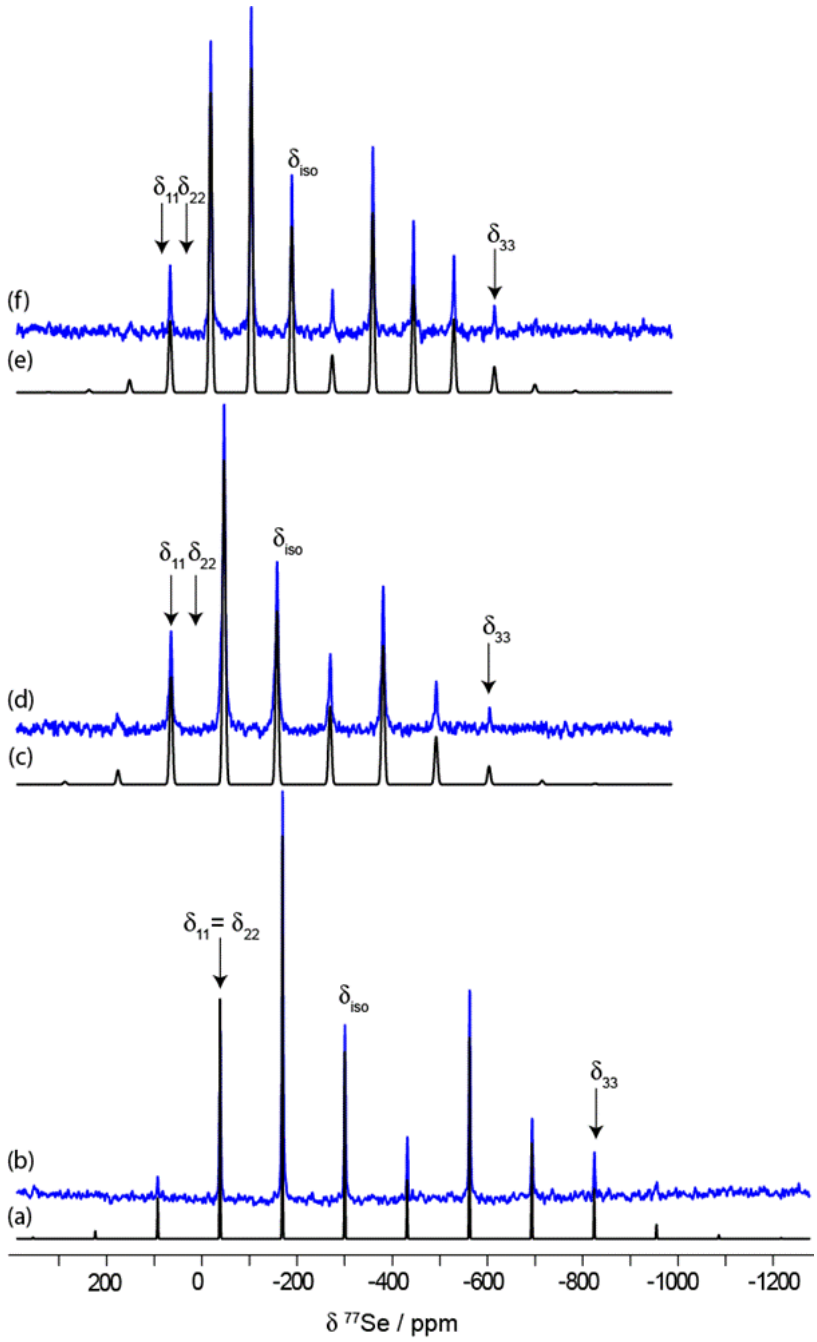

Figure 6.11 Experimental ^{77}Se CPMAS SSNMR spectra acquired at 9.4 T for (b) Me_4NSeCN (d) $(Me_4NSeCN)(p\text{-}C_6F_4I_2)_2$, (f) $(Me_4NSeCN)(o\text{-}C_6F_4I_2)_2$, and simulated spectra (a), (c), and (e), respectively. Isotropic peaks are indicated (-299.9 ppm, -158.2 ppm and -189.0 ppm, respectively). Spinning frequencies of 10 kHz, 8.5 kHz, and 6.0 kHz were used for (b), (d), and (f) respectively.

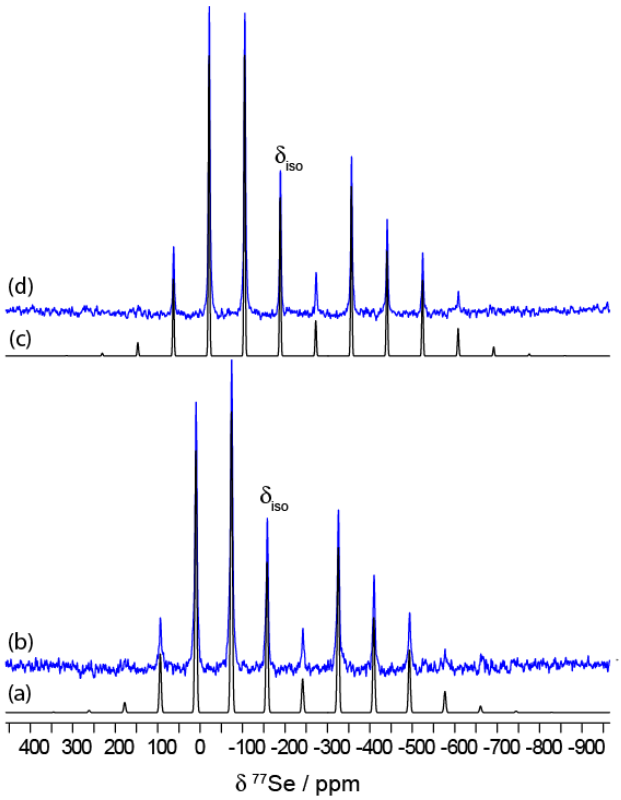

Figure 6.12 Experimental ^{77}Se CPMAS SSNMR spectra acquired at 11.75 T for (b) $(Me_4NSeCN)(p\text{-}C_6F_4I_2)_2$, (d) $(Me_4NSeCN)(o\text{-}C_6F_4I_2)_2$, and simulated spectra (b), and (c), respectively. Isotropic peaks are indicated (-158.2 ppm and -189.0 ppm, respectively). A spinning frequency of 8.0 kHz was used in both cases.

Most striking therefore is the substantial change in the ^{77}Se NMR spectral parameters in the halogen-bonded complexes compared to the simpler selenocyanate salts (Table 6.5). As determined through the spectral simulations shown in Figure 6.11, the span of the CS tensor decreases from 854 ppm in Me_4NSeCN to 642 ppm in $(Me_4NSeCN)(o\text{-}C_6F_4I_2)_2$ and 610 ppm in $(Me_4NSeCN)(p\text{-}C_6F_4I_2)_2$. These changes in span on the order of 25 % are substantially more than those observed simply by changing the counterion in simple $SeCN^-$ salts. Inspection of the principal components of the ^{77}Se CS tensors reveals

that the component which changes the most is by far the most shielded pseudo-unique δ_{33} component. The value of δ_{33} changes from -814 ppm in Me_4NSeCN to -611 ppm in $(Me_4NSeCN)(o\text{-}C_6F_4I_2)_2$ and -563 ppm in $(Me_4NSeCN)(p\text{-}C_6F_4I_2)_2$. These changes in the individual principal components explain the marked change in δ_{iso} as well, from -299.4 ppm in Me_4NSeCN to -189.0 ppm in $(Me_4NSeCN)(o\text{-}C_6F_4I_2)_2$ and -158.2 ppm in $(Me_4NSeCN)(p\text{-}C_6F_4I_2)_2$.

Table 6.5 Experimental and calculated[a] ^{77}Se CS tensors for selenocyanate compounds

compound	method	δ_{iso} / ppm	Ω / ppm	κ	δ_{11} / ppm	δ_{22} / ppm	δ_{33} / ppm
Me_4NSeCN[b]	expt	-299.4	854	1	-40	-40	-814
	calc	-551.8	1095	0.99	-179.8	-180.7	-1295
14	expt	-158.2(0.2)	610(5)	0.98(0.02)	47(5)	41(7)	-563(2)
	calc	-122.5	463	0.82	49	6	-422
15	expt	-189.0(0.1)	642(8)	0.93(0.01)	31(1)	13(2)	-611(4)
	calc	-180.7	468	0.71	2	-69	-475

[a] B3LYP/6-311++G** (Se, N, C, F) 6-311G**(I) calculation. [b] Values established by Bernard *et al*. where they estimate errors less than 0.5 ppm for δ_{iso}; those of the individual components are estimated to be on the order of 2-3% of the total span of the tensor. These values were reproduced independently (see Figure 6.11).

Bernard *et al*.[47] have presented an analysis of selenium CS tensors in the context of Ramsey's theory[48] of magnetic shielding. They showed how the paramagnetic part of the selenium shielding tensor changes in accordance with a small change in the energy gap between the occupied and unoccupied MOs in the $SeCN^-$ ion. For a linear molecule or ion with cylindrical symmetry, that is, C_∞, the shielding tensor will be axially symmetric with the unique component along the symmetry axis. Furthermore, since the contributions to paramagnetic shielding are zero along the symmetry axis, it is generally the case that the unique component is the one which is most shielded, *i.e.*, σ_{33}; this corresponds to the

smallest component of the chemical shift tensor, *i.e.*, δ_{33}. According to Ramsey's theory, it is the mixing of occupied and virtual orbitals in the plane perpendicular to the principal axis corresponding to a particular component which affects the value of that component. Presently, the marked reduction in the value of δ_{33} may therefore be attributable in $(Me_4NSeCN)(o\text{-}C_6F_4I_2)_2$ and $(Me_4NSeCN)(p\text{-}C_6F_4I_2)_2$ to the close iodine-selenium contacts in those compounds, specifically in the plane which is approximately perpendicular to the selenocyanate axis. Furthermore, we may speculate that the larger negative paramagnetic contribution to σ_{33} in the *para* compound correlates with the shorter average Se···I distance (3.40 Å) compared to the ortho compound (3.45 Å). These halogen bonding interactions are also reflected in the slight decrease in axial symmetry of the ^{77}Se CS tensor, going from a skew of 1.0 in simple selenocyanate salts 0.93 in $(Me_4NSeCN)(o\text{-}C_6F_4I_2)_2$.

As the ^{77}Se CS tensors are more responsive to structural changes than are ^{13}C or ^{15}N CS tensors in this study, B3LYP/6-311++G** computations were carried out of the ^{77}Se magnetic shielding tensors using models representative of the Se environment in Me_4NSeCN, $(Me_4NSeCN)(o\text{-}C_6F_4I_2)_2$, and $(Me_4NSeCN)(p\text{-}C_6F_4I_2)_2$. It is satisfying to see that the results, presented in Table 6.5, clearly reproduce the substantial changes in the CS tensors observed experimentally. The trend in the value of the isotropic chemical shift is also reproduced. The changes are overestimated by the calculations, but the important point is that changes on the order of hundreds of ppm are reproduced, and that it is the δ_{33} component which is mainly responsible for the changes. Reasons for the lack of quantitative agreement with experiment include the approximation of using a cluster model for these calculations, the limited availability of a large basis set for iodine, the exclusion

of relativistic effects on iodine, and, for the isotropic chemical shift, uncertainties in the ^{77}Se absolute shielding scale. Several theoretical[49] groups have investigated the chemical shift tensors of selenium to establish an absolute shielding scale.[37] This is not an easy task since selenium has a large chemical shift range (3000 ppm) and may itself be subject to relativistic effects.[50]

Examination of the computed ^{77}Se magnetic shielding tensor orientations in $(Me_4NSeCN)(o\text{-}C_6F_4I_2)_2$ and $(Me_4NSeCN)(p\text{-}C_6F_4I_2)_2$ show that the σ_{33} component remains approximately aligned along the local C_∞ axis of the $SeCN^-$ ion (Figure 6.13). This supports the arguments made above concerning the effect of the iodines on the δ_{33} component of the CS tensor.

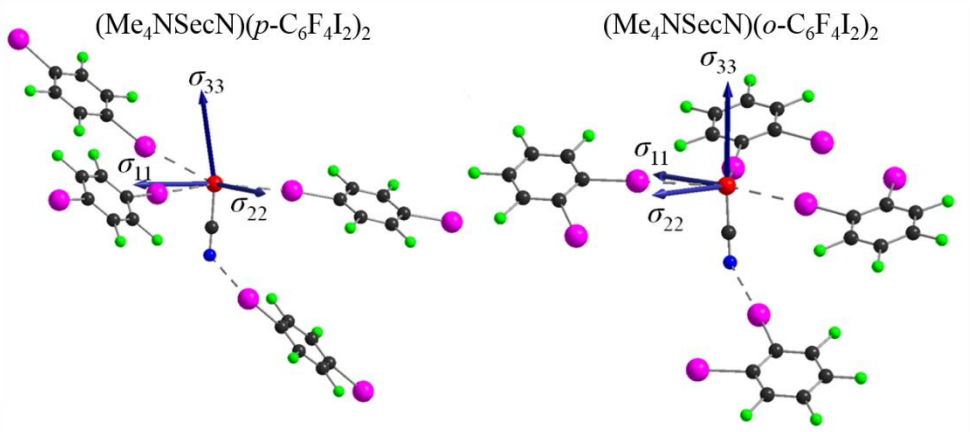

Figure 6.13 Calculated selenium magnetic shielding tensor orientations for **14** and **15**. Selenocyanate being a linear anion results in selenium having C_∞ site symmetry when the ion is isolated. Note that in the limit that κ = +1, the computed directions of σ_{11} and σ_{22} are not meaningful. For the compounds shown here, C_∞ site symmetry is not strictly maintained and there are thus small but measurable deviations from axial symmetry in the chemical shift and magnetic shielding tensors.

6.4 CONCLUSIONS

In this work, the preparation of novel thiocyanate and selenocyanate compounds is reported exhibiting close contacts which fall under the definition of halogen bonding, as well as their characterization by X-ray diffraction and multinuclear solid-state magnetic resonance spectroscopy. Selenocyanates $(Me_4NSeCN)(p\text{-}C_6F_4I_2)_2$ and $(Me_4NSeCN)(o\text{-}C_6F_4I_2)_2$ were prepared and their crystal structures revealed similarities and differences in the halogen bonding motifs for $SeCN^-$ versus the analogous SCN^- compounds described by Cauliez *et al.*[1] In particular, trifurcated I···$SeCN^-$ close contacts are observed with characteristic bonding angles near 90°. X-ray and $^{13}C/^{15}N$ SSNMR evidence indicates that the thiocyanate moieties in $(Me_4NSCN)(p\text{-}C_6F_4I_2)_2$ exhibit disorder. Also, the thiocyanate anion in compound **17** forms halogen bonds with iodine atoms, where both sulfur and nitrogen exhibit close contacts with two iodines. However, a non-linear angle is observed for the I···NC interaction (125°).

Over a broader range of thiocyanates, ^{13}C chemical shifts were found to increase slightly in complexes exhibiting halogen bonding relative to reference compounds with only simple counterions, while ^{15}N chemical shifts were found to decrease slightly under the same conditions. The opposite trends are observed for the selenocyanates. Much more substantial changes are observed in both the ^{77}Se isotropic chemical shift and in the pseudo-unique principal component of the ^{77}Se chemical shift tensor when comparing simple selenocyanates with those where the Se is engaged in halogen bonding interactions with iodine. These results were interpreted in the context of Ramsey's theory of paramagnetic shielding to show that the iodine-selenium interactions are reflected in the ^{77}Se SSNMR parameters, thereby providing an example of the potential of NMR methods for

characterizing halogen bonding interactions in the solid state. The arsenal of modern SSNMR methods now available offers a wealth of information which may be complementary to XRD studies in studying the magnetic and chemical environments of atoms involved in halogen bonding interactions.

6.5 REFERENCES FOR CHAPTER 6

1 P. Cauliez, V. Polo, T. Roisnel, R. Llusar, M. Fourmigué, (2010), *CrystEngComm*, 12, 558.

2 (a) H. Bock, S. Holl, (2002), *Z. Naturforsch*, 57b, 713. (b) H. Bock, S. Holl, (2002), *Z. Naturforsch*, 57b, 835. (c) H. Bock, S. Holl, (2002), *Z. Naturforsch*, 57b, 843.

3 P. Metrangolo, G. Resnati, (2008), *Halogen bonding: fundamentals and applications*, Berlin, London, Springer.

4 C. A. Bayse, E. R. Rafferty, (2010), *Inorg. Chem.*, 49, 5365.

5 R. S. Mulliken, W. B. Person, (1969), *Molecular Complexes*, New York, NY, Wiley-Interscience.

6 D. L. Bryce, G. M. Bernard, M. Gee, M. D. Lumsden, K. Eichele, R. E. Wasylishen, (2001), *Can. J. Anal. Sci. Spectrosc.*, 46, 46.

7 J. Songstad, L. J. Stangeland, (1970), *Acta Chem. Scand.*, 24, 804.

8 C. R. McCrosky, F. W. Bergstrom, G. Waitkins, (1940), *J. Am. Chem. Soc.*, 62, 2031.

9 C. R. McCrosky, F. W. Bergstrom, G. Waitkins, (1940), *J. Am. Chem. Soc.*, 62, 2031.

10 APEX Software Suite v.2010, (2005), Madison, WI, Bruker AXS.

11 R. Blessing, (1995), *Acta Crystallogr., Sect. A: Found. Crystallogr.*,51, 33.

12 G. M. Sheldrick, (2008), *Acta Crystallogr., Sect. A: Found. Crystallogr.*, 64, 112.

13 W. L. Earl, D. L. VanderHart, (1982), *J. Magn. Reson.*, 48, 35.

14 S. R. Hartmann, E. L. Hahn, (1962), *Phys. Rev.*, 128, 2042.

15 B. M. Fung, A. K. Khitrin, K. Ermolaev, (2000), *J. Magn. Reson.*, 142, 97.

16 P. R. Srinivasan, R. L. Lichter, (1977), *J. Magn. Reson.*, 28, 227.

17 M. J. Collins, C. I. Ratcliffe, J. A. Ripmeester, (1986), *J. Magn. Reson.*, 68, 172.

18 A. L. Bloom, J. N. Shoolery, (1955), *Phys. Rev.*, 97, 1261.

19 A. E. Bennett, C. M. Rienstra, M. Auger, K. V. Lakshmi, R. G. Griffin, (1995), *J. Chem. Phys.*, 103, 6951.

20 W. P. Rothwell, J. S. Waugh, (1980), *J. Chem. Phys.*, 74, 2721.

21 P. R. Srinivasan, R. L. Lichter, (1977), *J. Magn. Reson.*, 28, 227.

22 M. J. Collins, C. I. Ratcliffe, J. A. Ripmeester, (1986), *J. Magn. Reson.*, 68, 172.

23 B. M. Fung, A. K. Khitrin, K. Ermolaev, (2000), *J. Magn. Reson.*, 142, 97.

24 A. E. Bennett, C. M. Rienstra, M. Auger, K. V. Lakshmi, R. G. Griffin, (1995), *J. Chem. Phys.*, 103, 6951.

25 L. A. O'Dell, R. W. Schurko, (2008), *Chem. Phys. Lett.*, 464, 97.

26 R. Bhattacharyya, L. Frydman, (2007), *J. Chem. Phys.*, 127, 194503.

27 E. Kupče, R. Freeman, (1995), *J. Magn. Reson. A*, 115, 273.

28 F. H. Larsen, H. J. Jakobsen, P. D. Ellis, N. C. Nielsen, (1997), *J. Phys. Chem. A*, 101, 8597.

29 K. Eichele, R. E. Wasylishen, (2001), *WSOLIDS*, version 1.20.15, Halifax, NS.

30 D. W. Alderman, M. S. Solum, D. M. Grant, (1986), *J. Chem. Phys.*, 84, 3717.

31 J. Herzfeld, A. E. Berger, (1980), *J. Chem. Phys.*, 73, 6021.

32 K. Eichele, R. E. Wasylishen, (2001), *HBA: Herzfeld-Berger analysis program*, Version 1.6.14, Halifax, NS, Dalhousie University.

33 D. Massiot, F. Fayon, M. Capron, I. King, S. Le Calvé, B. Alonso, J. -O. Durand, B. Bujoli, Z. Gan, G. Hoatson, (2002), *Magn. Reson. Chem.*, 40, 70.

34 M. J. Frisch, G. W Trucks, H. B. Schlegel, G. E. Scuseria, M. A. Robb, J. R. Cheeseman, G Scalmani, V. Barone, B. Mennucci, G. A. Petersson, H. Nakatsuji, M. Caricato, X. Li, H. P. Hratchian, A. F. Izmaylov, J. Bloino, G. Zheng, J. L. Sonnenberg, M. Hada, M Ehara, K. Toyota, R. Fukuda, J. Hasegawa, M. Ishida, T. Nakajima, Y. Honda, O. Kitao, H. Nakai, T. Vreven, J. A. Jr. Montgomery, J. E. Peralta, F. Ogliaro, M. Bearpark, J. Heyd, E. Brothers, K. N. Kudin, V. N. Staroverov, R. Kobayashi, J. Normand, K. Raghavachari, A. Rendell, J. C. Burant, S. S. Iyengar, J. Tomasi, M. Cossi, N. Rega, N. J. Millam, M. Klene, J. E. Knox, J. B. Cross, V. Bakken, C, Adamo, J. Jaramillo, R. Gomperts, R. E. Stratmann, O. Yazyev, A. J. Austin, R. Cammi, C. Pomelli, J. W. Ochterski, R. L. Martin, K. Morokuma, V. G. Zakrzewski, G. A. Voth, P. Salvador, J. J. Dannenberg, S. Dapprich, A. D. Daniels, Farkas, J. B. Foresman, J. V. Ortiz, J. Cioslowski, D. J. Fox, (2009), *Gaussian 09*, Revision A.02, Wallingford, CT, Gaussian Inc.

35 A. D. Becke, (1993), *J. Chem. Phys.*, 98, 5648.

36 S. Adiga, D. Aebi, D. L. Bryce, (2007), *Can. J. Chem.*, 85, 496.

37 C. J. Jameson, A. K. Jameson, (1987), *Chem. Phys. Lett.*, 135, 254.

38 S. C. Nyburg, C. H. Faerman, (1985), *Acta Crystallogr., Sect. B: Struct. Sci.*, 41, 274.

39 D. Cinčić, T. Friščić, W. Jones, (2011), *CrystEngComm*, 13, 3224.

40 M. N. Akhtar, A. A. Isab, A. R. Al-Arfaj, (1997), *J. Inorg. Biochem.*, 66, 197.

41 M. Witanowski, L. Stefaniak, S. Szymański, H. Januszewski, (1977), *J. Magn. Reson.*, 28, 217.

42 J. A. Kargol, R. W. Crecely, J. L. Burmeister, (1979), *Inorg. Chem.*, 18, 2532.

43 N. Zumbulyadis, H. J. Gysling, (1982), *J. Am. Chem. Soc.*, 104, 3246.

44 E. R. Andrew, (1981), *Int. Rev. Phys. Chem.*, 1, 195.

45 K. Eichele, R. E. Wasylishen, (1992), *Solid State Nucl. Magn. Reson.*, 1, 159.

46 A. C. Olivieri, (1989), *J. Magn. Reson.*, 81, 201.

47 G. M. Bernard, K. Eichele, G. Wu, C. W. Kirby, R. E. Wasylishen, (2000), *Can. J. Chem.*, 78, 614.

48 N. F. Ramsey, (1950), *Phys. Rev.*, 78, 699.

49 (a) J. Jokisaari, P. Lazzeretti, P. Pyykkö, (1988), *Chem. Phys.*, 123, 339. (b) M. Buhl, W. Thiel, U. Fleischer, W. Kutzelnigg, (1995), *J. Phys. Chem.*, 99, 4000. (c) M. Bühl, J. Gauss, J. F. Stanton, (1995), *Chem. Phys. Lett.*, 241, 248. (c) G. Schreckenbach, Y. Ruiz-Morales, T. Ziegler, (1996), *J. Chem. Phys.*, 104, 8605.

50 W. Nakanishi, S. Hayashi, Y. Katsura, M. Hada, (2011), *J. Phys. Chem. A*, 115, 8721.

7 CONCLUSIONS

7.1 SUMMARY

By demonstrating experimentally and theoretically how the NMR parameters are dependent on the local halogen bonded environment, the work in this dissertation achieved the goal set in the introduction. A total of fourteen new halogen bonded compounds has been successfully synthesized and characterized by X-ray crystallography. This method allowed the determination of the presence of halogen bonds by identifying short contacts between the halogen bond donor and acceptor. Also, XRD methods made it possible to verify the alignment of the components of the interaction. In all cases, the halogen bond followed the predicted linear interaction between the σ-hole present along the I-C bond of the diiodobenzene and the XB acceptor. In this work, all the halogen bonded compounds used the *iconic* halogen bond donor diiodobenzene (*p*- DITFB, *o*- DITFB, *p*- DIB, *sym*-TITFB), and the different halogen bond acceptor were studied. A summary of the XB acceptors and donors are presented in Figure 7.1, and the XB compounds are summarized in a table with their crystal structure CCDC reference code (Appendix D).

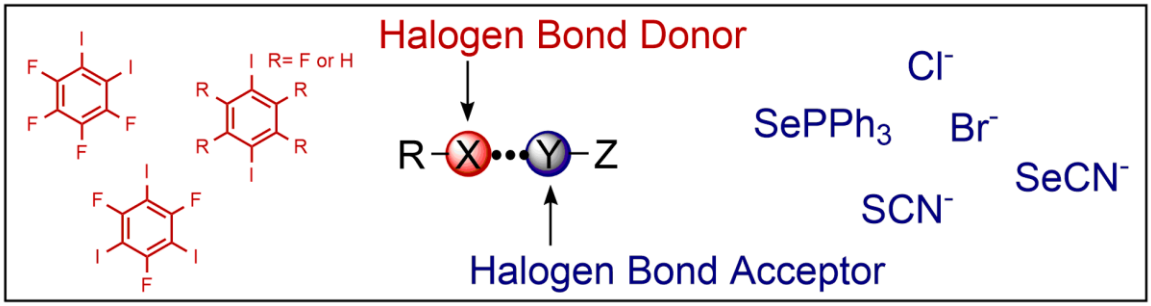

Figure 7.1 Summary of the halogen bond donors and acceptors used in this work.

In Chapter 3 and 4, the halogen bond acceptors employed are different ammonium or phosphonium halide salts. The onium halide (X^- = Cl or Br) was observed to form short contacts with the iodine in C-I···X^-···I-C type motifs and the majority of halogen bonded compounds formed one-dimensional polymeric zigzag chains. A particular XB compound, [(Ph_4PCl)(*p*-DITFB)], presented two unique onium Cl^- sites. One site formed four short contacts with iodine in a distorted square-planar geometry and the second site established six short contacts in a distorted octahedron geometry. Other XB compounds formed discrete entities dianionic motifs [Br···I—C_6H_4—I•••Br]$^{2-}$] and Br···I—C_6F_4—I•••Br]$^{2-}$. In Chapter 5, triphenylammonium selenide acted as the halogen bond acceptor and formed short contacts with iodine in -P=Se···I-C- type motifs. Also, Ph_3PSe was observed to act as a bidentate halogen bond acceptor, in some cases forming one-dimensional polymeric zigzag chains, and in other cases, forming simple discrete entities. In Chapter 6, thiocyanates (SCN^-) and selenocyanates ($SeCN^-$) operated as halogen bond acceptors. Selenocyanates showed characteristic I···$SeCN^-$ angles near 90° and trifurcated halogen bonds. Thiocyanate displayed one-dimensional architecture, where the I···NCS^- angle diverged from characteristic halogen bond interaction linearity with angle near 125°and acted as a bidentate XB acceptor.

A total of seventeen halogen bonded compounds were characterized by NMR in the solid-state. The three primary goals set in the beginning were attained:

- New benchmark NMR parameters for seventeen halogen bonded compounds have been described in the context of their related NMR data.
- Theoretical results have been generated from quantum calculations, where the incorporation of an NLMO analysis was added in some cases, and scalar and spin-

orbit relativistic effects were included when appropriate. Notably, the theoretical results are in agreement with the experimentally observed data.

- Clear trends in the observed NMR parameters and the local halogen bonded environment have been reported.

More precisely in Chapter 3, the halogen bonding interaction is reflected in the CS tensor of ^{13}C SSNMR spectroscopy. This finding was confirmed by investigating the halogen bonded compounds exhibiting the C—I···X$^-$ (where X = Br or Cl) type motif. It was clearly observed, for the first time, that the ^{13}C isotropic chemical shift of the carbon covalently bonded to iodine (C—I···X$^-$) increases by several ppm in the presence of the XB interaction compared to the respective pure starting material. It was also demonstrated that the increase in δ_{iso}(^{13}C) value is correlated to an increase in the C—I distance. In addition, this study demonstrated the importance of including scalar and spin-orbit relativistic effects in the quantum calculations of the ^{13}C chemical shift tensors to reproduce the experimental values where *heavy atom effects* are present.

Equally important in Chapter 4, halogen NMR parameters proved to be sensitive probes of the non-covalent interaction in a series of compounds containing C—I···X$^-$···I—C (where X = Br or Cl) halogen bonded motifs. I exposed how the $^{79/81}$Br and $^{35/37}$Cl quadrupolar coupling constant and asymmetry parameter varied as a function of the I···X$^-$···I angle. The results from an NLMO analysis, conducted on a cluster model, clarifies the dependence between the C_Q, η_Q values and the local halogen bonded geometry, I···X$^-$···I. Although the theoretical model is a simplification of the observed halogen bonding dynamic, it still conveys the nature of the interaction: a charge transfer from the halide to the σ*-antibonding orbital of the C-I halogen bond donor moiety. The theoretical

and observed experimental trend revealed how the C_Q and η_Q are dependent on the strength of the interaction and are a measure of the halogen bond.

In Chapter 5, I questioned the effect of a halogen bond on yet another NMR observable, the *J*-coupling value. For the first time, the measurements of $J(^{31}P,^{77}Se)$ couplings were obtained for compounds featuring P=Se···I-C halogen bonds in the solid state. The $J(^{31}P,^{77}Se)$ values have been found to be dependent on their halogen bonding environment: they correlate linearly with the strength of the interaction. An NLMO analysis provided insight into the relationship between the *J*-coupling and the strength of the interaction by revealing the major contributing molecular orbitals to *J*-coupling.

Chapter 6 continues the evaluation of halogen bond impacts on NMR observables by conducting a multinuclear magnetic resonance study on the bidentate halogen bond acceptors thiocyanate (SCN^-) and selenocyanate ($SeCN^-$) moieties. For a set of compounds, it was observed that the $\delta_{iso}(^{13}C)$ values of the SCN^- halogen bonded acceptor increases slightly with respect to their simple counterion, whereas the chemical shift values for ^{15}N decreases. The exact opposite trend is observed for the $SeCN^-$ halogen bonded acceptor. This study demonstrated that the halogen bonding interactions are reflected in the ^{77}Se CSA, thereby providing an example of the utility of NMR methods in characterizing the interactions in the solid state. It was clearly observed that both the $\delta_{iso}(^{77}Se)$ and $\delta_{33}(^{77}Se)$ values increase by several ppm in the presence of the XB interaction compared to the respective pure starting material, Me_4NSeCN. The change in the ^{77}Se CS tensor components was attributed to the close contacts between selenium···iodine, where the iodines are perpendicular with the $SeCN^-$ halogen bonded acceptor. In the context of Ramsey's theory, the value of the mixing between the virtual and occupied orbitals in the

perpendicular plane are due to the short Se···I contacts. The mixing affects the principal axis of the component of interest (δ_{33}) of the halogen bond acceptor, $SeCN^-$. The DFT computations of the shielding tensors for the synthesized compounds were in agreement with the experimental findings. Dipolar coupling, the through space phenomenon, is dependent on the motionally-averaged inverse cube of the internuclear distance between nuclear spins. Measurement of dipolar coupling constants between the ^{14}N and ^{13}C nuclei provided C-N bond lengths that were more precise than most often used X-ray crystallography technique.

7.2 CONTRIBUTIONS AND PERSPECTIVE

This section will try to contextualize the contribution of this research in a broader scientific scope by comparing it to the work of my peers. I hope to demonstrate that the work accomplished in this doctoral dissertation has helped further the knowledge and advanced the science in our field.

In 2012, researchers around the world, including our group, were invited to an IUPAC Workshop in Spain (IUCr Satellite Workshop on ″Categorizing Halogen Bonding and Other Noncovalent Interactions Involving Halogen Atoms″) to determine a universal scientific definition of the halogen bonding interaction (RX···YZ). Following this, it is now recognized that halogen bonds lead to characteristic changes in the nuclear resonance signal of RX and YZ moieties; [1] my work contributes to the IUPAC definition. It demonstrates not only how the nuclear resonance signal varies, but how the CS and EFG tensor components, as well as *J*-coupling values, undergo characteristic changes as a function of the local halogen bonding environment. Therefore, in this study the initial motivation was to use

SSNMR to characterize the halogen bonding interaction so that when a single crystal is not possible, SSNMR is a potential solution.

In addition to the work presented in this dissertation, other studies have been conducted with similar goals to characterize halogen bonds by SSNMR. For example, Attrell *et al.* investigated a series of haloanilium halides exhibiting weak halogen bonds (R_{XB} = 0.88 - 1.03) and competing hydrogen bonds.[2] They performed halogen NMR of the onium halide (Cl^-, Br^-, I^-) involved in the non-covalent interaction and concluded that compounds that isostructural compounds exhibit NMR parameters indicative of halogen bonding interactions. Specifically, in an isostructural series, the bromine C_Q will increase as the halogen bond weakens, and the opposite trend is observed for their span and isotropic CS tensor. The same overall trend was observed in this dissertation, the C_Q value increases for halogen bonded compounds, because the electronic symmetry is perturbed. Moreover, in this dissertation the C_Q values were correlated with the halogen bond environment. In their research, they demonstrated the feasibility of acquiring the ^{127}I SSNMR spectrum for two XB compounds, which is challenging due to extreme spectral breaths associated with the CT. In the literature, typical C_Q values range between 1700 to 2000 MHz for symmetric iodide environments. In Attrell *et al.*, the reported $C_Q(^{127}I)$ values of haloanilium iodide were 57.50(75) MHz and 152.50(25) MHz.

Other research conducted by the crystal engineer group Metrangolo and coworkers characterized halogen bonded networks with SSNMR. Baldrighi *et al.* reported pharmaceutical cocrystals involving iodinated antimicrobial product (*i.e.* 3-iodo-2-propynyl-N-butylcarbamate) and characterized them using SSNMR, enabling them to distinguish between polymorphic forms and changes in the chemicals shifts useful in

monitoring the formation of halogen-bonded adducts.[3] Once more, the ^{15}N chemical shift is shielded when halogen bonds are present, as described in this dissertation.

Another work by Baldrighi *et al.* studies a series of antifungal agent haloprogrin cocrystals.[4] Mainly, they observe the same overall trends as presented in the dissertation, the $\delta_{iso}(^{13}C)$ value is deshielded, whereas the $\delta_{iso}(^{15}N)$ values are shielded in the presence of the halogen bonding interaction when compared to the starting material. However, by using only the qualitative measurements of their chemical shift values to determine the halogen bond acceptor order (chloride < iodide < pyridine), they are making a bold statement. Such a statement should be supported by more data along with a quantitative and theoretical analysis.

Widdifield *et al.* studied halogen bonded complexes between decamethonium diiodide and various halogen bond donors, *p*-$C_6X_2Y_2$ (X = Br, I; Y = H, F), with multinuclear magnetic resonance.[5] The challenging ^{127}I SSNMR spectra are reported for the iodine ion of the decamethonium diiodide halogen bond acceptor and the C_Q values (48(2) MHz to 84.8(0.6) MHz) are the same as observed for the previously reported haloanilium iodides. The $C_Q(^{127}I)$ values increase indicating the presence of halogen bonds. Furthermore, they observed the same characteristic trend with ^{13}C SSNMR spectroscopy for their halogen bonded compounds and reported an increase in $\delta_{iso}(^{13}C)$ value of the covalently bond carbon to iodine when the C-I bond increase in halogen bonded complexes. They also acquired $^{14/15}N$ SSNMR of the cation, so the nucleus is not directly involved in the halogen bond. They stated that the $\delta_{iso}(^{15}N)$ value will increase for halogen bonded complexes compared to the starting materials, and the reverse trend was observed for the quadrupolar coupling constant of the ^{14}N nucleus. This behavior for $\delta_{iso}(^{15}N)$ and $C_Q(^{14}N)$

is also observed in the present thesis when the halogen bond acceptor, $SeCN^-$, is compared to Me_4NSeCN.

7.3 FUTURE WORK

The only way to determine the orientation of the CS or EFG tensor PAS with respect to the molecular frame is through single crystal NMR experiments. The known unit cell parameters of the single crystal help determine the orientation of the NMR interaction in the PAS with respect to the molecular frame. To do so, NMR experiments must be conducted as a function of the crystal orientation. This type of experiment will provide experimental insight into the orientation of the chemical shift tensor or electric field tensor in the molecular frame. As of now, the molecular orbital insight is a result of a theoretical NLMO analysis. Experimental validation of the molecular orbital analysis would be particularly useful. Hence, when a suitable single-crystal is grown it would be advantageous to perform single crystal NMR experiments.

Various halogen bonded systems were investigated for suitability in single crystal NMR experiments during the course of this work. Unfortunately, the systems under investigation provided a low signal to noise, thus it was not realistic to achieve a study in a timely matter. A total of sixty experiments needed to be performed. For each orthogonal axis the crystal needs to be rotated stepwise, usually by increments of 9° between 0° and 180° to acquire twenty data points in order to generate a rotation plot and extract the desired NMR parameters.

The first system probed was the halogen bonded compound [(*n*-Bu_4NCl)(*p*-DITFB))] using ^{35}Cl SSNMR. The difficulties associated with the application of chlorine NMR for the halogen bonded compound are the same as those encountered in their powdered sample: they have large *Q* and the nucleus is very dilute in the sample. Hence, no signal could be observed in a reasonable time.

The second system studied was a single crystal of the XB compound [(Ph_3PSe)(*o*-$C_6F_4I_2$)] where ^{77}Se SSNMR was initially used to investigate the orientation of the interaction with respect to the molecular frame. Unfortunately, no $\delta(^{77}Se)$ resonance was observed for that compound, probably due to strong dipolar coupling interactions, which are not averaged under static conditions. Hence, I think dipolar coupling between selenium and protons, fluorines, and iodines are overwhelming the selenium signal. Ideally, fluorines would be decoupled as well as protons to remove their dipolar coupling completely. In this second system, after selenium NMR, ^{31}P was used to probe the interaction even though it is not directly involved in the interaction. The acquisition of ^{31}P single crystal SSNMR spectra was possible, as shown in Figure 7.2. The ^{31}P signal is quite low and broad; this is probably due to dipolar coupling with fluorine, protons and iodine that are not averaged out in static experiments. The sixty spectra took a total of hundred and twenty hours of experimental time.

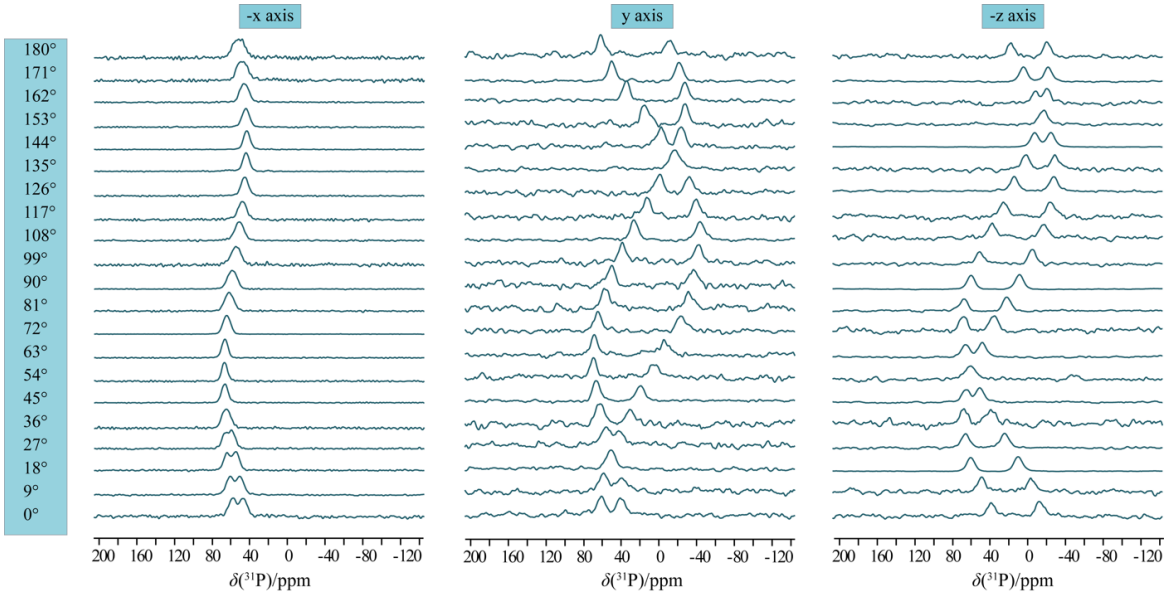

Figure 7.2 ^{31}P CPMAS NMR spectra acquired at 9.4 T of a single crystal of (Ph_3PSe)(*o*-DITFB) as a function of the crystal orientation. Experimental time is two hours for one ^{31}P spectrum. The spectra were recorded following a 9° increment (θ) about three different rotation axes.

The ^{31}P single crystal SSNMR spectra presented here are simply preliminary data, and efforts are currently underway in order to analyze the data.

In the pursuit of quality results for single crystal NMR, halogen bonded compounds isotopically labeled with ^{17}O have been synthesized. They exhibit P=O···I-C type non-covalent interactions in compounds of the form: [(Ph_3PO)(*o*- or *p*- $C_6F_4I_2$)], [(Ph_3PO)(*sym*-$C_6F_3I_3$)] and [(Ph_3PO)(*p*- $C_6H_4I_2$)]. Hopefully, a big enough single crystal can be grown, and combined with the fact the compound is enriched in ^{17}O, an NMR resonance will be observed in a timely manner. The study of those compounds will pave the way for the anticipated analysis of the CS and EFG tensor orientation with respect to the molecular frame.

As a follow-up project, the halogen bonded compounds exhibiting P=O···I-C type motifs may be characterized by multinuclear magnetic resonance (^{13}C, ^{31}P, ^{17}O) to increase the amount of benchmark data. The phosphorus SSNMR spectra exhibit *J*-coupling between the quadrupolar nuclide ^{17}O and ^{31}P. The objective shall be to characterize the complete CS and EFG tensors, as well as *J*-coupling, in order to relate to variations in the halogen bonded interaction. Preliminary ^{17}O SSNMR data are in agreement with the work presented in this Thesis and the previous work of Attrell *et al.*[2] as well as Widdifield *et al.*;[5] the C_Q value increases when the halogen bonding interaction is present, compared to the pure compound devoid of the interaction. Also, an NLMO analysis is anticipated, which will help determine the main contributions of the local halogen bond environment affecting the NMR parameters.

Furthermore, the work in this thesis focused on the *iconic* halogen bond donor diiodoperfluorobenzene. However, since there are multiple examples of bromine and chlorine halogen bonds donors the literature, it would be interesting to undergo a more systematic study of the characterization of halogen bond donors involving chlorine and bromine. In addition, it would be interesting to observe directly the halogen bond donor atom by NMR spectroscopy. As mentioned before, the halogens (i.e. iodine, chlorine, and bromine) are quadrupolar nuclei associated with a *Q* resulting in very broad powder patterns rendering NMR spectroscopy difficult. Acquiring the spectra of covalently bonded halogens is practically impossible due to much larger anisotropies of the local electronic environment. However, there are recent examples in the literature of covalently bonded chlorine with NMR spectra acquired at very high fields (21.1 T).[6] This motivated our group

to pursue the investigation of halogen bonded compounds where the halogen bond donor is chlorine. No report exist in the literature for covalently bond bromine or iodine.

Due to their colossal quadrupolar interactions, other methods are used to acquire their EFG tensor parameters. The method is nuclear quadrupole resonance (NQR) and successfully demonstrated the presence of halogen bonds in the 60s by demonstrating that the shifts in quadrupole frequency are attributed to a charge-transfer phenomenon. For example, Semin *et al.* reported changes in the ^{127}I NQR frequencies of $I(CF_2)_2I$ when it halogen bonds with $NH(C_2H_5)_2$. Bowmaker has also made significant contributions to this area.[7,8,9,10]

To date, only X···Y *J*-couplings have been measured across halogen bonds (Chapter 5, $J(^{77}Se, ^{31}P)$) although, in principle one would also expect *J*-couplings between the **R**(X)···**Y** nuclei. The dependence of the *J* values on the halogen bond strength was valuable information. In practice, the *J*(R,Y) should be difficult to measure due to the strong quadrupole interactions of the X nuclei and weak coupling expected between the R and Y nuclei. The hypothetical observation of *J*(R,Y) coupling in halogen bonded compounds could be indicative of the degree of covalency as was the case in hydrogen bond studies.[11,12,13]

Finally, our group, the Bryce laboratory, is involved in the characterization of not only halogen bonds with SSNMR, but all σ- hole bonding interactions such as tetral bonds and pnicogen bonds. A change in the chemical shift value is expected for a compound where sigma-hole bonding is present versus the pure material. The objective will also be to determine a causality in the variation of the NMR parameters. For example, is it due to the presence of the sigma-hole bonding?

7.4 REFERENCES FOR CHAPTER 7

1 G. R. Desiraju, P. S. Ho, L. Kloo, A. C. Legon, R. Marquardt, P. Metrangolo, P. A. Politzer, G. Resnati, K. Rissanen, (2013), *Pure Appl. Chem.*, 85, 1711.

2 R. J. Attrell, C. M. Widdifield, I. Korobkov, D. L. Bryce, (2012), *Cryst. Growth Des.*, 12, 1641.

3 M. Baldrighi, G. Cavallo, M. R. Cherotti, R. Gobetto, P. Metrangolo, T. Pilati, G. Resnati, G. Terraneo, (2013), *Mol. Pharmaceutics*, 10, 1760.

4 M. Baldrighi, D. Bartesaghi, G. Cavallo, M. R. Chierotti, R. Gobetto, P. Metrangolo, T. Pilati, G. Resnati, G. Terraneo, (2014), *CrystEngComm*, 16, 5897.

5 C. M. Widdifield, G. Cavallo, G. A. Facey, T. Pilati, J. Lin, P. Metrangolo, G. Resnati, D. L. Bryce, (2013), *Chem. Eur. J.*, 19, 11949.

6 F. A. Perras, D. L. Bryce, (2012), *Angew. Chem. Int. Ed.*, 51, 4227.

7 G. A. Bowmaker, (1976), *J. Chem. Soc. Faraday Trans.*, 2, 1964.

8 G. A. Bowmaker, S. Hacobian, (1968), *Aust. J. Chem.*, 21, 551.

9 G. A. Bowmaker, S. Hacobian, (1969), *Aust. J. Chem.*, 22, 2047.

10 G. A. Bowmaker, P. D. W. Boyd, (1987), *J. Chem. Soc. Faraday Trans.*, 2, 2211.

11 I. Alkorta, J. Elguero, G. S. Denisov, (2008), *Magn. Reson. Chem.*, 46, 599.

12 A. E. Aliev, (2004), *Struct. Bond*, 108, 1.

13 E. Brunner, U. Sternberg, (1998), *Prog Nucl Magn Reson Spectrosc.*, 32, 21.

APPENDIX A: COMPLEMENTARY DATA FOR CHAPTER 3

Additional X-ray Crystal Structures

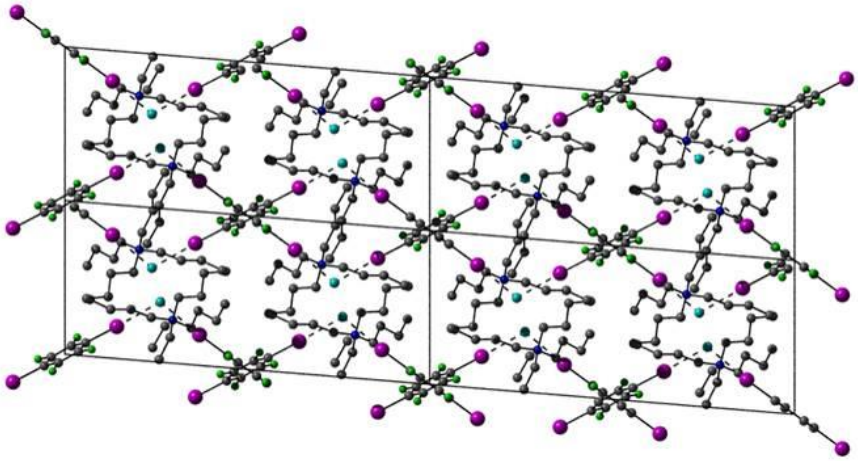

Figure A.1 2 x 2 x 2 super cell of compound **1** along the *b* axis. Hydrogens are omitted for clarity.

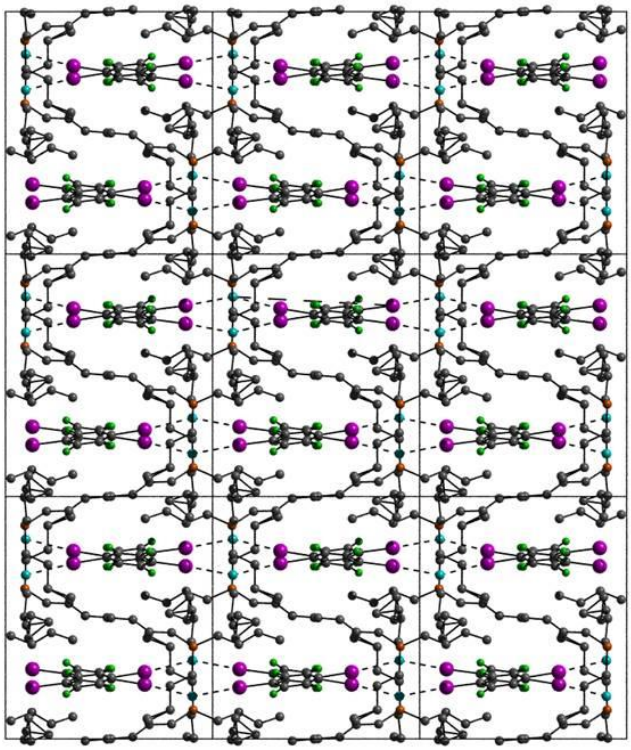

Figure A.2 3 x 3 x 3 super cell of compound **2** shown along the *c* axis. Hydrogens are omitted for clarity.

CASTEP Calculations

CASTEP software was used: Clark, S. J.; Segall, M. D.; Pickard, C. J.; Hasnip, P. J.; Probert, M. I. J.; Refson, K.; Payne,M. C. Z. Kristallogr. (2005), 220, 567; Pickard, C. J.; Mauri, F. Phys. Rev. B (2001), 63, 245101.

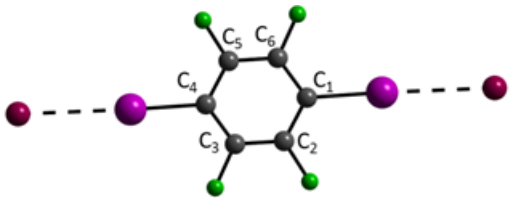

Figure A.3 Labelling scheme for calculated $\delta_{iso}(^{13}C)$ values of GIPAW DFT calculations. (See Table 01.)

Table A.1 GIPAW DFT calculations of $\delta_{iso}(^{13}C)$, with GGA PBE functional.[a]

$\delta_{iso}(^{13}C)$	*p*-DITFB[b]	**1**	**2**	**5**
C_1—I---Cl	113.3	130.8	133.3	131.0
C_4—I---Cl	113.3	132.8	137.1	131.0
C_2—F	157.5	163.8	120.1	162.3
C_3—F	162.6	163.0	101.6	162.9
C_5—F	157.5	163.8	164.2	162.3
C_6—F	162.6	163.0	167.0	162.9

[a] The kinetic energy cut-off is 450 eV and the k-point grid used is 1 x 1 x 1.

[b] The kinetic energy cut-off energy is 500 eV and the k-point grid is 2 x 2 x 1.

Pseudopotentials used:

C 2|1.4|9.187|11.025|12.862|20UU:21UU(qc=6)[]

F 2|1.4|16.537|18.375|20.212|20UU:21UU(qc=7.5)[]

I 2|2|2|1.6|6|7.3|9.9|50U=-0.65U=+0:51U=-0.265U=+0[]

Cl 2|1.7|5.88|7.35|9.187|30UU:31UU:32LGG[]

P 2|1.8|3.675|5.512|6.982|30UU:31UU:32LGG[]

Br 2|2|2|1.4|5.6|6.6|8.8|40U=-0.74U=+0.25:41U=-0.295U=+0.25[]

H 1|0.8|3.675|7.35|11.025|10UU(qc=6.4)[]

N 2|1.5|11.025|12.862|14.7|20UU:21UU(qc=6)[]

ADF Calculations and Theoretical Assignment of ^{13}C CS resonances

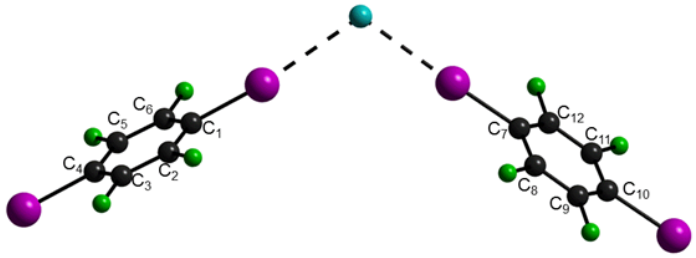

Figure A.4 Labelling scheme for calculated $\delta_{iso}(^{13}C)$ values. (See Tables 02 to 10.)

Table A.2 ZORA-DFT calculations of $\delta_{iso}(^{13}C)$ with scalar and spin orbit relativistic effects (GGA PBE, ZORA/TZP basis set)

	compound					
$\delta_{iso}(^{13}C)$	*p*-DITFB	**1**	**2**	**3**	**4**	**5**
C_1—I---Cl[a]	74.03	87.52	97.62	103.32	122.74	98.10
C_7—I---Cl		117.23	101.14	79.28	68.80	
C_4—I	74.03	90.85	81.16	78.24	55.19	80.42
C_{10}—I		67.76	79.17	76.40	103.97	
C_2—F	147.38	151.68	152.44	152.19	151.78	153.07
C_3—F	149.89	149.13	149.55	149.84	143.29	148.84
C_5—F	147.39	149.02	149.83	149.76	149.81	149.18
C_6—F	149.89	152.49	153.25	153.29	146.74	152.95
C_8—F		152.73	152.12	137.26	151.47	
C_9—F		149.64	149.94	134.03	148.84	
C_{11}—F		150.30	149.89	142.12	148.06	
C_{12}—F		152.01	153.13	145.61	151.90	

[a] Except for *p*-DITFB where this is simply C_1-I.

Table A.3 ZORA-DFT calculations of $\delta_{iso}(^{13}C)$ with scalar and spin orbit relativistic effects (GGA PBE, ZORA/TZP basis set, and AUG/ATZP for halide)

	Compound					
$\delta_{iso}(^{13}C)$	*p*-DITFB	**1**	**2**	**3**	**4**	**5**
$\underline{C_1}$—I---Cl[a]	74.03	86.79	96.85	95.10	121.30	97.57
$\underline{C_7}$—I---Cl		117.22	100.38	70.97	68.10	
$\underline{C_4}$—I	74.03	90.60	80.94	69.70	54.96	80.19
$\underline{C_{10}}$—I		67.48	78.92	67.62	103.70	
$\underline{C_2}$—F	147.38	151.64	151.89	151.60	151.40	152.77
$\underline{C_3}$—F	149.89	149.02	149.38	149.42	143.09	148.79
$\underline{C_5}$—F	147.39	148.90	149.77	149.41	149.44	149.10
$\underline{C_6}$—F	149.89	152.23	152.95	152.53	146.07	152.48
$\underline{C_8}$—F		152.32	151.55	136.71	151.09	
$\underline{C_9}$—F		149.49	149.76	133.65	148.72	
$\underline{C_{11}}$—F		150.14	149.81	141.75	148.04	
$\underline{C_{12}}$—F		151.66	152.87	145.10	151.73	

[a] Except for *p*-DITFB where this is simply $\underline{C_1}$-I.

Table A.4 ZORA-DFT calculations of $\delta_{iso}(^{13}C)$ without relativistic effects (GGA PBE, TZP basis set)

	compound					
$\delta_{iso}(^{13}C)$	*p*-DITFB	**1**	**2**	**3**	**4**	**5**
$\underline{C_1}$—I---Cl[a]	91.94	127.10	126.57	127.94	126.75	128.14
$\underline{C_7}$—I---Cl		129.26	127.98	110.50	123.59	
$\underline{C_4}$—I	91.94	96.23	95.55	97.72	96.56	95.19
$\underline{C_{10}}$—I		96.26	94.41	90.34	95.01	
$\underline{C_2}$—F	148.34	153.45	154.50	154.18	153.97	154.75
$\underline{C_3}$—F	151.17	151.44	151.47	152.37	145.83	151.99
$\underline{C_5}$—F	148.34	151.66	152.42	152.36	151.95	152.20
$\underline{C_6}$—F	151.17	154.41	155.10	155.31	148.16	154.94
$\underline{C_8}$—F		154.87	154.04	140.04	153.44	
$\underline{C_9}$—F		151.49	152.00	136.52	151.68	
$\underline{C_{11}}$—F		152.31	152.30	144.95	151.05	
$\underline{C_{12}}$—F		154.12	155.02	148.00	154.13	

[a] Except for *p*-DITFB where this is simply $\underline{C_1}$-I.

Table A.5 ZORA-DFT calculations of $\delta_{iso}(^{13}C)$ without relativistic effects (GGA PBE, TZP basis set, and AUG/ATZP for halide)

	compound					
$\delta_{iso}(^{13}C)$	*p*-DITFB	**1**	**2**	**3**	**4**	**5**
C_1—I---Cl[a]	91.94	126.93	125.79	127.08	125.94	127.40
C_7—I---Cl		129.12	127.24	109.79	122.63	
C_4—I	91.94	95.98	95.35	97.51	96.30	94.81
C_{10}—I		95.94	94.17	90.13	94.77	
C_2—F	148.34	153.25	154.07	153.79	153.58	154.32
C_3—F	151.17	151.33	151.34	152.24	145.68	151.87
C_5—F	148.34	151.52	152.27	152.27	151.81	152.06
C_6—F	151.17	154.02	154.60	154.78	147.63	154.45
C_8—F		154.55	153.55	139.65	152.89	
C_9—F		151.37	151.86	136.42	151.56	
C_{11}—F		152.17	152.16	144.86	150.90	
C_{12}—F		153.78	154.56	147.63	153.68	

[a] Except for *p*-DITFB where this is simply C_1-I.

Table A.6 ZORA-DFT calculations of $\delta_{iso}(^{13}C)$ with scalar and spin orbit relativistic effects (GGA revPBE, ZORA/TZP basis set)

	compound					
$\delta_{iso}(^{13}C)$	*p*-DITFB	**1**	**2**	**3**	**4**	**5**
C_1—I---Cl[a]	72.12	85.87	95.53	93.80	119.27	96.13
C_7—I---Cl		114.28	98.97	70.00	68.14	
C_4—I	72.12	87.98	78.87	63.13	54.44	78.08
C_{10}—I		66.30	76.93	65.63	100.21	
C_2—F	144.57	148.62	149.42	149.00	148.97	150.05
C_3—F	147.05	146.42	146.76	146.68	140.34	146.04
C_5—F	144.57	146.30	146.96	146.65	146.72	146.42
C_6—F	147.05	149.42	150.24	150.05	144.01	149.92
C_8—F		149.84	149.12	134.38	148.25	
C_9—F		146.65	147.13	131.32	146.31	
C_{11}—F		147.27	147.01	139.14	145.52	
C_{12}—F		149.15	150.14	142.55	148.72	

[a] Except for *p*-DITFB where this is simply C_1-I.

Table A.7 ZORA-DFT calculations of $\delta_{iso}(^{13}C)$ with scalar and spin orbit relativistic effects (GGA revPBE, ZORA/TZP basis set, and AUG/ATZP for halide)

	Compound					
$\delta_{iso}(^{13}C)$	*p*-DITFB	**1**	**2**	**3**	**4**	**5**
C_1—I---Cl[a]	72.12	85.22	94.74	92.95	117.66	95.62
C_7—I---Cl		114.17	98.21	69.53	67.54	
C_4—I	72.12	87.73	78.64	67.91	54.19	77.84
C_{10}—I		66.01	76.67	65.43	99.98	
C_2—F	144.57	148.58	148.86	148.66	148.56	149.75
C_3—F	147.05	146.31	146.59	146.55	140.13	145.98
C_5—F	144.57	146.18	146.88	146.54	146.35	146.25
C_6—F	147.05	149.16	149.95	149.55	143.29	149.43
C_8—F		149.41	148.53	134.00	147.89	
C_9—F		146.50	146.95	131.18	146.16	
C_{11}—F		147.12	146.91	139.08	145.48	
C_{12}—F		148.76	149.88	142.28	148.57	

[a] Except for *p*-DITFB where this is simply C_1-I.

Table A.8 ZORA-DFT calculations of $\delta_{iso}(^{13}C)$ without relativistic effects (GGA revPBE, TZP basis set)

	compound					
$\delta_{iso}(^{13}C)$	*p*-DITFB	**1**	**2**	**3**	**4**	**5**
C_1—I---Cl[a]	89.68	124.41	123.89	125.27	124.12	125.55
C_7—I---Cl		126.57	125.29	108.03	120.98	
C_4—I	89.68	93.96	93.30	95.43	94.28	92.92
C_{10}—I		93.99	92.15	88.17	92.76	
C_2—F	145.55	150.54	151.57	151.25	151.03	151.81
C_3—F	148.33	148.57	148.59	149.48	143.07	149.10
C_5—F	145.55	148.77	149.52	149.45	149.04	149.30
C_6—F	148.33	151.49	151.15	152.36	145.36	151.99
C_8—F		151.93	151.11	137.39	150.51	
C_9—F		148.61	149.11	133.93	148.79	
C_{11}—F		149.41	149.40	142.22	148.17	
C_{12}—F		151.20	152.08	145.21	151.12	

[a] Except for *p*-DITFB where this is simply C_1-I.

Table A.9 ZORA-DFT calculations of $\delta_{iso}(^{13}C)$ without relativistic effects (GGA revPBE, TZP basis set, and AUG/ATZP for halide)

	compound					
$\delta_{iso}(^{13}C)$	*p*-DITFB	**1**	**2**	**3**	**4**	**5**
$\underline{C_1}$—I---Cl[a]	89.68	124.20	123.09	124.39	123.28	124.76
$\underline{C_7}$—I---Cl		126.38	124.53	107.31	120.00	
$\underline{C_4}$—I	89.68	93.71	93.09	95.21	94.02	92.53
$\underline{C_{10}}$—I		93.67	91.91	87.95	92.52	
$\underline{C_2}$—F	145.55	150.33	151.12	150.85	150.62	151.36
$\underline{C_3}$—F	148.33	148.46	148.45	149.35	142.91	148.98
$\underline{C_5}$—F	145.55	148.63	149.37	149.36	148.90	149.17
$\underline{C_6}$—F	148.33	151.07	151.64	151.82	144.82	151.49
$\underline{C_8}$—F		151.60	150.61	136.99	149.95	
$\underline{C_9}$—F		148.49	148.96	133.83	148.67	
$\underline{C_{11}}$—F		149.26	149.26	142.12	148.02	
$\underline{C_{12}}$—F		150.83	151.61	144.82	150.67	

[a] Except for *p*-DITFB where this is simply $\underline{C_1}$-I.

Table A.10 Summary of ZORA-DFT calculations of $\delta_{iso}(^{13}C)$ with relativistic effects of carbons covalently bonded to iodine

compound	experimental	PBE	PBE[a]	revPBE	revPBE[a]
p-DITFB	76.50(0.50)	74.03	74.03	72.12	72.12
1	83.92(0.01)	117.23	117.22	114.28	114.17
	80.64(0.02)	87.52	90.60	85.87	85.22
2	81.75(0.45)	97.62	96.85	95.53	94.74
	83.65(0.15)	101.14	100.38	98.97	98.21
3	84.72(0.10)	103.32	95.10	93.80	92.95
	81.84(0.01)	79.28	70.97	70.00	69.53
4	83.80(0.06)	68.80	68.10	68.14	67.54
	83.00(0.02)	122.74	121.3	119.27	117.66
5	84.50(0.25)	98.10	97.57	96.13	95.62

[a] Along with the usual basis used (ZORA/TZP), a diffuse basis set is added to the halide, AUG/ATZP.

APPENDIX B: COMPLEMENTARY DATA FOR CHAPTER 4

Experimental Details for Halogen Static SSNMR Experiments

Table B.1 Experimental parameters used for the acquisition of $^{35/37}$Cl NMR spectra at 21.1 T.

sample	B_0 / T	nuclide	window / kHz	points	π/2 pulse / μs	scans/ piece	recycle delay / s	τ_1; τ_2 / μs	details
1	21.1	^{35}Cl	500	1024	4	16k	1	45; 0	5 mm static; solid-echo; offset positioned at 0Hz, ^{1}H decoupling (CW, 30 kHz)
		^{37}Cl	500	1024	3.5	48k	1	50; 0	5 mm static; solid-echo; offsets 0 Hz; ^{1}H decoupling (CW, 30 kHz)
2	21.1	^{35}Cl	500	1024	4	24k	1	45; 0	5 mm static; solid-echo; VOCS offsets: 30/-70 kHz; ^{1}H decoupling (CW, 30 kHz)
		^{37}Cl	500	1024	3.5	12k	1	50; 0	5 mm static; solid-echo; offsets 0 Hz; ^{1}H decoupling (CW, 30 kHz)
6	21.1	^{35}Cl	500	1024	4	14k	2	45; 0	5 mm static; solid-echo; VOCS offsets at 20 kHz and -80 kHz; ^{1}H decoupling (CW, 30 kHz)
		^{37}Cl	500	1024	3.5	48k	1	50; 0	5 mm static; solid-echo; offsets 0 Hz; ^{1}H decoupling (CW, 30 kHz)
8	21.1	^{35}Cl	500	1024	4	32k	2	45; 0	5 mm static; solid-echo; VOCS offsets: 30/-30 kHz; ^{1}H decoupling (CW, 30 kHz)
10	21.1	^{35}Cl	500	1024	4	14k	1	50; 0	5 mm static; solid-echo; VOCS offsets: 30/-30 kHz; ^{1}H decoupling (CW, 30 kHz)
		^{37}Cl	500	1024	3.5	49k	1	50; 0	5 mm static; solid-echo; offsets 0 Hz; ^{1}H decoupling (CW, 30 kHz)

Table B.2 Experimental parameters used for the acquisition of $^{35/37}$Cl NMR spectra at 9.4 T.

sample	B_0 / T	nuclide	window / MHz	points	WURST / μs	scans/ piece	spikelet separation / kHz; #echoes;sp1/db	details
1	9.4	^{35}Cl	2	100k	50	16k	5; 128; 10	5 mm static; WURST-QCPMG; offset positioned at 0 Hz, ^{1}H decoupling (CW, 30 kHz), recycle delay (D1) = 4s
		^{37}Cl	2	100k	50	7200	5; 128; 10	5 mm static; WURST-QCPMG; offsets 0 Hz; ^{1}H decoupling (CW, 30 kHz), D1 = 4s
2	9.4	^{35}Cl	2	100k	50	13048	5; 128; 10	5 mm static; WURST-QCPMG; 5 VOCS 100kHz separations; ^{1}H decoupling (CW, 30kHz), D1 = 4s
		^{37}Cl	2	100k	50	12k	5; 128; 10	5 mm static; WURST-QCPMG; VOCS offsets: 0, 100, 200, -100, -200, -300 kHz;; ^{1}H decoupling (CW, 30 kHz), D1 = 4 s
6	9.4	^{35}Cl	2	100k	50	14k	5; 128; 10	5 mm static; WURST-QCPMG; VOCS offsets at 20, -30, -80 kHz; ^{1}H decoupling (CW, 30 kHz), D1 = 2s
		^{37}Cl	2	100k	50	39992	5; 128; 10	5 mm static; WURST-QCPMG; VOCS offsets 20, -80 kHz; ^{1}H decoupling (CW, 30 kHz), D1 = 2s
8	9.4	^{35}Cl	2	100k	50	20k	5; 128; 10	5 mm static; WURST-QCPMG; VOCS offsets: 20/-80 kHz; ^{1}H decoupling (CW, 30 kHz), D1 = 1s
		^{37}Cl	2	100k	50	106200	5; 128; 10	5 mm static; WURST-QCPMG; VOCS offsets 30, -30 kHz; ^{1}H decoupling (CW, 30 kHz), D1 = 1s
10	9.4	^{35}Cl	2	100k	50	14k	5; 128; 10	5 mm static; WURST-QCPMG; VOCS offsets: 30, -30 kHz; ^{1}H decoupling (CW, 8db), D1= 1s
		^{37}Cl	2	100k	50	24k	5; 128; 10	5 mm static; WURST-QCPMG; VOCS offsets: 30, -20 kHz; ^{1}H decoupling (CW, 30 kHz), D1 = 4s

Table B.3 Experimental parameters used for the acquisition of $^{79/81}$Br NMR spectra at 21.1 T.

sample	B_0 / T	nuclide	window / MHz	points	π/2 pulse / μs	scans/ piece	recycle delay / s	τ_1; τ_2 / μs	details
3	21.1	^{81}Br	2	2048	1.5	24k	0.2	18; 0	5 mm static; solid-echo; VOCS, 500 kHz separations: offsets 500 to -1500 kHz, ^{1}H decoupling (CW, 40 kHz)
4	21.1	^{81}Br	2	2048	1.5	14k	0.2	38; 0	5 mm static; solid-echo; 9 VOCS, 250 kHz separations: 500 to -1500 kHz; ^{1}H decoupling (CW, 40 kHz)
		^{79}Br	2	2048	1.5	24k	0.2	18; 0	5 mm static; solid-echo; VOCS, 400 kHz separations: offsets 400 to -2000, kHz; ^{1}H decoupling (CW, 40 kHz)
5	21.1	^{81}Br	2	2048	1.0	6k	0.2	18; 0	5 mm static; solid-echo; VOCS offsets: 500, 0, -500, -1000 kHz; ^{1}H decoupling (CW, 40 kHz)
7	21.1	^{81}Br	2	2048	1.0	2k	0.2	18; 0	5 mm static; solid-echo; VOCS offsets: 125, 0, -125 kHz; ^{1}H decoupling (CW, 40 kHz)
9	21.1	^{81}Br	2	2048	1.0	965	0.2	175; 0	5 mm static; solid-echo; VOCS offsets: 500, 0, -500 kHz; ^{1}H decoupling (CW, 40 kHz)
		^{79}Br	2	2048	1.5	8k	0.2	18; 0	5 mm static; solid-echo; VOCS offsets: 0, 150, 550, -250, -650 kHz; ^{1}H decoupling (CW, 40 kHz)

Powder X-ray Diffraction

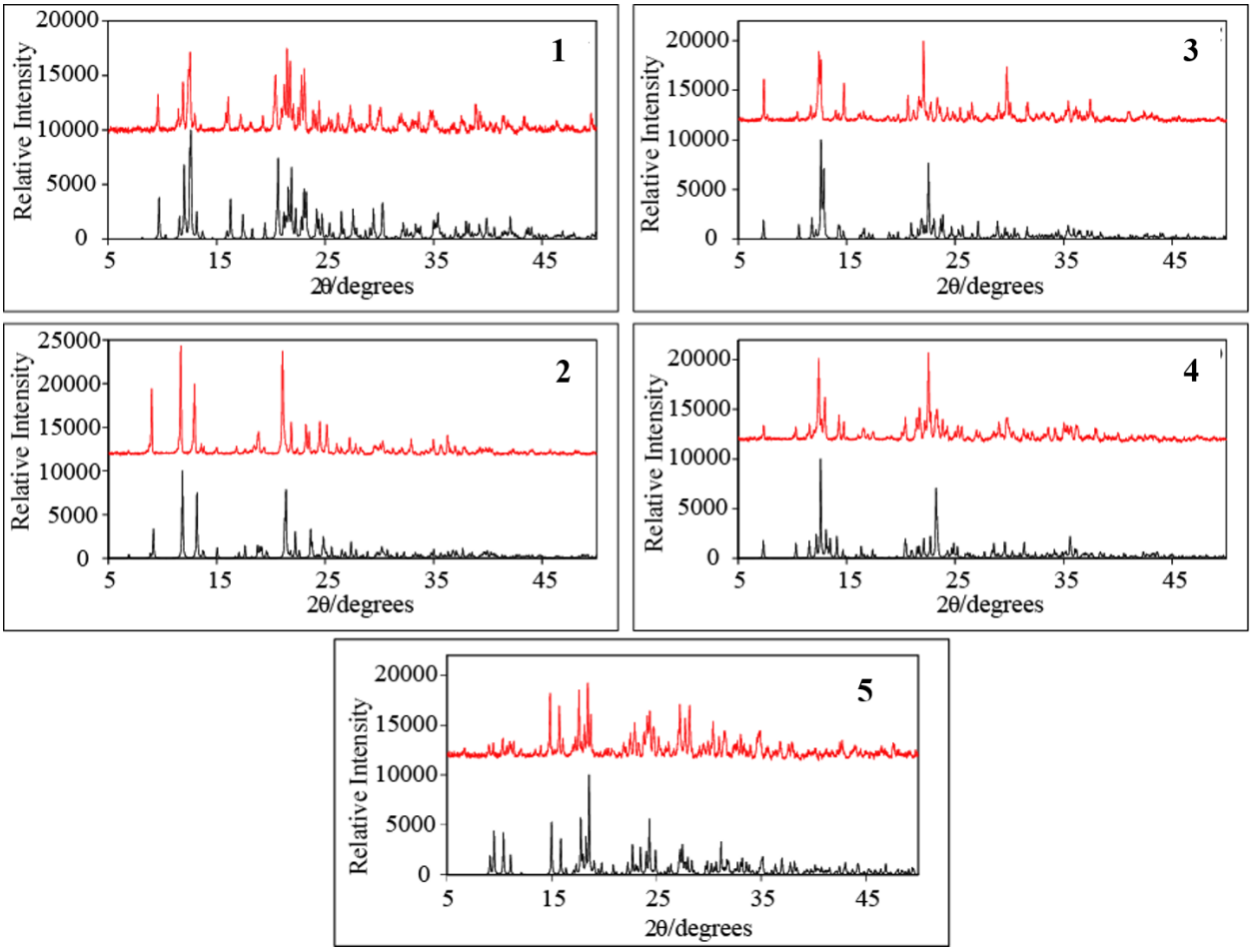

Figure B.1 Experimental PXRD patterns (red traces) of XB compounds **1**, **2**, **3**, **4** and **5** along with their respective simulations in black based on the single-crystal X-ray structure data. All experiments were carried out using a Rigaku Ultima IV instrument with 2θ ranging between 5 and 50° in increments of 0.02° at a rate of 0.6° per minute. Simulations were generated using Mercury software available from CCDC.

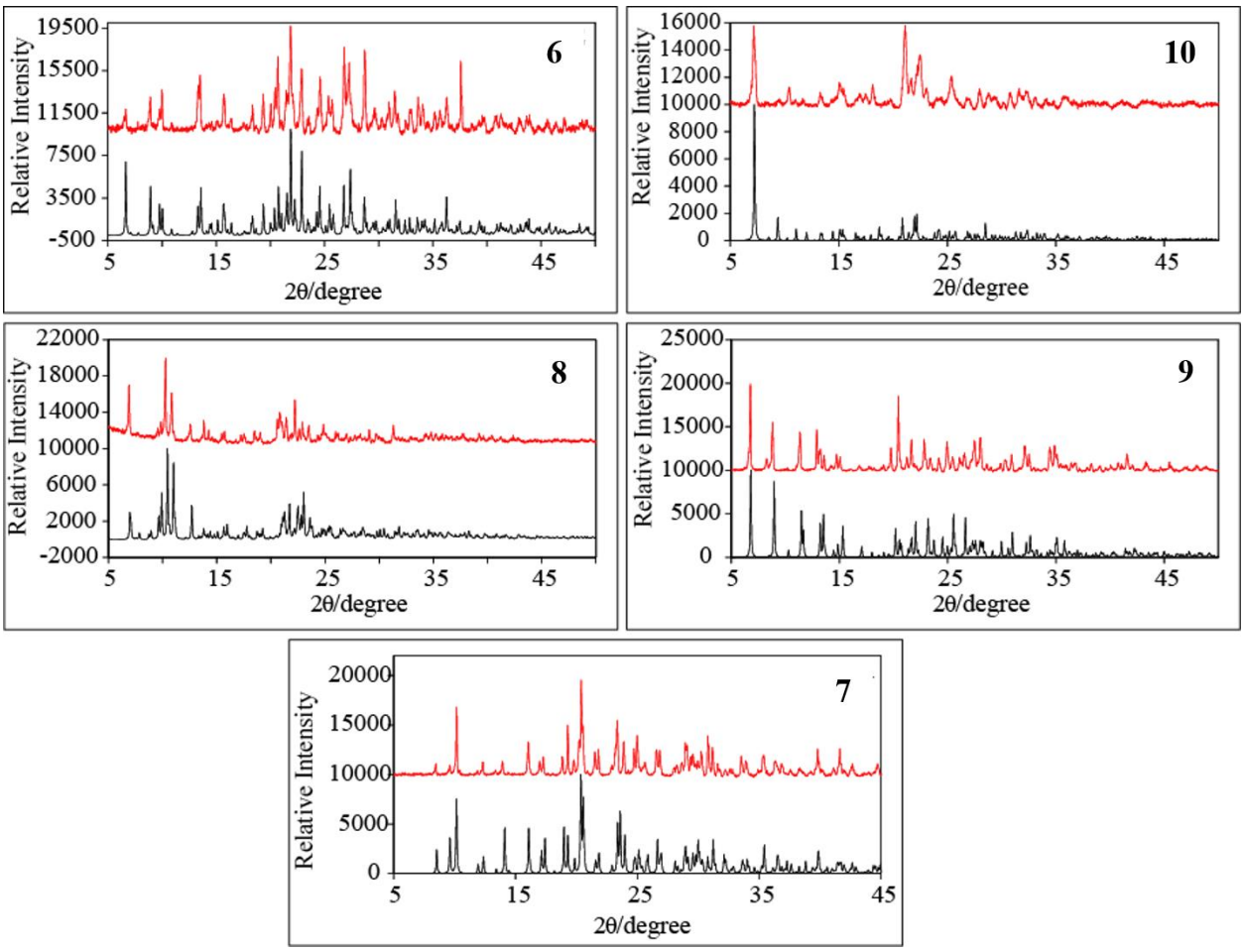

Figure B.2 Experimental PXRD patterns (red traces) of new XB compounds (**6**, **7**, **8**, **9**, and **10**) along with their respective simulations in black based on single-crystal X-ray structure data. All experiments were carried out using a Rigaku Ultima IV instrument with 2θ ranging between 5 and 50° in increments of 0.02° at a rate of 0.3° (**8**, **6**, **5**) or 0.2° (**9**, **10**) per minute. Simulations were generated using Mercury software available from CCDC. Small differences in intensities between the experimental and simulated powder patterns, along with small high-angle shifts, are known to be due to slight preferential crystallite alignment and non-uniform crystallite size (see Scardi, P.; Leoni, M. "Diffraction line profiles from polydisperse crystalline systems", *Acta Cryst. A*, **2001**, *57*, 604-613).

Full ^{13}C CPMAS SSNMR Spectra

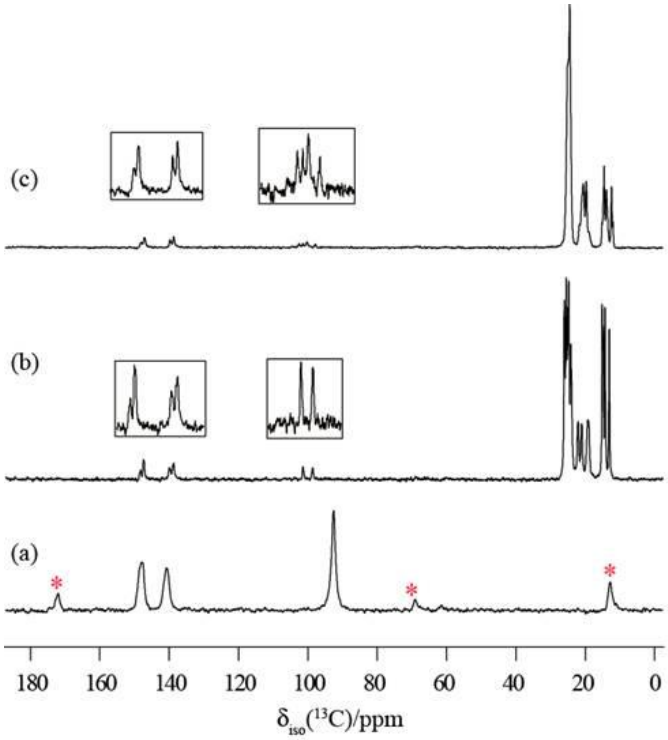

Figure B.3 Full ^{13}C CPMAS SSNMR spectra of halogen bonded complexes for the series of compounds where the halogen bonding donor is *o*-DITFB: (b) **9**, (c) **8**, recorded at 21.1 T. The spectrum of pure *o*-DITFB is shown in (a). The insets show vertical expansions and the asterisks denote spinning sidebands.

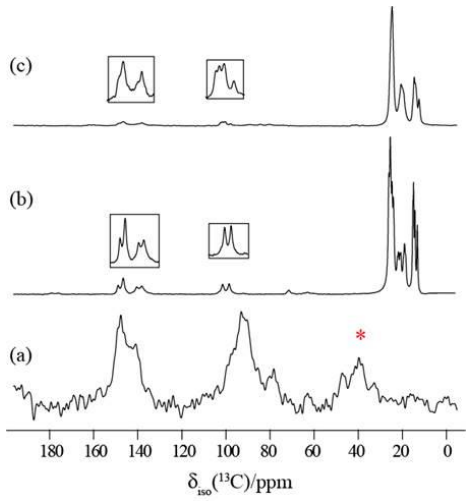

Figure B.4 Full ^{13}C CPMAS SSNMR spectra of halogen bonded complexes for the series of compounds where the halogen bonding donor is *o*-DITFB: (b) **9**, (c) **8**, recorded at 9.4 T. The spectrum of pure *o*-DITFB is shown in (a). The insets show vertical expansions and the asterisk denotes a spinning sideband.

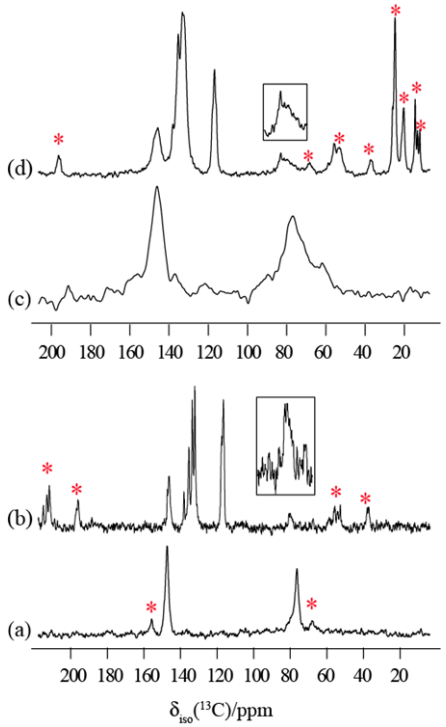

Figure B.5 Full ^{13}C CPMAS SSNMR spectra of starting material, *p*-DITFB ((a) and (c)) and XB compound **6** ((b) and (d)), recorded at 21.1 T and 9.4 T, respectively. The asterisks indicate spinning sidebands (18 kHz MAS). The insets show vertical expansions.

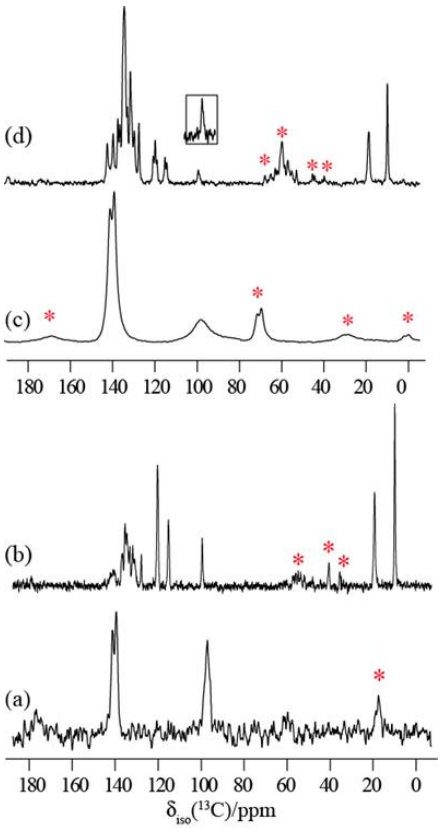

Figure B.6 Full ^{13}C CPMAS SSNMR spectra of *p*-DIB ((a) and (c)) and **7** ((b) and (d)) recorded at 21.1 T and 9.4 T, respectively. The asterisks indicate spinning sidebands (18 kHz MAS). The insets show vertical expansions.

^{13}C CS resonance assignments follow the labelling depicted in Figure B7

Figures B3-B4

^{13}C NMR: (a) *o*-DITFB: δ 148.2(meta, C—F), 140.5 (ortho, C—F)), 92.62 (C—I) ppm; (b) **9** δ 148.4-147.3(meta, C—F), 139.8-138.8 (ortho, C—F)), 101.40 and 98.63 (C—I), 26.0, 25.4, 24.7, 24.2 ($C_\alpha H_2$), 22.1, 21.0 ($C_\beta H_2$), 19.5 ($C_\gamma H_2$), 15.12,14.9, 14.3, 13.0 (CH_3) ppm; (c) **8** δ 148.1-147.1(meta, C—F), 139.8-138.6 (ortho, C—F)), 102.54, 101.41, 100.23, 97.85 (C—I), 25.7-24.1 ($C_\alpha H_2$), 21.8, 20.6, 19.7, 19.0 ($C_\beta H_2$), 15.3, 15.0, 13.9, 13.6 ($C_\gamma H_2$), 12.5,12.0 (CH_3) ppm.

Figure B5

^{13}C NMR: (a) *p*-DITFB: δ 147.3(C—F), 76.50 (C—I) ppm; (b) **6** δ 146.5 (C—F), 80.20 (C—I), Ph_4: 138.1, 135.5, 133.6, 132.1, 117.5, 116.5 ppm.

Figure B6

^{13}C NMR: (a) *p*-DIB: δ 141.2- 139.5 (C—F)), 97.13 (C—I) ppm; (b) **7** δ 140.7 (C—F, m), 99.50 (C—I), Ph_3: 120.4, 115.2, 137.0, 135.4, 134.6, 133.1, 131.7, 131.0, 127.8 ppm (CH), 19.4 (CH_2), 9.9 (CH_3) ppm.

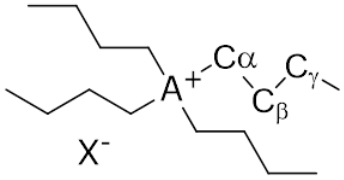

Figure B.7 Figure showing the substituent labels for the butyl chains, where A is either phosphorus or nitrogen and X is chlorine or bromine.

Elemental Analysis (C, H, N, S):

6 Calc., Found for $C_{42}H_{20}ClF_{12}I_6P$: C (31.92, 32.37), H(1.28, 1.20).

10 Calc., Found for $C_{31}H_{22}Cl_3F_4I_2P$: C (43.21, 43.60), H(2.57, 2.59).

8 Calc., Found for $C_{66}H_{108}Cl_3F_{12}I_6P_3$: C (37.92, 37.96), H(5.21, 5.28).

9 Calc., Found for $C_{22}H_{36}BrF_4I_2P$: C (35.65, 35.90), H(4.90, 5.09).

7 Calc., Found for $C_{46}H_{44}Br_2I_2P_2$: C (51.52, 50.97), H(4.14, 4.14).

Elemental analyses were performed by Elena Nadezhina and Francine Bélanger-Gariépy at the Laboratoire d'Analyse Elementaire de l'Université de Montréal.

^{81}Br Static SSNMR Spectra of Simulations Without CSA

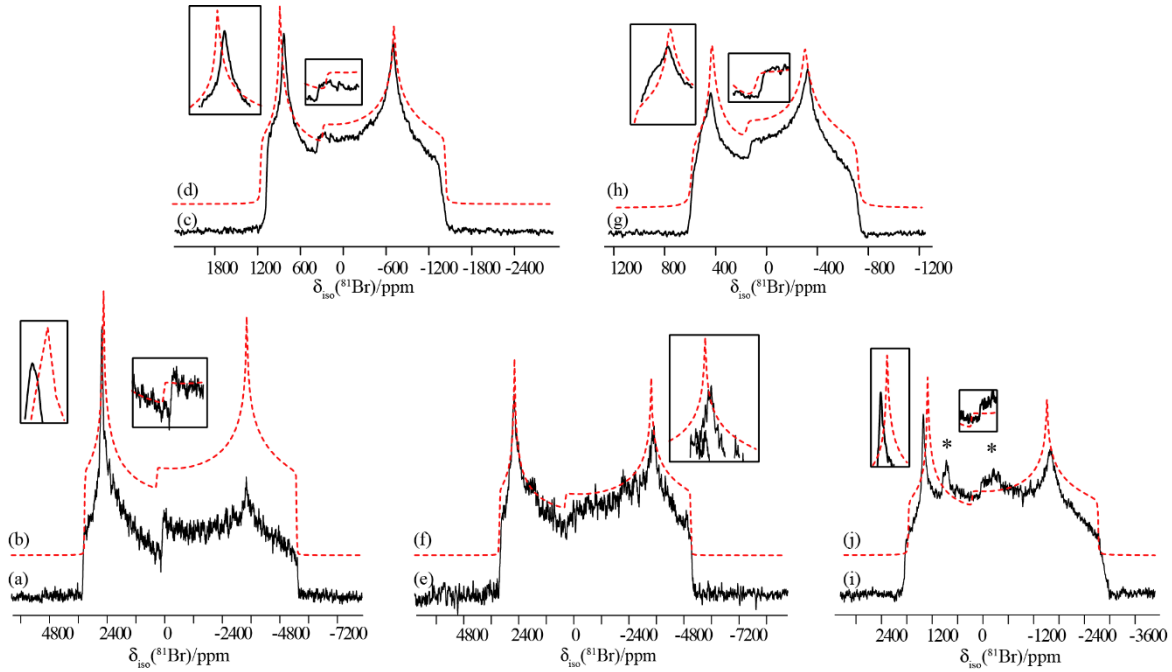

Figure B.8 ^{81}Br solid-state NMR spectra of stationary powdered halogen-bonded compounds acquired at 21.1 T. Experimental spectra are shown in (a) **4**, (c) **9**, (e) **4**, (g) **7**, (k) **5** and their respective simulated spectra with no CSA are in (b), (d), (f), (h), and (j). Asterisks in (i) mark an impurity. Insets highlight the mismatch between experimental and simulated spectra when CSA is excluded from the fits.

NLMO Analysis of XB Compounds

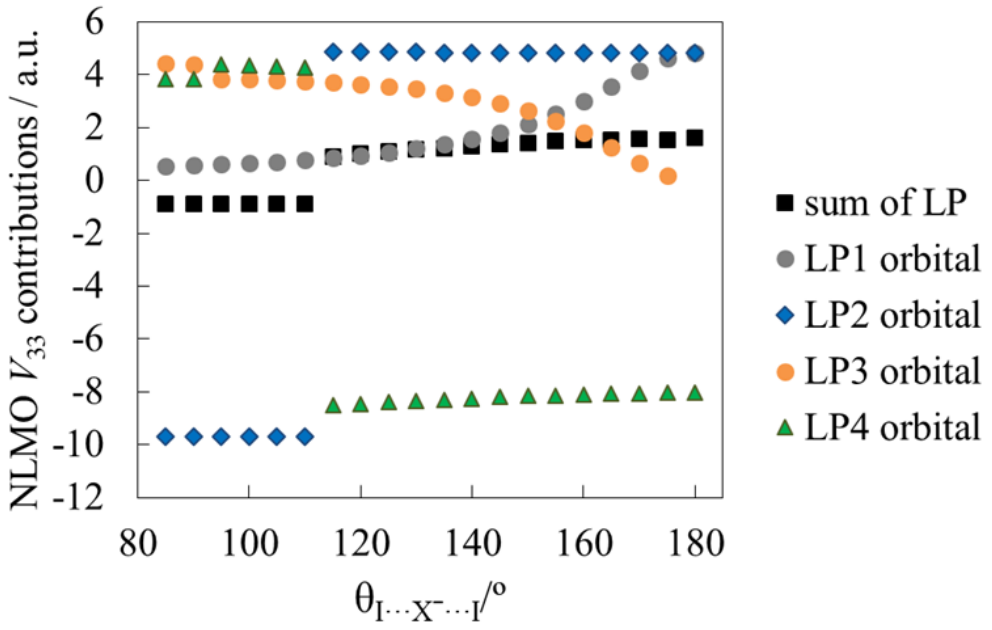

Figure B.9 Plot of calculated lone pair NLMO contributions to V_{33} for ^{35}Cl in a $F_3C—I\cdots Cl^-\cdots I—CF_3$ model system, where the $I\cdots Cl^-\cdots I$ angle is varied systematically between 85 and 180° in 5° increments. It can be observed that changes due to contributions from the LP1 and LP3 orbitals cancel each other out. The main lone pair orbitals which have an effect on the sum of the lone pair orbital contribution of the chloride anion are LP2 and LP4, and are presented in Figure 4.16 of the dissertation.

Table B.4 Analysis of Calculated Chlorine EFG Tensor NLMO Contributions to the Largest Principal Component (V_{33}) in a Model Halogen-Bonded Compound, $F_3C—I\cdots Cl^-\cdots I—CF_3$.[a]

$\theta_{I\cdots Cl^-\cdots I}$ / °	sum (LP)	LP1	LP2	LP3	LP4	core (Cl^-)[b]	sum[c]	V_{33}
85	-0.884	0.530	-9.710	4.442	3.854	-0.097	-0.981	-0.829
90	-0.883	0.569	-9.709	4.408	3.849	-0.096	-0.979	-0.831
95	-0.887	0.611	-9.709	3.835	4.376	-0.096	-0.983	-0.833
100	-0.887	0.659	-9.707	3.816	4.345	-0.096	-0.983	-0.834
105	-0.884	0.715	-9.705	3.791	4.315	-0.096	-0.980	-0.834
110	-0.882	0.780	-9.702	3.755	4.285	-0.095	-0.977	-0.833
115	0.914	0.865	4.854	3.712	-8.517	0.105	1.019	0.871
120	1.002	0.956	4.853	3.650	-8.457	0.112	1.114	0.954
125	1.080	1.065	4.851	3.569	-8.405	0.126	1.206	1.034
130	1.157	1.197	4.848	3.465	-8.353	0.137	1.294	1.112
135	1.234	1.358	4.845	3.330	-8.299	0.145	1.379	1.185
140	1.299	1.557	4.841	3.155	-8.254	0.154	1.453	1.254
145	1.373	1.808	4.837	2.935	-8.207	0.160	1.533	1.318
150	1.430	2.122	4.834	2.640	-8.166	0.168	1.598	1.376
155	1.477	2.512	4.830	2.265	-8.130	0.175	1.652	1.427
160	1.519	2.993	4.827	1.800	-8.101	0.183	1.702	1.472
165	1.553	3.555	4.823	1.251	-8.076	0.188	1.741	1.507
170	1.578	4.143	4.821	0.671	-8.057	0.189	1.767	1.533
175	1.593	4.626	4.820	0.193	-8.046	0.194	1.787	1.549
180	1.610	4.820	4.820	< 0.08	-8.042	0.192	1.790	1.554

[a] Scalar relativistic ADF calculation (LDA VWN, GGA rev PBE; AUG/ATZP basis set for chloride and ZORA/TZP for the other atoms).

[b] Sum of all Lewis and non-Lewis contributing orbitals. The 'lone pair' sum contains contributions from four contributing NLMOs which may be approximated as three '*p*' and one '*s*' type.

[c] Sum of 'core' and 'sum(LP)'. Values obtained in this way differ from the total calculated V_{33} (final column) because not all of the contributions are printed.

ZORA-DFT Calculations of ^{13}C Chemical Shifts and Assignments

Table B.5 Calculated $\delta_{iso}(^{13}C)$ and assignments for compounds with o-DITFB as XB donors

compound	output #	$d_{I\cdots C}$ /Å	δ_{iso} (^{13}C) / ppm	Figure of XB compound and C# output
o-DITFB	2	2.0833	103.41	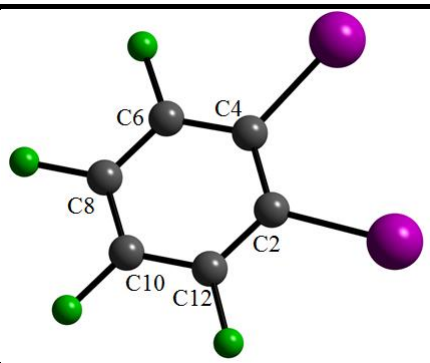
	4	2.0823	99.71	
	6		148.80	
	8		142.19	
	10		144.44	
	12		150.28	
9	15	2.1047	104.98	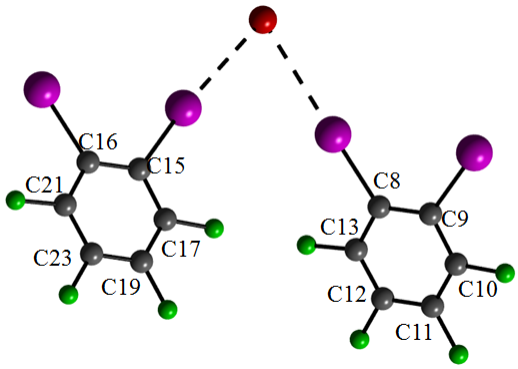
	8	2.10843	110.00	
	9		93.25	
	10		146.96	
	11		140.96	
	12		142.76	
	13		147.14	
	16		96.46	
	17		147.08	
	19		141.91	
	21		147.87	
	23		142.79	
8 Cl1	4	2.0968	102.45	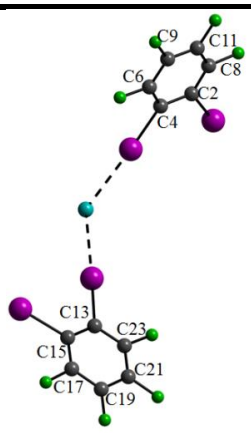
	13	2.1174	116.19	
	2		85.37	
	6		147.27	
	8		144.11	
	9		144.11	
	11		143.85	
	15		106.5	
	17		145.95	
	19		140.34	
	21		143.55	
	23		143.81	
Cl2	15	2.0868	182.01	

	2	2.1156	181.98	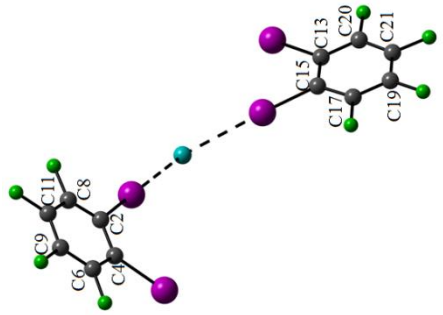
	4		184.10	
	6		184.10	
	8		184.10	
	9		184.10	
	11		184.10	
	13		184.10	
	17		184.10	
	19		184.10	
	20		184.10	
	21		184.10	
Cl3	2	2.0944	128.16	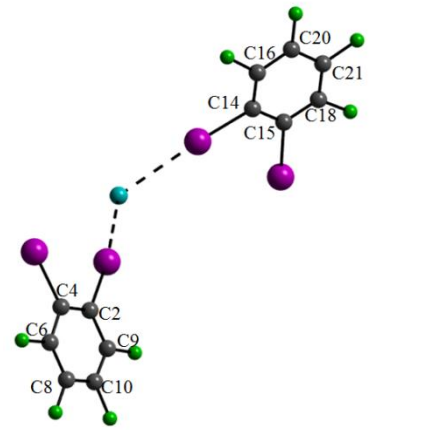
	14	2.115	96.98	
	4		111.88	
	6		150.91	
	8		136.43	
	9		146.91	
	10		138.81	
	15		78.98	
	16		141.41	
	18		142.42	
	20		147.78	
	21		148.41	

*Table B.6 Calculated $\delta_{iso}(^{13}C)$ and assignment for compound **7** and p-DIB as XB donors*

compound	output #	$d_{I\text{—}C}$ /Å	δ_{iso} (^{13}C) / ppm	Figure of XB compound and C# output
p-DIB	2	2.09635	105.86	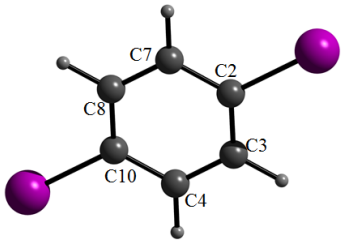
	12	2.09635	105.86	
	4		136.48	
	6		138.68	
	8		138.68	
	10		136.48	
7	2	2.11257	113.43	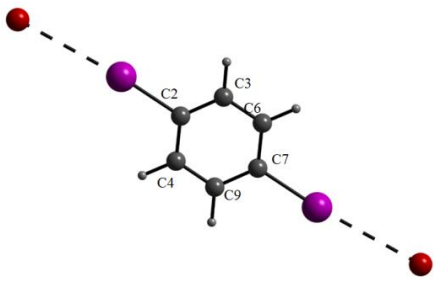
	7	2.11257	113.43	
	3		132.72	
	4		134.22	
	6		134.22	
	9		132.72	

*Table B.7 Calculated $\delta_{iso}(^{13}C)$ and assignment for compound **6** and p-DITFB as XB donors*

compound	output #	$d_{I—C}$ /Å	δ_{iso} (^{13}C) / ppm	Figure of XB compound and C# output
6 Cl1	28	2.0931	84.86	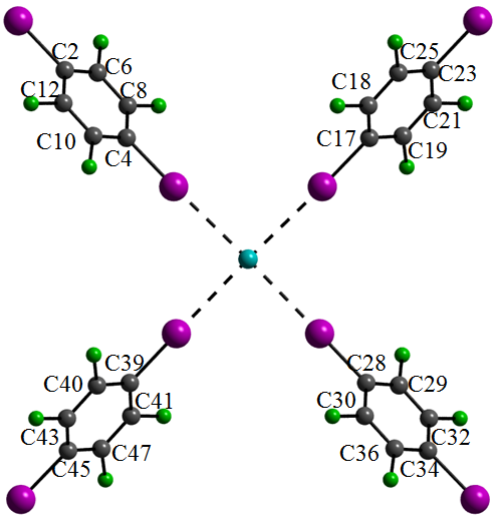
	39	2.0931	96.18	
	4	2.0952	94.42	
	17	2.0952	82.78	
	2		76.41	
	6		147.40	
	8		148.80	
	10		148.15	
	12		146.60	
	18		148.87	
	19		148.42	
	21		146.46	
	23		85.83	
	25		147.36	
	29		149.41	
	30		148.66	
	32		146.85	
	34		84.00	
	36		146.41	
	40		149.07	
	41		148.48	
	43		146.95	
	45		74.40	
	47		146.51	
Cl2	8		106.45	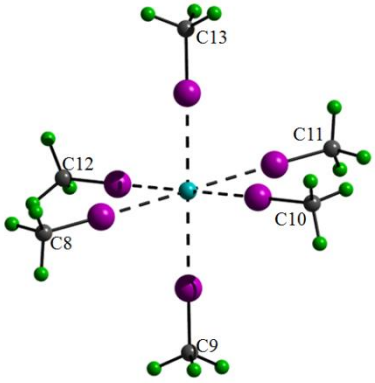
	9		108.08	
	10		107.14	
	11		106.30	
	12		107.37	
	13		108.06	

APPENDIX C: COMPLEMENTARY DATA FOR CHAPTER 5

Experimental Details for CPMAS SSNMR Experiments

Table C.1 Experimental parameters used for the acquisition of ^{13}C, ^{31}P, and ^{77}Se NMR CPMAS spectra

	B_0 / T	nuclide	window / kHz	points	MAS / Hz	$\pi/2$ pulse / µs	scans	contact times / µs	recycle delay	decoupling
11	9.4	^{13}C	340	3k	8k	3.25	4204	5000	35	Spinal64
	9.4	^{31}P	400	4k	3k	2.5	307	5000	6	TPPM
	11.75	^{31}P	494	4k	10k	4.5	2865	2000	20	CW
	9.4	^{77}Se	494	4k	6.5k	3.75	5568	20000	30	CW
	9.4	^{77}Se	1489	2k	8k	3.75	2512	20000	34	CW
12	9.4	^{13}C	338	3k	5k	3.25	1200	5000	10	Spinal64
	9.4	^{31}P	400	4k	2.1k	2.5	504	5000	6	TPPM
	11.75	^{31}P	494	4k	10k	4.5	1089	2000	30	CW
	9.4	^{77}Se	1489	4k	3.2k	3.70	6592	20000	20	CW
	9.4	^{77}Se	820	6k	5k	7.0	2392	5000	100	CW
	11.75	^{77}Se	1048	8k	3k	2.8	1024	20000	100	CW
	21.1	^{77}Se	1533	8k	10k	4.0	2560	20000	30	CW
13	9.4	^{13}C	354	3k	10k	3.50	6060	2000	15	Spinal64
	9.4	^{31}P	400	4k	3k	3.00	600	5000	5	TPPM
	11.75	^{31}P	494	4k	10k	4.50	2400	2000	30	CW
	9.4	^{77}Se	494	4k	5.5k	3.75	3280	20000	30	CW
	9.4	^{77}Se	1489	4k	8k	3.75	2744	20000	30	CW

NLMO Analysis of XB Compounds

Table C.2 Hybridization/polarization analysis of NLMOs.[a,b]

compound			NLMO #	Orbital type/%	Percent from parent NBO/%	Atomic hybrid contribution
11	(Ph_3PSe)(*p*-$C_6F_4I_2$)	Site 1	161	LP Se	0.14 I	1s(10.28%)p8.56(87.94%)d0.17(1.78%)
					98.72 Se	27s(87.52%)p0.14(12.47%)d0.00(0.01%)
			61	BD P-Se	0.06 I	1s(9.83%)p9.01(88.51%)d0.17(1.66%)
					46.26 Se	27s(12.61%)p6.86(86.56%)d0.07(0.82%)
					52.14 P	28s(32.63%)p2.05(66.79%)d0.02(0.57%)
		Site 2	238	LP Se	0.11 I	1s(10.43%)p8.43(87.91%)d0.16(1.67%)
					98.74 Se	35s(87.83%)p0.14(12.16%)d0.00(0.01%)
			76	BD P-Se	0.06 I	1s(12.08%)p7.15(86.35%)d0.131.57%)
					46.48 Se	35s(12.19%)p7.13(86.97%)d0.07(0.83%)
					51.78 P	36s(31.32%)p2.17(68.09%)d0.02(0.58%)
12	(Ph_3PSe)(*o*-$C_6F_4I_2$)		238	LP Se	0.14 I	1s(9.37%)p9.51(89.05%)d0.17(1.58%)
					98.66 Se	35s(87.94%)p0.14(12.04%)d0.00(0.01%)
			201	Cr Se	98.98 Se	1s(9.37%)p9.51(89.05%)d0.17(1.58%)
					0.01 P	36s(20.40%)p2.80(57.16%)d1.10(22.45%)
13	(Ph_3PSe)(*sym*-$C_6F_3I_3$)	Site 1	195	LP Se	0.07 I	1s(8.92%)p10.04(89.65%)d0.16(1.43%)
					98.85 Se	31s(87.59%)p0.14(12.40%)d0.00(0.01%)
			61	BD P-Se	0.04 I	1s(6.90%)p13.28(91.65%)d0.21(1.45%)
					46.13 Se	31s(12.51%)p6.93(86.66%)d0.07(0.83%)
					52.17 P	32s(32.16%)p2.09(67.28%)d0.02(0.57%)
		Site 2	186	LP Se	0.09 I	1s(8.64%)p10.27(88.75%)d0.30(2.61%)
					98.72 Se	4s(87.76%)p0.14(12.22%)d0.00(0.01%)
				BD P-Se	0.05 I	1s(11.26%)p7.70(86.65%)d0.19(2.09%)
					46.71 Se	4s(12.36%)p7.02(86.78%)d0.07(0.86%)
					51.56	5s(31.24%)p2.18(68.16%)d0.02(0.60%)

[a] Selected largest NLMO contributions.

[b] See J. Autschbach, *J. Chem. Phys.*, 2007, **127**, 124106 for further information on the output.

APPENDIX D: GENERAL CRYSTALLOGRAPHIC DATA AND INPUT FILES

X-ray Crystal Structures

Table D.1 Summary of XB Compounds and Symbol used in the Dissertation as well as the Cambridge Crystallographic Data Center Reference Number and Publication Journal Reference of the Crystal Structures

XB compound	Chapter	Symbol	CCDC ref code	Published in
[(*n*-Bu_4NCl)(*p*-$C_6F_4I_2$)]	3,4	**1**	907313	*b*
[(*n*-Bu_4PCl)(*p*-$C_6F_4I_2$)]		**2**	907312	*b*
[(*n*-Bu_4PBr)(*p*-$C_6F_4I_2$)]		**3**	907314	*b*
[(*n*-Bu_4NBr)(*p*-$C_6F_4I_2$)]		**4**	731757	*e*
[($EtPh_3PBr$)$_2$(*p*-$C_6F_4I_2$)]		**5**	907315	*b*
[(Ph_4PCl)(*p*-$C_6F_4I_2$)]		**6**	n.a.	*a*
[($EtPh_3PBr$)$_2$(*p*-$C_6H_4I_2$)]		**7**	n.a.	*a*
[(*n*-Bu_4PCl)(*o*-$C_6F_4I_2$)]	4	**8**	n.a.	*a*
[(*n*-Bu_4PBr)(*o*-$C_6F_4I_2$)]		**9**	n.a.	*a*
[(Ph_4PCl)(*o*-$C_6F_4I_2$)]·(CH_2Cl_2)$_2$		**10**	n.a.	*a*
[(Ph_3PSe)(*p*-$C_6F_4I_2$)]	5	**11**	660406	*f*
[(Ph_3PSe)(*o*-$C_6F_4I_2$)]		**12**	987457	*c*
[(Ph_3PSe)(*sym*-$C_6F_3I_3$)]		**13**	987456	*c*
[(Me_4NSeCN)(*o*-$C_6F_4I_2$)$_2$]	6	**14**	863466	*d*
[(Me_4NSeCN)(*p*-$C_6F_4I_2$)$_2$]		**15**	863467	*d*
[(*n*-Bu_4NSCN)(*p*-$C_6F_4I_2$)]		**16**	739583	*g*
[(Me_4NSCN)(*p*-$C_6F_4I_2$)$_2$]		**17**	863465	*d*

[a] J. Viger-Gravel, S. Leclerc, I. Korobkov, D. L. Bryce, (2013) *CrystEngComm*, 15, 3168-3177. [b] J. Viger-Gravel, S. Leclerc, I. Korobkov, D. L. Bryce, (2014) *J. Am. Chem. Soc.*, 136, 6929-6942. [c] J. Viger-Gravel, J. E. Meyer, I. Korobkov, D. L. Bryce, (2014) *CrystEngComm*, 16, 7285-7297. [d] J. Viger-Gravel, I. Korobkov, D. L. Bryce, (2011) *Cryst. Growth Des.*, 11, 4984-4995. [e] A. Abate, S. Biella, G. Cavallo, F. Meyer, H. Neukirch, P. Metrangolo, T. Pilati, G. Resnati, G. Terraneo, (2009) *J. Fluorine Chem*., 130, 1171-1177. [f] H. D. Arman, E. R. Rafferty, C. A. Bayse, W. T. Pennington (2012) *Cryst. Growth Des.*, 12, 4315-4323. [g] P. Cauliez, V. Polo, T. Roisnel, R. Llusar, M. Fourmigué (2010) *CrystEngComm*, 12, 558-566.

Example of Quantum Calculation Input files

ADF – CS tensors calculation with relativistic effects

```
#!/bin/bash
#$ -N CStensor.run
#$ -S /bin/bash

#$ -m be

#$ -o CStensor.out
#$ -e CStensor.err

#$ -cwd
#$ -V

#$ -pe dist.pe 12

#!/bin/sh

$ADFBIN/adf << eor
CS tensor of XB compound 1

Basis
 Cl AUG/ATZP/Cl
 Type ZORA/TZP
 core none
End

Symmetry NOSYM

relativistic spinorbit zora

Atoms
 I                   0.76000000    0.32230000   13.96340000
 I                   0.26580000    0.04870000   18.89410000
 Cl                  2.22360000    0.61220000   16.55190000
 F                   0.11450000    2.40090000   11.60300000
 F                  -1.01190000    2.34880000   20.65460000
 C                  -0.21090000    0.12650000   12.10370000
 C                  -0.38800000    1.20470000   11.26020000
 C                  -0.97420000   -0.00170000   20.58380000
 C                  -1.38700000    1.17480000   21.18320000
 C                  -1.39240000   -1.17530000   21.17430000
 F                  -1.02140000   -2.35080000   20.64330000
 C                  -2.17800000   -1.17520000   22.30070000
 F                  -2.55310000   -2.34860000   22.82930000
 C                  -2.59110000    0.00180000   22.90010000
 I                  -3.83090000   -0.04880000   24.58980000
 C                  -2.17270000    1.17530000   22.30960000
 F                  -2.54370000    2.35080000   22.84060000
 C                  -1.05430000    1.08390000   10.06260000
 F                  -1.18290000    2.17070000    9.27640000
 C                  -1.57150000   -0.12680000    9.63820000
 I                  -2.54280000   -0.32230000    7.77860000
 C                  -1.39440000   -1.20430000   10.48180000
```

```
 F                 -1.89690000   -2.40110000   10.13890000
 C                 -0.72830000   -1.08390000   11.67930000
 F                 -0.59960000   -2.17070000   12.46550000
End

Integration 6.0

charge -1

XC
   GGA revPBE
End

End Input
eor

$ADFBIN/nmr << eor
NMR
  U1K BEST
  Out TENS
  Atoms all
  SCF 1.d-4
END
eor
```

ADF – NLMO analysis of EFG tensors

```
#!/bin/bash
#$ -N EFGNLMO.run
#$ -S /bin/bash

#$ -m be

#$ -o test.out
#$ -e test.err

#$ -cwd
#$ -V

#$ -pe dist.pe 32

#!/bin/sh

$ADFBIN/adf <<eor
EFG NLMO calculation for XB compound 2- EFG calc

Atoms
 I                  0.76000000    0.32230000   13.96340000
 I                  0.26580000    0.04870000   18.89410000
 Cl                 2.22360000    0.61220000   16.55190000
 F                  0.11450000    2.40090000   11.60300000
 F                 -1.01190000    2.34880000   20.65460000
```

```
 C                  -0.21090000    0.12650000   12.10370000
 C                  -0.38800000    1.20470000   11.26020000
 C                  -0.97420000   -0.00170000   20.58380000
 C                  -1.38700000    1.17480000   21.18320000
 C                  -1.39240000   -1.17530000   21.17430000
 F                  -1.02140000   -2.35080000   20.64330000
 C                  -2.17800000   -1.17520000   22.30070000
 F                  -2.55310000   -2.34860000   22.82930000
 C                  -2.59110000    0.00180000   22.90010000
 I                  -3.83090000   -0.04880000   24.58980000
 C                  -2.17270000    1.17530000   22.30960000
 F                  -2.54370000    2.35080000   22.84060000
 C                  -1.05430000    1.08390000   10.06260000
 F                  -1.18290000    2.17070000    9.27640000
 C                  -1.57150000   -0.12680000    9.63820000
 I                  -2.54280000   -0.32230000    7.77860000
 C                  -1.39440000   -1.20430000   10.48180000
 F                  -1.89690000   -2.40110000   10.13890000
 C                  -0.72830000   -1.08390000   11.67930000
 F                  -0.59960000   -2.17070000   12.46550000
End

charge -1

xc
 lda vwn
 gga revPBE
end

Relativistic scalar ZORA

Integration
 accint 4.5
 accsph 5.5
End

Basis
Cl AUG/ATZP/Cl
CORE NONE
TYPE ZORA/TZP
End

FULLFOCK
AOMAT2FILE
SAVE TAPE15
SYMMETRY NOSYM

Qtens

End Input
eor

$ADFBIN/adfnbo <<eor
write
fock
```

```
spherical
end input
eor

$ADFBIN/gennbo < FILE47

$ADFBIN/adf <<eor
EFG NLMO calculation for XB compound 2- generate NBO

Atoms
 I                   0.76000000    0.32230000   13.96340000
 I                   0.26580000    0.04870000   18.89410000
 Cl                  2.22360000    0.61220000   16.55190000
 F                   0.11450000    2.40090000   11.60300000
 F                  -1.01190000    2.34880000   20.65460000
 C                  -0.21090000    0.12650000   12.10370000
 C                  -0.38800000    1.20470000   11.26020000
 C                  -0.97420000   -0.00170000   20.58380000
 C                  -1.38700000    1.17480000   21.18320000
 C                  -1.39240000   -1.17530000   21.17430000
 F                  -1.02140000   -2.35080000   20.64330000
 C                  -2.17800000   -1.17520000   22.30070000
 F                  -2.55310000   -2.34860000   22.82930000
 C                  -2.59110000    0.00180000   22.90010000
 I                  -3.83090000   -0.04880000   24.58980000
 C                  -2.17270000    1.17530000   22.30960000
 F                  -2.54370000    2.35080000   22.84060000
 C                  -1.05430000    1.08390000   10.06260000
 F                  -1.18290000    2.17070000    9.27640000
 C                  -1.57150000   -0.12680000    9.63820000
 I                  -2.54280000   -0.32230000    7.77860000
 C                  -1.39440000   -1.20430000   10.48180000
 F                  -1.89690000   -2.40110000   10.13890000
 C                  -0.72830000   -1.08390000   11.67930000
 F                  -0.59960000   -2.17070000   12.46550000
End

charge -1

xc
 lda vwn
 gga revPBE
end

Relativistic scalar ZORA

Integration
 accint 4.5
 accsph 5.5
End

Basis
Cl AUG/ATZP/Cl
CORE NONE
TYPE ZORA/TZP
```

```
End

Qtens

FULLFOCK
AOMAT2FILE
SAVE TAPE15
SYMMETRY NOSYM

Aoresponse
donothing
end

Qtens

End Input
eor

$ADFBIN/adfnbo <<eor
write
fock
spherical
end input
eor

$ADFBIN/gennbo < FILE47

$ADFBIN/adfnbo <<eor
copy
fock
spherical
end input
eor

$ADFBIN/adfnbo <<eor
read
fock
spherical
end input
eor

$ADFBIN/adf <<eor
EFG NLMO calculation for XB compound 2- generate MO to be viewed

Atoms
 I                  0.76000000    0.32230000   13.96340000
 I                  0.26580000    0.04870000   18.89410000
 Cl                 2.22360000    0.61220000   16.55190000
 F                  0.11450000    2.40090000   11.60300000
 F                 -1.01190000    2.34880000   20.65460000
 C                 -0.21090000    0.12650000   12.10370000
 C                 -0.38800000    1.20470000   11.26020000
 C                 -0.97420000   -0.00170000   20.58380000
 C                 -1.38700000    1.17480000   21.18320000
 C                 -1.39240000   -1.17530000   21.17430000
```

```
 F                  -1.02140000   -2.35080000   20.64330000
 C                  -2.17800000   -1.17520000   22.30070000
 F                  -2.55310000   -2.34860000   22.82930000
 C                  -2.59110000    0.00180000   22.90010000
 I                  -3.83090000   -0.04880000   24.58980000
 C                  -2.17270000    1.17530000   22.30960000
 F                  -2.54370000    2.35080000   22.84060000
 C                  -1.05430000    1.08390000   10.06260000
 F                  -1.18290000    2.17070000    9.27640000
 C                  -1.57150000   -0.12680000    9.63820000
 I                  -2.54280000   -0.32230000    7.77860000
 C                  -1.39440000   -1.20430000   10.48180000
 F                  -1.89690000   -2.40110000   10.13890000
 C                  -0.72830000   -1.08390000   11.67930000
 F                  -0.59960000   -2.17070000   12.46550000
End

charge -1

xc
 lda vwn
 gga revPBE
end

Relativistic scalar ZORA

Integration
 accint 4.5
 accsph 5.5
End

Basis
Cl AUG/ATZP/Cl
CORE NONE
TYPE ZORA/TZP
End

Qtens

FULLFOCK
AOMAT2FILE
SAVE TAPE15
SYMMETRY NOSYM

Aoresponse
 efg 5 nbo
end

Qtens

End Input
eor

$ADFBIN/adfnbo <<eor
write
```

```
fock
spherical
end input
eor

$ADFBIN/gennbo < FILE47

$ADFBIN/adfnbo <<eor
copy
fock
spherical
end input
eor

$ADFBIN/adfnbo <<eor
read
fock
spherical
end input
eor
```

ADF– NLMO analysis of J-coupling

Input file to calculate J-coupling values and determine NLMO contribution

```
#!/bin/bash
#$ -N JcouplingNLMO.run
#$ -S /bin/bash

#$ -m be

#$ -o test.out
#$ -e test.err

#$ -cwd
#$ -V

#$ -pe dist.pe 28

#!/bin/sh

$ADFBIN/adf << eor

ATOMS
 I                 -3.06460000   10.65700000    2.75020000
 C                 -4.07740000   11.28390000    1.07750000
 Se                -2.14160000    9.48580000    5.79890000
 P                 -0.58520000    8.06660000    5.64030000
 C                  1.06310000    8.82020000    5.56250000
 C                 -0.58350000    6.92900000    7.05660000
 C                 -0.65490000    7.01350000    4.16100000
```

```
 F                  -3.48060000   13.55290000    1.43380000
 C                  -4.14280000   12.64720000    0.73850000
 F                  -4.92460000   14.34830000   -0.60460000
 C                  -4.90290000   13.03200000   -0.34550000
 C                  -4.78510000   10.43220000    0.34540000
 C                  -5.61050000   12.18030000   -1.07760000
 C                   2.10820000    8.33700000    4.77000000
 C                   1.29700000    9.91130000    6.37870000
 C                   2.53780000   10.50740000    6.41110000
 C                   3.56000000   10.00290000    5.62950000
 C                   3.36080000    8.94940000    4.79820000
 C                   0.47100000    6.07730000    7.27900000
 C                  -1.69380000    6.87730000    7.92660000
 C                   0.44040000    5.19740000    8.35210000
 C                  -0.64730000    5.17380000    9.22440000
 C                  -1.70050000    6.01380000    9.01280000
 C                  -0.79290000    5.63620000    4.21920000
 C                  -0.61960000    7.63760000    2.90860000
 C                  -0.92260000    4.91820000    3.04020000
 C                  -0.89730000    5.55410000    1.83320000
 C                  -0.74260000    6.91270000    1.76640000
 H                   0.47950000   10.31650000    6.98200000
 H                   2.71430000   11.36900000    7.06010000
 H                   4.54340000   10.48460000    5.66650000
 H                   4.16510000    8.56460000    4.16650000
 H                   1.94530000    7.47920000    4.11350000
 H                   1.34900000    6.08890000    6.62870000
 H                   1.28720000    4.52710000    8.52220000
 H                  -0.64380000    4.48580000   10.07530000
 H                  -2.56280000    6.00950000    9.68570000
 H                  -2.53330000    7.55320000    7.74610000
 H                  -0.83160000    5.11530000    5.17730000
 H                  -1.04670000    3.83250000    3.08910000
 H                  -1.00660000    4.97130000    0.91290000
 H                  -0.72180000    7.41860000    0.79710000
 H                  -0.50430000    8.72200000    2.85400000
 F                  -4.76330000    9.11590000    0.60450000
 C                  -5.54510000   10.81700000   -0.73860000
 F                  -6.20740000    9.91130000   -1.43390000
 I                  -6.62340000   12.80720000   -2.75030000
END

save TAPE15
FULLFOCK
AOMAT2FILE

BASIS
 type ZORA/DZP
 core None
END

XC
  metaGGA TPSS
End
```

```
SCF
 converge 1.0e-8
END

SYMMETRY nosym

INTEGRATION
 accint 4.5
 accsph 5.5
end

relativistic scalar zora

end input
eor

$ADFBIN/adfnbo << eor
write
spherical
fock
TESTJOB
end input
eor

rm adfnbo.37 adfnbo.39 adfnbo.49 adfnbo.48
cp TAPE21 NLMO.t21
$ADFBIN/gennbo < FILE47

$ADFBIN/adfnbo << eor
 copy
 spherical
 fock
end input
eor

$ADFBIN/adfnbo << eor
 spherical
 fock
 read
end input
eor

rm adfnbo.37 adfnbo.39 adfnbo.49 adfnbo.48

rm TAPE15 TAPE21 TAPE13 logfile

$ADFBIN/cpl << eor
maxmemoryusage 40
nmrcoupling
atompert {3}
atomresp {4}
 dso
 pso
 sd
 fc
```

```
 scf {convergence=1e-7}
 contributions 1e19 nbo
end
endinput
eor

rm TAPE15 TAPE21 TAPE13 logfile

$ADFBIN/adf << eor
ATOMS
 I                 -3.06460000   10.65700000    2.75020000
 C                 -4.07740000   11.28390000    1.07750000
 Se                -2.14160000    9.48580000    5.79890000
 P                 -0.58520000    8.06660000    5.64030000
 C                  1.06310000    8.82020000    5.56250000
 C                 -0.58350000    6.92900000    7.05660000
 C                 -0.65490000    7.01350000    4.16100000
 F                 -3.48060000   13.55290000    1.43380000
 C                 -4.14280000   12.64720000    0.73850000
 F                 -4.92460000   14.34830000   -0.60460000
 C                 -4.90290000   13.03200000   -0.34550000
 C                 -4.78510000   10.43220000    0.34540000
 C                 -5.61050000   12.18030000   -1.07760000
 C                  2.10820000    8.33700000    4.77000000
 C                  1.29700000    9.91130000    6.37870000
 C                  2.53780000   10.50740000    6.41110000
 C                  3.56000000   10.00290000    5.62950000
 C                  3.36080000    8.94940000    4.79820000
 C                  0.47100000    6.07730000    7.27900000
 C                 -1.69380000    6.87730000    7.92660000
 C                  0.44040000    5.19740000    8.35210000
 C                 -0.64730000    5.17380000    9.22440000
 C                 -1.70050000    6.01380000    9.01280000
 C                 -0.79290000    5.63620000    4.21920000
 C                 -0.61960000    7.63760000    2.90860000
 C                 -0.92260000    4.91820000    3.04020000
 C                 -0.89730000    5.55410000    1.83320000
 C                 -0.74260000    6.91270000    1.76640000
 H                  0.47950000   10.31650000    6.98200000
 H                  2.71430000   11.36900000    7.06010000
 H                  4.54340000   10.48460000    5.66650000
 H                  4.16510000    8.56460000    4.16650000
 H                  1.94530000    7.47920000    4.11350000
 H                  1.34900000    6.08890000    6.62870000
 H                  1.28720000    4.52710000    8.52220000
 H                 -0.64380000    4.48580000   10.07530000
 H                 -2.56280000    6.00950000    9.68570000
 H                 -2.53330000    7.55320000    7.74610000
 H                 -0.83160000    5.11530000    5.17730000
 H                 -1.04670000    3.83250000    3.08910000
 H                 -1.00660000    4.97130000    0.91290000
 H                 -0.72180000    7.41860000    0.79710000
 H                 -0.50430000    8.72200000    2.85400000
 F                 -4.76330000    9.11590000    0.60450000
 C                 -5.54510000   10.81700000   -0.73860000
```

```
 F                 -6.20740000    9.91130000   -1.43390000
 I                 -6.62340000   12.80720000   -2.75030000
END

BASIS
 type ZORA/DZP
 core None
END

XC
  metaGGA TPSS
End

SYMMETRY nosym

SCF
 converge 1.0e-8
END

INTEGRATION
 accint 4.5
 accsph 5.5
end

relativistic spinorbit zora

end input
eor

rm TAPE15

$ADFBIN/cpl << eor
maxmemoryusage 40
nmrcoupling
atompert {3}
atomresp {4}
 dso
 pso
 sd
 fc
 scf {convergence=1e-7}
 contributions 1e19 nbo
end
endinput
eor
```

Input file to generate NLMO which can be viewed in ADFVIEW

```
#!/bin/bash
#$ -N NLMO.run
#$ -S /bin/bash

#$ -m be

#$ -o NLMO.out
```

```
#$ -e NLMO.err

#$ -cwd
#$ -V

#$ -pe dist.pe 12

#!/bin/sh

$ADFBIN/adf << eor

ATOMS
 I                 -3.06460000   10.65700000    2.75020000
 C                 -4.07740000   11.28390000    1.07750000
 Se                -2.14160000    9.48580000    5.79890000
 P                 -0.58520000    8.06660000    5.64030000
 C                  1.06310000    8.82020000    5.56250000
 C                 -0.58350000    6.92900000    7.05660000
 C                 -0.65490000    7.01350000    4.16100000
 F                 -3.48060000   13.55290000    1.43380000
 C                 -4.14280000   12.64720000    0.73850000
 F                 -4.92460000   14.34830000   -0.60460000
 C                 -4.90290000   13.03200000   -0.34550000
 C                 -4.78510000   10.43220000    0.34540000
 C                 -5.61050000   12.18030000   -1.07760000
 C                  2.10820000    8.33700000    4.77000000
 C                  1.29700000    9.91130000    6.37870000
 C                  2.53780000   10.50740000    6.41110000
 C                  3.56000000   10.00290000    5.62950000
 C                  3.36080000    8.94940000    4.79820000
 C                  0.47100000    6.07730000    7.27900000
 C                 -1.69380000    6.87730000    7.92660000
 C                  0.44040000    5.19740000    8.35210000
 C                 -0.64730000    5.17380000    9.22440000
 C                 -1.70050000    6.01380000    9.01280000
 C                 -0.79290000    5.63620000    4.21920000
 C                 -0.61960000    7.63760000    2.90860000
 C                 -0.92260000    4.91820000    3.04020000
 C                 -0.89730000    5.55410000    1.83320000
 C                 -0.74260000    6.91270000    1.76640000
 H                  0.47950000   10.31650000    6.98200000
 H                  2.71430000   11.36900000    7.06010000
 H                  4.54340000   10.48460000    5.66650000
 H                  4.16510000    8.56460000    4.16650000
 H                  1.94530000    7.47920000    4.11350000
 H                  1.34900000    6.08890000    6.62870000
 H                  1.28720000    4.52710000    8.52220000
 H                 -0.64380000    4.48580000   10.07530000
 H                 -2.56280000    6.00950000    9.68570000
 H                 -2.53330000    7.55320000    7.74610000
 H                 -0.83160000    5.11530000    5.17730000
 H                 -1.04670000    3.83250000    3.08910000
 H                 -1.00660000    4.97130000    0.91290000
 H                 -0.72180000    7.41860000    0.79710000
 H                 -0.50430000    8.72200000    2.85400000
```

```
 F                  -4.76330000    9.11590000    0.60450000
 C                  -5.54510000   10.81700000   -0.73860000
 F                  -6.20740000    9.91130000   -1.43390000
 I                  -6.62340000   12.80720000   -2.75030000
END

save TAPE15

FULLFOCK
AOMAT2FILE

BASIS
 type ZORA/DZP
 core None
END

XC
  metaGGA TPSS
End

INTEGRATION
 accint 4.5
 accsph 5.5
end

SCF
 converge 1.0e-8
END

relativistic scalar zora

eor

$ADFBIN/adfnbo << eor
write
spherical
fock
TESTJOB
end input
eor

rm adfnbo.37 adfnbo.39 adfnbo.49 adfnbo.48

$ADFBIN/gennbo < FILE47

$ADFBIN/adfnbo << eor
 copy
 spherical
 fock
end input
eor

$ADFBIN/adfnbo << eor
 read
 spherical
```

```
 fock
end input
eor


rm adfnbo.37 adfnbo.39 adfnbo.49 adfnbo.48
cp TAPE21 NLMO.t21
rm TAPE15 TAPE21 logfile
```

Gaussian – Simpson Simulation of ^{77}Se CPMAS spectra with J(^{31}P,^{77}Se) coupling

```
spinsys {
       channels  77Se 31P
       nuclei    77Se 31P

      shift 1 -162.9p -139p 0.75 0 0 0
      jcoupling 1 2 -663 0 0 0 0 0
      dipole 1 2 -669 0 0 0
}

par {
       proton_frequency              400e6
       crystal_file                        zcw232
      spin_rate                     6500
       gamma_angles                 20
       verbose                      1101
       start_operator                I1x
       detect_operator               I1p
       np                                  1024
       variable sw                        100000
       variable dw                         1.0e6/sw


}

proc pulseq {} {
       global par

       for {set k 0} {$k < $par(np)} {incr k} {
              acq
              delay $par(dw)
       }
}

proc main {} {
       global par

       set f [fsimpson]

       fsave $f $par(name).fid
       faddlb $f 650 0
       fzerofill $f [expr 4*$par(np)]
       fft $f
       fsave $f $par(name).spe
}
```